

NASA-CR-198794

FINAL  
IN-20-CR  
6 REF  
0 CIT  
5059  
P-165

FINAL REPORT  
SPACE POWER SYSTEMS TECHNOLOGY  
NASA Grant Number NCC 3-23  
Cleveland State University

(NASA-CR-198794) SPACE POWER  
SYSTEMS TECHNOLOGY Final Report, 22  
Nov. 1982 - 31 Mar. 1994  
(Cleveland State Univ.) 165 p

N96-11024

Unclass

George A. Coulman  
Principal Investigator

**FINAL REPORT**

**SPACE POWER SYSTEMS TECHNOLOGY**

**NASA Grant Number NCC 3-23**

**Period of Performance, November 22, 1982 - March 31, 1994**

**Cleveland State University  
1983 East 24th Street  
Cleveland, Ohio 44115**

**George A. Coulman  
Principal Investigator**

## ABSTRACT

Reported here is a series of studies which examine several potential catalysts and electrodes for some fuel cell systems, some materials for space applications, and mathematical modeling and performance predictions for some solid oxide fuel cells and electrolyzers. The fuel cell systems have a potential for terrestrial applications in addition to solar energy conversion in space applications. Catalysts and electrodes for phosphoric acid fuel cell systems and for polymer electrolyte membrane (PEM) fuel cell and electrolyzer systems were examined.

## Table of Contents

ABSTRACT . . . . .	i
INTRODUCTION . . . . .	1
RESULTS AND DISCUSSION . . . . .	1
Phosphoric Acid Fuel Cells . . . . .	1
Materials . . . . .	3
Flight Qualified . . . . .	3
Moving Belt Radiator . . . . .	4
Regenerative Fuel Cell Systems . . . . .	4
Dedicated . . . . .	4
Unitized . . . . .	7
Solid Oxide Fuel Cells and Electrolyzers . . . . .	8
EXPERIMENTAL . . . . .	9
REFERENCES	
APPENDIX	

## Introduction

This report is a summary of studies funded by the National Aeronautics and Space Administration which address some problems inherent in energy conversion. One specific aspect of energy conversion is involved with electrocatalysis, which is one of the processes central to the conversion of solar radiation to forms useful to spacecraft and to planetary settlements. By use of regenerative fuel cells which require reliable and efficient electrocatalysis, solar energy can be stored during dark periods. The fuel cell systems have a potential for terrestrial applications in addition to solar energy conversion in space applications. Catalyst and electrodes for phosphoric acid fuel cells were developed and evaluated. Catalysts and electrodes for polymer electrolyte membrane (PEM) fuel cell and electrolyzer systems are under development and evaluation. Materials for a moving belt radiator in space and the means of qualifying materials for spaceflight missions were examined. Mathematical modeling and performance predictions for some solid oxide fuel cells and electrolyzers were developed.

This report will consist of a general reporting of what has been accomplished in the areas described above. Results which have already been published in the open literature will be summarized and commented on. The actual papers will be included as appendices. Results which have not yet been published will be reported as well.

## Results and Discussion

### **Phosphoric Acid Fuel Cells (Ref. 1, 2, 3, 4, 5)**

Research and technical analyses were conducted in the areas of fuel cell catalysts and electrodes for phosphoric acid fuel cells. The purpose was to provide major improvements in electrode performance and life, in addition in

aiding in reducing fuel cell costs. The baseline catalyst is platinum. Binary and ternary alloys of platinum were developed and evaluated. Improved activity and stability were the goals, together with attention being given to understanding the reason(s) for the increased activity. Attention was also given to the problem of the catalyst support and the need for corrosion-resistant materials.

The issue of costs was addressed by seeking organometallic catalysts as enhancers and as replacements for platinum at the cathode. Improved performance with mixed (i.e., Pt plus organometallic) catalysts was observed over that of platinum alone, and also reasonably good performance was found for mixed catalysts that contained no noble metal. A model for the improved performance observed with the mixed catalyst was developed.

Diffusion processes in gas diffusion electrode structures were studied since it was recognized that the preparation of efficient gas diffusion electrodes is to a large extent an art, and the detailed mechanisms of their operation are not understood. Guidelines for making improvements in electrode structures were developed, using both experimental and theoretical approaches. Computer software for a mathematical theory of mass transport of reactants in porous gas diffusion electrodes was developed. In the theory a simplified model for the electrode structure was used and fitted to experimental data. Electrocatalysts for phosphoric acid fuel cells typically consist of platinum which is prepared in a finely divided form dispersed uniformly over the surface of a conductive carbon black. Much current research is aimed at enhancing the efficiency as well as extending the lifetime of the fuel cell electrodes, primarily the oxygen electrode. Both catalyst deactivation as well as electrode degradation mechanisms are involved, and simultaneous

achievement of high efficiency and long life is a difficult task. Two major causes of performance decay are support corrosion and catalyst deactivation, mainly through surface area loss due to sintering of metal particles. Several modifications of carbon blacks and substitute conductive materials such as TiC are being investigated to improve the corrosion resistance of supports, and modifications of platinum are being investigated to enhance the efficiency and lifetime of the platinum catalyst. Heat-treatment and alloying of the platinum have been investigated.

### Materials

#### **Flight qualified materials for advanced concentrators (Ref. 6)**

The purpose of this effort was to aid in assessing the technical base for flight qualified materials for advanced concentrators. No firm technical data base exists for concentrator materials. Thus, no material is commercially available that can be certified for long-term application. Included in the consideration of concentrator materials are materials of construction, optical films, and coatings. The literature survey included laboratory reports and workshops. Applicable materials were identified from shuttle spacecraft and photovoltaic programs carried out by NASA and DOD. And the procedures used for qualifying the materials were identified and evaluated. Identified also were the different environment(s) and subsequent different criteria that needed to be addressed depending on the intended mission(s), e.g., a 30-yr lifetime in Low Earth Orbit or a 5-15 yr. lifetime for missions subject to high energy radiation. Further, the study showed that it was critical that testing of materials be done in a suitable combined simulation of the space environmental conditions, in which simultaneous irradiation could be done.

The means of obtaining a reliable data base for materials for long-term application in space were summarized. They included the ability to develop a reliable prediction model to assess the effects of long-term exposure of materials to the LEO environment, the ability of ground-based facilities to simulate the space environment, and aerometric determination of low earth orbit environment composition.

#### **Moving Belt Radiator (Ref. 7)**

The purpose of this effort was to aid in establishing a data base of candidate materials which can be used in a Moving Belt Radiator system. The database was to include the materials to be used for the heat exchange fluid bath, the fluid bath containment, and the belt to be used in the MBR concept. The hybrid belt and the solid belt were the ones to be considered. The report focuses on belt materials only, since there was nothing obvious to suggest a better bath material than gallium, and containment with certain types of stainless steels has been demonstrated. The focus of this report was the search for belt materials having a heat of fusion of about 300 kJ/kg (400-800K) and an emissivity of 0.8.

#### **Regenerative Fuel Cell Systems**

##### **Dedicated (Ref. 8, 9)**

NASA's planning for the future exploration of the Solar System includes the establishment of manned outposts, as well as central basestations on the Moon and Mars. Supporting human expeditions to, and operations on, the surface of the Moon or Mars represents a substantial technology challenge for current and projected power system capabilities. A solar-based surface power system must



supply usable power continuously, that is during the day as well as the night, and thus, a regenerative system is required. The highest potential for successfully achieving the required surface power storage capabilities was judged to lie in the regenerative fuel cell concept. During the light portion of the orbit, photovoltaic solar arrays generate sufficient power to service the system electrical loads plus a water electrolysis unit. The amount of electrical energy required by the electrolysis unit is determined by the amount of hydrogen and oxygen needed to generate power in a fuel cell, which supplies electrical power during the dark portion of the orbit. Water is produced by the fuel cell as a by-product of the electrochemical reaction. It is collected and stored for use in the electrolyzer in the succeeding orbit. To meet the mass, energy, and life requirements for operating on the Moon or Mars requires substantial improvements in the technology areas of solar power generation, energy storage, and electrical power management. For energy storage, two candidate fuel cell and electrolyzer technologies were considered, the alkaline and the proton exchange membrane (PEM). The state-of-the-art of alkaline systems had been very much advanced over that of PEM technology because of the use and development of alkaline systems in previous NASA space missions. However, recent technology efforts on fuel cells for transportation applications have advanced the PEM technology. Thus, a technology assessment was undertaken to provide guidelines for selecting the technology to be carried into full development. Given the history of prior development, the technology assessment considered alkaline fuel cells and electrolyzers as baseline. The first activity, thus, was to determine the viability of PEM fuel cells as a competing technology. Despite the lack of background development in PEM fuel cells, it was determined that there was a high probability of

success in attaining the basic technology improvements needed to meet the RFC system requirements within a reasonable time. Further, it was determined that a PEM, metal hardware fuel cell stack appeared to be the only candidate that could meet the performance and life requirements needed for repeated start-up and turn-down cycles necessary to follow the solar cycles on the lunar surface. PEM electrolysis stacks were also selected.

Most of the tests in PEM systems have been made with Nafion 120 and 117 membranes, which are perfluorinated sulfonic acid membranes made by DuPont. These are relatively thick and of higher equivalent weight and thus of higher resistance than found for thinner Nafions and for other newer ion exchange polymeric material. In general, thicker membranes give lower electrical output than thinner membranes and higher equivalent weight material gives lower electrical output than lower equivalent weight material. Under consideration are membranes made by DOW and Asahi, which are of similar composition and structure to Nafion. Some properties of typical membranes are given in TABLE I.

TABLE I. Physico-chemical Characteristics of Polymer Electrolyte Membranes

Membrane	Equiv. Weight	Conductivity S/cm $\times 10^2$	Membrane	Equiv. Weight	Thickness, mm	Conductivity, S/cm $\times 10^2$
Nafion	1100	7.5	Nafion	1100	100	5.9
Nafion	1200	5.0	DOW	800	125	11.4
Nafion	1500	3.3	Asahi	1000	120	10.8

Recently, linear polymeric chain perfluorinated bis-sulfonimides have been synthesized. They are stable strong acids, and like sulfonic acids are hydronium ion conductors which require the presence of water to obtain significant ionic conductivity. They show promise of conductivity better than  $10^{-2}$  S/cm.

Unitized (Ref. 13, 14)

Some of the more desirable characteristics for hydrogen-oxygen fuel cell systems, particularly for long-time automated operation, are high energy density, small volume, high efficiency, high reliability, and long life. A recent GEO mission analysis indicated that a significant increase in energy density is possible if a two-unit alkaline fuel cell and electrolyzer system is replaced with a single-unit alkaline fuel cell/electrolyzer system. The efficiencies of fuel cell and electrolyzer systems under load are considerably less than 100 percent due, primarily, to the irreversibility of the oxygen electrode. Therefore, active bifunctional  $O_2$  electrocatalysts are needed to increase the kinetics for both  $O_2$  reduction and evolution to maximize the efficiency of a single-unit alkaline fuel cell/electrolyzer system. Metals and oxides have been investigated for monofunctional  $O_2$  electrocatalysts for alkaline fuel cells and electrolyzers. Studies of bifunctional  $O_2$  electrocatalysts are rare. Long-life candidates must be stable under both reducing and oxidizing conditions. Although Pt and Pt alloys exhibit moderate bifunctional  $O_2$  electrode activity, long-time stability for Pt, particularly during  $O_2$  evolution, is questionable. Pt bronzes, composed of oxides of Pt and an alkali metal, are believed to have greater stability than metallic Pt particularly under oxidizing potentials. Na-Pt bronze powders (i.e.,  $Na_xPt_3O_4$ ) have been prepared (Giner, Inc.) as a single phase and in moderately high surface area. Porous gas diffusion electrodes using mixtures of  $Na_xPt_3O_4$  powders as the electrocatalyst and polytetrafluoroethylene (PTFE) as the binder were fabricated.  $O_2$  reduction and evolution activities and stabilities of these PTFE-bonded electrodes were determined under both reducing and oxidizing

conditions.

### Solid Oxide Fuel Cells and Electrolyzers (Ref. 10, 11, 12)

Development of predictive techniques, with regard to cell behavior, under various operating conditions is needed to improve cell performance, increase energy density, reduce manufacturing cost, and to broaden utilization of various fuels. Such technology would be especially beneficial for the solid oxide fuel cell at its early demonstration stage. Thus, computer models were developed to calculate the temperature, current density, and reactant distributions in tubular and monolithic solid oxide fuel cells. The results indicate that problems of non-uniform heat generation and fuel gas depletion may be encountered in the tubular cell module during fuel cell operation. In the monolithic (MOD  $\phi$ ) design, problems of size limitations may be encountered. A computer model was used to estimate the effects that the current-voltage characteristics, the average array temperature, and the inlet reactant gas temperatures have upon the range of feasible fuel utilization ratios and oxidant utilization ratios. The results can be used as constraints for system optimization studies.

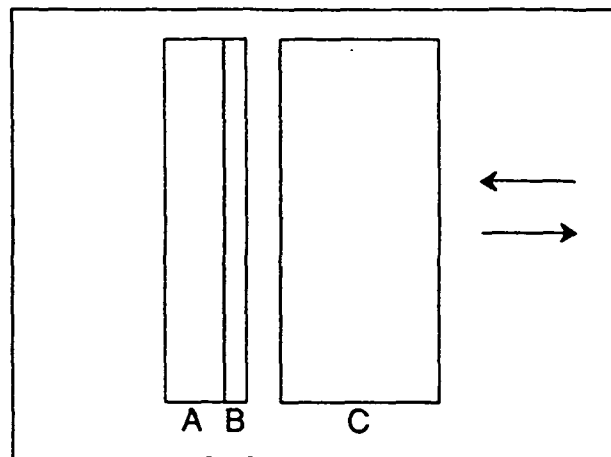
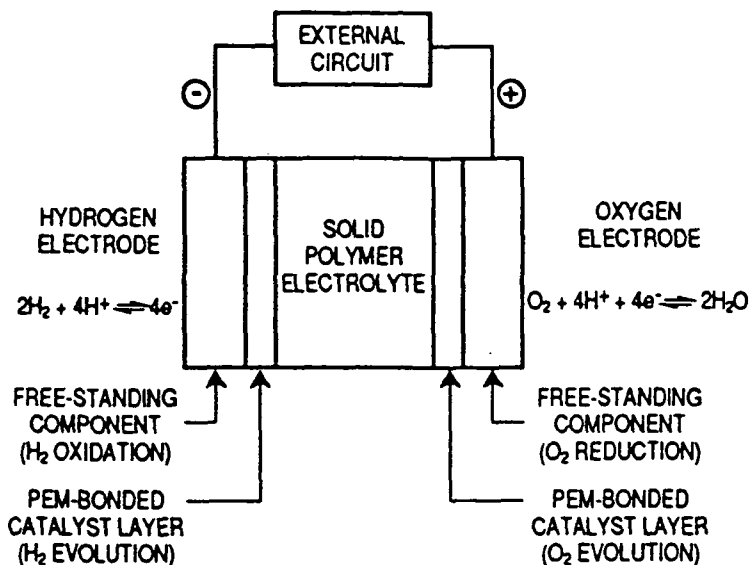
Fuel cell operation has been demonstrated with monolithic solid oxide fuel cells. It is also possible to operate the monolithic structure in the reverse, or electrolysis, mode. Performance predictions of monolithic solid oxide electrolyzer arrays were made by revising the computational algorithm previously formulated for the fuel cell arrays. Computer modeling results of this type may be used to aid the design of a monolithic solid oxide electrolysis sub-system and of a regenerative fuel cell system.

### Experimental (Ref. 13, 14)

Prior work in developing electrocatalyst systems and electrode structures for single-unit regenerative fuel cells looked at a large number of candidate bifunctional positive electrode catalysts. These catalysts were evaluated for chemical and electrochemical stability and for catalytic activity in 30% KOH at 80°C. As a result, two potentially bifunctional catalyst systems were identified:  $\text{Na}_x\text{Pt}_3\text{O}_4$  and metal/metal oxide combinations of Rh, Pt and Ir. For the regenerative PEM fuel cell, many of the same catalysts are being considered.

To alternate between oxygen reduction and oxygen evolution on the same electrode, it is necessary to have a structure that can perform in both of these modes. The approach taken was to develop catalyst/binder compositions optimized separately at the particulate level for either oxygen reduction or oxygen evolution and then combine these at an optimal ratio in a single electrode, referred to as an "integrated dual-character" (IDC) electrode. In this approach the catalyst for each function can be the same material if it shows bifunctional activity (e.g.,  $\text{Na}_x\text{Pt}_3\text{O}_4$ ) or two different monofunctional catalysts (e.g., Pt for  $\text{O}_2$  reduction and  $\text{I}_2\text{O}_2$  evolution). For PEM systems a two-layer structure is used to achieve an appropriate interface to the proton exchange membrane.

The electrodes used in this study were prepared by Giner, Inc. The measurements were made in half cells as part of the research program to develop a detailed understanding of how the different components of porous gas-fed oxygen electrodes function. The results are preliminary and presented in the figures.



A - NAFION 117  
 B -  $IrO_2(Pt)$  -  $O_2$  EVOLUTION  
 C - FREE STANDING -  $O_2$  REDUCTION

Figure 1: Schematic of a Bifunctional Hydrogen-Oxygen PEM Cell with Giner, Inc. Composite Electrodes

Figure 2: Giner Dual Function System (Two Electrodes)

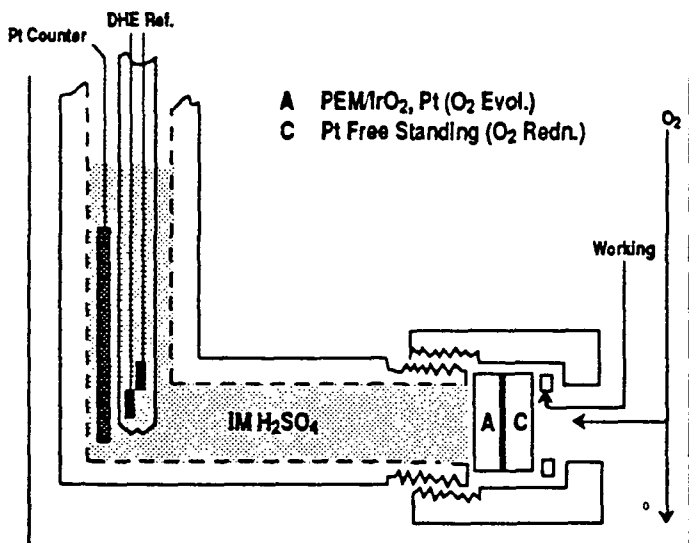
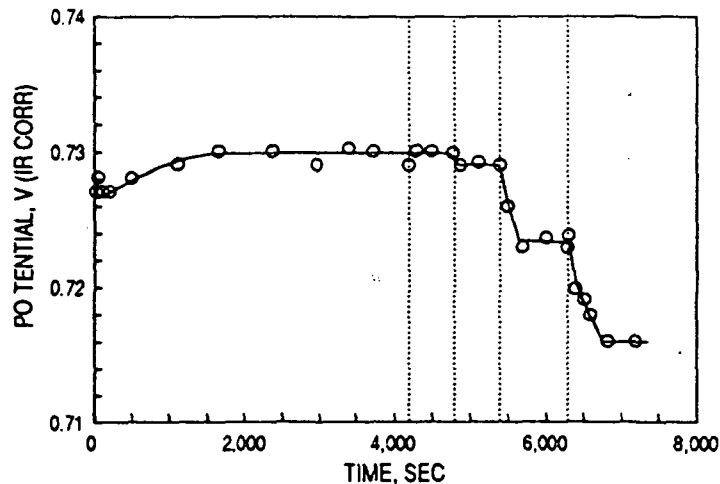
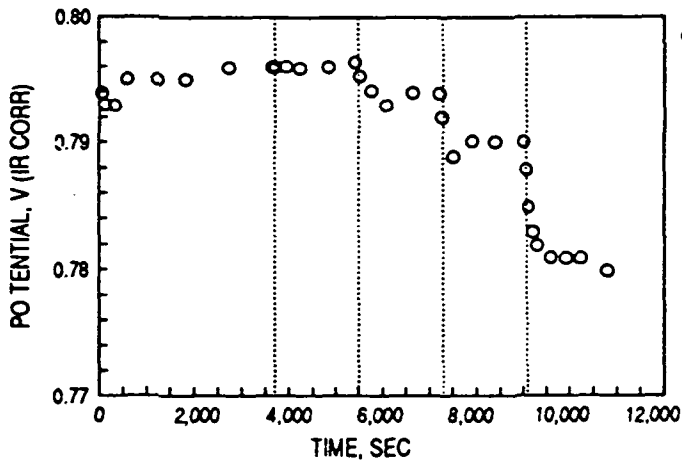


Figure 3: Teflon Half Cell for  $O_2$  Reduction & Evolution



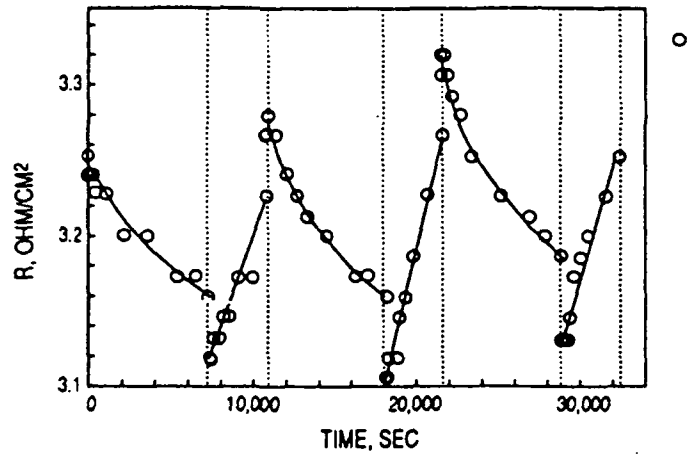
START 500CC/MIN  $O_2$  ( $H_2O$ ) $O_2$  SIDE  
 THEN 200, 100, 50, 25) GPT/ $IrO_2$ /25  
 25CC/MIN  $O_2$  ABOUT 70X  $O_2$  NEEDED  
 (PREHEATED 100°C) EQUILIBRATED) GPT25

Figure 4:  $O_2$  Reduction Potential with  $O_2$  Flow Rate ( $H_2O$ ) for Giner PEM/ $IrO_2$ ,PT & PT Free-Standing Electrode (-0.1A, 24°C, 1M  $H_2SO_4$ )



START 500CC/MIN O<sub>2</sub> (DRY) O<sub>2</sub> SIDE 25C MP ABOUT 10X STOICHIOMETRIC  
 THEN 200, 100, 50, 25 GPT412

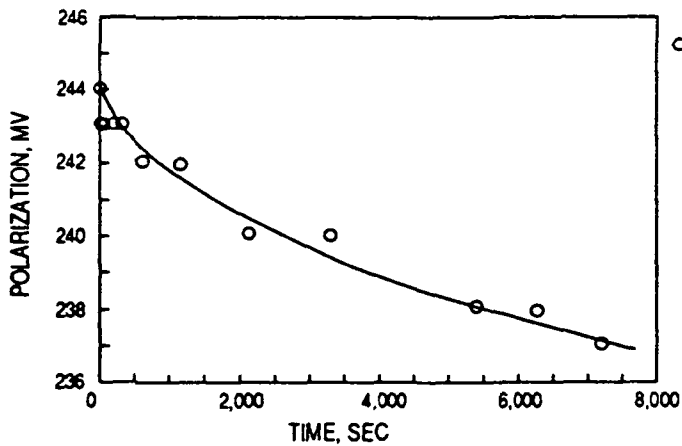
Figure 5: O<sub>2</sub> Reduction Potential with O<sub>2</sub> Flow Rate (Dry) for Giner PEM/IRO<sub>2</sub>,PT & PT Free-Standing Electrode (-0.1A, 24°C, 1M H<sub>2</sub>SO<sub>4</sub>)



1, 3, 5 CYCLE (-0.05A FOR 2 HR)  
 2, 4, 6 CYCLE (+0.05A FOR 1 HR)

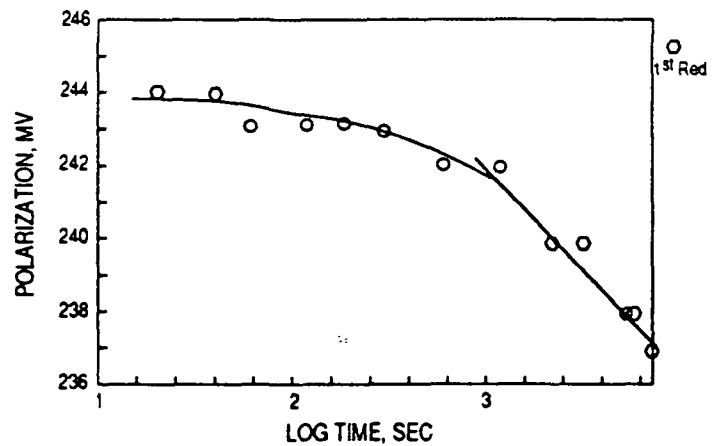
GPT510

Figure 6: R with Time during cycling at -0.05A & +0.05A Giner PEM/IRO<sub>2</sub>,PT & PT Free-Standing Electrode (23°C, 1M H<sub>2</sub>SO<sub>4</sub>)



GPT510

Figure 7: R Polarization with Time during Cycling Giner PEM/IRO<sub>2</sub>,PT & PT Free-Standing Electrode (-0.05 & +0.05A, RT, 1M H<sub>2</sub>SO<sub>4</sub>)



GPT511

Figure 8: R Polarization with Log Time during Cycling Giner PEM/IRO<sub>2</sub>,PT & PT Free-Standing Electrode (-0.05 & +0.05A, RT, 1M H<sub>2</sub>SO<sub>4</sub>)

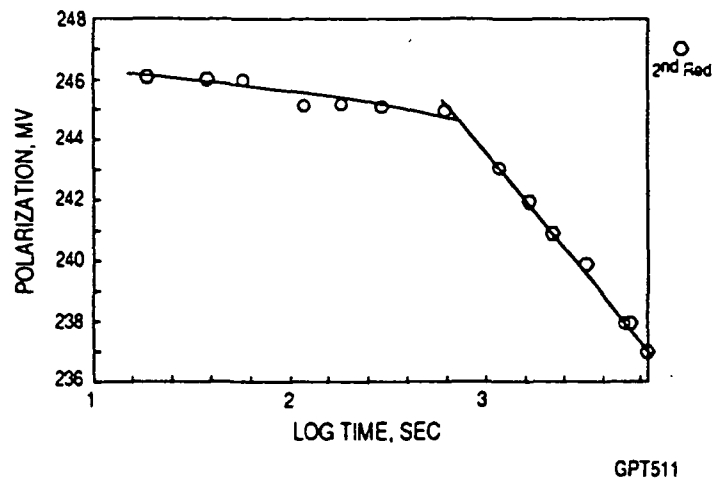
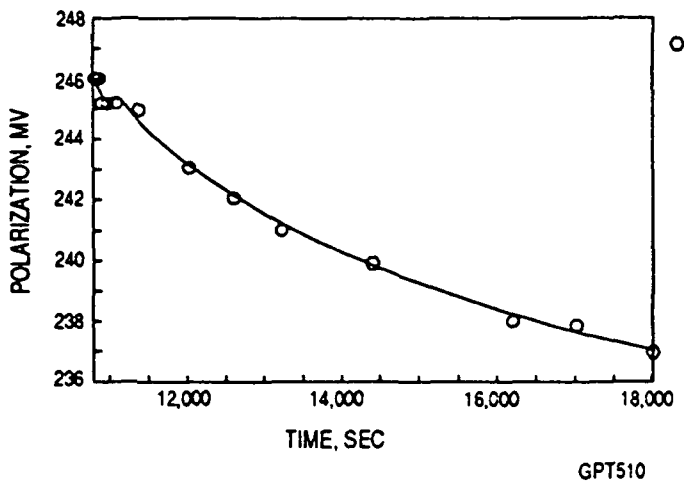


Figure 9: R Polarization with Time during Cycling Giner PEM/IRO<sub>2</sub>,PT & PT Free-Standing Electrode (-0.05 & +0.05A, RT, 1M H<sub>2</sub>SO<sub>4</sub>)

Figure 10: R Polarization with Log Time during Cycling Giner PEM/IRO<sub>2</sub>,PT & PT Free-Standing Electrode (-0.05 & +0.05A, RT, 1M H<sub>2</sub>SO<sub>4</sub>)

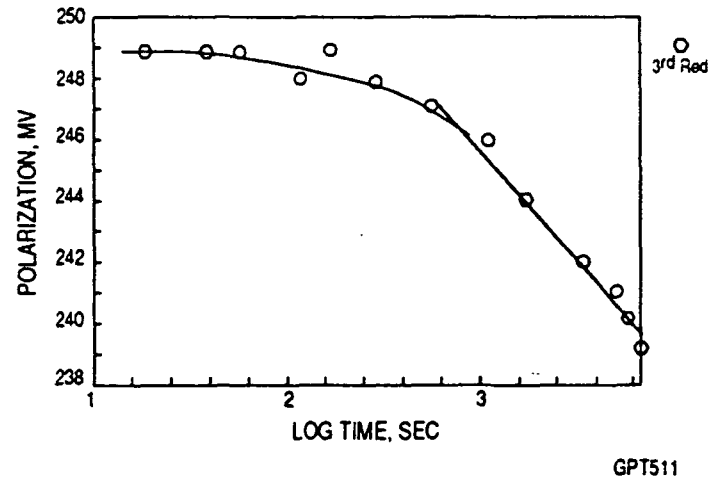
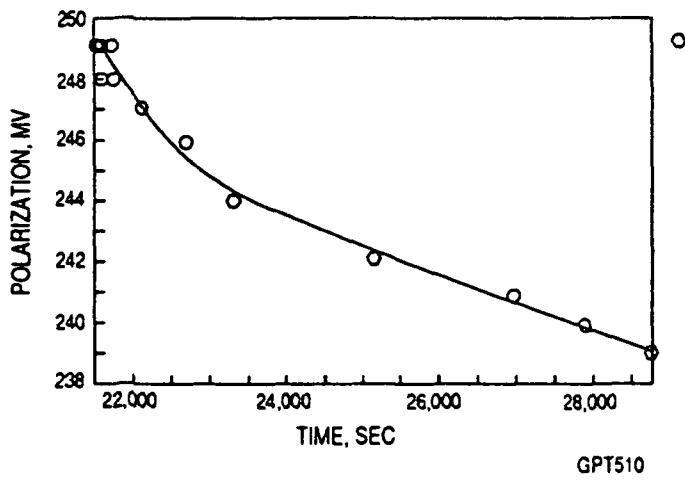
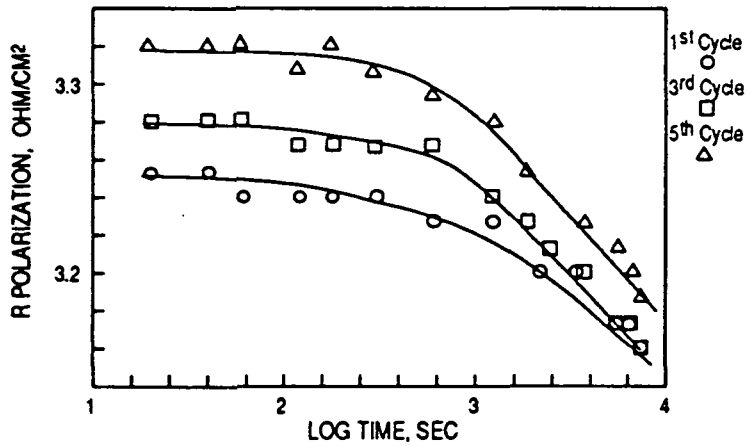


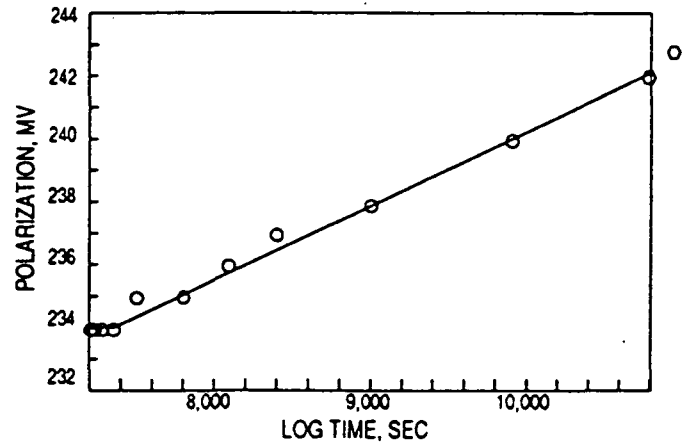
Figure 11: R Polarization with Time during Cycling Giner PEM/IRO<sub>2</sub>,PT & PT Free-Standing Electrode (-0.05 & +0.05A, RT, 1M H<sub>2</sub>SO<sub>4</sub>)

Figure 12: R Polarization with Log Time during Cycling Giner PEM/IRO<sub>2</sub>,PT & PT Free-Standing Electrode (-0.05 & +0.05A, RT, 1M H<sub>2</sub>SO<sub>4</sub>)





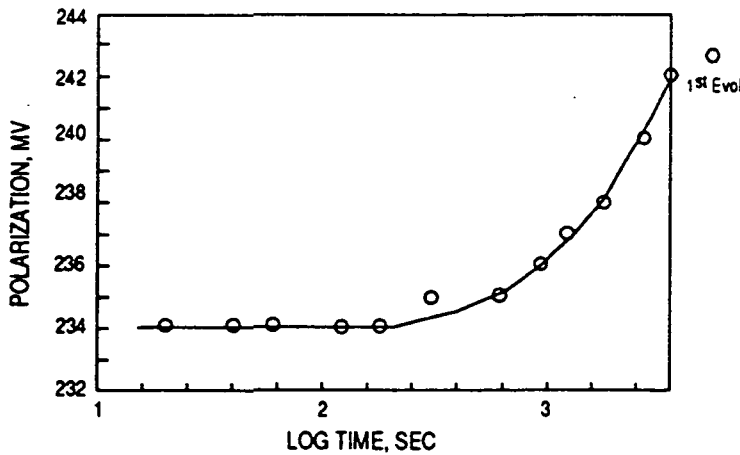
1, 3, 5 CYCLE (-0.05A FOR 2 HR) DATA DURING O<sub>2</sub> REDUCTION  
 2, 4, 6 CYCLE (+0.05A FOR 1 HR) GPT511



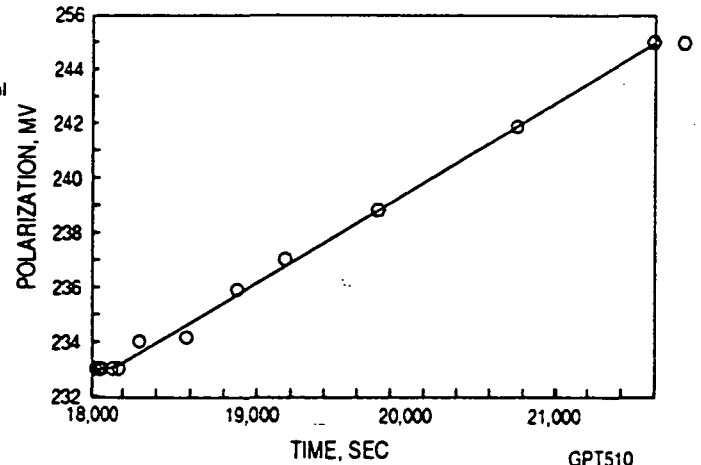
GPT510

Figure 13: R Polarization with Log Time (O<sub>2</sub> Reduction)  
 Giner PEM/IRO<sub>2</sub>,PT & PT Free-Standing Electrode  
 (Cycle at -0.05 & + 0.05A, 23°C, 1M H<sub>2</sub>SO<sub>4</sub>)

Figure 14: R Polarization with Time during Cycling  
 Giner PEM/IRO<sub>2</sub>,PT & PT Free-Standing Electrode (-0.05 & +0.05A, 23°C, 1M H<sub>2</sub>SO<sub>4</sub>)



GPT511



GPT510

Figure 15: R Polarization with Time during Cycling  
 Giner PEM/IRO<sub>2</sub>,PT & PT Free-Standing Electrode (-0.05 & +0.05A, RT, 1M H<sub>2</sub>SO<sub>4</sub>)

Figure 16: R Polarization with Time during Cycling  
 Giner PEM/IRO<sub>2</sub>,PT & PT Free-Standing Electrode (-0.05 & +0.05A, RT, 1M H<sub>2</sub>SO<sub>4</sub>)

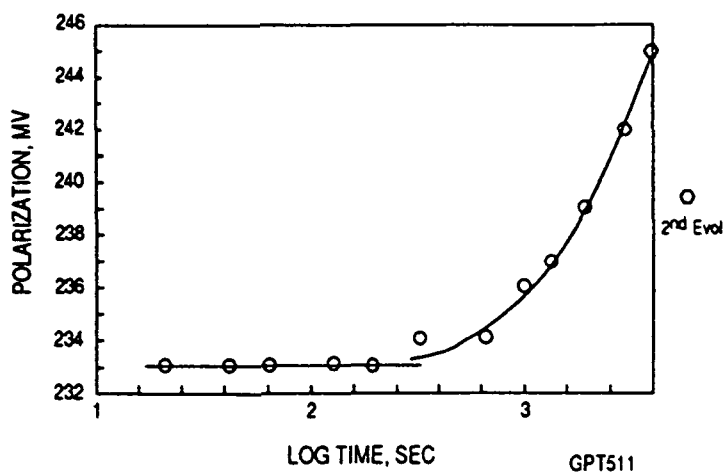


Figure 17: R Polarization with Log Time during Cycling Giner PEM/IRO<sub>2</sub>,PT & PT Free-Standing Electrode (-0.05 & +0.05A, RT, 1M H<sub>2</sub>SO<sub>4</sub>)

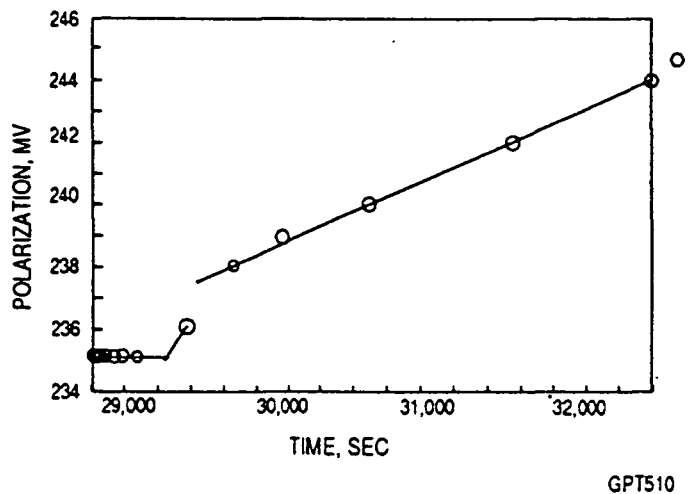


Figure 18: R Polarization with Time during Cycling Giner PEM/IRO<sub>2</sub>,PT & PT Free-Standing Electrode (-0.05 & +0.05A, RT, 1M H<sub>2</sub>SO<sub>4</sub>)

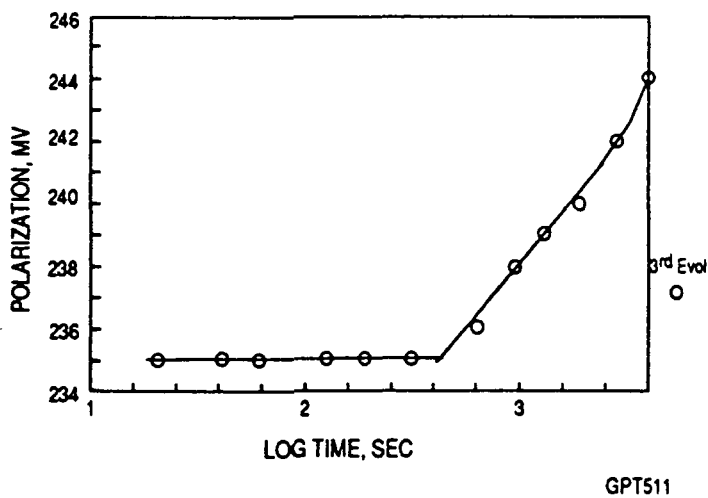


Figure 19: R Polarization with Log Time during Cycling Giner PEM/IRO<sub>2</sub>,PT & PT Free-Standing Electrode (-0.05 & +0.05A, RT, 1M H<sub>2</sub>SO<sub>4</sub>)

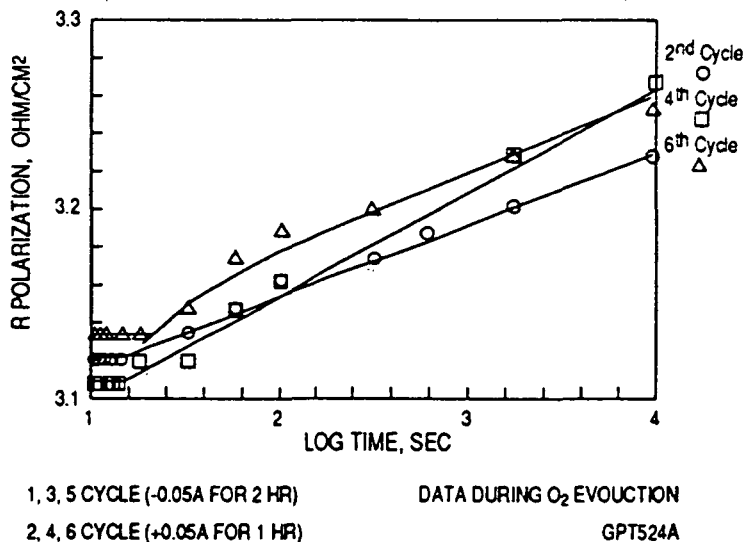
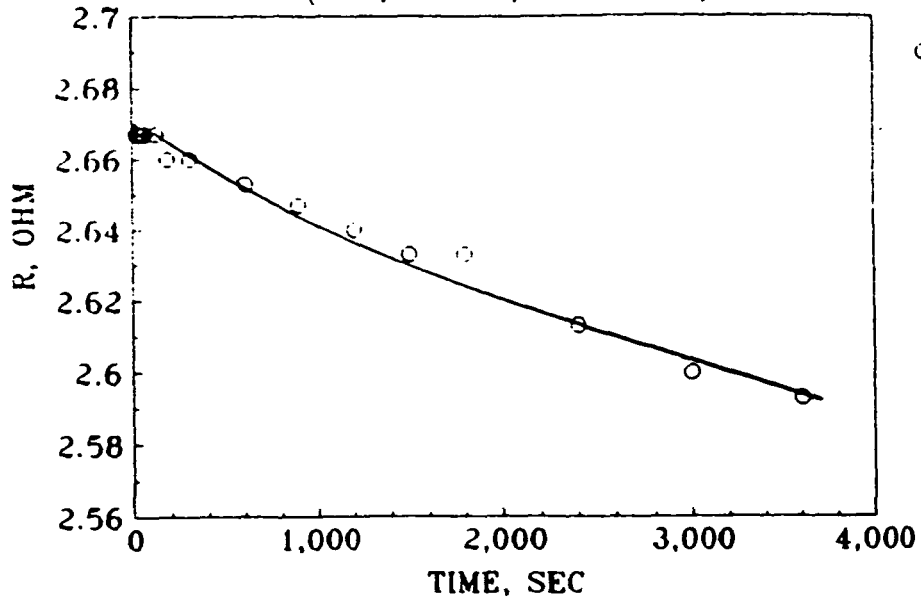


Figure 20: R Polarization with Time (O<sub>2</sub> Evolution) Giner PEM/IRO<sub>2</sub>,PT & PT Free-Standing Electrode (Cycle at -0.05 & + 0.05A, 23°C, 1M H<sub>2</sub>SO<sub>4</sub>)

Figure 21. R WITH TIME FOR O<sub>2</sub> REDUCTION AT -0.15A  
 GINER PEM/IR02,PT & PT FREE STANDING ELECTRODE  
 (H<sub>2</sub>O, 80.6°C, 1M H<sub>2</sub>SO<sub>4</sub>)

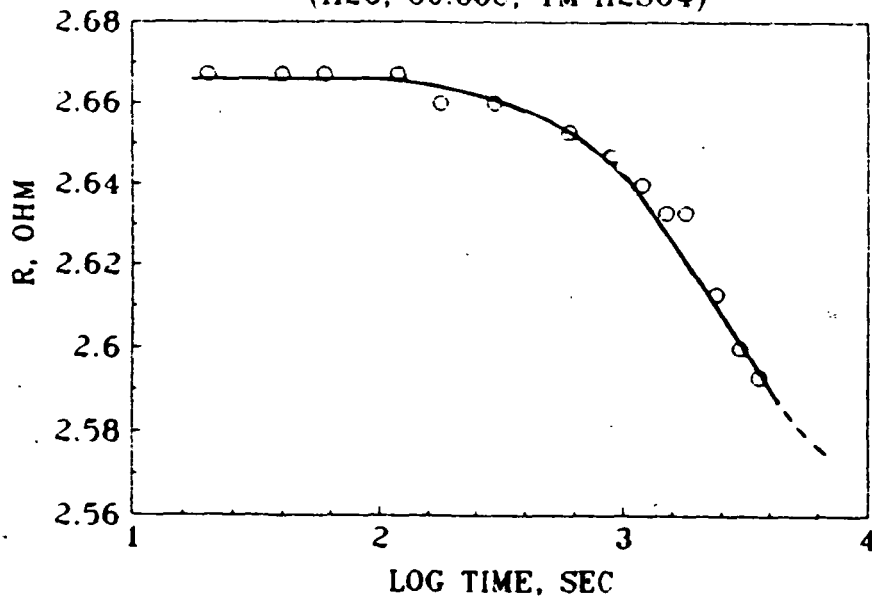


GPEMFS52

200CC/MIN O<sub>2</sub>(H<sub>2</sub>O)/O<sub>2</sub> SIDE  
 (PREHEAT 80°C FOR 60)

GPT391

Figure 22. R WITH LOG TIME FOR O<sub>2</sub> REDUCTION AT -0.15A  
 GINER PEM/IR02,PT & PT FREE STANDING ELECTRODE  
 (H<sub>2</sub>O, 80.6°C, 1M H<sub>2</sub>SO<sub>4</sub>)



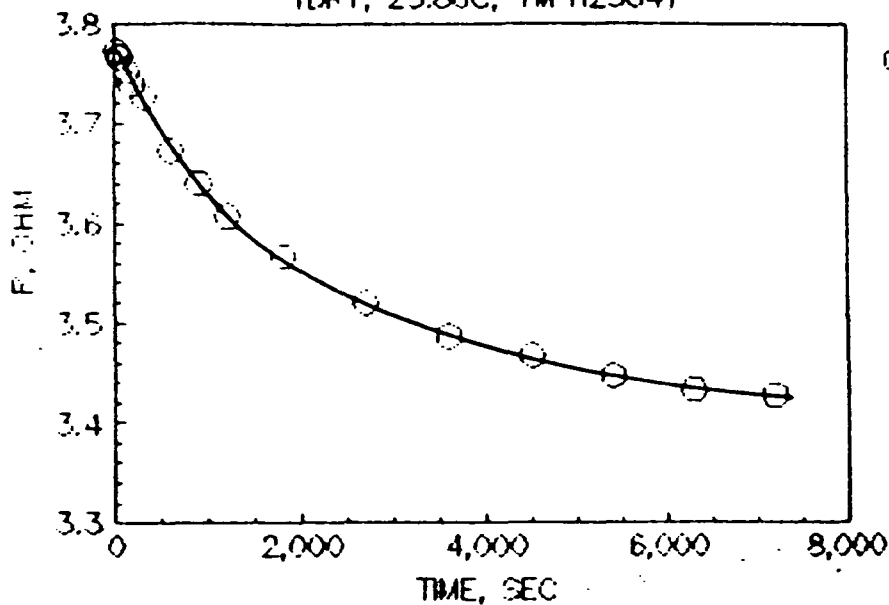
GPEMFS52

200CC/MIN O<sub>2</sub>(H<sub>2</sub>O)/O<sub>2</sub> SIDE  
 (PREHEAT 80°C FOR 60)

GPT393

ORIGINAL PAGE IS  
 OF POOR QUALITY

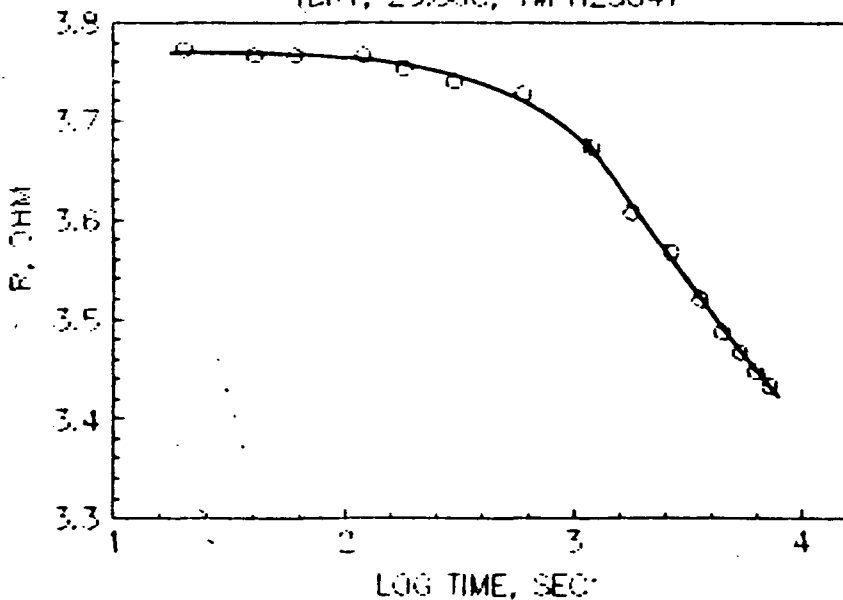
Figure 23. R FOR O2 REDUCTION WITH TIME AT -0.15A  
 GINER PEM/IR02,PT & PT FREE STANDING ELECTRODE  
 (DFY, 23.8°C, 1M H2SO4)



50000/MIN O2(DFY)/O2 SIDE

GFEMFS54  
 GPT405

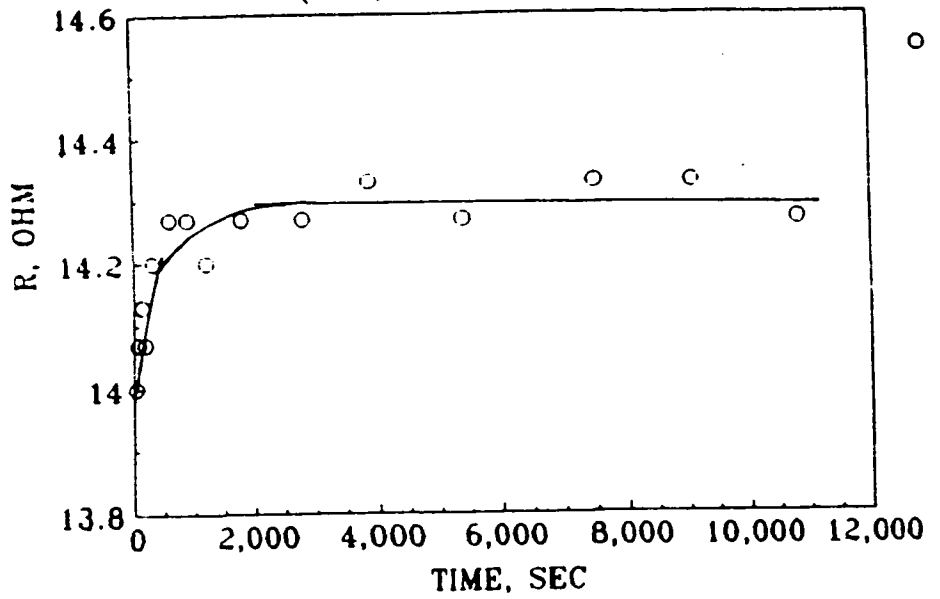
Figure 24. R FOR O2 REDUCTION WITH LOG TIME AT -0.15A  
 GINER PEM/IR02,PT & PT FREE STANDING ELECTRODE  
 (DFY, 23.9°C, 1M H2SO4)



50000/MIN O2(DFY)/O2 SIDE

GFEMFS54  
 GPT406

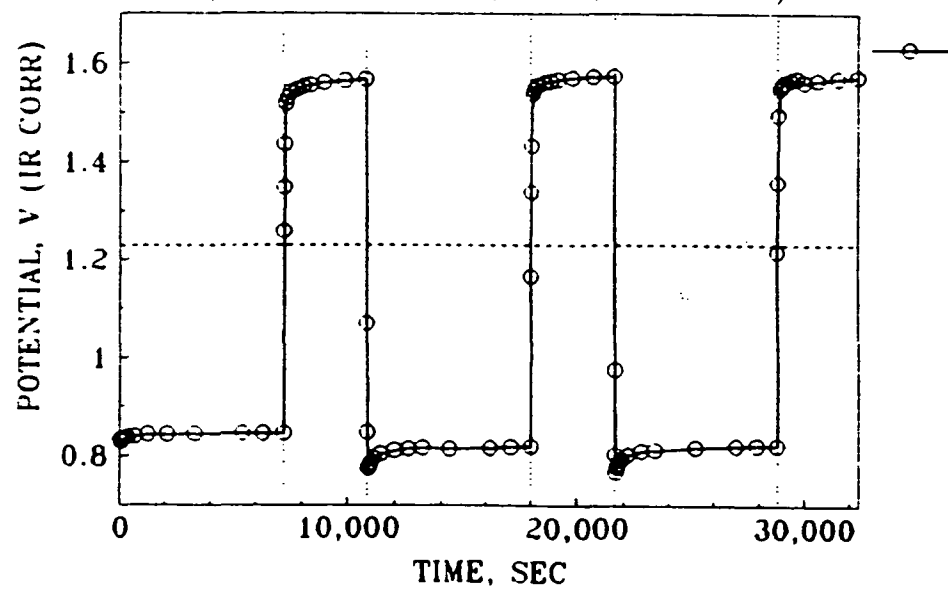
Figure 25. R FOR O2 REDUCTION WITH TIME AT -0.015A  
 GINER PT FREE STANDING ELECTRODE ONLY  
 (H2O, 22.2oC, 1M H2SO4)



200CC/MIN O2(H2O)/O2 SIDE.

GFS50  
 GPT462

Figure 26. POTENTIAL WITH TIME DURING CYCLING  
 GINER PEM/IR02,PT & PT FREE STANDING ELECTRODE  
 (-0.05A & +0.05A, 23oC, 1M H2SO4)

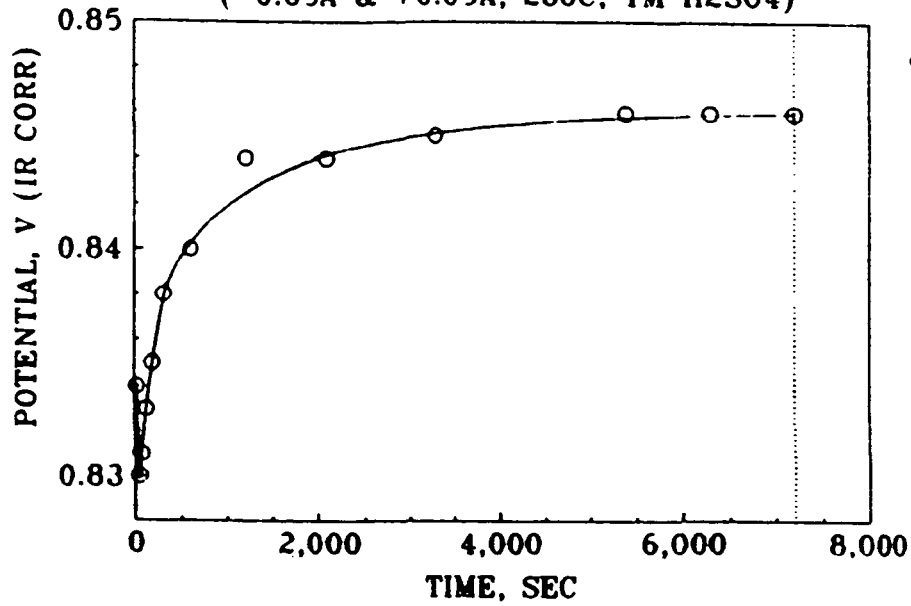


1,3,5 CYCLE(-0.05A FOR 2 HR)  
 2,4,6 CYCLE(+0.05A FOR 1 HR)

GPT512

ORIGINAL PAGE IS  
 OF POOR QUALITY

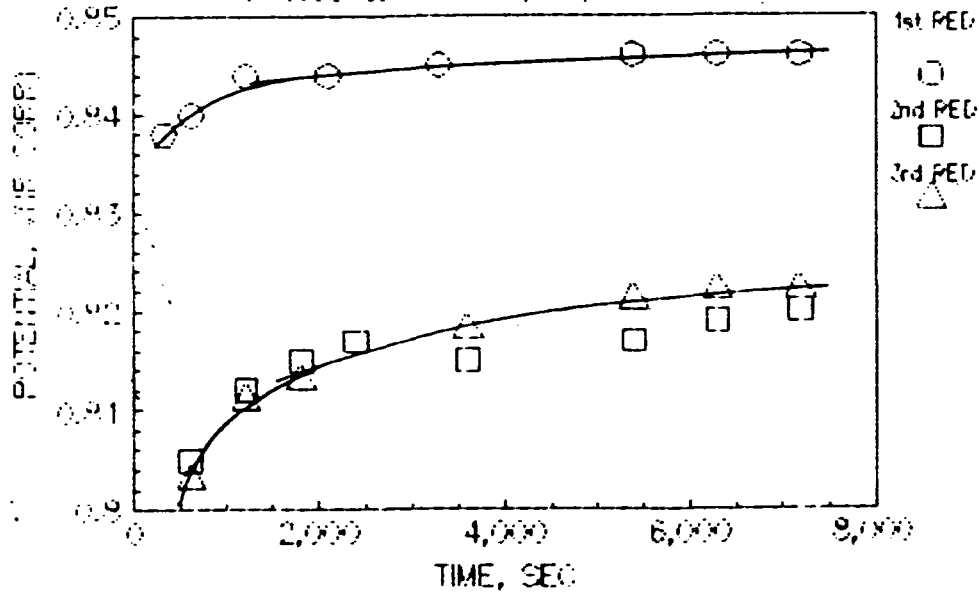
**Figure 27. POTENTIAL WITH TIME DURING CYCLING  
GINER PEM/IR02,PT & PT FREE STANDING ELECTRODE  
(-0.05A & +0.05A, 23°C, 1M H2SO4)**



1ST CYCLE(-0.05A FOR 2 HR)

GPT512

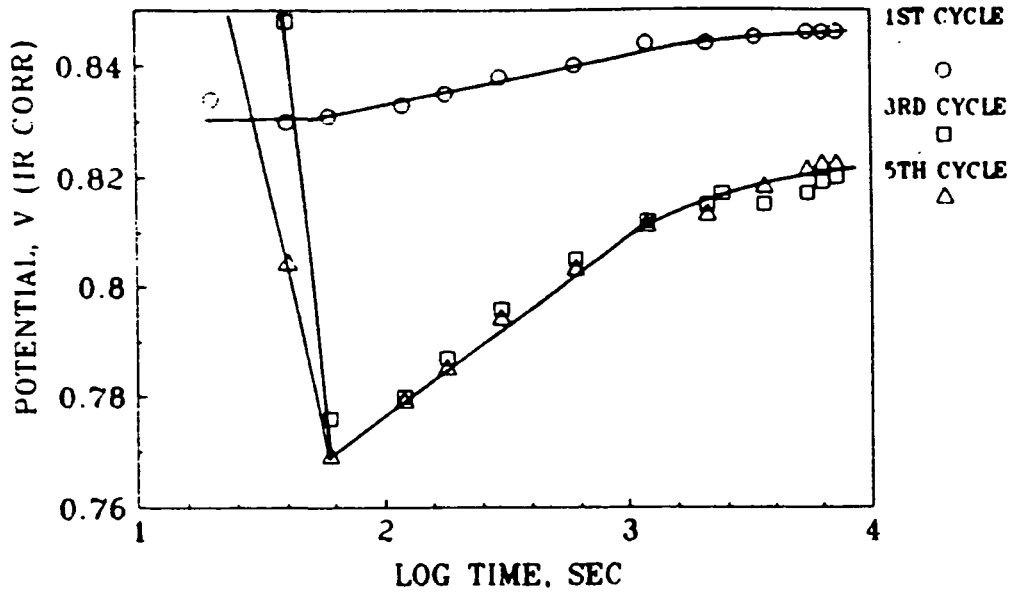
**Figure 28. POTENTIAL WITH TIME DURING CYCLING  
GINER PEM/IR02,PT & PT FREE STANDING ELECTRODE  
(-0.05 & + 0.05A, PT, 1M H2SO4)**



O2 REDUCTION

GPT513

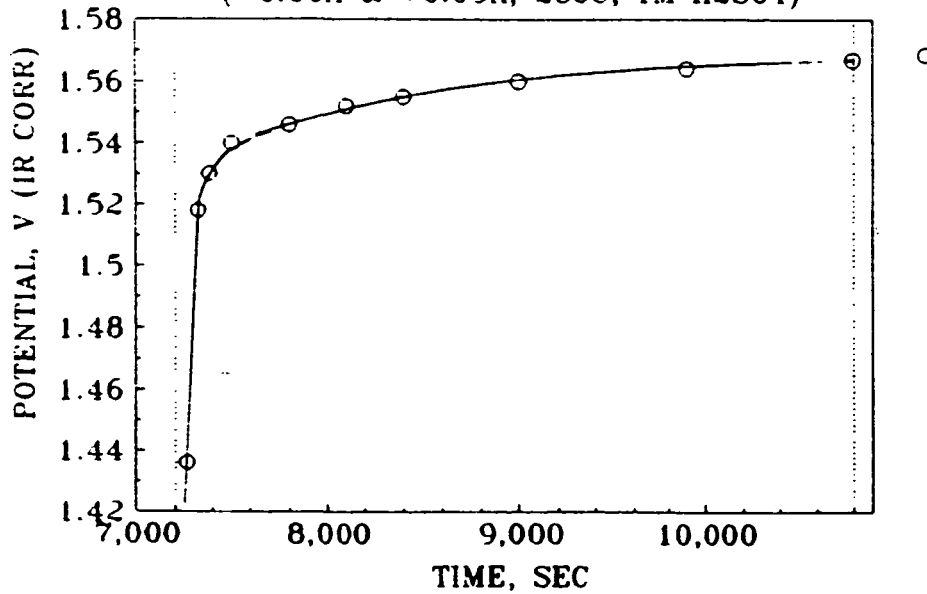
**Figure 29. O<sub>2</sub> REDUCTION POTENTIAL WITH LOG TIME  
GINER PEM/IR<sub>2</sub>O<sub>3</sub>,PT & PT FREE STANDING ELECTRODE  
(CYCLE -0.05A & +0.05A, 23°C, 1M H<sub>2</sub>SO<sub>4</sub>)**



1,3,5 CYCLE(-0.05A FOR 2 HR)

GPT515

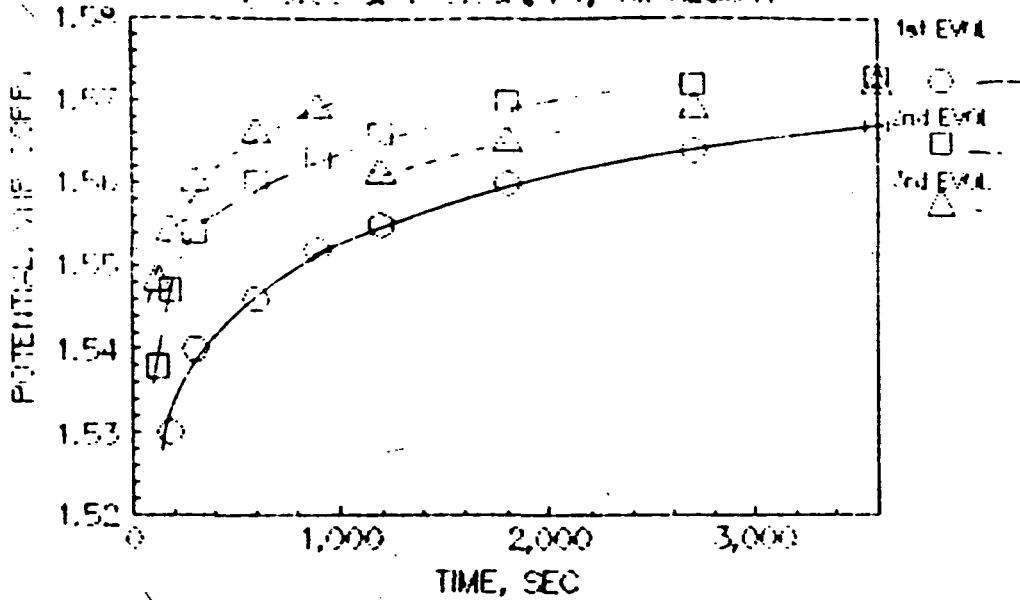
**Figure 30. POTENTIAL WITH TIME DURING CYCLING  
GINER PEM/IR<sub>2</sub>O<sub>3</sub>,PT & PT FREE STANDING ELECTRODE  
(-0.05A & +0.05A, 23°C, 1M H<sub>2</sub>SO<sub>4</sub>)**



2ND CYCLE(+0.05A FOR 1 HR)

GPT512

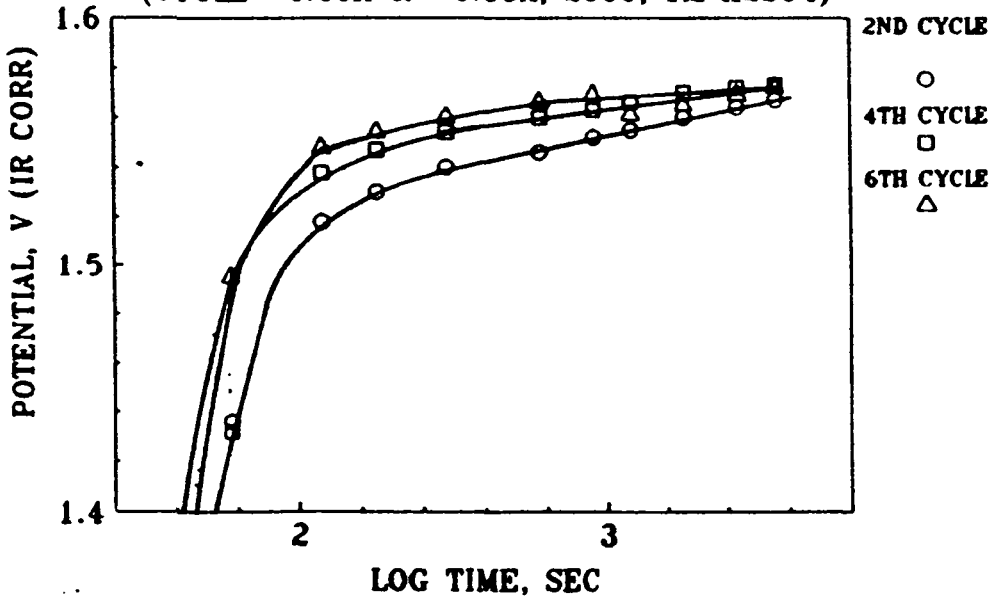
Figure 31. POTENTIAL WITH TIME DURING CYCLING  
 GINER PEM/IR02,PT & PT FREE STANDING ELECTRODE  
 (-0.05 & + 0.05A, RT, 1M H2SO4)



O2 EVOLUTION

GPT514

Figure 32. O2 EVOLUTION POTENTIAL WITH LOG TIME  
 GINER PEM/IR02,PT & PT FREE STANDING ELECTRODE  
 (CYCLE -0.05A & +0.05A, 23oC, 1M H2SO4)

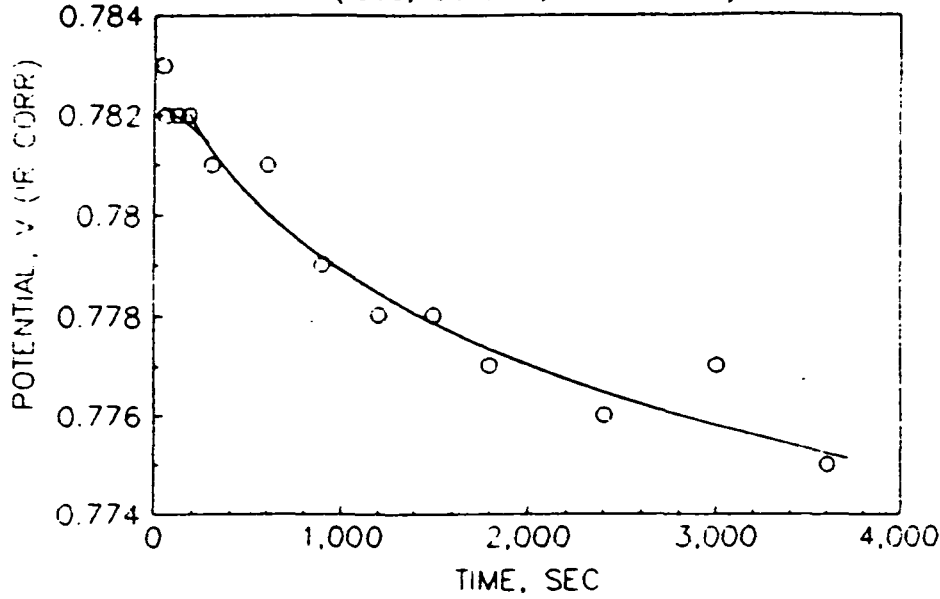


2.4.6 CYCLE(+0.05A FOR 1 HR)

GPT516



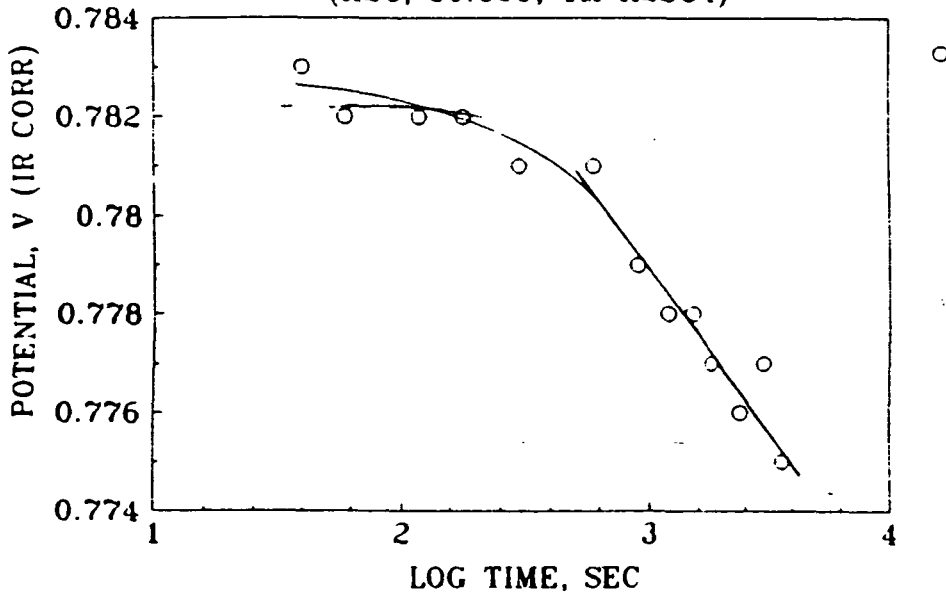
**Figure 33.** O<sub>2</sub> REDUCTION POTENTIAL WITH TIME AT -0.15A  
 GINER PEM/IR02,PT & PT FREE STANDING ELECTRODE  
 (H<sub>2</sub>O, 80.6°C, 1M H<sub>2</sub>SO<sub>4</sub>)



200CC/MIN O<sub>2</sub>(H<sub>2</sub>O)/O<sub>2</sub> SIDE  
 (PREHEAT 80°C FOR 60)

GPEMFS52  
 GPT394

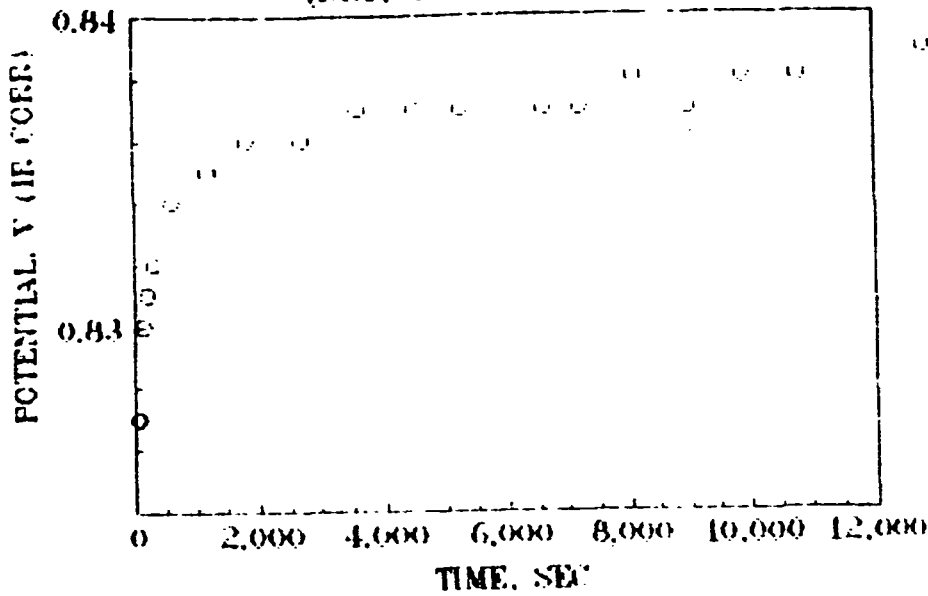
**Figure 34.** O<sub>2</sub> REDUCTION POTENTIAL WITH LOG TIME AT -0.15A  
 GINER PEM/IR02,PT & PT FREE STANDING ELECTRODE  
 (H<sub>2</sub>O, 80.6°C, 1M H<sub>2</sub>SO<sub>4</sub>)



200CC/MIN O<sub>2</sub>(H<sub>2</sub>O)/O<sub>2</sub> SIDE  
 (PREHEAT 80°C FOR 60)

GPEMFS52  
 GPT396

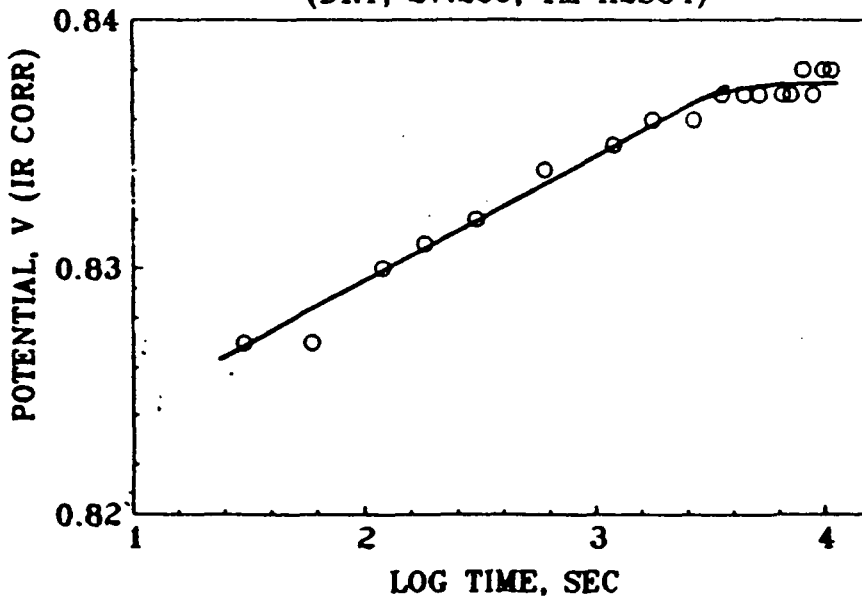
**Figure 35. O<sub>2</sub> REDUCTION POTENTIAL WITH TIME AT -0.06A  
 GINER PEM/IR02,PT & PT FREE STANDING ELECTRODE  
 (DRY, 27.2oC, 1M H2SO4)**



(PREHEAT 900C FOR 30)  
 500CC/MIN O<sub>2</sub>(DRY)/O<sub>2</sub> SIDE

GPEMFS53  
 GPT403

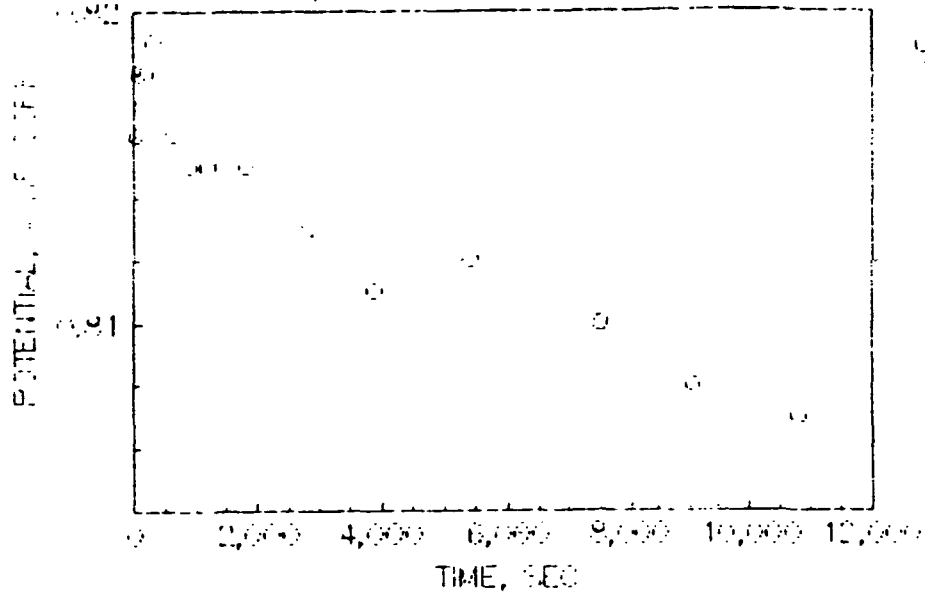
**Figure 36. O<sub>2</sub> REDUCTION POTENTIAL WITH LOG TIME AT -0.06A  
 GINER PEM/IR02,PT & PT FREE STANDING ELECTRODE  
 (DRY, 27.2oC, 1M H2SO4)**



500CC/MIN O<sub>2</sub>(DRY)/O<sub>2</sub> SIDE

GPEMFS53  
 GPT404

Figure 37. O<sub>2</sub> REDUCTION POTENTIAL WITH TIME AT -0.015A  
 GINER PT FREE STANDING ELECTRODE ONLY  
 (H<sub>2</sub>O, 22.2°C, 1M H<sub>2</sub>SO<sub>4</sub>)

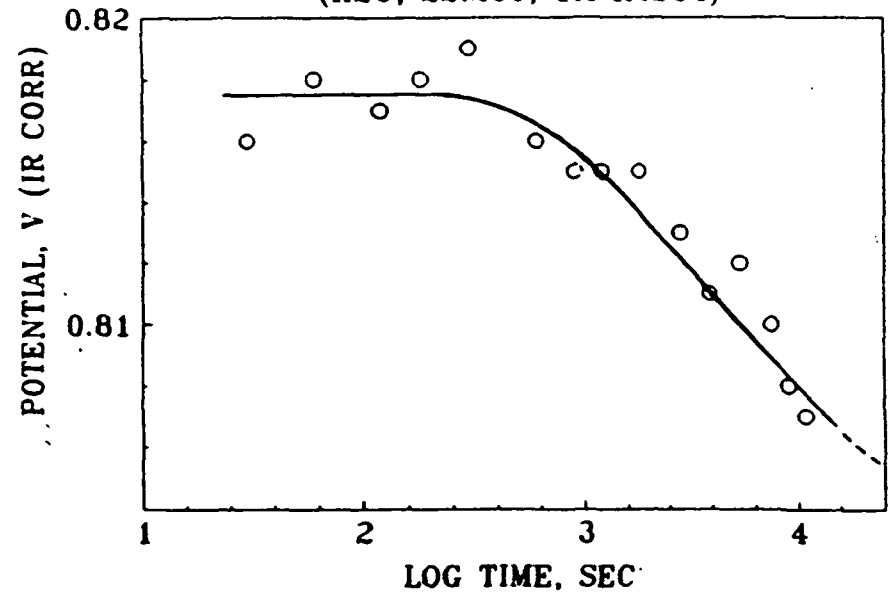


200CC/MIN O<sub>2</sub>(H<sub>2</sub>O)/O<sub>2</sub> SIDE

GPT465

27

Figure 38. O<sub>2</sub> REDUCTION POTENTIAL WITH LOG TIME AT -0.015A  
 GINER PT FREE STANDING ELECTRODE ONLY  
 (H<sub>2</sub>O, 22.2°C, 1M H<sub>2</sub>SO<sub>4</sub>)



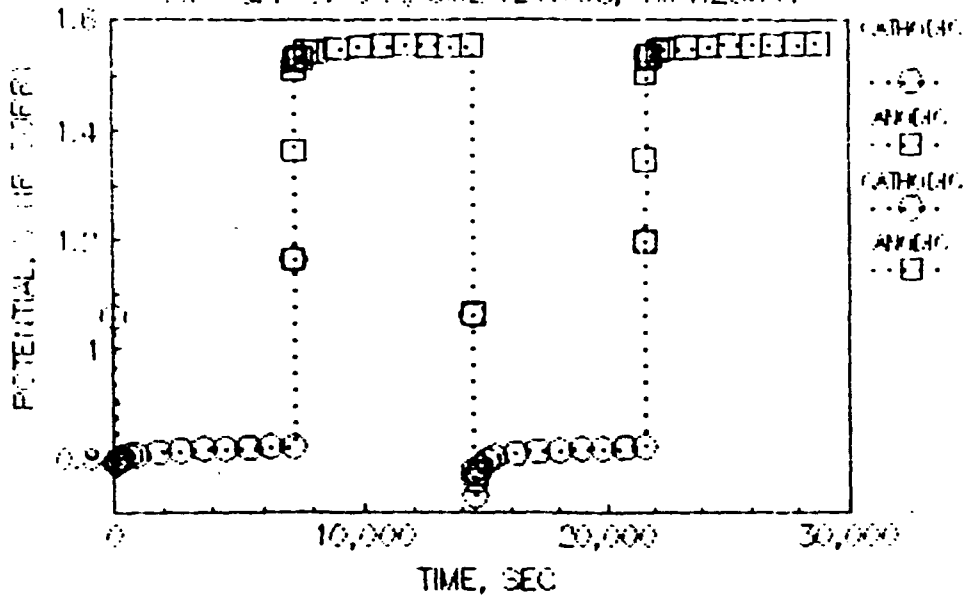
200CC/MIN O<sub>2</sub>(H<sub>2</sub>O)/O<sub>2</sub> SIDE

GPT466

35

ORIGINAL PAGE IS  
 OF POOR QUALITY

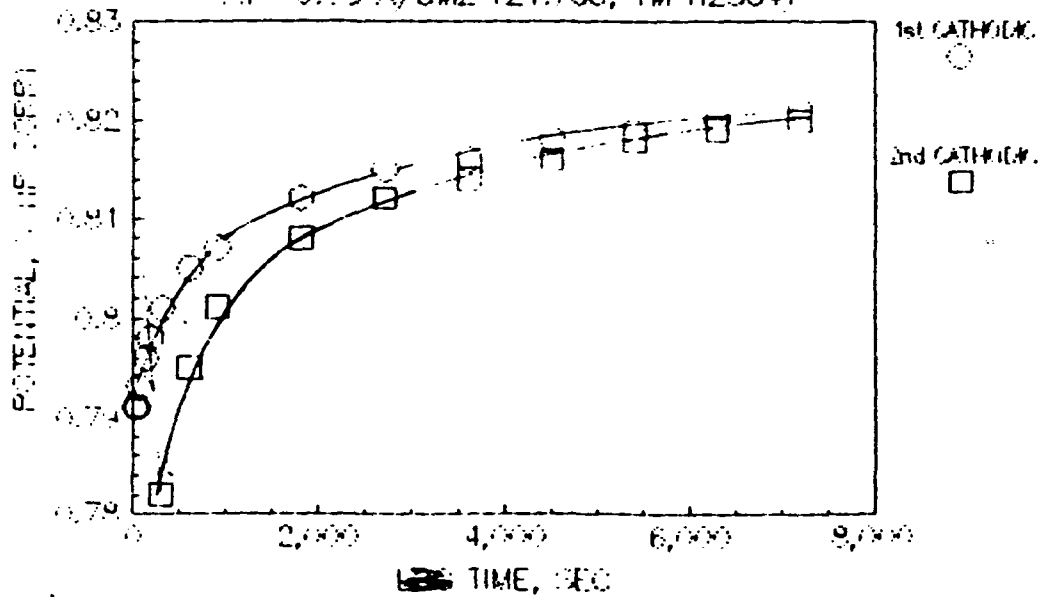
Figure 39. TWO HOUR CYCLING OF O<sub>2</sub> REDUCTION & EVOLUTION  
 GINER PEM/IRQ2,PT & PT FREE STANDING ELECTRODE  
 AT -&+ 0.05 A/CM<sup>2</sup> (21.7°C, 1M H<sub>2</sub>SO<sub>4</sub>)



FROM 0CV, START AT -0.05 A/CM<sup>2</sup>, THEN AT +0.05

GFT251  
 50000/MIN O<sub>2</sub>(H<sub>2</sub>O)/O<sub>2</sub> SIDE

Figure 40. POTENTIAL VS TIME WITH 2 HOUR CYCLING  
 GINER PEM/IRQ2,PT & PT FREE STANDING ELECTRODE  
 AT -0.05 A/CM<sup>2</sup> (21.7°C, 1M H<sub>2</sub>SO<sub>4</sub>)



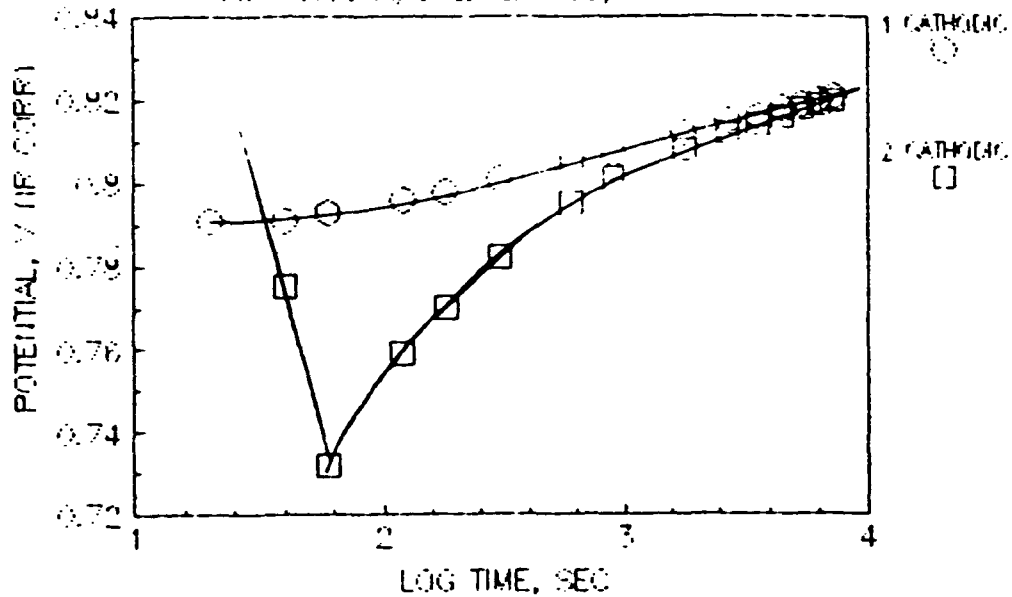
FROM 0CV, START AT -0.05 A/CM<sup>2</sup>, THEN +0.05 A  
 FOR -0.05 DATA

GFT501  
 50000/MIN O<sub>2</sub>(H<sub>2</sub>O)/O<sub>2</sub> SIDE

ORIGINAL PAGE IS  
 OF POOR QUALITY

5/7/82

Figure 41. POTENTIAL VS LOG TIME WITH 2 HOUR CYCLING  
 GINER PEM/IR02,PT & PT FREE STANDING ELECTRODE  
 AT  $-0.05 \text{ A/CM}^2$  (21.7°C, 1M H2SO4)



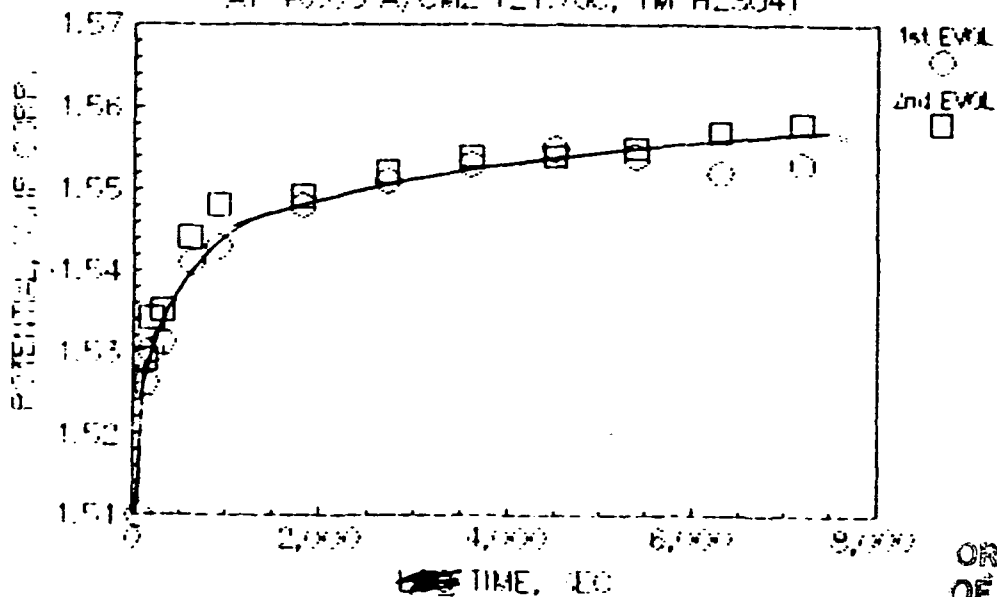
FROM 00V, START AT  $-0.05 \text{ A/CM}^2$ , THEN  $+0.05 \text{ A}$   
 FOR  $-0.05$  DATA

GPT500

50000/MIN 02(H2O)/02 SIDE

12/76

Figure 42. POTENTIAL VS ~~LOG~~ TIME WITH 2 HOUR CYCLING  
 GINER PEM/IR02,PT & PT FREE STANDING ELECTRODE  
 AT  $+0.05 \text{ A/CM}^2$  (21.7°C, 1M H2SO4)



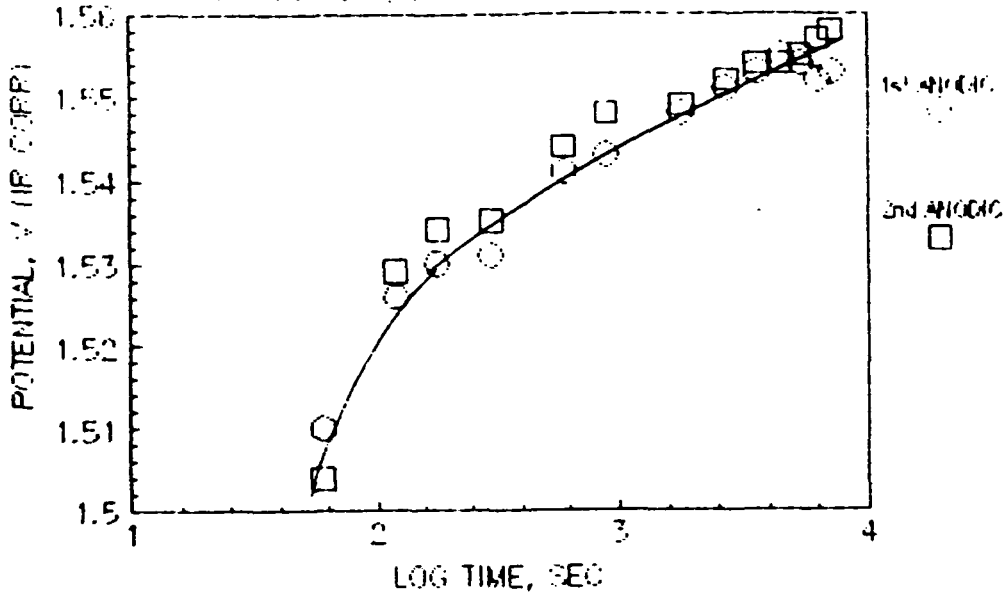
FROM 00V, START AT  $-0.05 \text{ A/CM}^2$ , THEN AT  $+0.05$   
 FOR  $-0.05$  DATA

ORIGINAL PAGE IS  
 OF POOR QUALITY

GPT253

50000/MIN 02(H2O)/02 SIDE

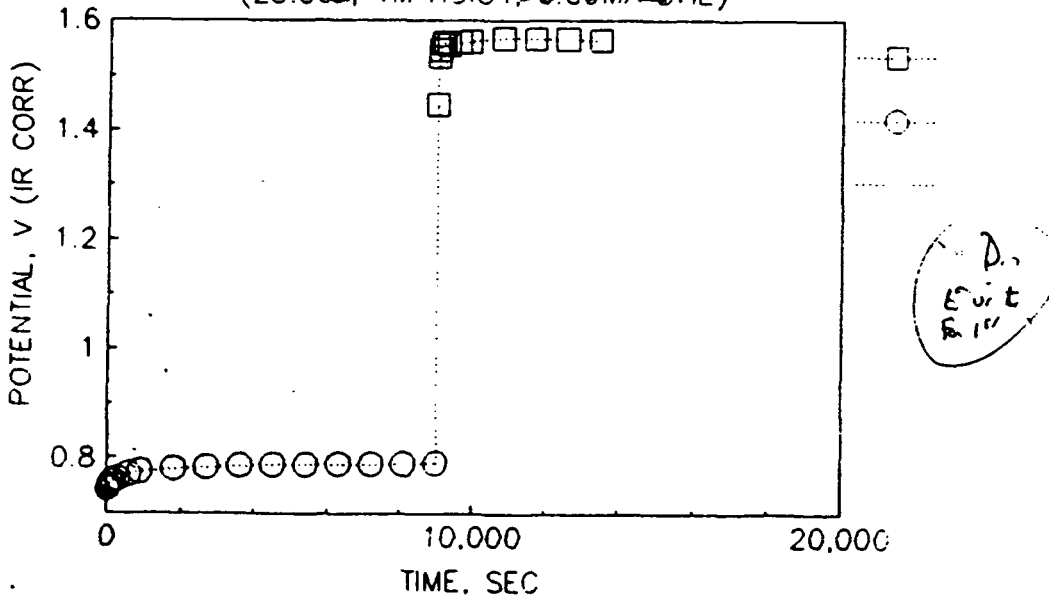
Figure 43. POTENTIAL VS LOG TIME WITH 2 HOUR CYCLING  
 GINER PEM/IR02,PT & PT FREE STANDING ELECTRODE  
 AT +0.05 A/CM2 (21.760, 1M H2SO4)



FROM OCV, START AT -0.05A/CM2, THEN AT +0.05  
 FOR +0.05 DATA

GPT252  
 50000/MIN O2(H2O)/O2 SIDE

Figure 44. POTENTIAL VS TIME WITH CYCLING  
 GINER PEM/PT/IR02 & PT FREE STANDING ELECTRODE  
 (23.30C, 1M HClO4, 0.001M OME)



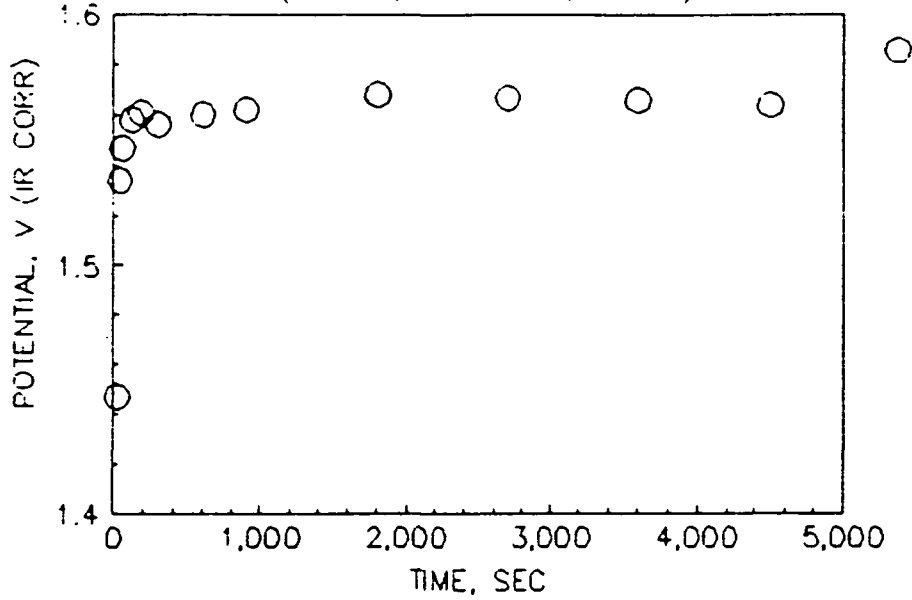
D.  
 E. v. t  
 R. 11

~~START FROM OCV AT -0.1 THEN AT +0.1 A~~

GPT248  
 500CC/MIN O2(H2O)/O2 SIDE

ORIGINAL PAGE IS  
 OF POOR QUALITY

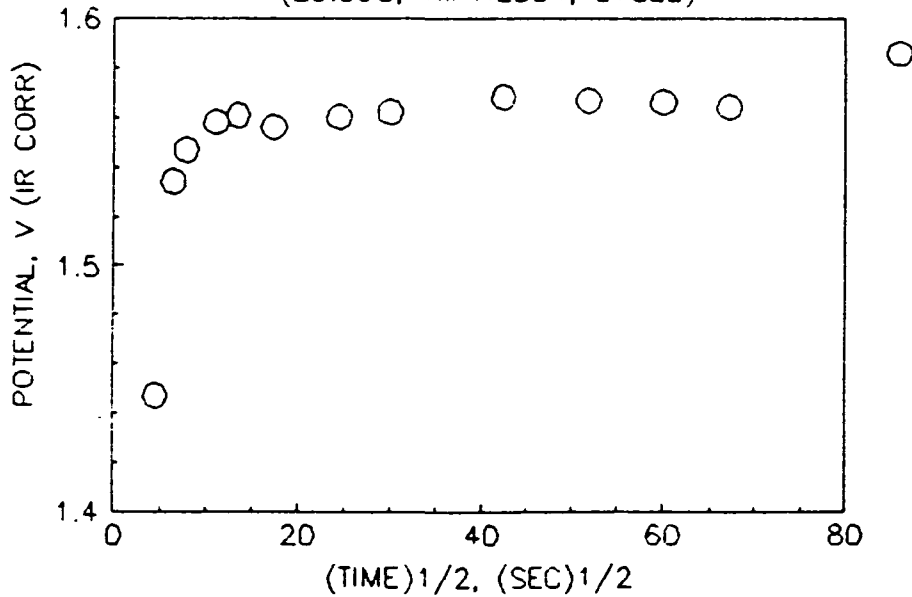
Figure 45. ANODIC POTENTIAL VS TIME AT 0.1A  
 GINER PEM/PT/IRO2 & PT FREE STANDING ELECTRODE  
 (23.3oC, 1M H2SO4, CYCLE)



AFTER -0.1A FOR 2.5 HR  
 (FROM 0.79 V)(BUBBLES?)

GPT328  
 500CC/MIN O2(H2O)/O2 SIDE

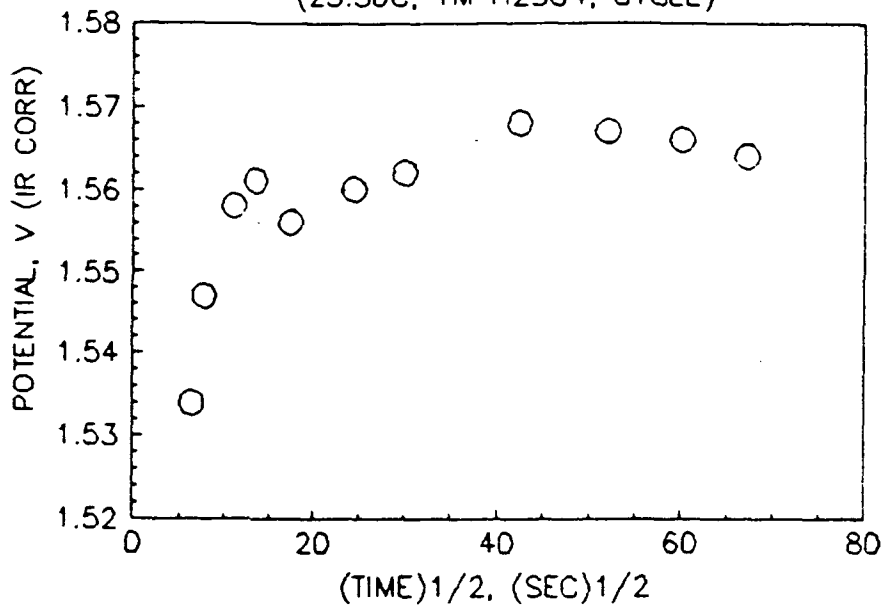
Figure 46. ANODIC POTENTIAL VS (TIME)<sup>1/2</sup> AT 0.1A  
 GINER PEM/PT/IRO2 & PT FREE STANDING ELECTRODE  
 (23.3oC, 1M H2SO4, CYCLE)



AFTER -0.1A FOR 2.5 HR  
 (FROM 0.79 V)(BUBBLES?)

GPT329  
 500CC/MIN O2(H2O)/O2 SIDE

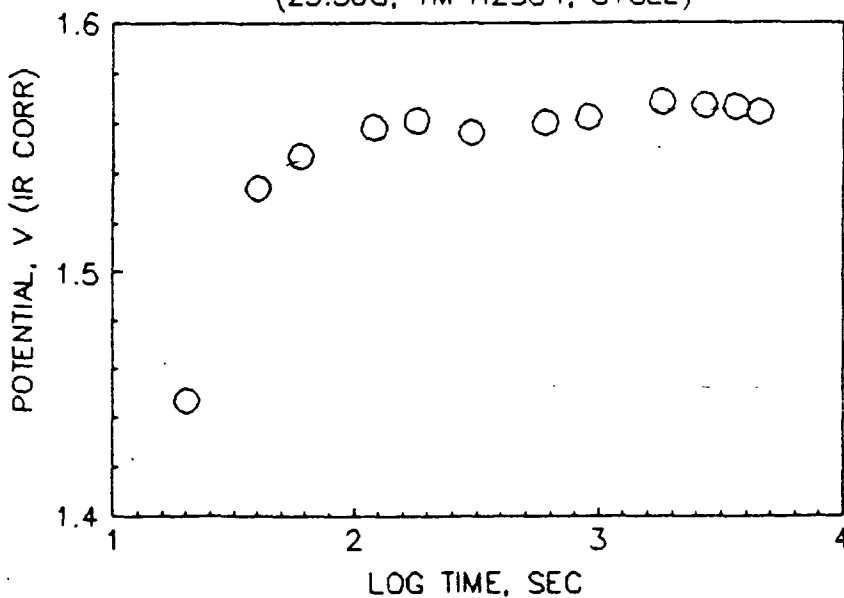
Figure 47. ANODIC POTENTIAL VS (TIME)<sup>1/2</sup> AT 0.1A  
 GINER PEM/PT/IRO2 & PT FREE STANDING ELECTRODE  
 (23.3oC, 1M H2SO4, CYCLE)



AFTER -0.1A FOR 2.5 HR  
 (FROM 0.79 V)(BUBBLES?)

GPT329  
 500CC/MIN O2(H2O)/O2 SIDE

Figure 48. ANODIC POTENTIAL VS LOG TIME AT 0.1A  
 GINER PEM/PT/IRO2 & PT FREE STANDING ELECTRODE  
 (23.3oC, 1M H2SO4, CYCLE)

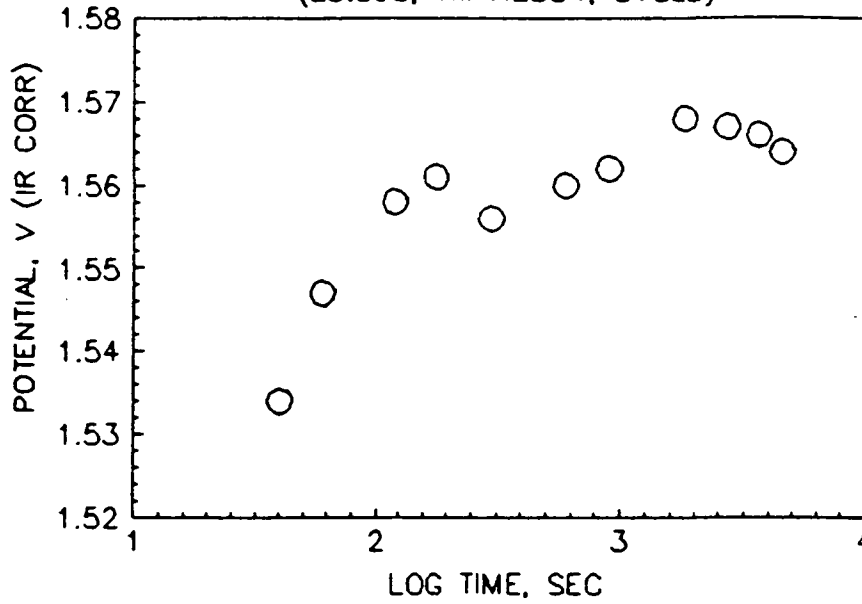


AFTER -0.1A FOR 2.5 HR  
 (FROM 0.79V)(BUBBLES?)

GPT117  
 500CC/MIN O2(H2O)/O2 SIDE



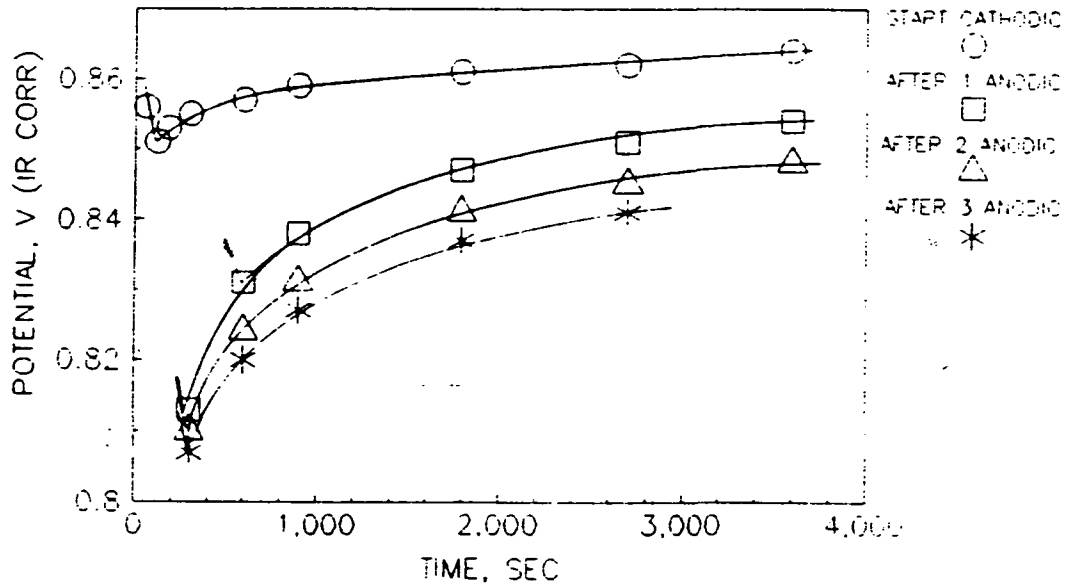
Figure 49. ANODIC POTENTIAL VS LOG TIME AT 0.1A  
 GINER PEM/PT/IRO2 & PT FREE STANDING ELECTRODE  
 (23.3oC, 1M H2SO4, CYCLE)



AFTER -0.1A FOR 2.5 HR  
 (FROM 0.79V)(BUBBLES?)

GPT117  
 500CC/MIN O2(H2O)/O2 SIDE

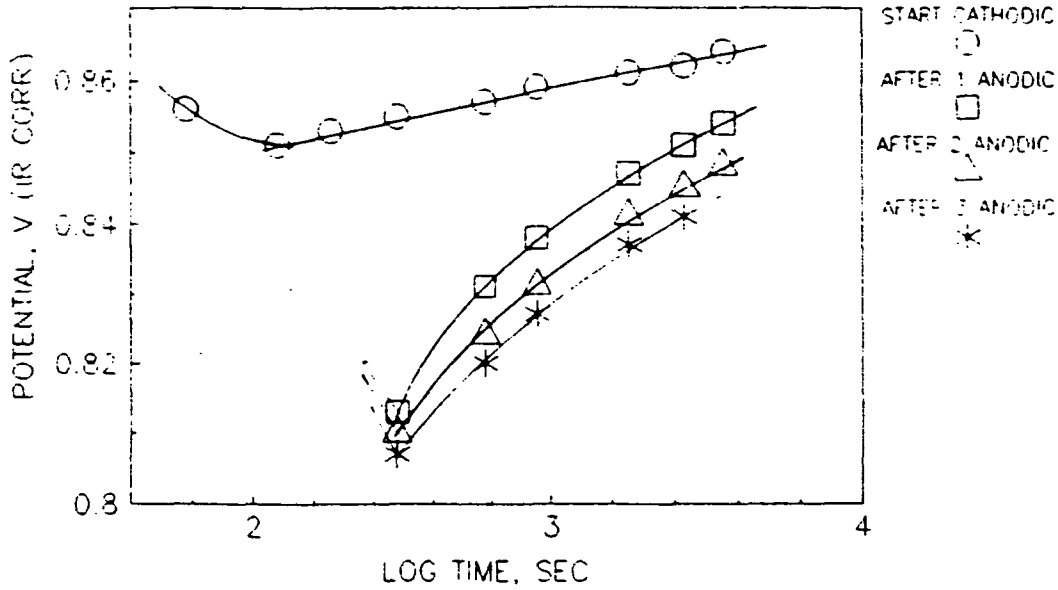
Figure 50. CATHODIC POTENTIAL VS TIME/START & AFTER ANODIC  
 GINER PEM/PT/IRO2 & PT FREE STANDING ELECTRODE  
 ALTERNATE 1 HR CATHODIC & ANODIC AT 0.01A



(22.2oC, 1M H2SO4)  
 500CC/MIN O2(H2O)/O2 SIDE

GPT243

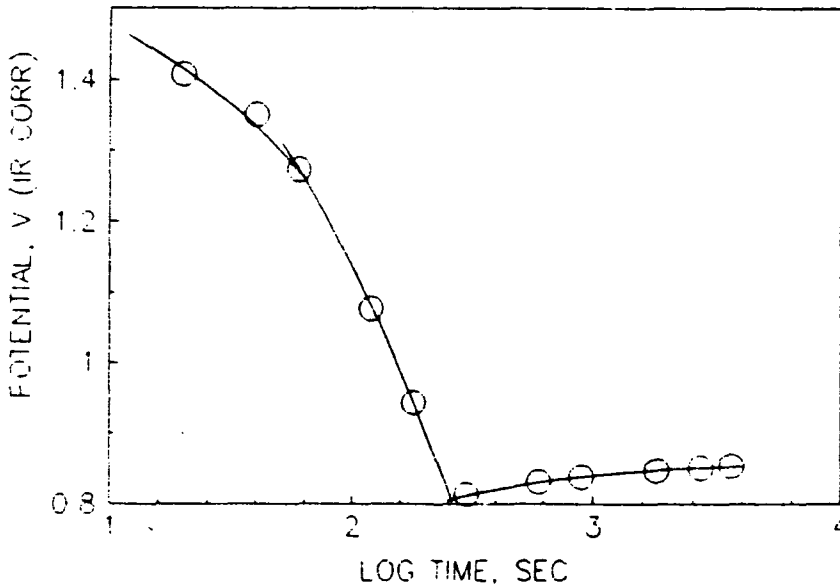
**Figure 51.** CATHODIC POTENTIAL VS LOG TIME/START & AFTER  
 GINER PEM/PT/IRO2 & PT FREE STANDING ELECTRODE  
 ALTERNATE 1 HR CATHODIC & ANODIC AT 0.01A



(22.2oC, 1M H2SO4)  
 500CC/MIN O2(H2O)/O2 SIDE

GPT246

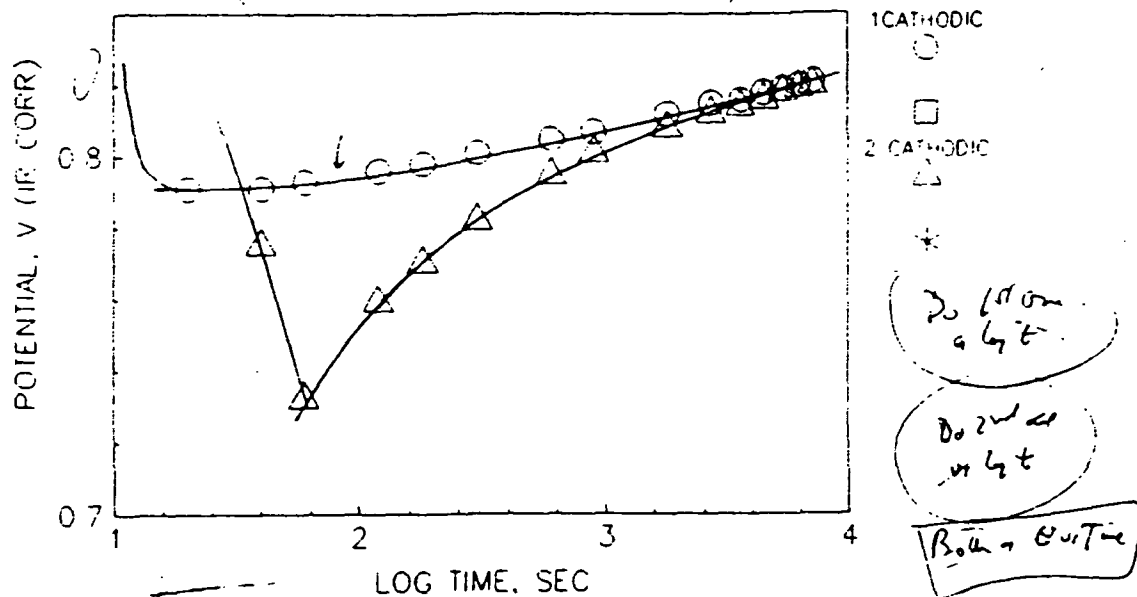
**Figure 52.** CATHODIC POTENTIAL VS LOG TIME AFTER 1 ANODIC  
 GINER PEM/PT/IRO2 & PT FREE STANDING ELECTRODE  
 ALTERNATE 1 HR CATHODIC & ANODIC AT 0.01A



(22.2oC, 1M H2SO4)  
 500CC/MIN O2(H2O)/O2 SIDE

GPT245

Figure 53. Cathodic POTENTIAL VS LOG TIME <sup>AT -0.05A</sup> (CYCLING)  
 GINER PEM/PT/IRO2 & PT FREE STANDING ELECTRODE  
 (22.20C, 1M H2SO4, 0.001M E)

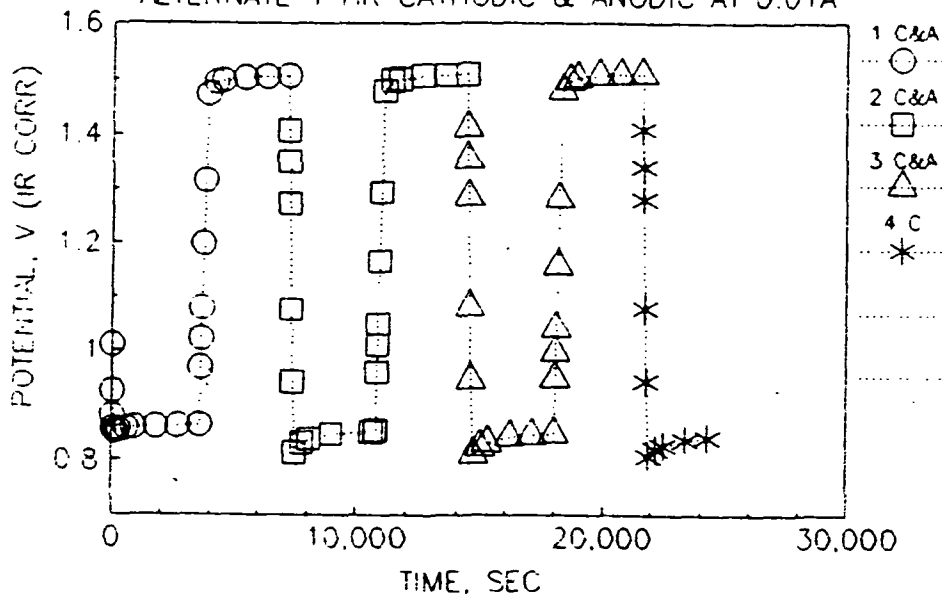


START FROM OCV AT -0.05A THEN AT +0.05 A

GPT252  
 500CC/MIN O2(H2O)/O2 SIDE

4-19

Figure 54. POTENTIAL VS TIME WITH CYCLING  
 GINER PEM/PT/IRO2 & PT FREE STANDING ELECTRODE  
 ALTERNATE 1 HR CATHODIC & ANODIC AT 0.01A

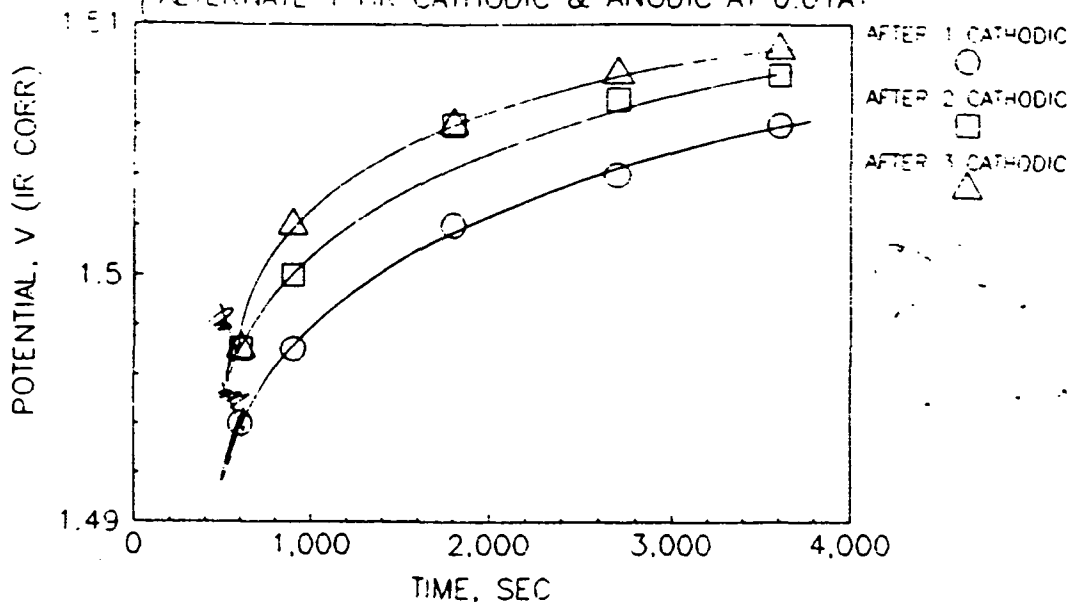


(22.20C, 1M H2SO4)  
 500CC/MIN O2(H2O)/O2 SIDE

GPT241

At 0.01A

Figure 55. ANODIC POTENTIAL VS TIME AFTER CATHODIC  
GINER PEM/PT/IRO2 & PT FREE STANDING ELECTRODE  
ALTERNATE 1 HR CATHODIC & ANODIC AT 0.01A.

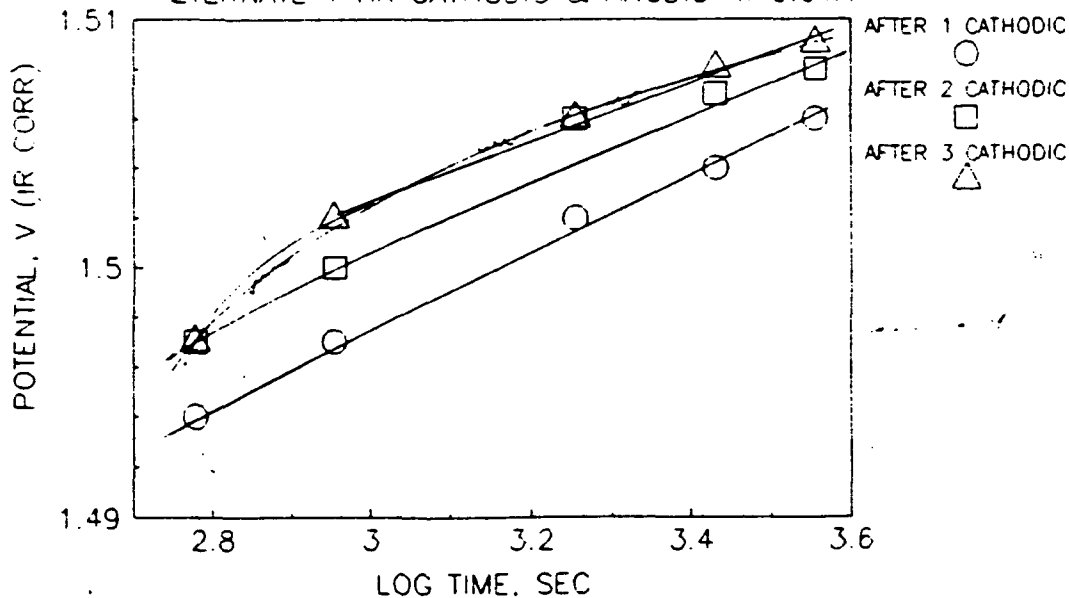


(22.2oC, 1M H2SO4)  
500CC/MIN O2(H2O)/O2 SIDE

GPT244

At 0.01A

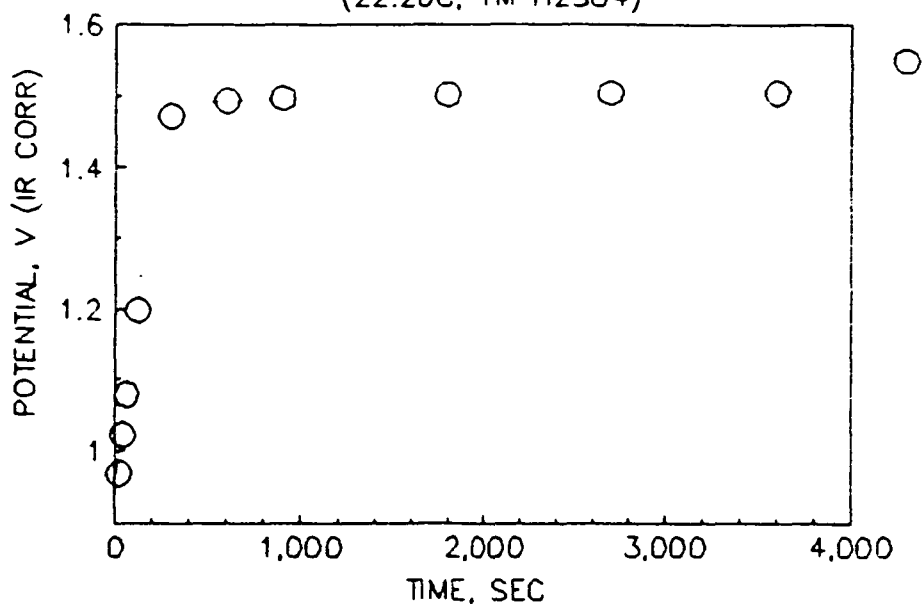
Figure 56. ANODIC POTENTIAL VS LOG TIME AFTER CATHODIC  
GINER PEM/PT/IRO2 & PT FREE STANDING ELECTRODE  
ALTERNATE 1 HR CATHODIC & ANODIC AT 0.01A



(22.2oC, 1M H2SO4)  
500CC/MIN O2(H2O)/O2 SIDE

GPT247

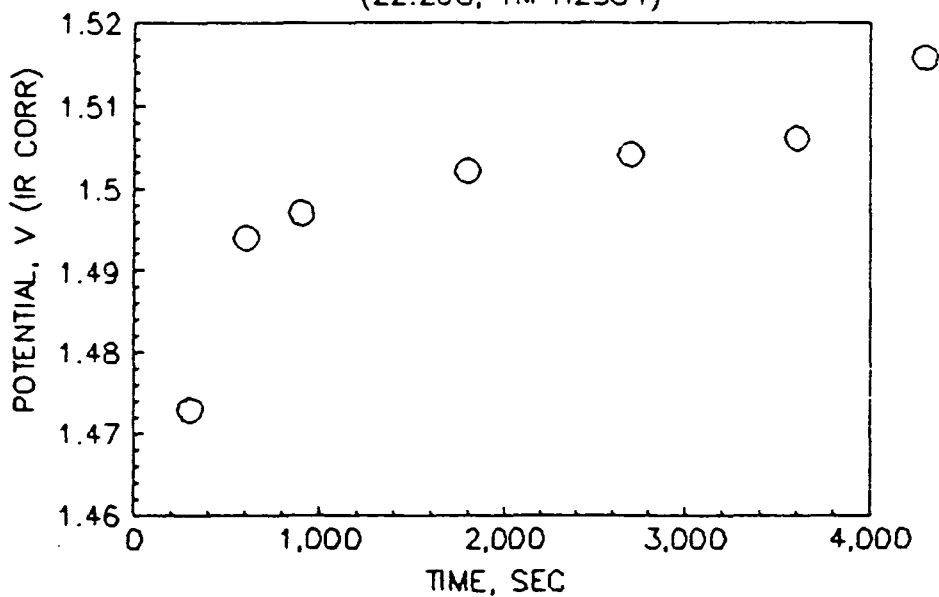
Figure 57. ANODIC POTENTIAL VS TIME AT 0.01A  
GINER PEM/PT/IRO2 & PT FREE STANDING ELECTRODE  
(22.2oC, 1M H2SO4)



AFTER -0.01A FOR 1 HR  
500CC/MIN O2(H2O)/O2 SIDE

GPT326

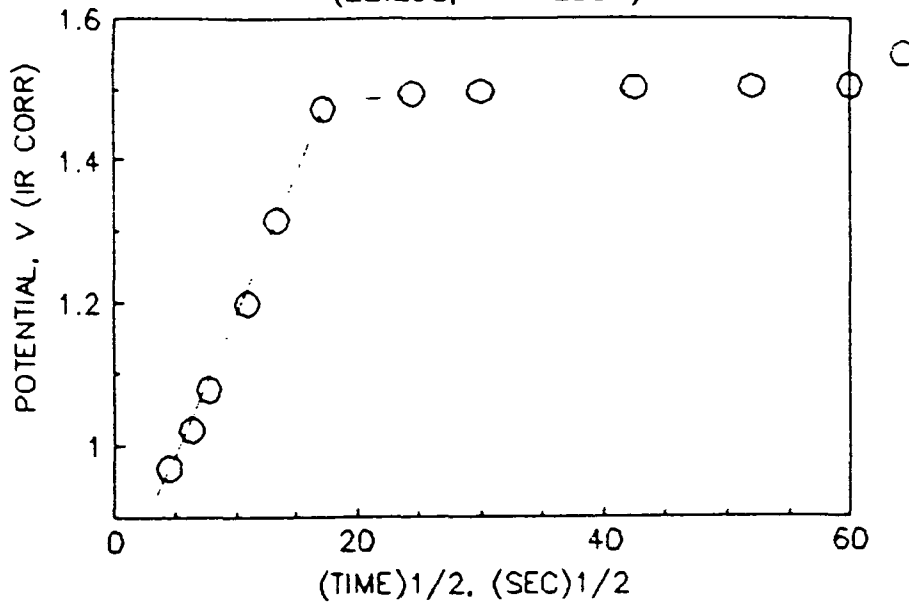
Figure 58. ANODIC POTENTIAL VS TIME AT 0.01A  
GINER PEM/PT/IRO2 & PT FREE STANDING ELECTRODE  
(22.2oC, 1M H2SO4)



AFTER -0.01A FOR 1 HR  
500CC/MIN O2(H2O)/O2 SIDE

GPT326

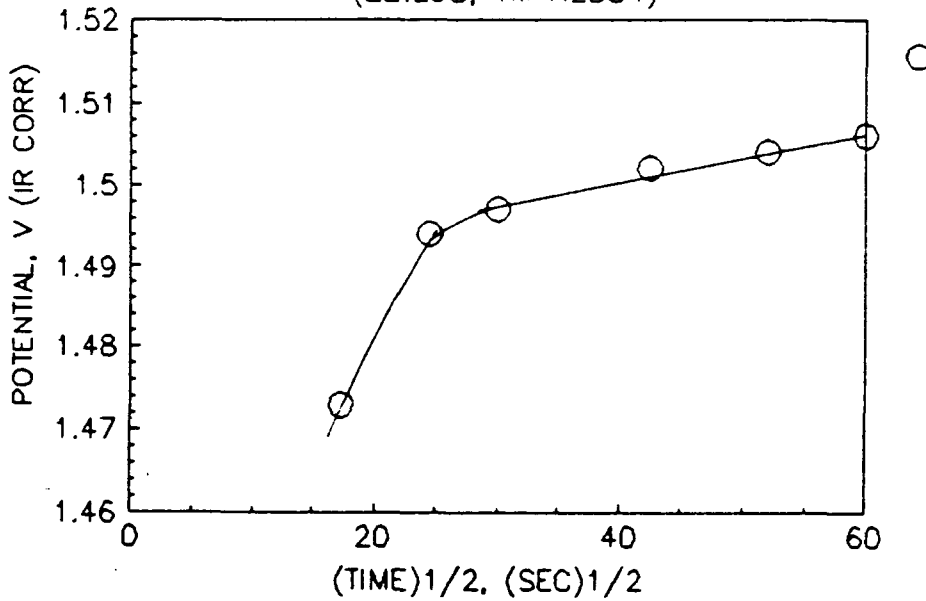
Figure 59. ANODIC POTENTIAL VS (TIME)<sup>1/2</sup> AT 0.01A  
GINER PEM/PT/IRO2 & PT FREE STANDING ELECTRODE  
(22.2oC, 1M H2SO4)



AFTER -0.01A FOR 1 HR  
500CC/MIN O2(H2O)/O2 SIDE

GPT327

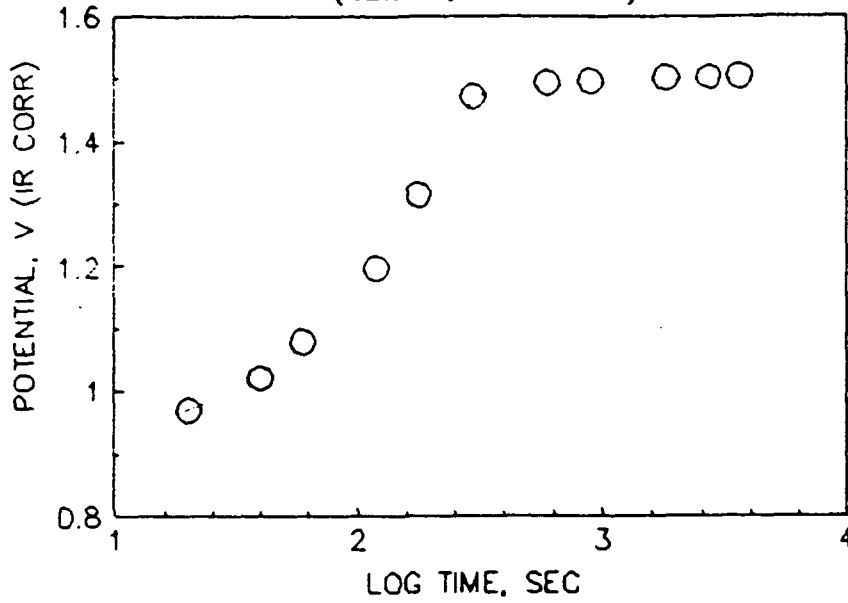
Figure 60. ANODIC POTENTIAL VS (TIME)<sup>1/2</sup> AT 0.01A  
GINER PEM/PT/IRO2 & PT FREE STANDING ELECTRODE  
(22.2oC, 1M H2SO4)



AFTER -0.01A FOR 1 HR  
500CC/MIN O2(H2O)/O2 SIDE

GPT327

Figure 61. ANODIC POTENTIAL VS LOG TIME AT 0.01A  
GINER PEM/PT/IRO2 & PT FREE STANDING ELECTRODE  
(22.2oC, 1M H2SO4)

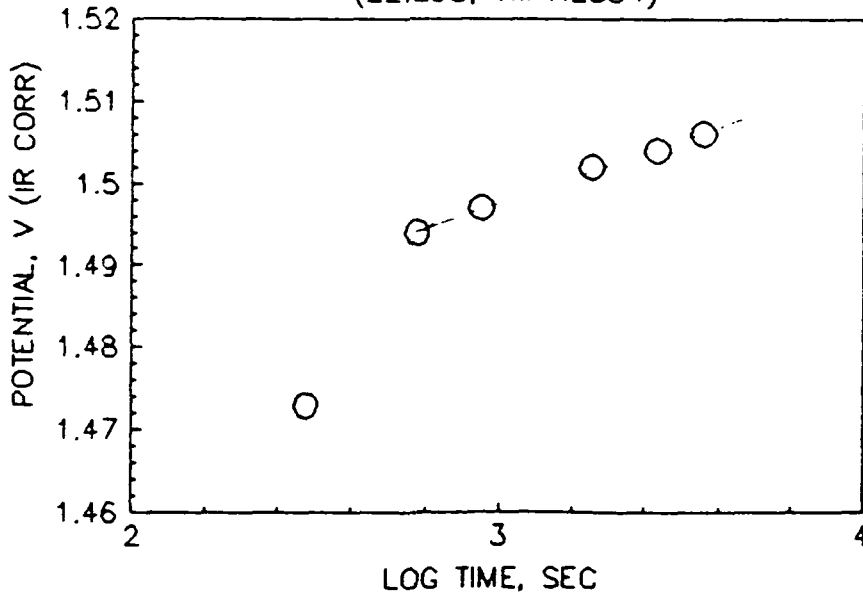


AFTER -0.01A FOR 1 HR  
500CC/MIN O2(H2O)/O2 SIDE

GPT242

*1/8/72*

Figure 62. ANODIC POTENTIAL VS LOG TIME AT 0.01A  
GINER PEM/PT/IRO2 & PT FREE STANDING ELECTRODE  
(22.2oC, 1M H2SO4)



AFTER -0.01A FOR 1 HR  
500CC/MIN O2(H2O)/O2 SIDE

GPT242

*1/8/72*

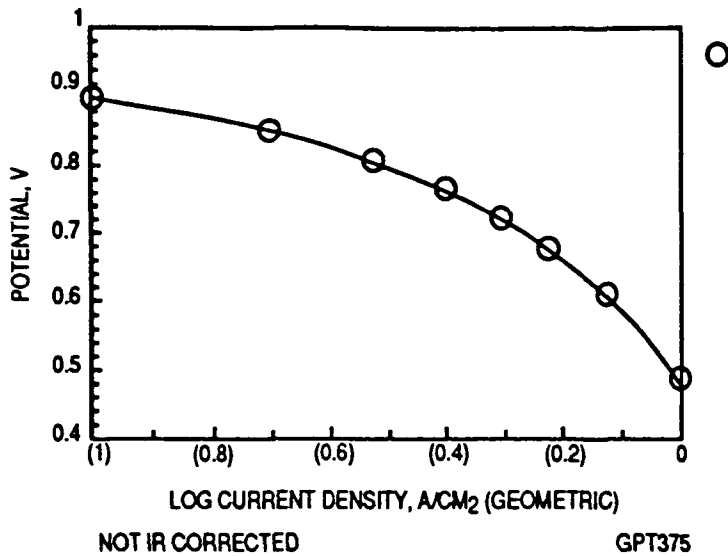


Figure 63. Giner Data for O<sub>2</sub> Reduction at 80 C  
63. PEM/IRo<sub>2</sub>,PT & PT Free Standing Electrode Single Cell (3 ATM)

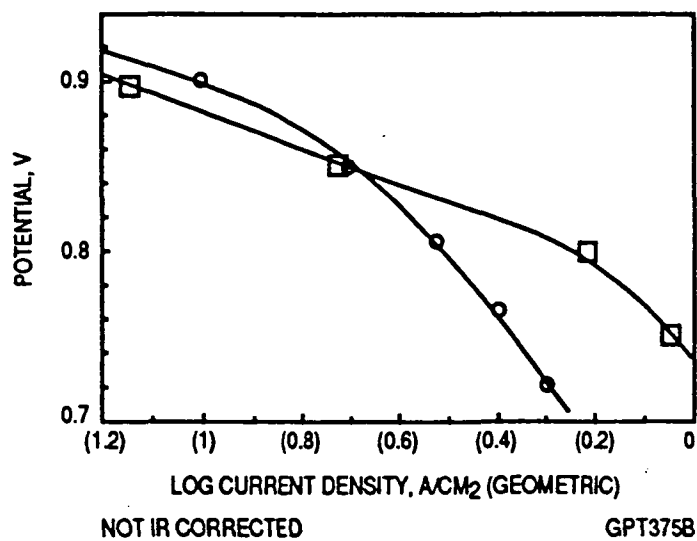


Figure 65. Giner and Laer Data for O<sub>2</sub> Reduction at 80 C  
Giner: NAFION, 3 ATM  
Laer: DOW, 5 ATM

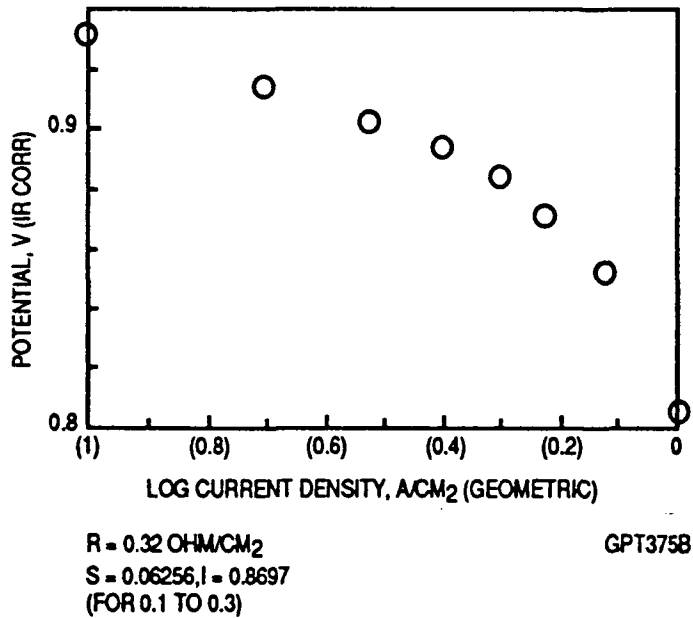


Figure 64. Giner Data for O<sub>2</sub> Reduction at 80 C PEM/IRo<sub>2</sub>,PT & PT Free Standing Electrode Single Cell (3 ATM)

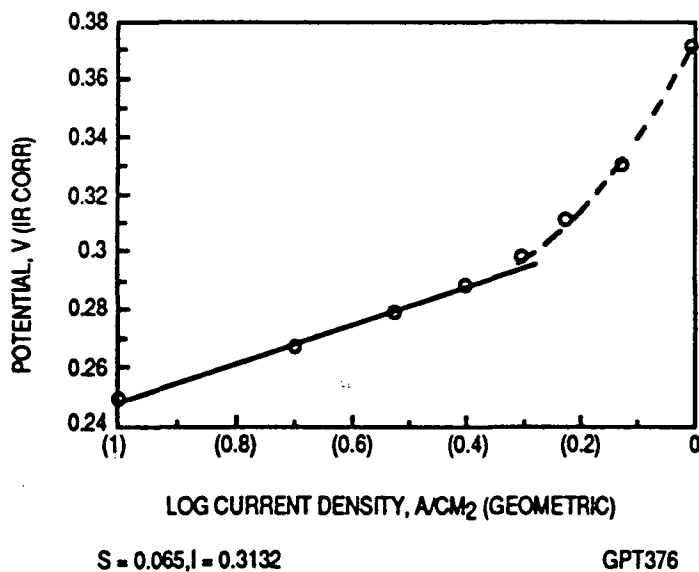


Figure 66. Giner Tafel Data for O<sub>2</sub> Reduction Giner  
66. PEM/IRo<sub>2</sub>, PT & PT Free Standing Electrode Single Cell (3 ATM)



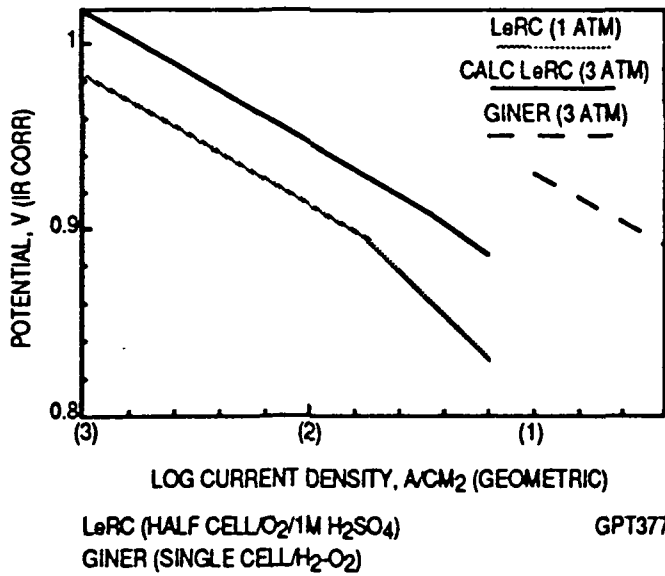


Figure 69: Compare O<sub>2</sub> Reduction of LeRC & Giner Data  
67. PEM/IRO<sub>2</sub>,PT & PT Free Standing Electrode (80 C, 1 ATM O<sub>2</sub> for LeRC, 3 ATM for Giner)

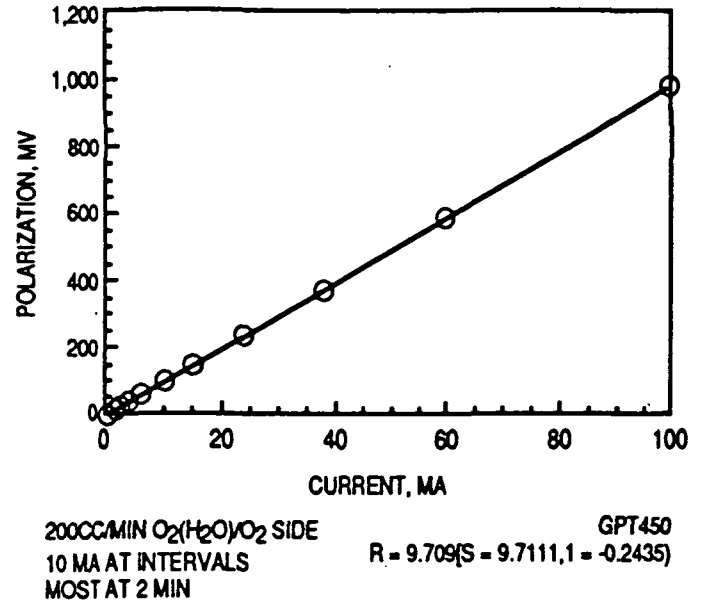


Figure 69: Cathodic R Polarization for Giner Electrode PT Free Standing Only (81,DoC, 1M H<sub>2</sub>SO<sub>4</sub>, 0.09MA DHE)

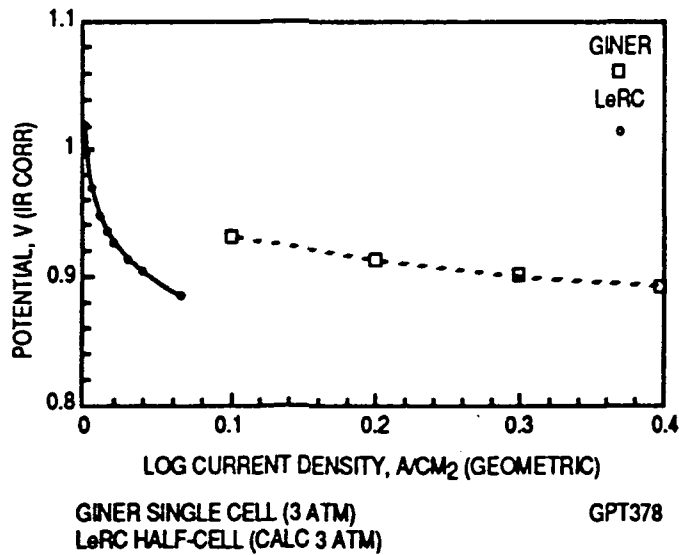


Figure 70: Potential-Current Plots for O<sub>2</sub> Reduction Giner  
68. PEM/IRO<sub>2</sub>,PT & PT Free Standing Electrode Comparison Giner (3 ATM) with CALC LeRC (3 ATM)

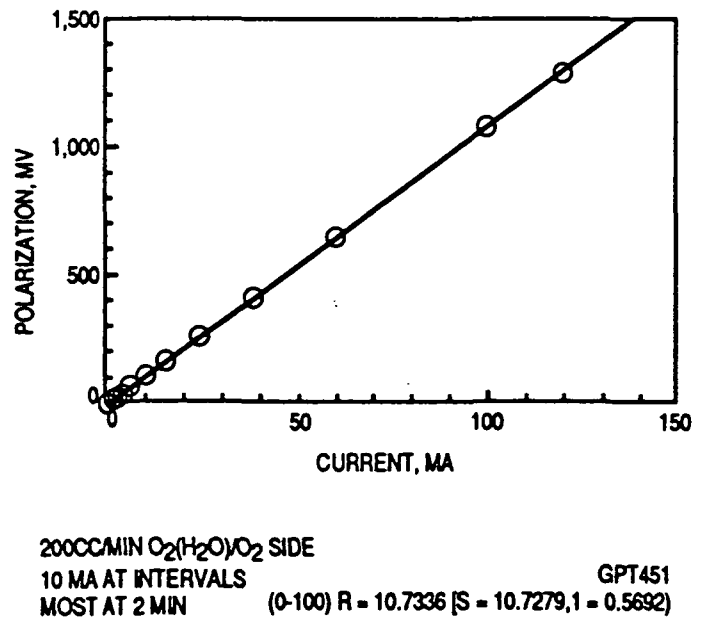
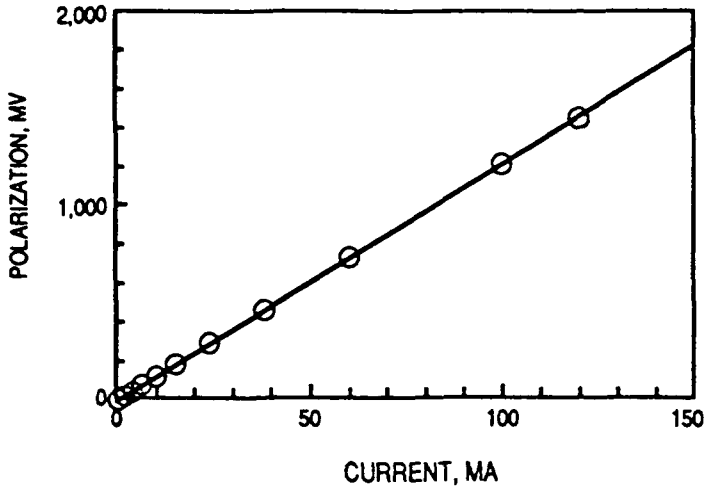
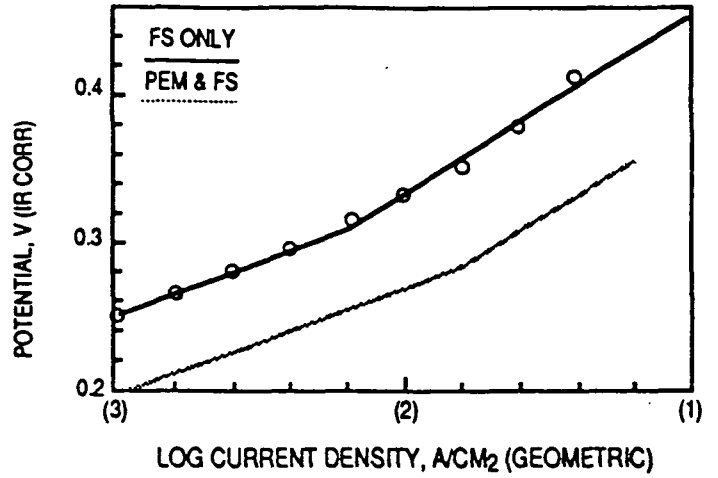


Figure 70: Cathodic R Polarization for Giner Electrode PT Free Standing Only (60,DoC, 1M H<sub>2</sub>SO<sub>4</sub>, 0.09MA DHE)



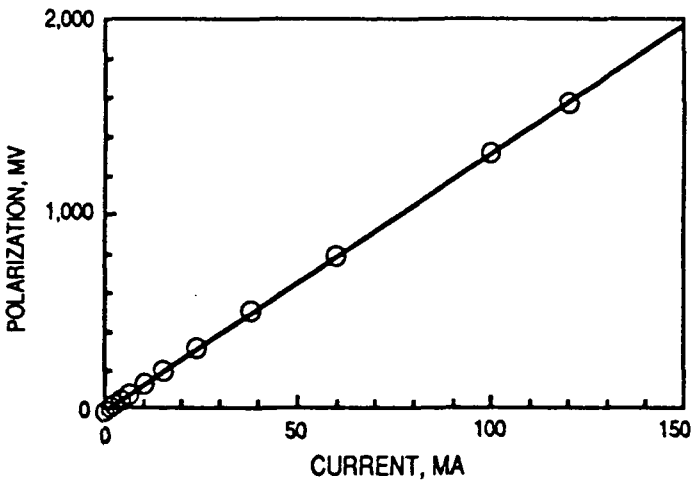
200CC/MIN O<sub>2</sub>(H<sub>2</sub>O)/O<sub>2</sub> SIDE  
 10 MA AT INTERVALS  
 MOST AT 2 MIN  
 GPT452  
 (0-100) R = 12.0509 [S = 12.04926, 11 = 0.15979]

Figure 71. Cathodic R Polarization for Giner Electrode PT Free Standing Only (39.4°C, 1M H<sub>2</sub>SO<sub>4</sub>, 0.09MA DHE)



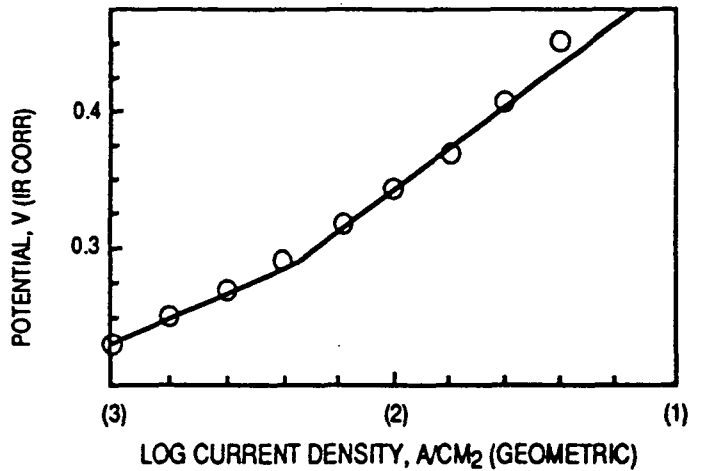
200CC/MIN O<sub>2</sub>(H<sub>2</sub>O)/O<sub>2</sub> SIDE  
 S = 0.0715 (I = 0.4656 (-2.185))  
 S = 0.12 (I = 0.5717)  
 COMPARE PEM & FS  
 GFS3-12  
 GPT454

Figure 75. Tafel Plot for O<sub>2</sub> Reduction Giner PT Free Standing Electrode Only (81.0°C, 1M H<sub>2</sub>SO<sub>4</sub>)



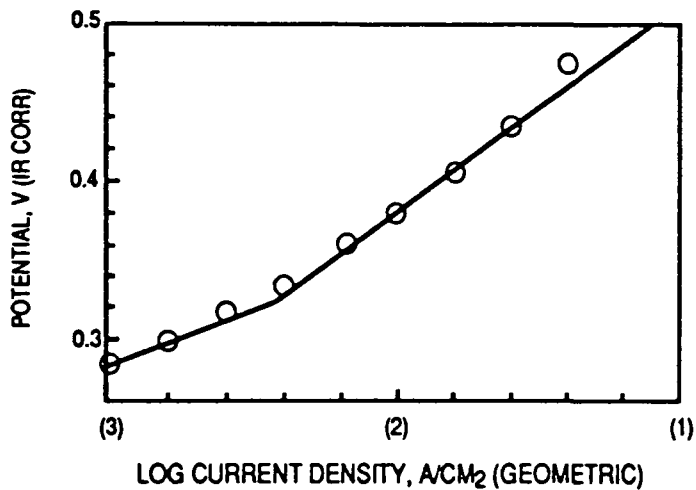
200CC/MIN O<sub>2</sub>(H<sub>2</sub>O)/O<sub>2</sub> SIDE  
 10 MA AT INTERVALS  
 MOST AT 2 MIN  
 GPT453  
 (0-100) R = 13.0948 [S = 13.0948, 1 = 0.7451]

Figure 72. Cathodic R Polarization for Giner Electrode PT Free Standing Only (26.1°C, 1M H<sub>2</sub>SO<sub>4</sub>, 0.09MA DHE)



200CC/MIN O<sub>2</sub>(H<sub>2</sub>O)/O<sub>2</sub> SIDE  
 S = 0.071,1 (I = 0.4784 (-2.358))  
 S = 0.12,1 0.5939  
 GFS14-24  
 GPT455

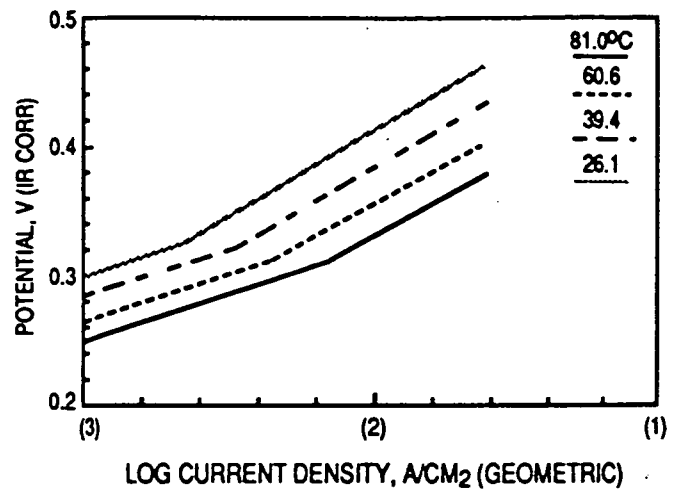
Figure 76. Tafel Plot for O<sub>2</sub> Reduction Giner PT Free Standing Electrode Only (60.0°C, 1M H<sub>2</sub>SO<sub>4</sub>)



S = 0.070,1 (I = 0.4943 (-2.435)  
 S = 0.13,1 0.6404  
 200CC/MIN O<sub>2</sub>(H<sub>2</sub>O)/O<sub>2</sub> SIDE

GFS26-36  
 GPT456

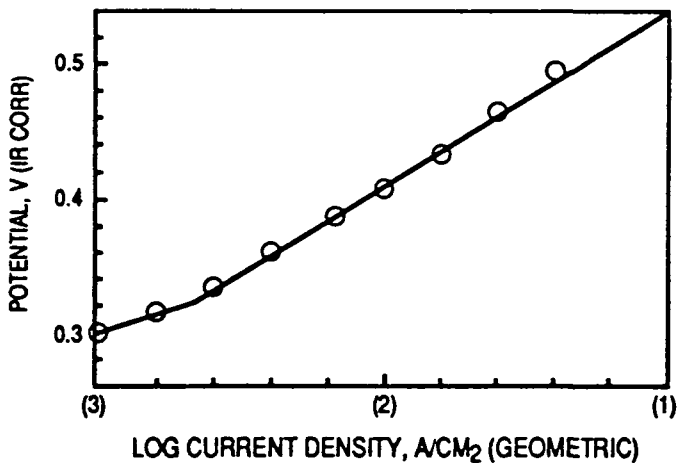
Figure 75: Tafel Plot for O<sub>2</sub> Reduction Giner PT Free Standing Electrode Only (39.4°C, 1M H<sub>2</sub>SO<sub>4</sub>)



200CC/MIN O<sub>2</sub>(H<sub>2</sub>O)/O<sub>2</sub> SIDE

GPT458

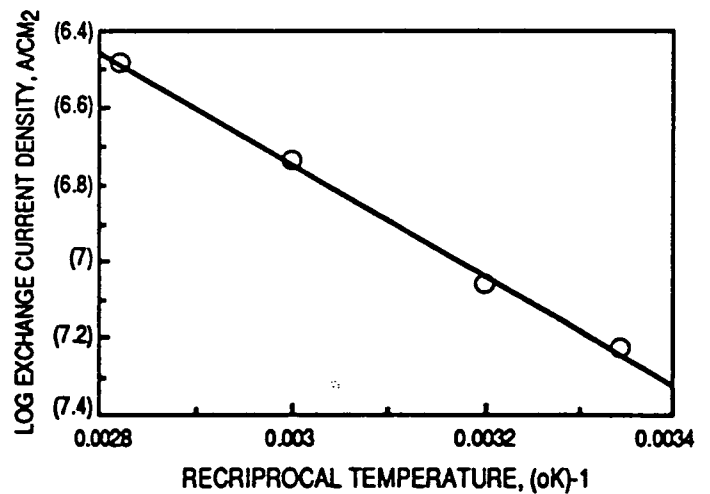
Figure 76: Tafel Plot for O<sub>2</sub> Reduction Giner PT Free Standing Electrode Only (1M H<sub>2</sub>SO<sub>4</sub>)



S = 0.071,1 (I = 0.5132 (-2.656)  
 S = 0.13,1 0.6699  
 200CC/MIN O<sub>2</sub>(H<sub>2</sub>O)/O<sub>2</sub> SIDE

GFS37-48  
 GPT457

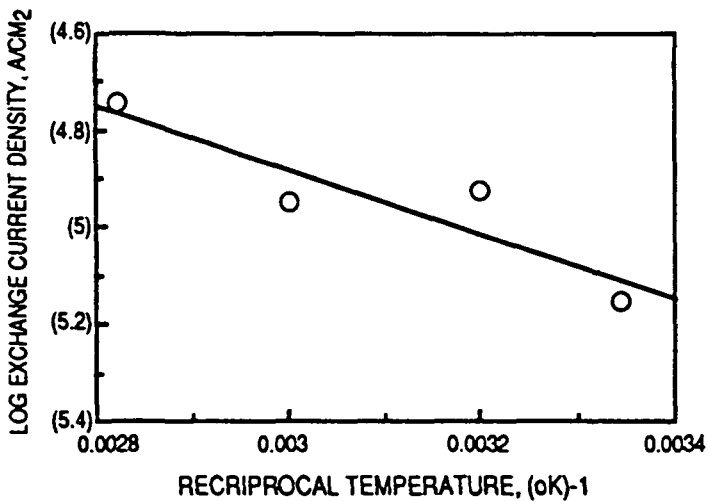
Figure 77: Tafel Plot for O<sub>2</sub> Reduction Giner PT Free Standing Electrode Only (26.1°C, 1M H<sub>2</sub>SO<sub>4</sub>)



E<sub>a</sub> = 6.7KCAL/M (S = -1464.9, I = 2.347)  
 200CC/MIN O<sub>2</sub>(H<sub>2</sub>O)/O<sub>2</sub> SIDE (GEOMETRIC)

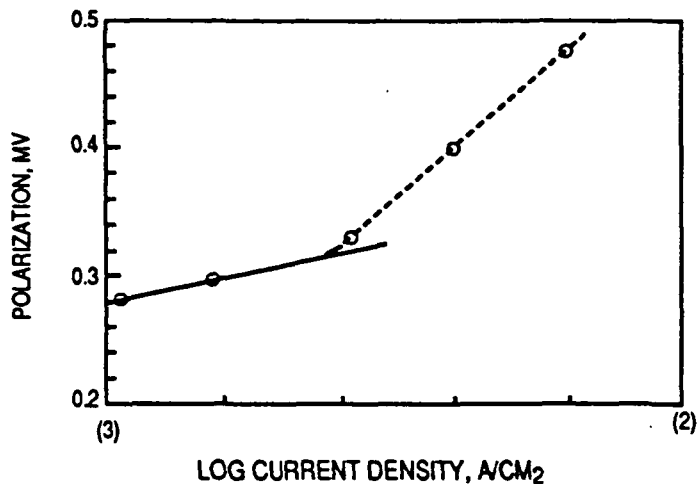
GPT459

Figure 78: Activation Energy for O<sub>2</sub> Reduction Giner PT Free Standing Electrode Only for 0.06 Region (1M H<sub>2</sub>SO<sub>4</sub>)



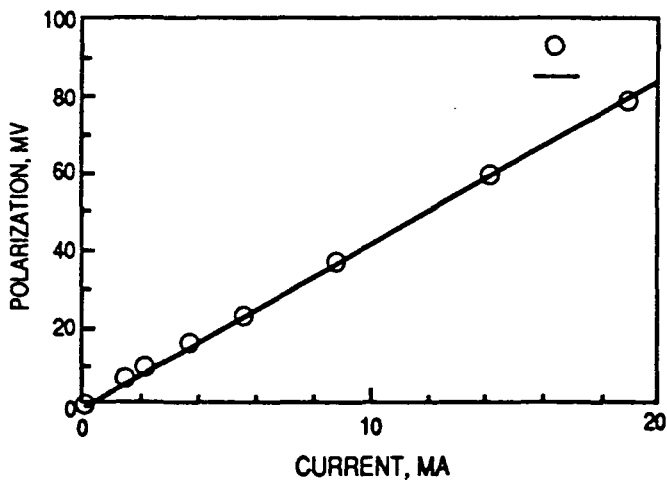
$E_a = 3.1 \text{KCAL/M}$  ( $S = -673.1, I = 2.861$ )  
 200CC/MIN  $O_2(H_2O)/O_2$  SIDE  
 10 MA AT INTERVALS  
 MOST AFTER 2 MIN  
 GPT460

Figure 84: Activation Energy for  $O_2$  Reduction Giner PT  
 79. Free Standing Electrode Only for 0.12 Region  
 ( $1M H_2SO_4$ )



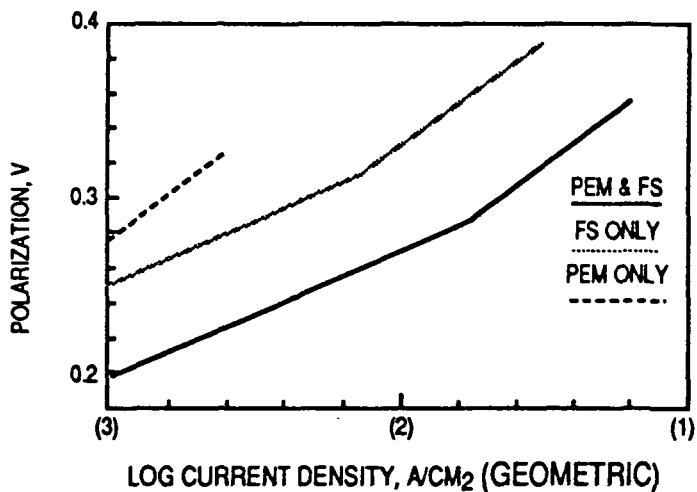
0.12 (0.6371)  
 (PREHEAT  $90^\circ C$  BEFORE)  
 GPT/ $IRO_2$ 47  
 GPT487

Figure 85: Tafel Plot of  $O_2$  Reduction Giner PEM/ $IRO_2$ ,PT  
 81. Electrode Only ( $78.9^\circ C, 1.5M H_2SO_4$ )



$R = 4.163$  ( $S = 4.145, I = 0.4374$ )  
 200CC/MIN  $O_2(H_2O)/O_2$  SIDE  
 PREHEAT TO  $90^\circ C$   
 GPT/ $IRO_2$ 47  
 GPT70

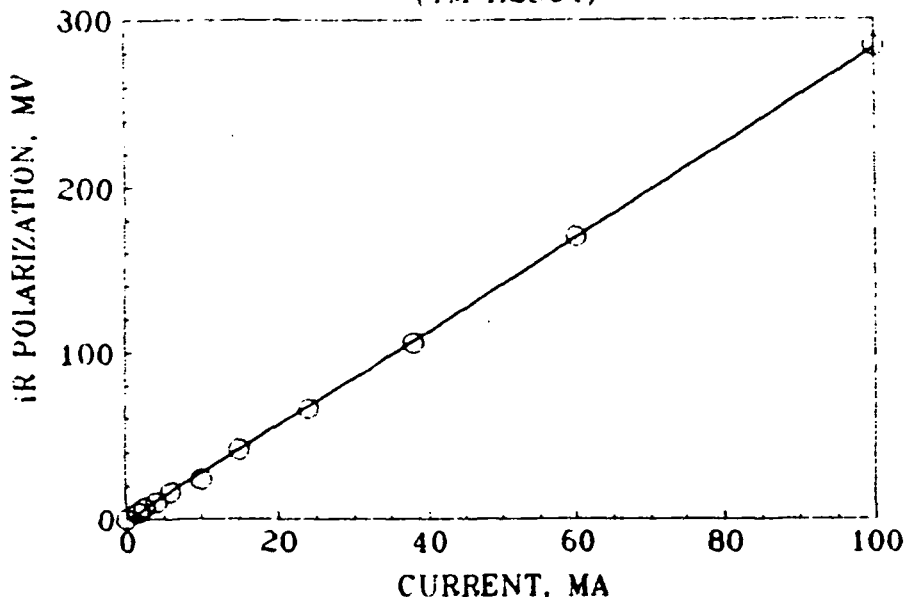
Figure 82: R Polarization vs. Current for  $O_2$  Reduction  
 Giner PEM/PT/ $IRO_2$  Electrode (No Free  
 Standing) ( $80.6^\circ C, 3N H_2SO_4$ , After 1-2 Min)



PEM & FS ( $80.0^\circ C$ )  
 FS ONLY ( $81.0^\circ C$ )  
 PEM ONLY ( $80.0^\circ C$ )  
 GPT461

Figure 84: Compare Tafel Plots for  $O_2$  Reduction at  $80^\circ C$   
 82. Giner Electrodes ( $1M H_2SO_4$ )

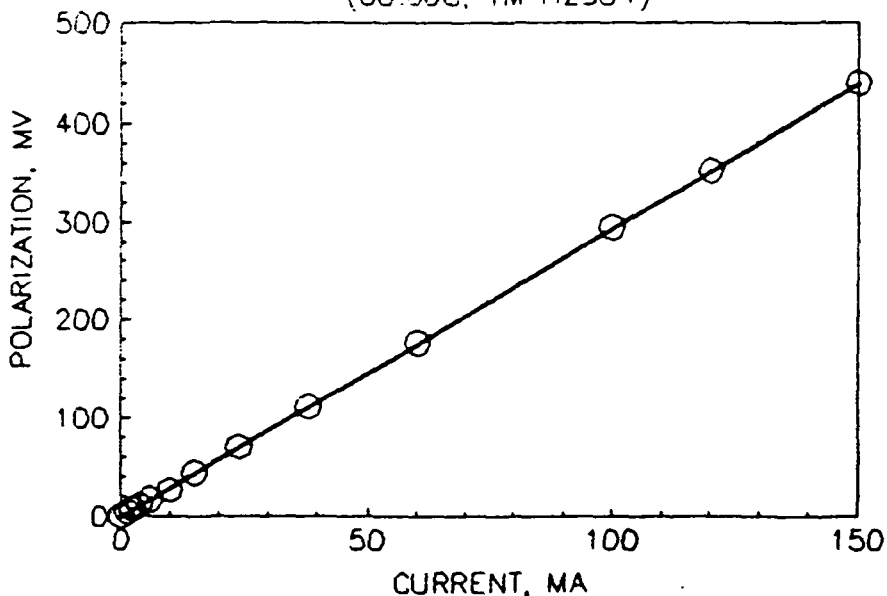
Figure 83. R FOR O2 REDUCTION AT 80.0°C (GALVANOSTATIC)  
 GINER PEM/IR02,PT & PT FREE STANDING ELECTRODE  
 (1M H2SO4)



(PREHEAT 80°C FOR 30)  
 EACH DATA POINT TAKEN AFTER ABOUT 2 MIN  
 R=2.835 OHM (1.89 OHM/CM2)

GPEMFS1-12  
 GPT365

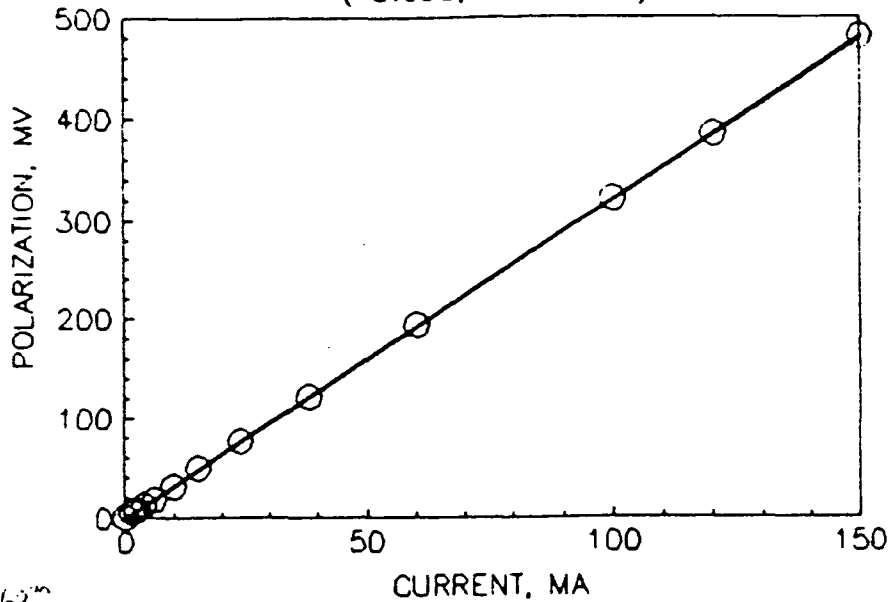
Figure 84. R POLARIZATION FOR O2 REDUCTION  
 GINER PEM/PT/IR02 & PT FREE STANDING ELECTRODE  
 (60.6°C, 1M H2SO4)



80°C FOR 30, 60°C FOR 30  
 200CC/MIN O2(H2O)/O2 SIDE  
 0-100(R=2.9367)120(2.9370)150(2.9335)

GPEMFS13-24  
 GPT367

Figure 85. R POLARIZATION FOR O2 REDUCTION  
GINER PEM/PT/IRO2 & PT FREE STANDING ELECTRODE  
(40.6oC, 1M H2SO4)

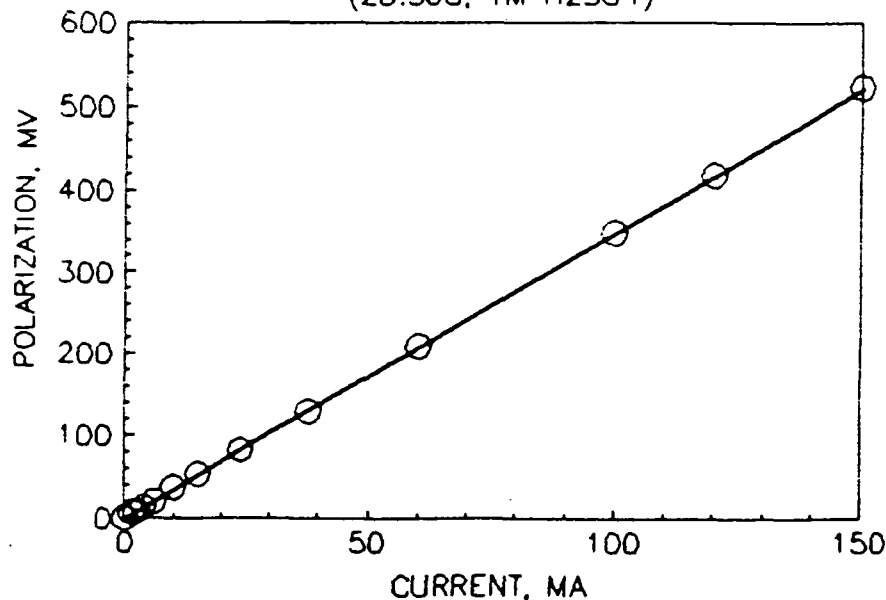


80oC, FOR 30, 40oC FOR 30  
200CC/MIN O2(H2O)/O2 SIDE  
0-120(R=3.2000,S=3.2021,I=-0.2530)

150(R=2.2060,S=3.2211,I=-2.2622)

GPEMFS25-37  
GPT369

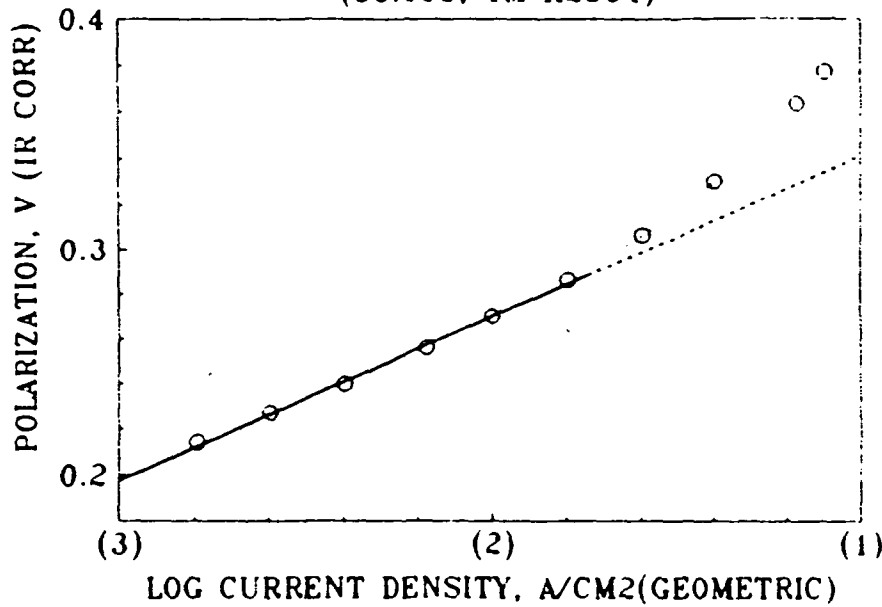
Figure 86. R POLARIZATION FOR O2 REDUCTION  
GINER PEM/PT/IRO2 & PT FREE STANDING ELECTRODE  
(28.3oC, 1M H2SO4)



80oC, 60oC, 40oC, 28oC FOR 30  
200CC/MIN O2(H2O)/O2 SIDE  
R=3.4826(S=3.4835,I=-0.1310)

GPEMFS38-49  
GPT371

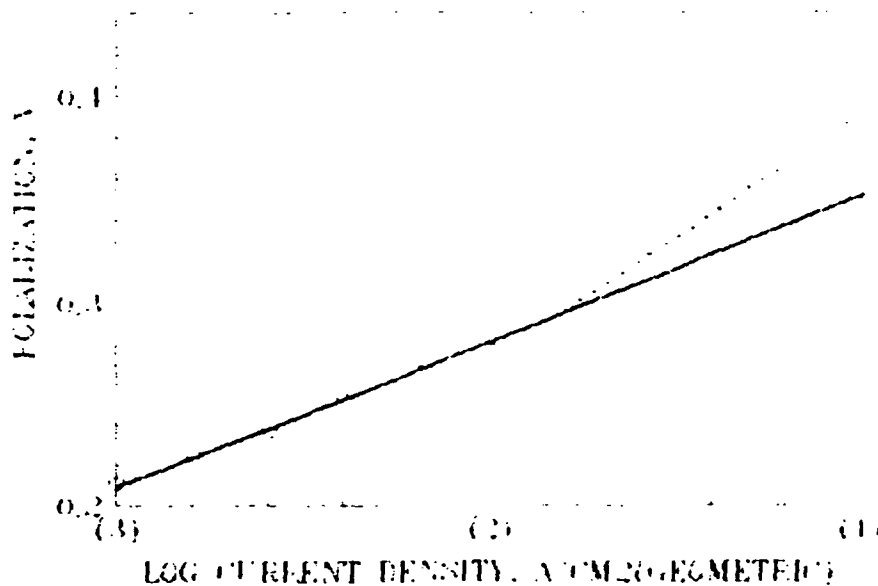
Figure 87. TAFEL PLOT FOR O2 REDUCTION  
 GINER PEM/IR02,PT & PT FREE STANDING ELECTRODE  
 (80.0°C, 1M H2SO4)



(PREHEAT 80°C FOR 30)  
 200CC/MIN O2(H2O)/O2 SIDE  
 S=0.0715(I=0.4128),0.12(0.4978)

GPEMFS1-12  
 GPT366

Figure 88. TAFEL PLOT FOR O2 REDUCTION  
 GINER PEM/IR02,PT & PT FREE STANDING ELECTRODE  
 (60.0°C, 1M H2SO4)

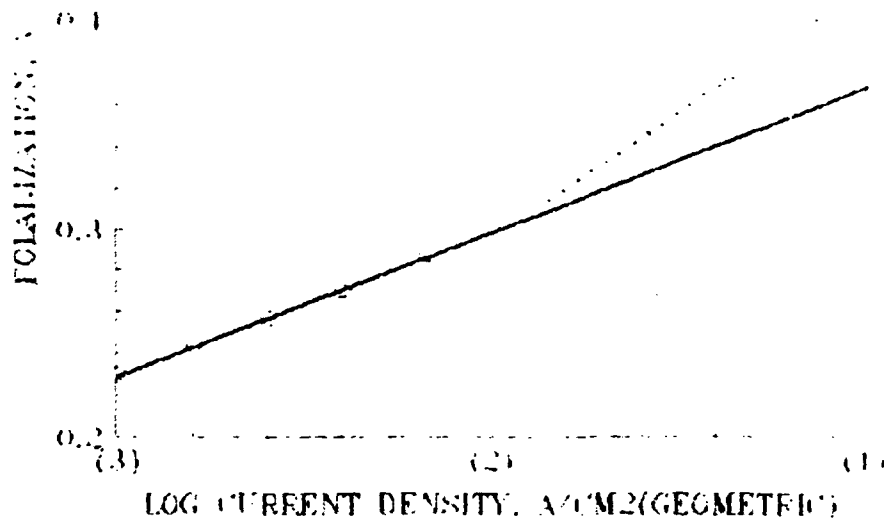


(PREHEAT 60°C FOR 30)  
 300CC/MIN O2(H2O)/O2 SIDE  
 S=0.0712(I=0.4204),0.12(0.5122)

GPEMFS1-14  
 GPT368

ORIGINAL PAGE IS  
 OF POOR QUALITY

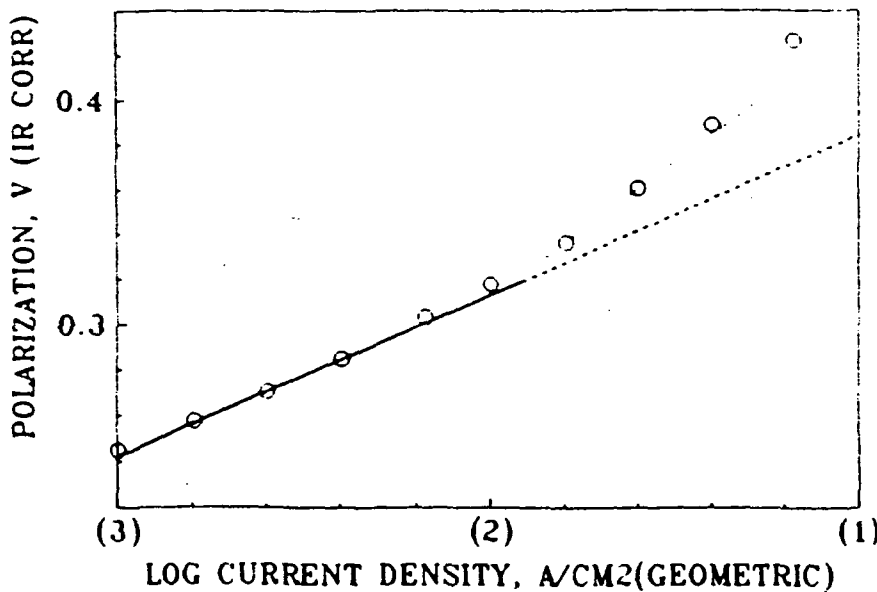
Figure 89. TAFEL PLOT FOR O<sub>2</sub> REDUCTION  
 GINER PEM/IR02,PT & PT FREE STANDING ELECTRODE  
 (19.3°C, 1M H<sub>2</sub>SO<sub>4</sub>)



(PREHEAT 80o, 60o, 40oC FOR 30)  
 200CC/MIN O<sub>2</sub>(H<sub>2</sub>O)/O<sub>2</sub> SIDE  
 S=0.0706(I=0.4394),0.12(0.5368)

GPEMFS25-27  
 GPT370

Figure 90. TAFEL PLOT FOR O<sub>2</sub> REDUCTION  
 GINER PEM/IR02,PT & PT FREE STANDING ELECTRODE  
 (28.3oC, 1M H<sub>2</sub>SO<sub>4</sub>)



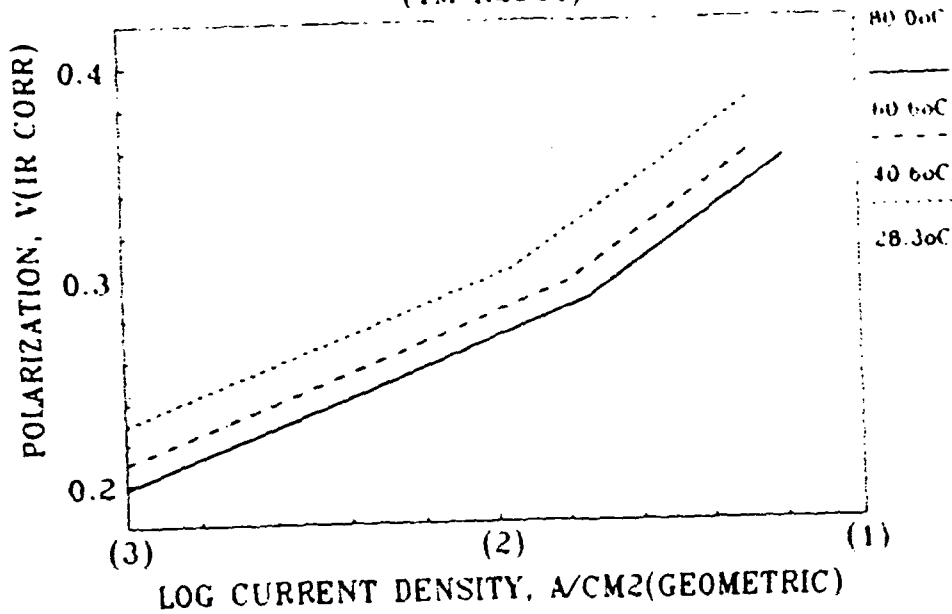
(PREHEAT 80o, 60o, 40o, 28oC FOR 30)  
 200CC/MIN O<sub>2</sub>(H<sub>2</sub>O)/O<sub>2</sub> SIDE  
 S=0.0706(I=0.4554),0.12(0.5526)

GPEMFS38-49  
 GPT372

ORIGINAL PAGE IS  
 OF POOR QUALITY

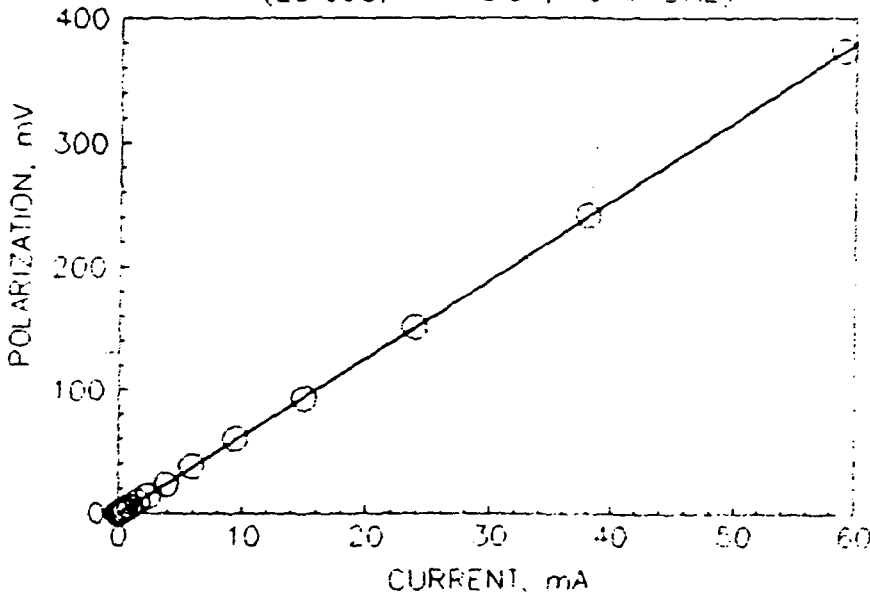


Figure 91. TAFEL PLOTS FOR O<sub>2</sub> REDUCTION  
GINER PEM/IRO<sub>2</sub>,PT & PT FREE STANDING ELECTRODE  
(1M H<sub>2</sub>SO<sub>4</sub>)



GPT442

Figure 92. R VS POLARIZATION FOR O<sub>2</sub> REDUCTION FOR GINER  
PEM/PT/IRO<sub>2</sub> & FREE STANDING ELECTRODE  
(25 6oC, 1M HClO<sub>4</sub>, 10mA DHE)



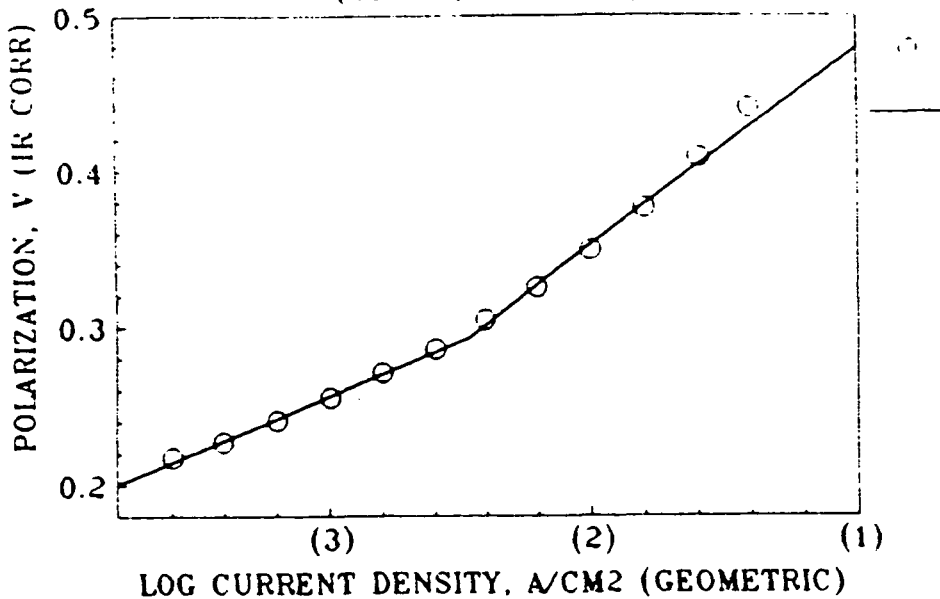
$R=6.336(S=6.3455, I=-0.5402)$

GPT143

FROM HIGH CURRENT  
50000/MIN O<sub>2</sub> H<sub>2</sub>O - 100% H<sub>2</sub>O

ORIGINAL PAGE IS  
OF POOR QUALITY

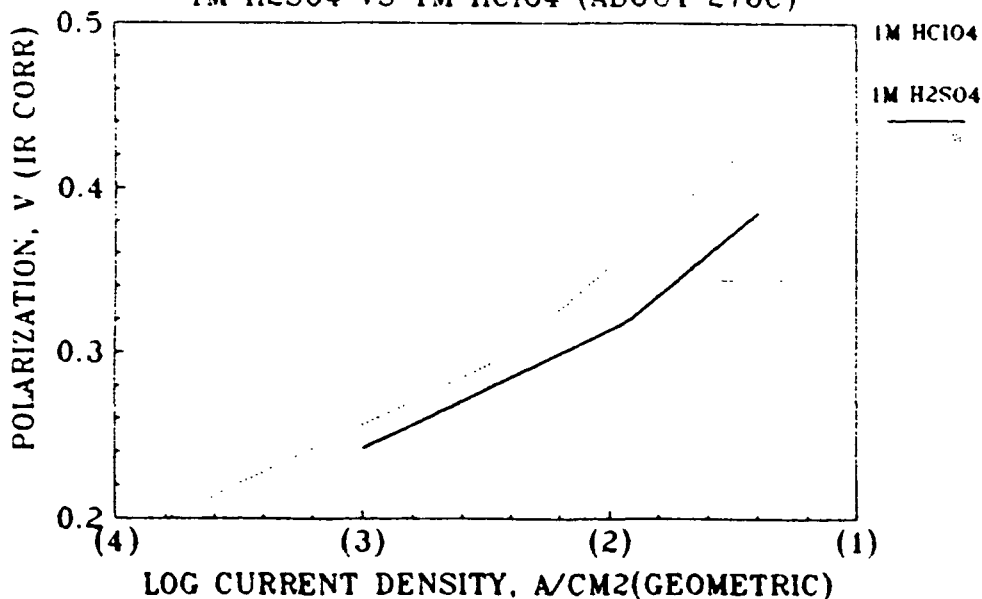
Figure 93. TAFEL PLOT FOR O2 REDUCTION  
 GINER PEM/IR02,PT & PT FREE STANDING ELECTRODE  
 (25.6oC, 1M HClO4)



S=0.0694(I=0.4647)(-2.47)  
 S=0.127(I=0.6066)

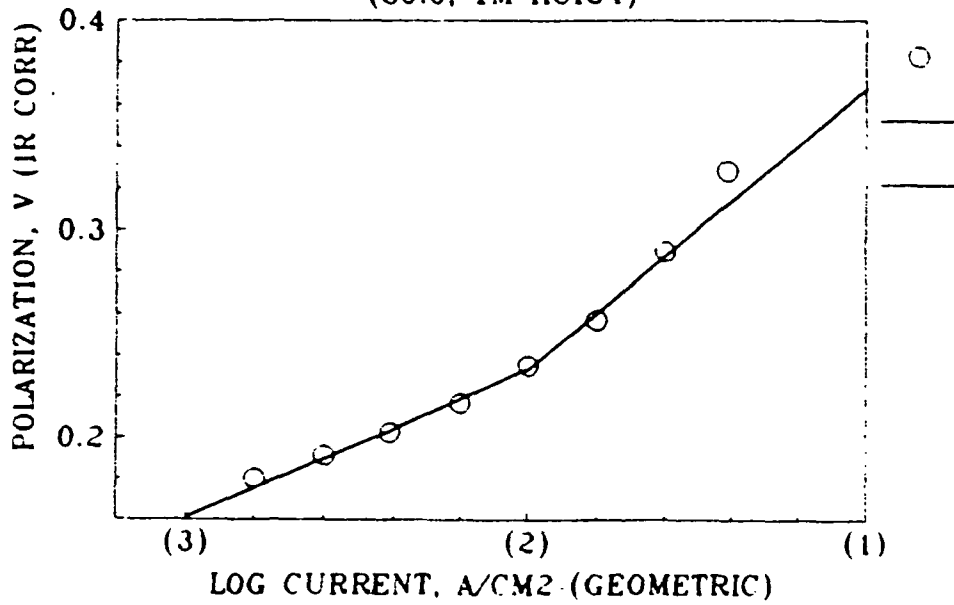
500CC/MIN O2(H2O)/O2 SIDE  
 GPT488

Figure 94. COMPARISON OF TAFEL PLOTS FOR O2 REDUCTION  
 GINER PEM/IR02,PT & PT FREE STANDING ELECTRODE  
 1M H2SO4 VS 1M HClO4 (ABOUT 27oC)



1M H2SO4(28.3oC) 1M HClO4(25.6oC)

Figure 95. TAFEL PLOT FOR O2 REDUCTION  
GINER PEM/IR02,PT & PT FREE STANDING ELECTRODE  
(80.6, 1M HClO4)

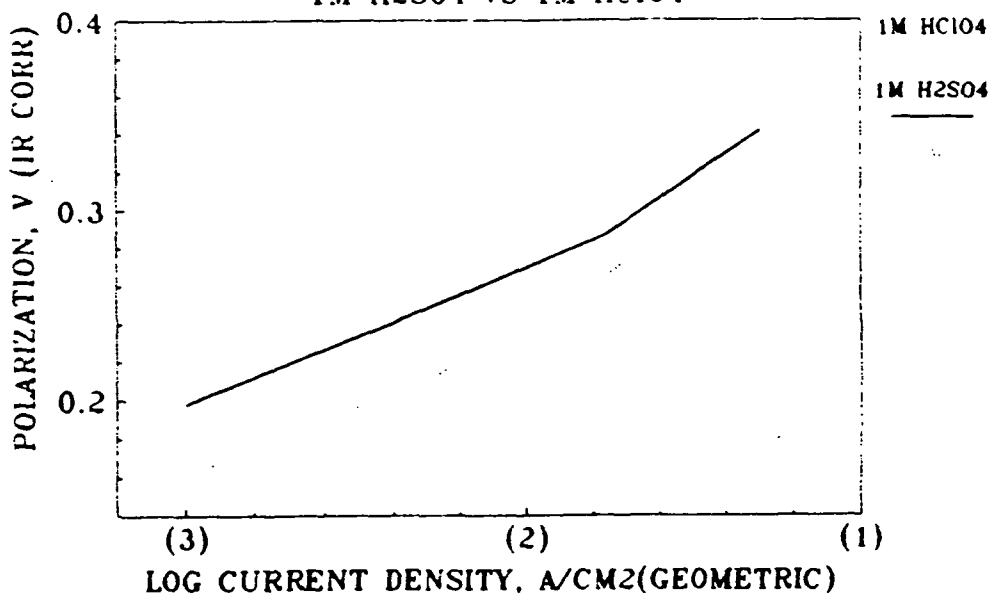


$S=0.0694(I=0.4647)(-2.47)$

$S=0.127(I=0.6066)$

500CC/MIN O2(H2O)/O2 SIDE  
GPT488B

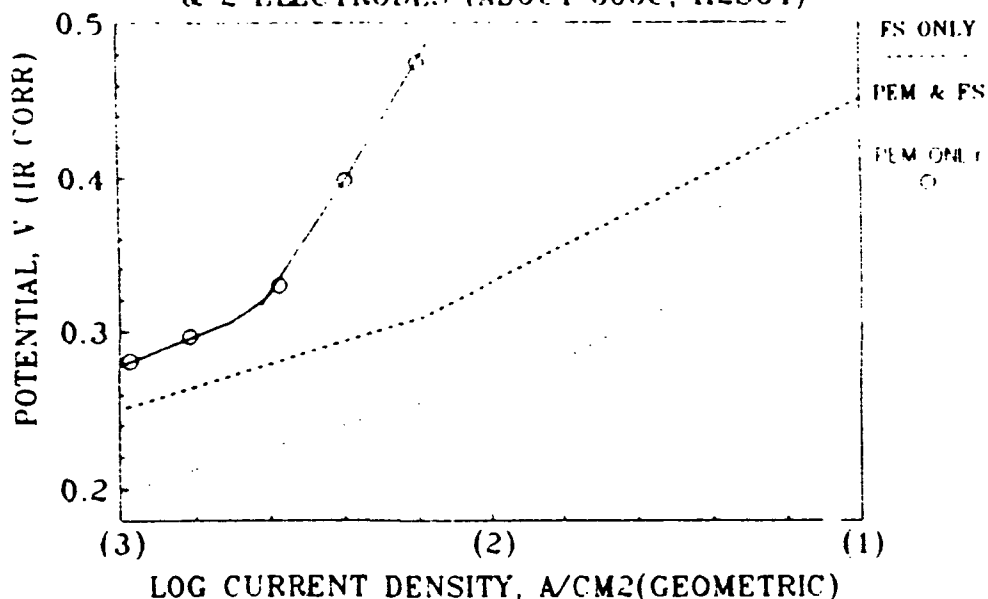
Figure 9b. COMPARISON OF TAFEL PLOTS FOR O2 REDUCTION  
GINER PEM/IR02,PT & PT FREE STANDING ELECTRODE  
1M H2SO4 VS 1M HClO4



1M H2SO4(80.0oC) 1M HClO4(80.6oC)

GPT490B

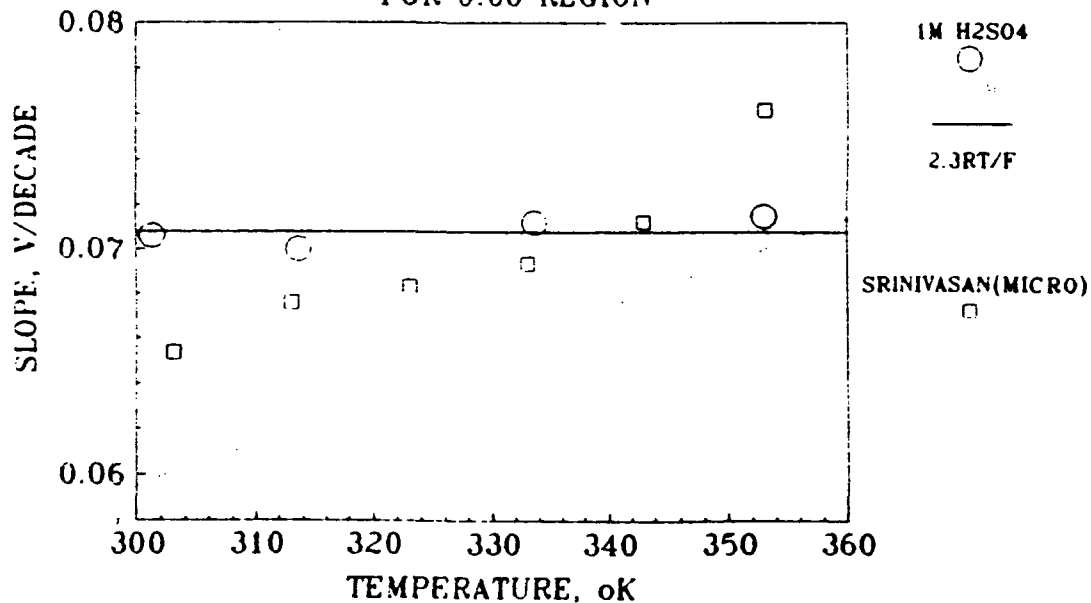
Figure 97. TAFEL PLOTS FOR O<sub>2</sub> REDUCTION  
 GINER PEM/IR<sub>2</sub>O<sub>3</sub>,PT VS PT FREE STANDING ELECTRODE  
 & 2 ELECTRODES (ABOUT 80°C, H<sub>2</sub>SO<sub>4</sub>)



PEM, S=0.12 (I=0.6371)

GPT454B

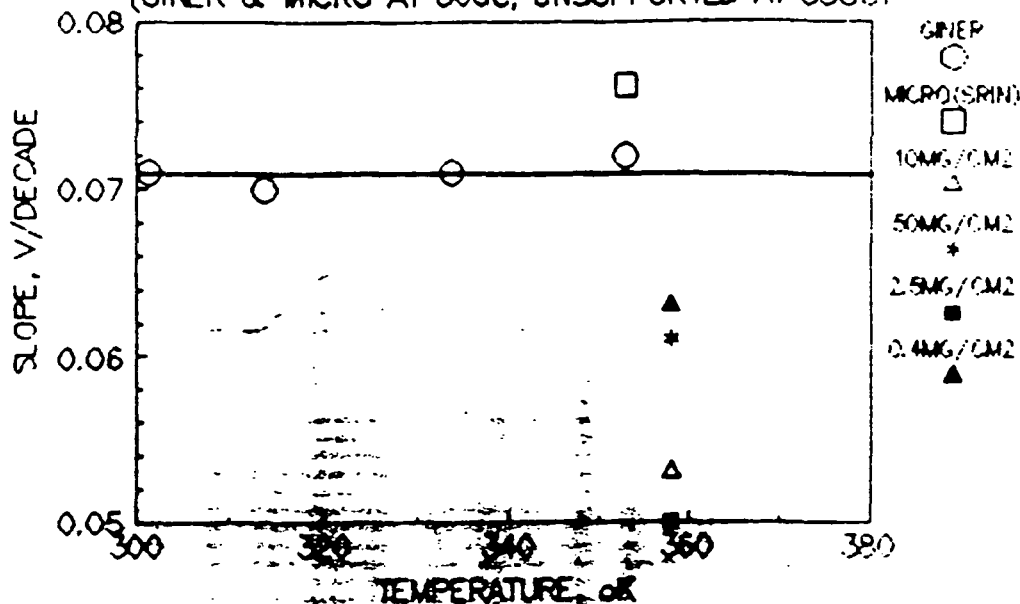
Figure 98. O<sub>2</sub> REDUCTION SLOPES WITH TEMPERATURE  
 GINER PEM/IR<sub>2</sub>O<sub>3</sub>,PT & PT FREE STANDING ELECTRODE  
 FOR 0.06 REGION



AVERAGE S=0.0708

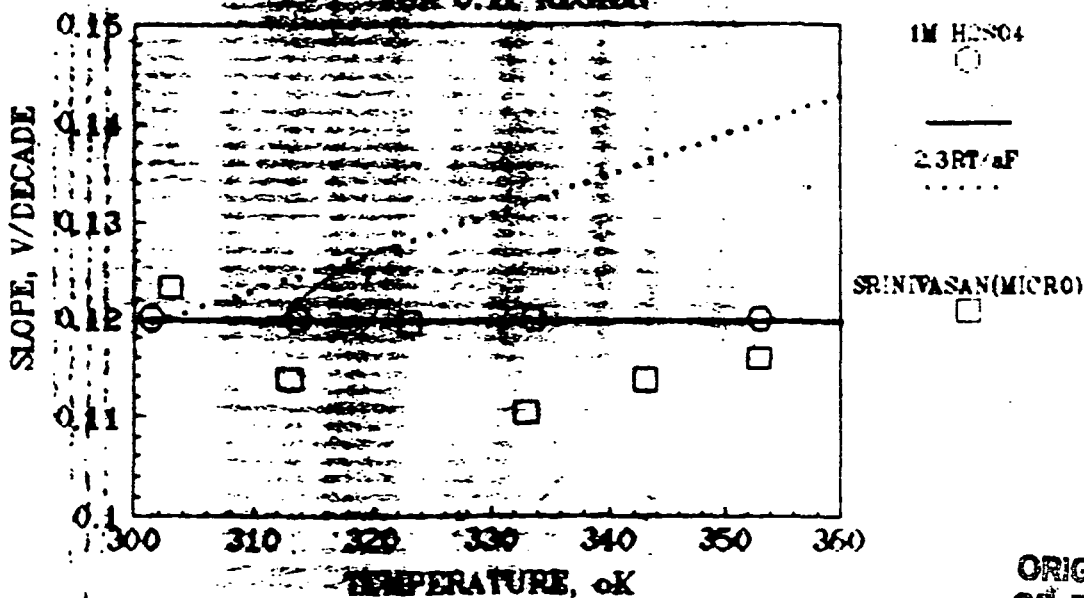
GPT373

Figure 99. SLOPES FOR O<sub>2</sub> REDUCTION AT ABOUT 800°C  
 0.06 REGION  
 (GINER & MICRO AT 800°C, UNSUPPORTED AT 850°C)



GPT3738

Figure 100. O<sub>2</sub> REDUCTION SLOPES WITH TEMPERATURE  
 GINER PERFORMING AT PT FILE STANDING ELECTRODE  
 FOR 0.12 REGION

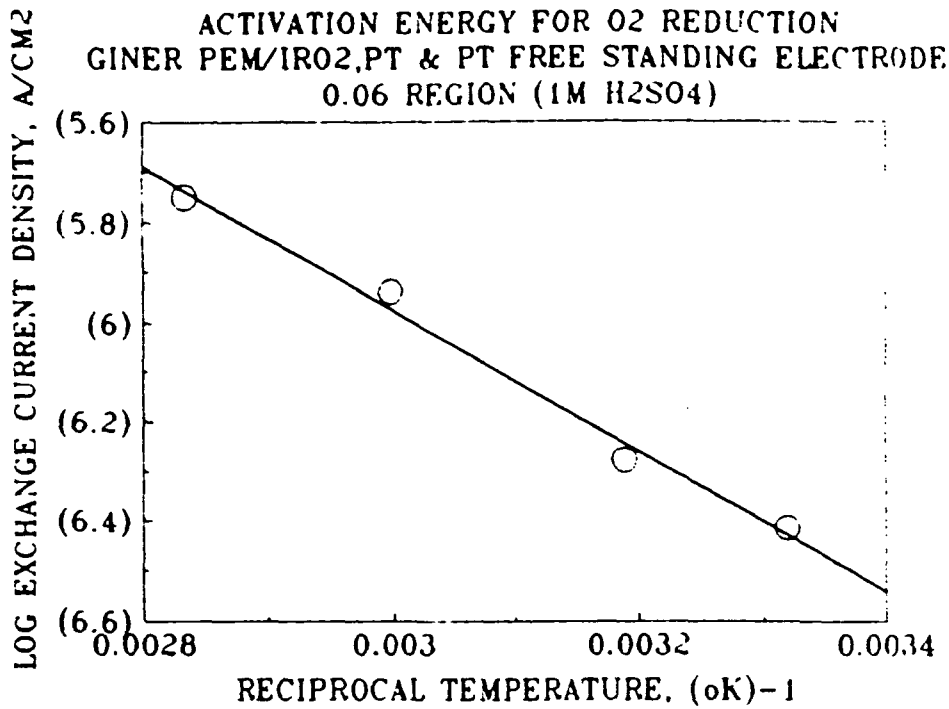


ORIGINAL PAGE IS  
 OF POOR QUALITY

2000C/MIN O<sub>2</sub>(H<sub>2</sub>O)/O<sub>2</sub> SIDE

GPT485

Figure 101.



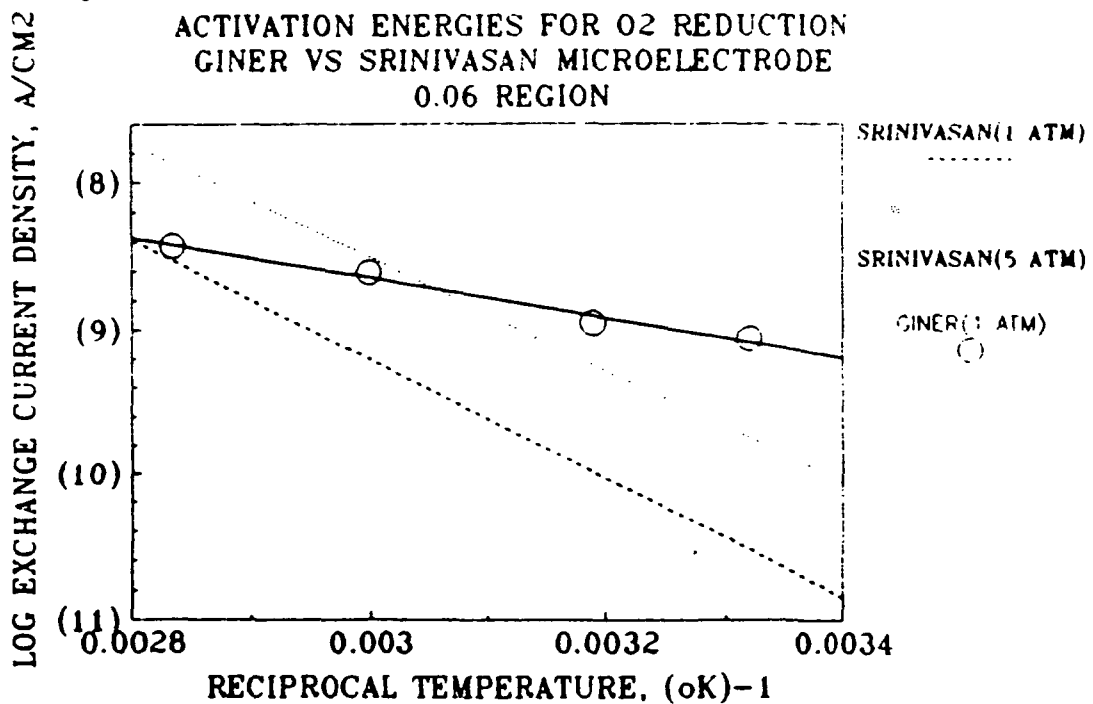
$E_a = 6.5 \text{KCAL/M}$  ( $S = -1423.5, I = -1.703$ )

EXCHANGE CURRENT DENSITY IS GEOMETRIC

GPT374

200CC/MIN O<sub>2</sub>(H<sub>2</sub>O)/O<sub>2</sub> SIDE

Figure 102.



GINER  $E_a = 6.5 \text{KCAL/M}$  (TRUE CM<sup>2</sup>, 1 ATM)

ASSUME SRINIVASAN FOR 80°C

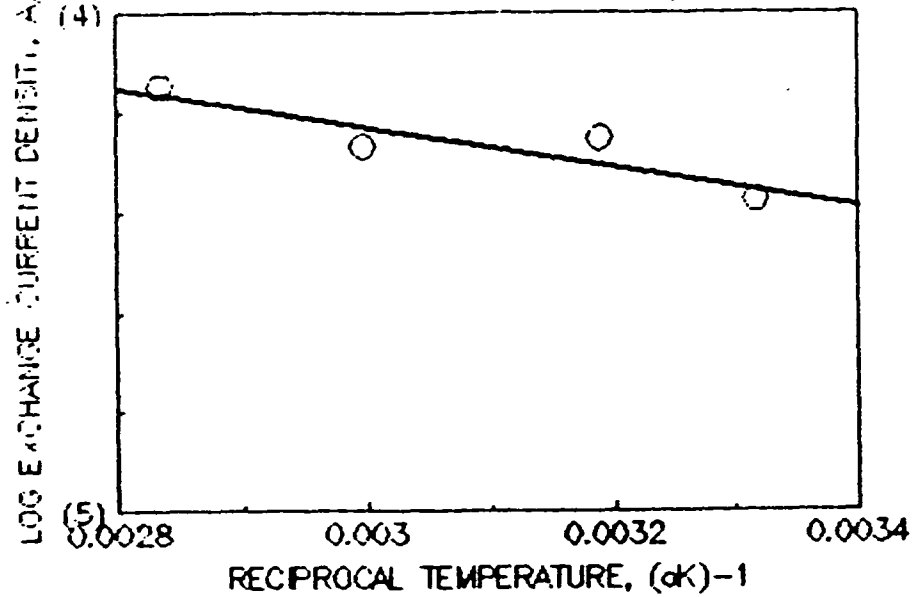
SRINIVASAN  $E_a = 17.8$  (5 ATM, MICRO)

FACTOR OF 470 CM<sup>2</sup>/CM<sup>2</sup>

GPT374C

Figure 103.

ACTIVATION ENERGY FOR O<sub>2</sub> REDUCTION  
GINER PEM/IRO<sub>2</sub>,PT & PT FREE STANDING ELECTRODE  
0.12 REGION (1M H<sub>2</sub>SO<sub>4</sub>)

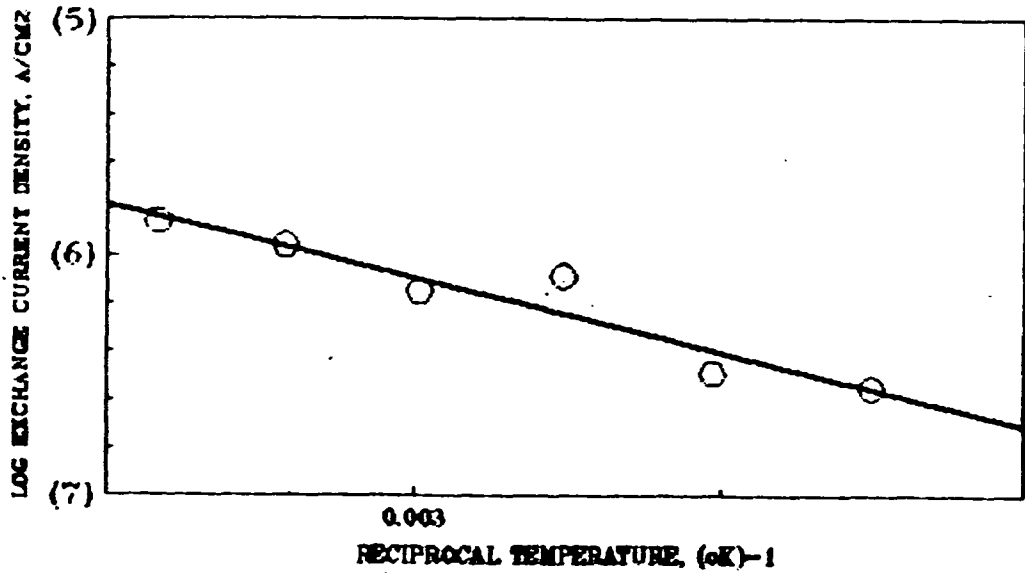


$E_a = 1.8 \text{ Kcal/M} (S = -390.59, I = -3.056)$

GPT374B  
200CC/MIN O<sub>2</sub>(H<sub>2</sub>O)/O<sub>2</sub> SIDE

7.25 10.4

Figure 104. SRINIVASAN ACTIVATION ENERGY FOR 0.12 REGION  
MICROELECTRODE/NAFION  
(5 ATM O<sub>2</sub>)

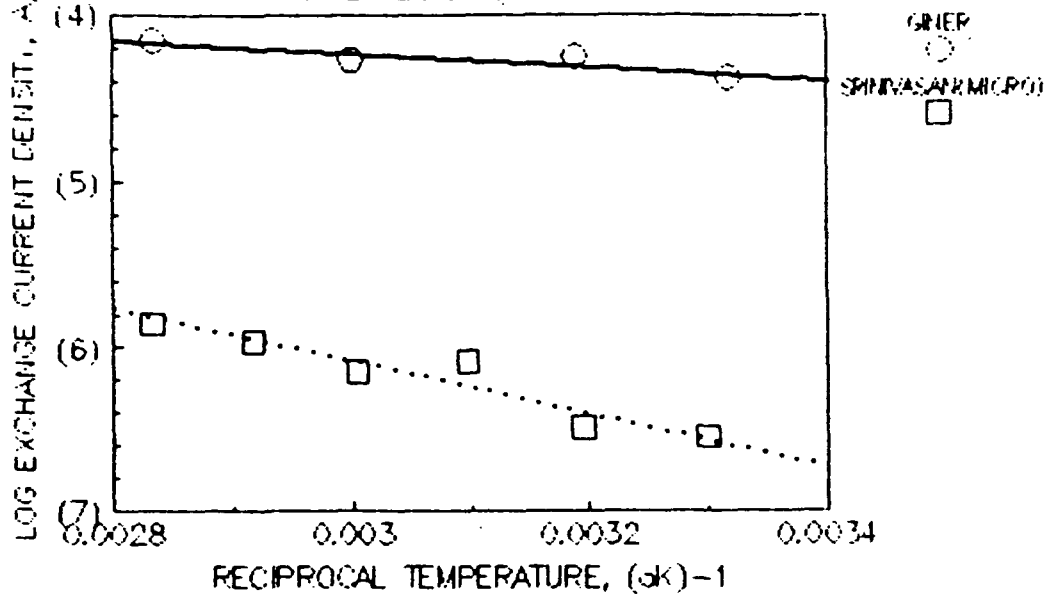


$E_a = 7.1 \text{ Kcal/M} (S = -1537.1, I = -1.4848)$

E

Figure 105.

ACTIVATION ENERGY FOR O<sub>2</sub> REDUCTION  
GINER PEM/IRO<sub>2</sub>/PT & PT FREE STANDING ELECTRODE  
0.12 REGION (1M H<sub>2</sub>SO<sub>4</sub>)



GINER  $E_a = 1.9 \text{ kcal/M}$

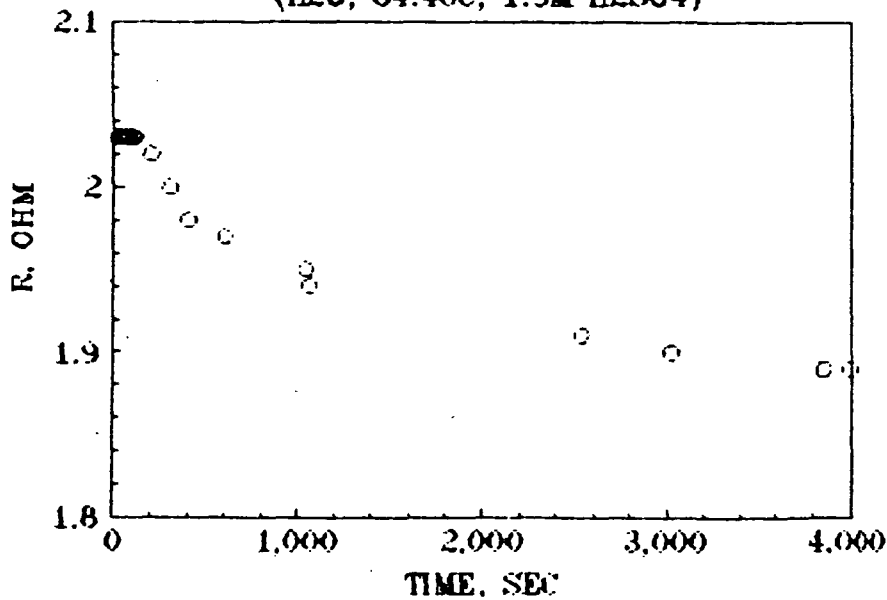
SPINIVASAN  $E_a = 7.4 \text{ kcal/M}$

$\beta = -1615, \gamma = -1.232$

GPT3740

20000/MIN O<sub>2</sub>(H<sub>2</sub>O)/O<sub>2</sub> SIDE

Figure 106. R WITH TIME FOR O<sub>2</sub> EVOLUTION AT +0.1A  
GINER PT FREE STANDING ELECTRODE ONLY  
(H<sub>2</sub>O, 84.4°C, 1.5M H<sub>2</sub>SO<sub>4</sub>)



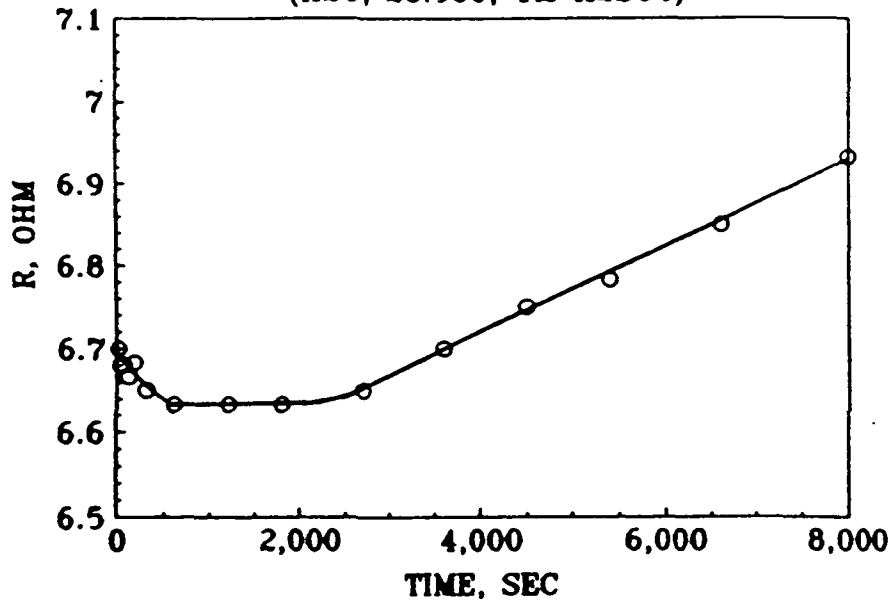
20000/MIN O<sub>2</sub>(H<sub>2</sub>O)/O<sub>2</sub> SIDE  
(PREHEAT 90, 80°C FOR 30)

GPT/IRO<sub>2</sub>/42  
GPT255

ORIGINAL PAGE IS  
OF POOR QUALITY



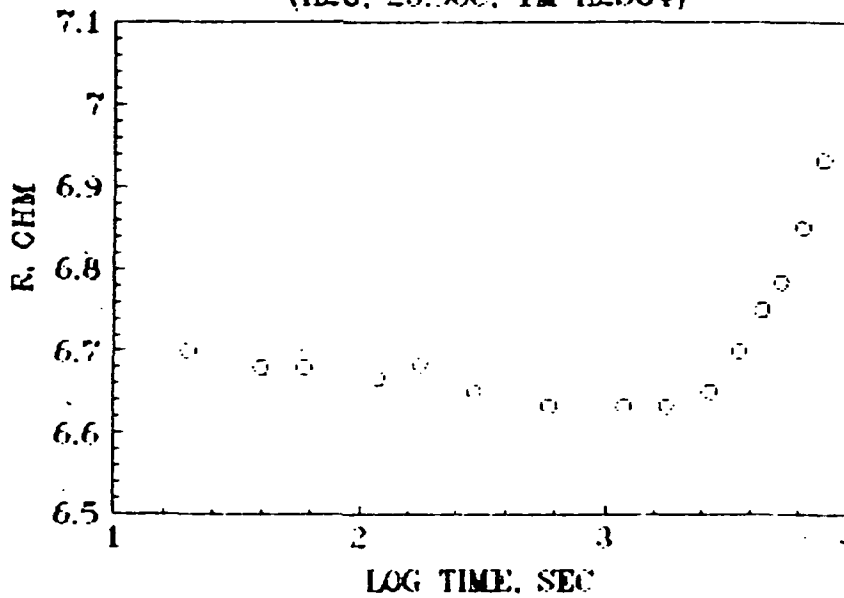
Figure 107. R WITH TIME FOR O2 EVOLUTION AT +0.06A  
 GINER PEM/IR02,PT & PT FREE STANDING ELECTRODE  
 (H2O, 23.9oC, 1M H2SO4)



100CC/MIN O2(H2O)/O2 SIDE  
 PREHEAT 80oC

GPEMFS59  
 GPT432

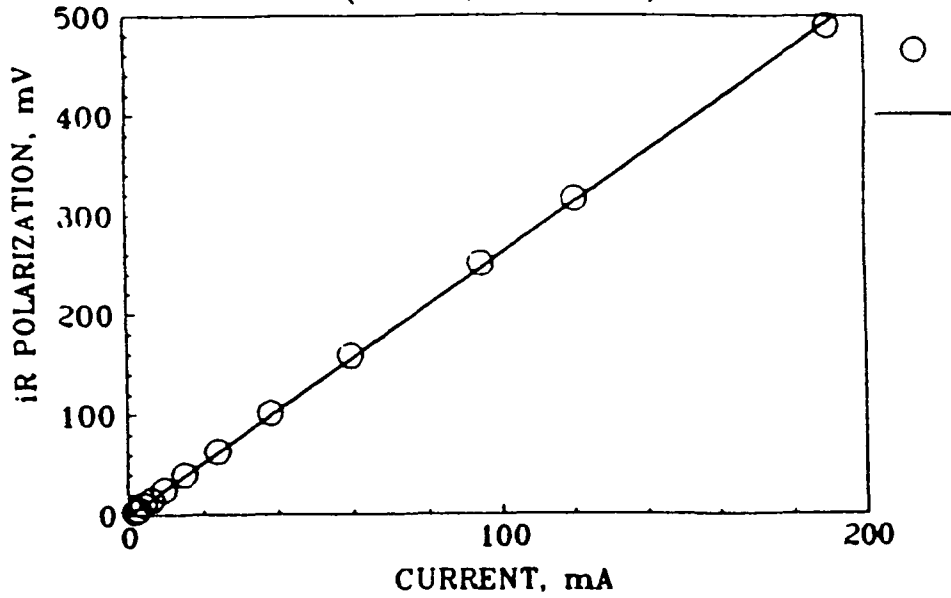
Figure 108. R WITH TIME FOR O2 EVOLUTION AT +0.06A  
 GINER PEM/IR02,PT & PT FREE STANDING ELECTRODE  
 (H2O, 23.9oC, 1M H2SO4)



100CC/MIN O2(H2O)/O2 SIDE

GPEMFS59  
 GPT464

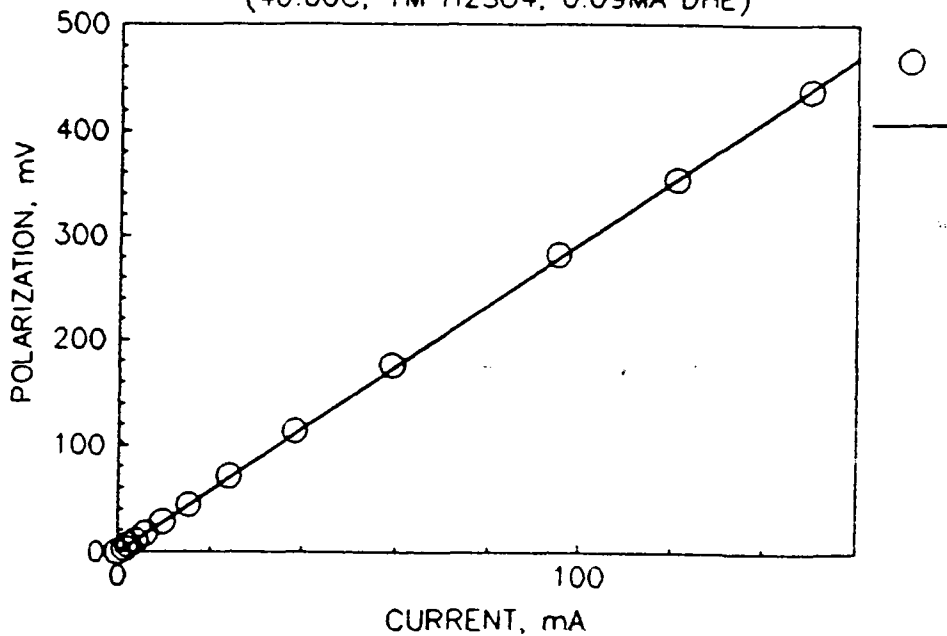
Figure 109. R POLARIZATION FOR O2 EVOLUTION  
GINER PEM/IR02,PT & PT FREE STANDING ELECTRODE  
(77.2oC, 1M H2SO4)



R=2.603(1.735 OHM/CM2)  
500CC/MIN O2(H2O)/O2 SIDE  
90, 80oC FOR 60

DATA AFTER 2-3 MIN  
GPT1  
GPT224

Figure 110. R VS POLARIZATION FOR O2 EVOLUTION FOR GINER  
ELECTRODE (PEM/PT/IR02 & FREE STANDING )  
(40.0oC, 1M H2SO4, 0.09MA DHE)

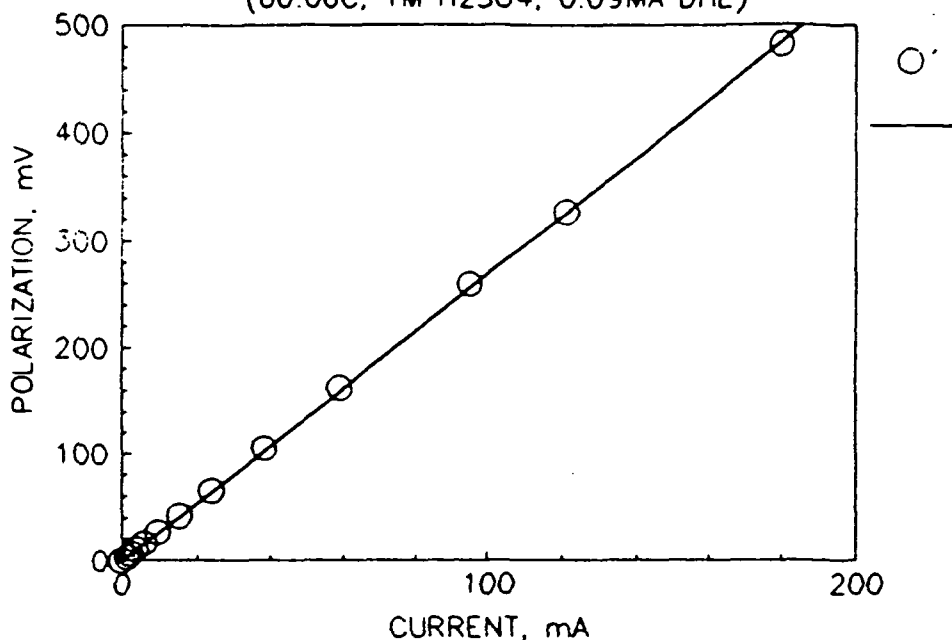


R=2.937(S=2.9363,I=0.09540)  
500CC/MIN O2(H2O)/O2 SIDE

GPT228

ORIGINAL PAGE IS  
OF POOR QUALITY

Figure 111. R VS POLARIZATION FOR O2 EVOLUTION FOR GINER ELECTRODE (PEM/PT/IRO2 & FREE STANDING ) (60.0oC, 1M H2SO4, 0.09MA DHE)

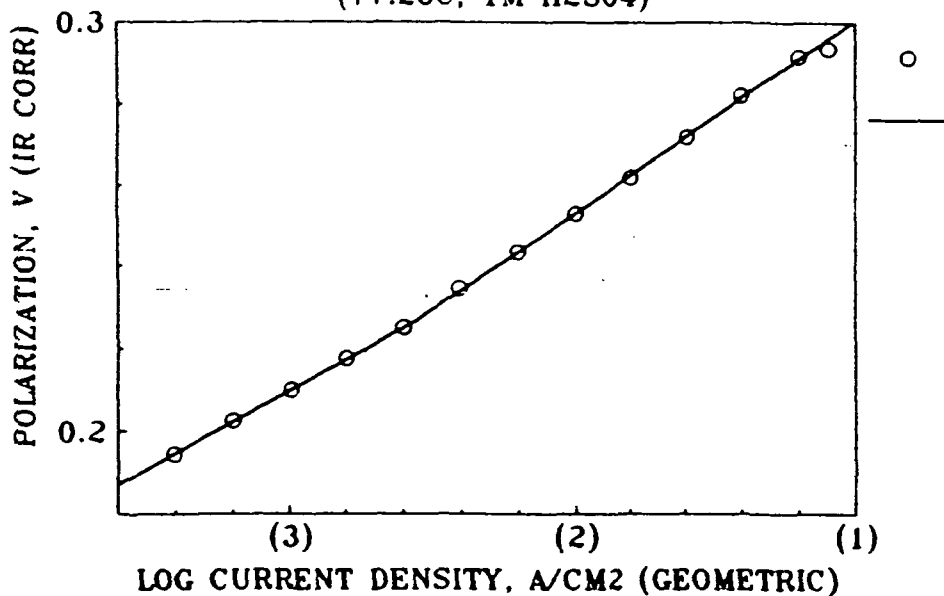


R=2.693(S=2.6897,I=0.6000)  
500CC/MIN O2(H2O)/O2 SIDE

GPT226

1.2 hL

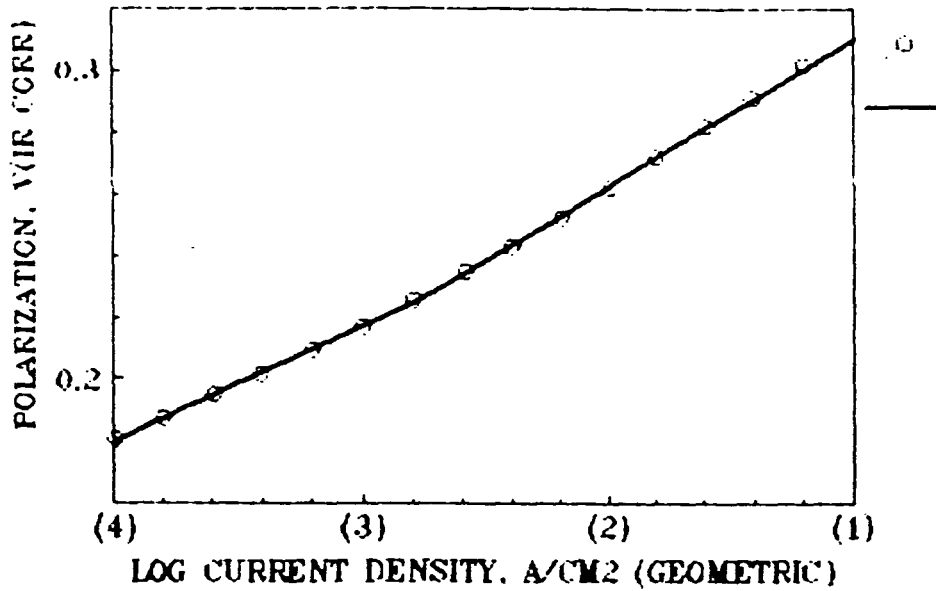
Figure 112. TAFEL PLOT OF O2 EVOLUTION GINER PEM/IRO2,PT & PT FREE STANDING ELECTRODE (77.2oC, 1M H2SO4)



S=0.0475(I=0.3482)(-2.555)  
S=0.0379(I=0.3237)  
500CC/MIN O2(H2O)/O2 SIDE

90, 80oC FOR 60  
GPT1

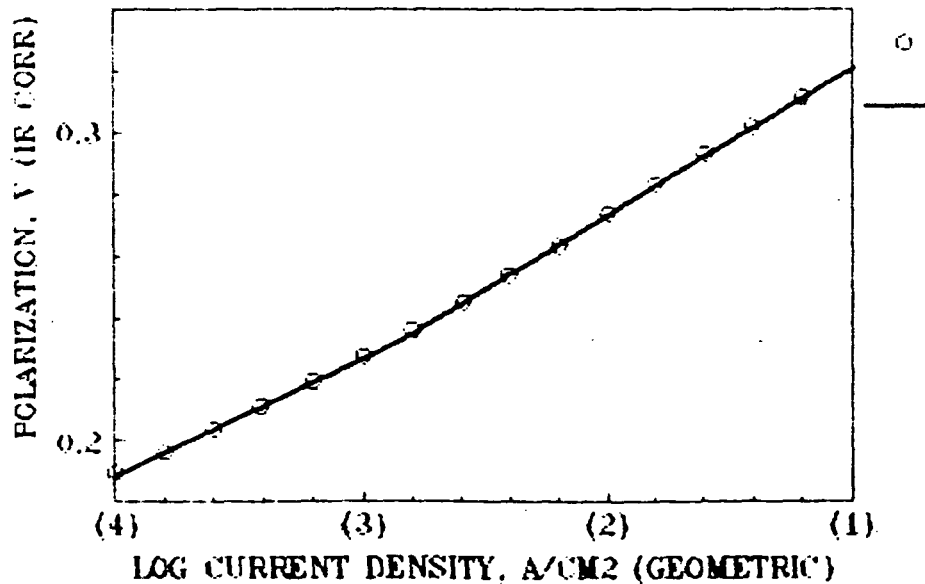
Figure 113. TAFEL PLOT OF O<sub>2</sub> EVOLUTION  
 GINER PEM/IR02,PT & PT FREE STANDING ELECTRODE  
 (60.0°C, 1M H<sub>2</sub>SO<sub>4</sub>)



$S=0.0479(I=0.3586)(-2.8)$   
 $S=0.0373(I=0.3291)$   
 AFTER 2-3 MIN

GPT2  
 500CC/MIN O<sub>2</sub>(H<sub>2</sub>O)/O<sub>2</sub> SIDE  
 90,80,60°C FOR 60

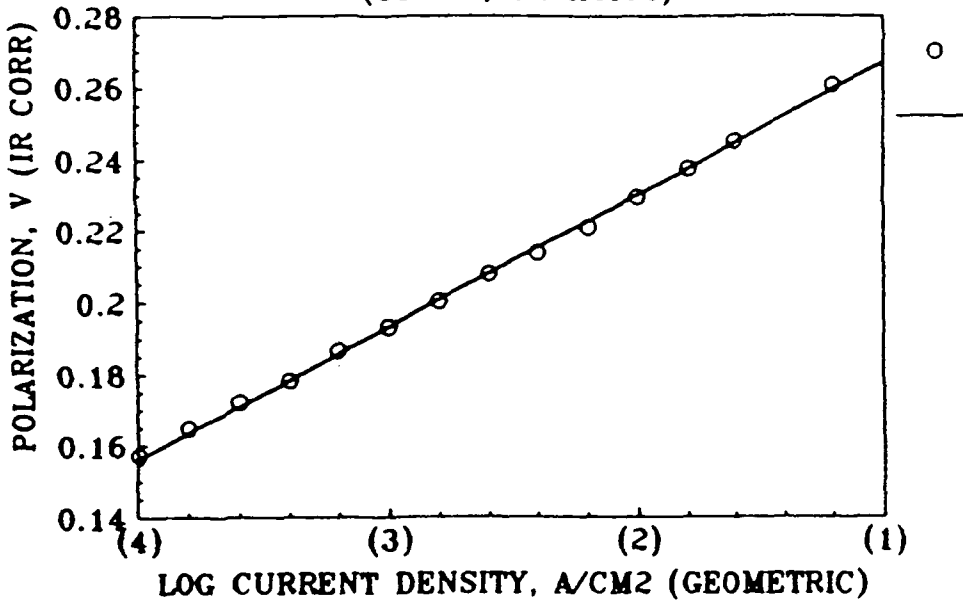
Figure 114. TAFEL PLOT OF O<sub>2</sub> EVOLUTION  
 GINER PEM/IR02,PT & PT FREE STANDING ELECTRODE  
 (40.0°C, 1M H<sub>2</sub>SO<sub>4</sub>)



$S=0.0477(I=0.3688)(-2.875)$   
 $S=0.0379(I=0.3406)$   
 AFTER 2-3 MIN

GPT3  
 500CC/MIN O<sub>2</sub>(H<sub>2</sub>O)/O<sub>2</sub> SIDE  
 90,80,60,40°C FOR 60

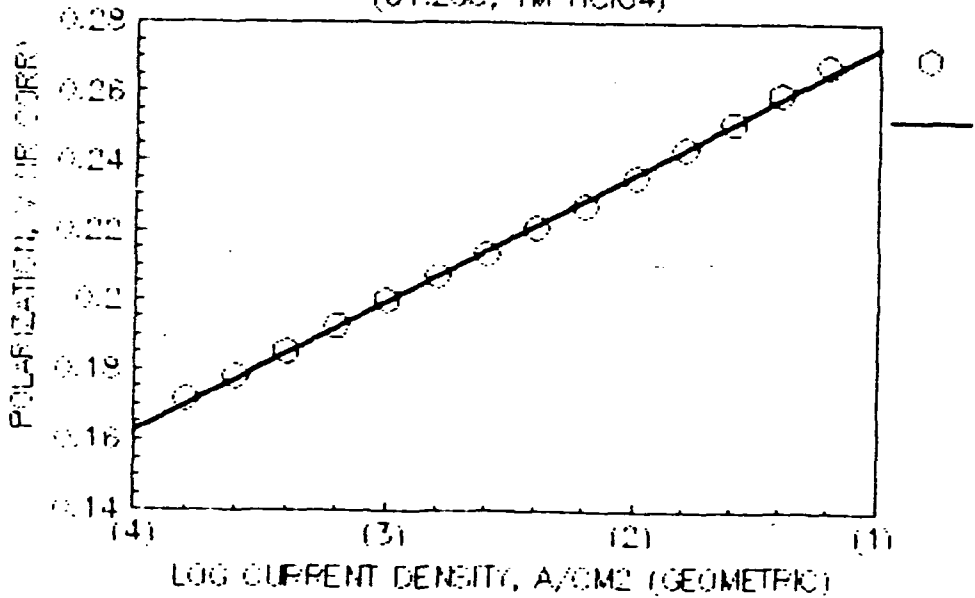
Figure 115. TAFEL PLOT OF O2 EVOLUTION  
 GINER PEM/IR02,PT & PT FREE STANDING ELECTRODE  
 (81.7°C, 1M HClO4)



S=0.037(I=0.3043)  
 90,80°C for 60  
 500CC/MIN O2(H2O)/O2 SIDE

PREREDUCED  
 GPT209

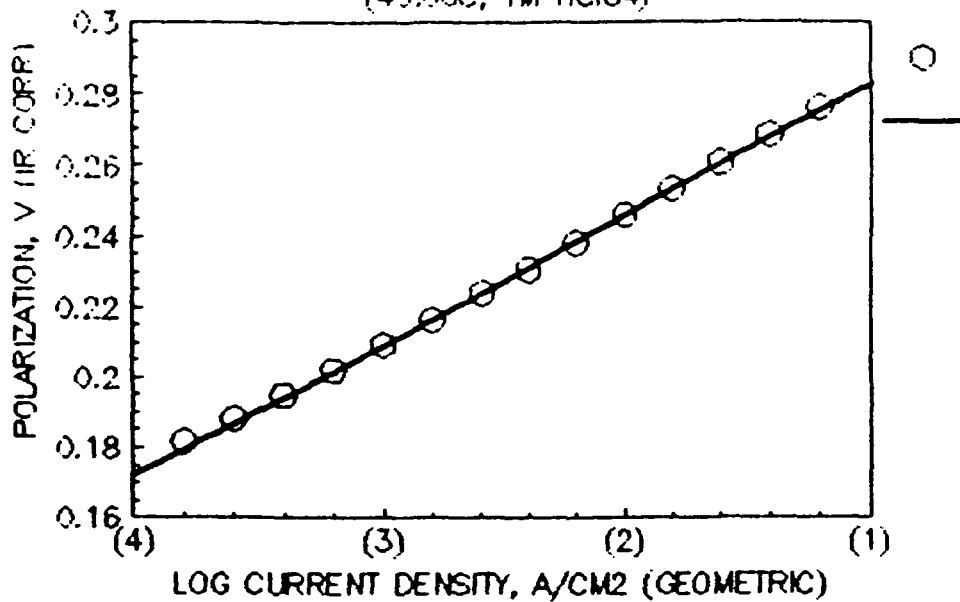
Figure 116. TAFEL PLOT OF O2 EVOLUTION  
 GINER PEM/IR02,PT & PT FREE STANDING ELECTRODE  
 (61.2°C, 1M HClO4)



0.037(I=0.3107)  
 90,80°C FOR 60  
 500CC/MIN O2(H2O)/O2 SIDE

GP1210  
 PREREDUCED

**Figure 117. TAFEL PLOT OF O2 EVOLUTION**  
 GINER PEM, IR02, PT & PT FREE STANDING ELECTRODE  
 (40.0°C, 1M HClO4)

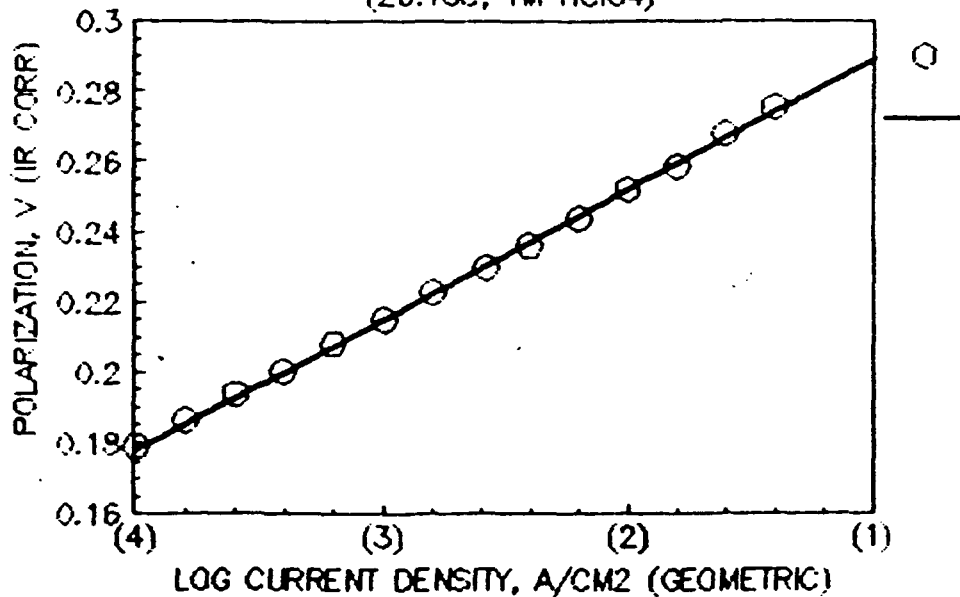


$S=0.037(1-0.3202)$

90,80,60,40°C FOR 60 . . . . . PREREDUCED (-0.1A), 90,80,60,40°C FOR 60  
 500CC/MIN O2(H2O)/O2 SIDE . . . . . GFT211

V/192

**Figure 118. TAFEL PLOT OF O2 EVOLUTION**  
 GINER PEM, IR02, PT & PT FREE STANDING ELECTRODE  
 (26.1°C, 1M HClO4)

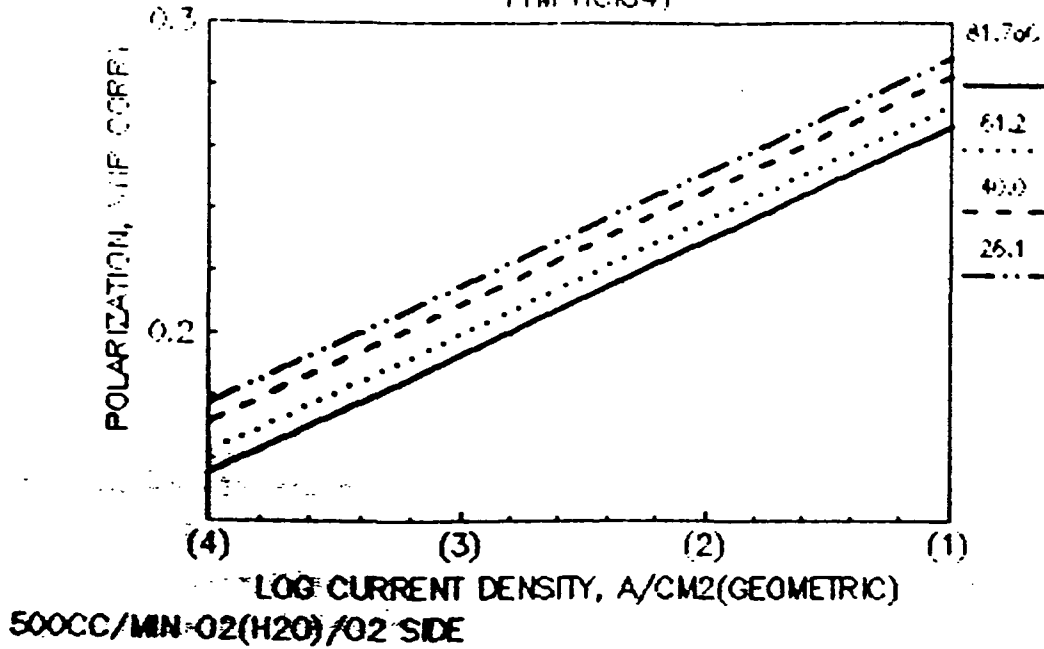


$S=0.037(1-0.3263)$

90,90,60,40,RT FOR 60 . . . . . PREREDUCED  
 500CC/MIN O2(H2O)/O2 SIDE . . . . . GFT212

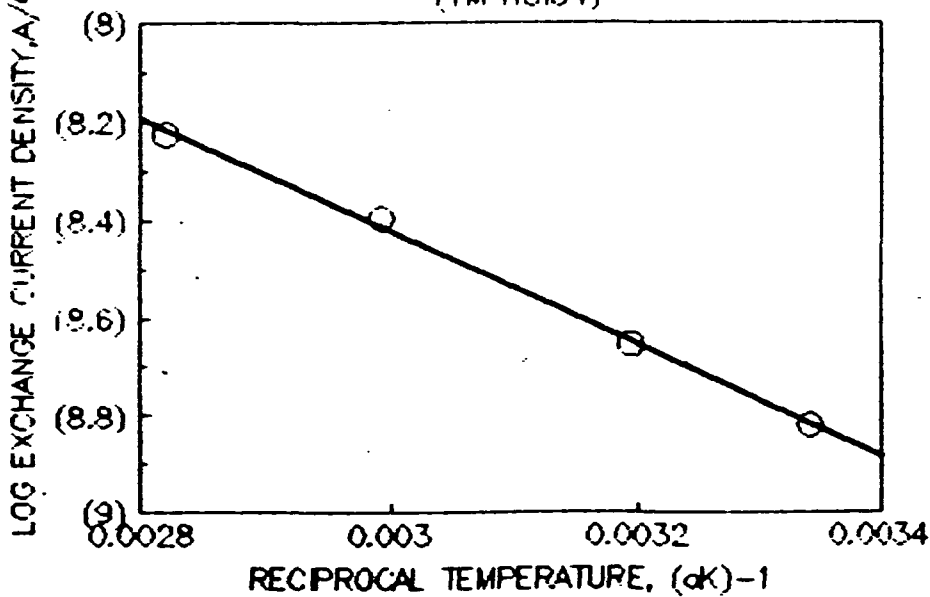
ORIGINAL PAGE IS  
 OF POOR QUALITY

**Figure 119.** TAFEL PLOTS WITH TEMPERATURE FOR O<sub>2</sub> EVOLUTION  
 GINER PEM, IR<sub>02</sub>, PT & PT FREE STANDING ELECTRODE  
 (1M HClO<sub>4</sub>)



GPT502

**Figure 120.** ACTIVATION ENERGY FOR O<sub>2</sub> EVOLUTION  
 GINER PEM, IR<sub>02</sub>, PT & PT FREE STANDING ELECTRODE  
 (1M HClO<sub>4</sub>)



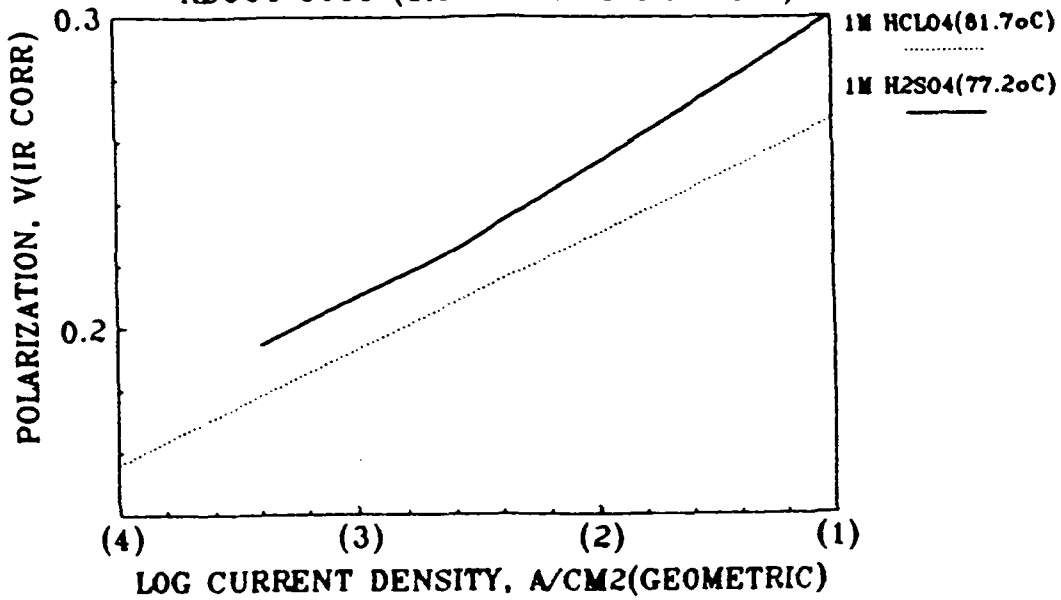
0.037 REGION

$E_a = 5.3 \text{ KCAL/M(S} = -1152, I = -4.968)$

50000/MIN O<sub>2</sub>(H<sub>2</sub>O)/O<sub>2</sub> SIDE

GPT504

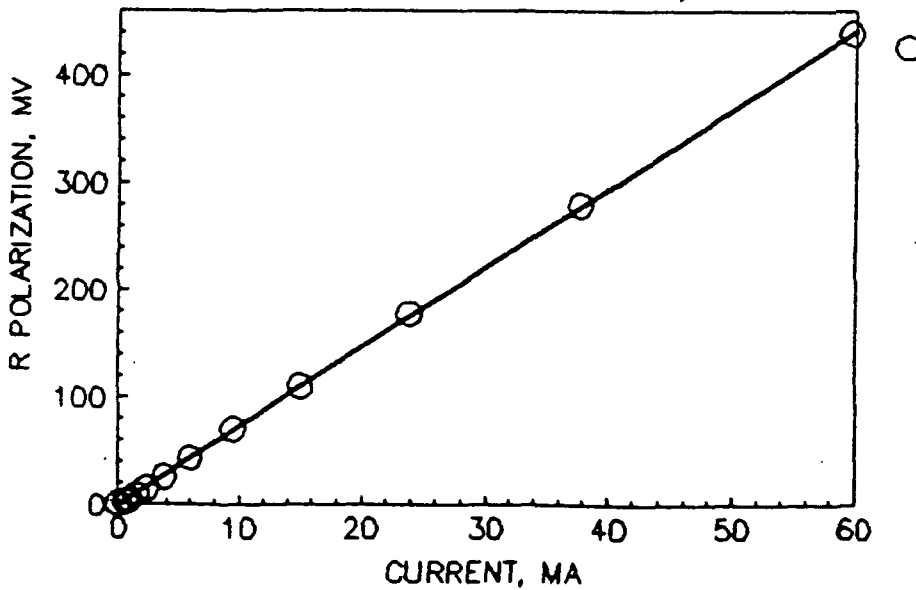
Figure 121. COMPARISON OF TAFEL PLOTS FOR O2 EVOLUTION  
GINER PEM/IRO2,PT & PT FREE STANDING ELECTRODE  
ABOUT 80°C (1M H2SO4 VS 1M HClO4)



H2SO4(77.2°C), HClO4(81.7°C)  
500CC/MIN O2(H2O)/O2 SIDE

GPT505

Figure 122. ANODIC R POLARIZATION FOR GINER ELECTRODE  
PEM/IRO2,PT ELECTRODE ONLY  
(H2O, 27.2°C, 1M H2SO4)



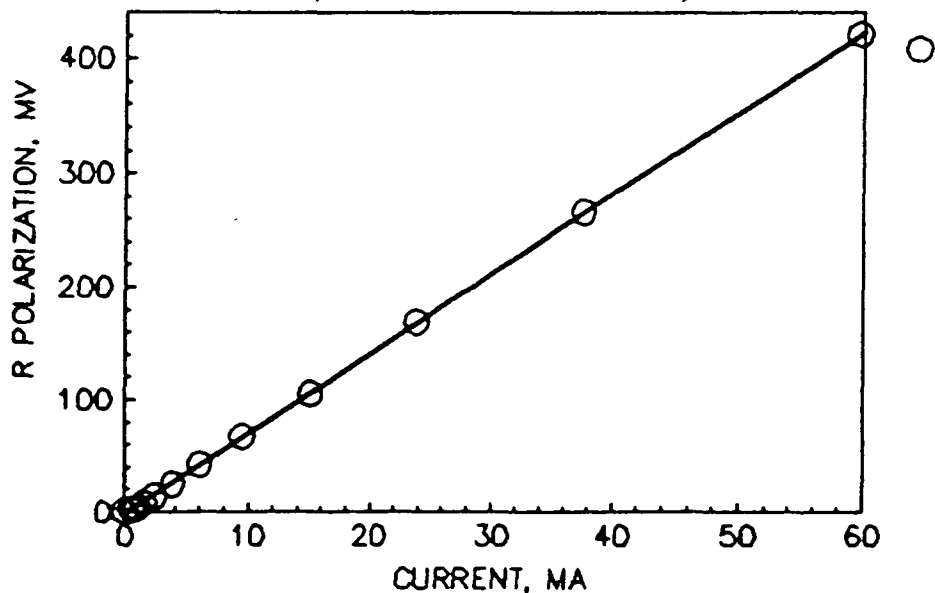
200CC/MIN O2(H2O)/O2 SIDE  
80°C, 60°C, 40°C, RT FOR 30  
R=7.384(S=7.4101, I=-1.5597)

GPT470

4/4/92



Figure 123. ANODIC R POLARIZATION FOR GINER ELECTRODE  
 PEM/IRO2,PT ELECTRODE ONLY  
 (H2O, 40.0oC, 1M H2SO4)

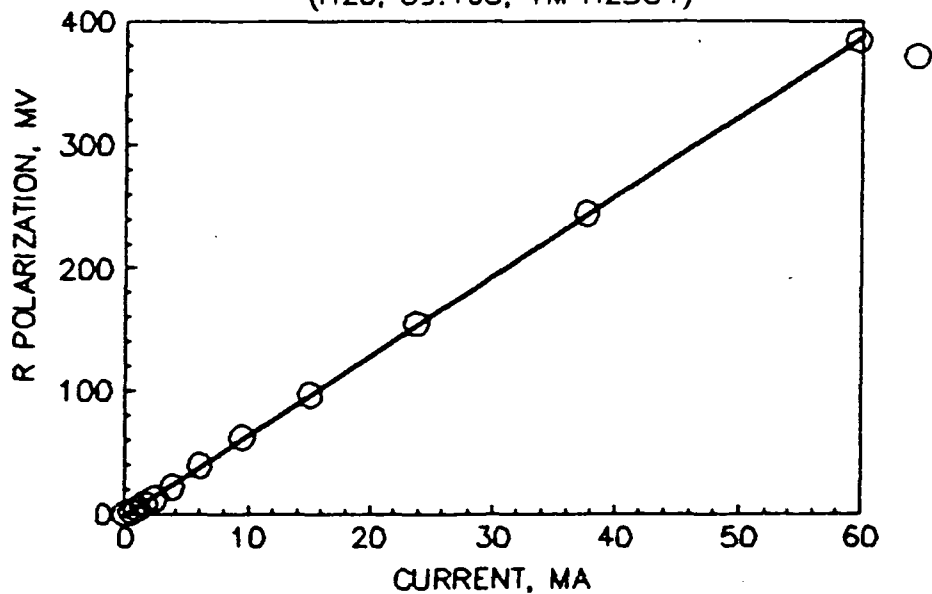


200CC/MIN O2(H2O)/O2 SIDE  
 80o,60o,40oC FOR 30  
 $R=7.065(S=7.0921,l=-1.631)$

GPT469

2/11/92

Figure 124. ANODIC R POLARIZATION FOR GINER ELECTRODE  
 PEM/IRO2,PT ELECTRODE ONLY  
 (H2O, 59.4oC, 1M H2SO4)

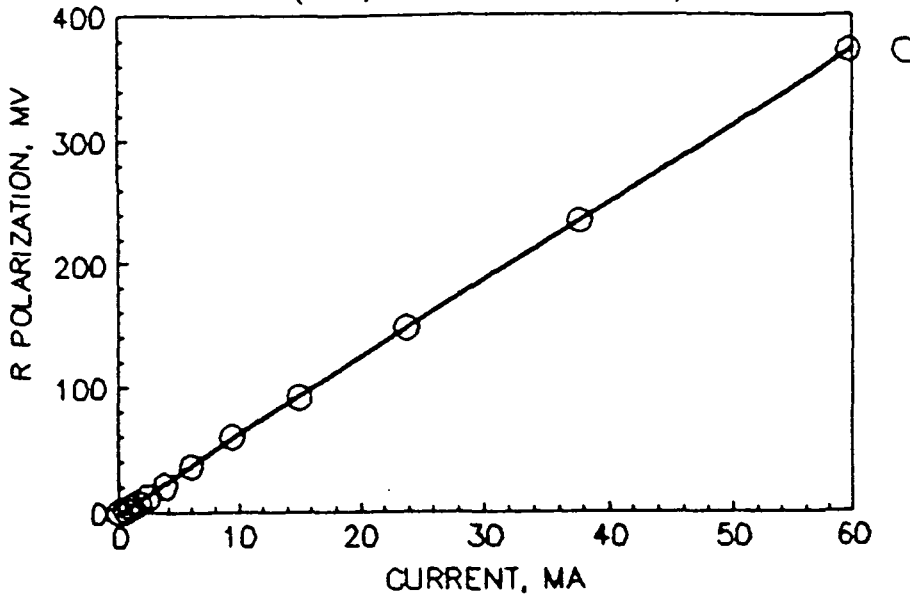


200CC/MIN O2(H2O)/O2 SIDE  
 80o,60oC FOR 30  
 $R=6.460(S=6.4758,l=-0.9552)$

GPT468

2/11/92

Figure 125. ANODIC R POLARIZATION FOR GINER ELECTRODE  
 PEM/IR02,PT ELECTRODE ONLY  
 (H2O, 80.0oC, 1M H2SO4)



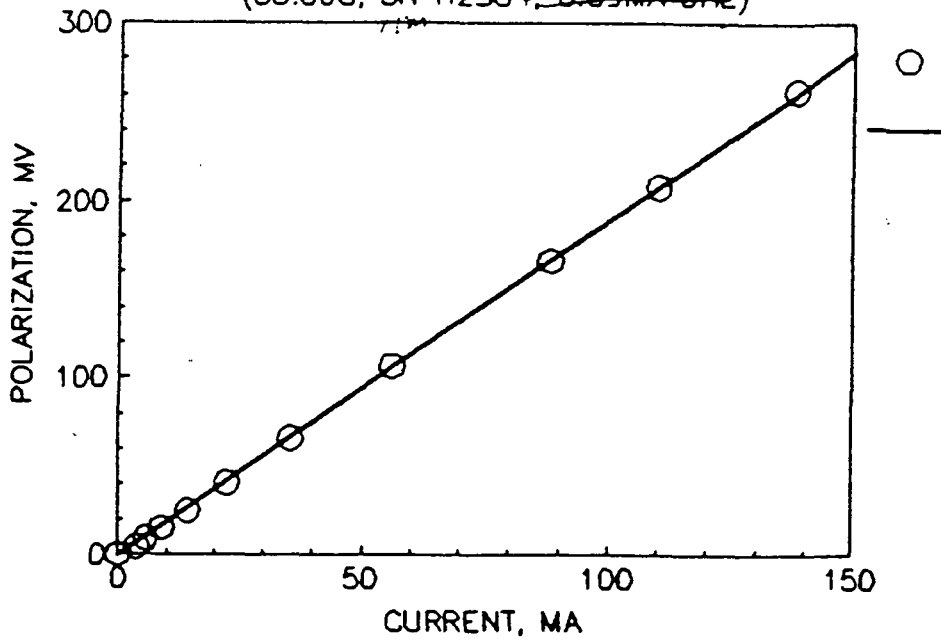
200CC/MIN O2(H2O)/O2 SIDE  
 80oC FOR 30  
 $R=6.233(S=6.2603, I=-1.6496)$

GPT467

8/11/92

23

Figure 126. R POLARIZATION VS CURRENT FOR O2 EVOLUTION  
 GINER FREE STANDING ELECTRODE ONLY (NO PEM)  
 (85.0oC, 3M H2SO4, 0.09MA DHE)

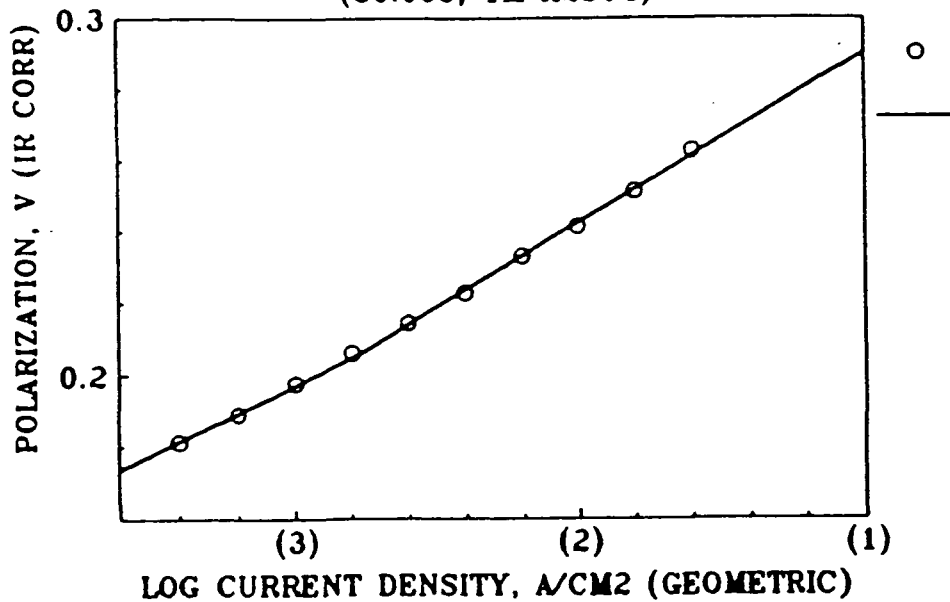


$R=1.897(S=1.9102, I=-1.8545)$   
 200CC/MIN O2(H2O)/O2 SIDE

GPT/IR02/42  
 GPT64

26

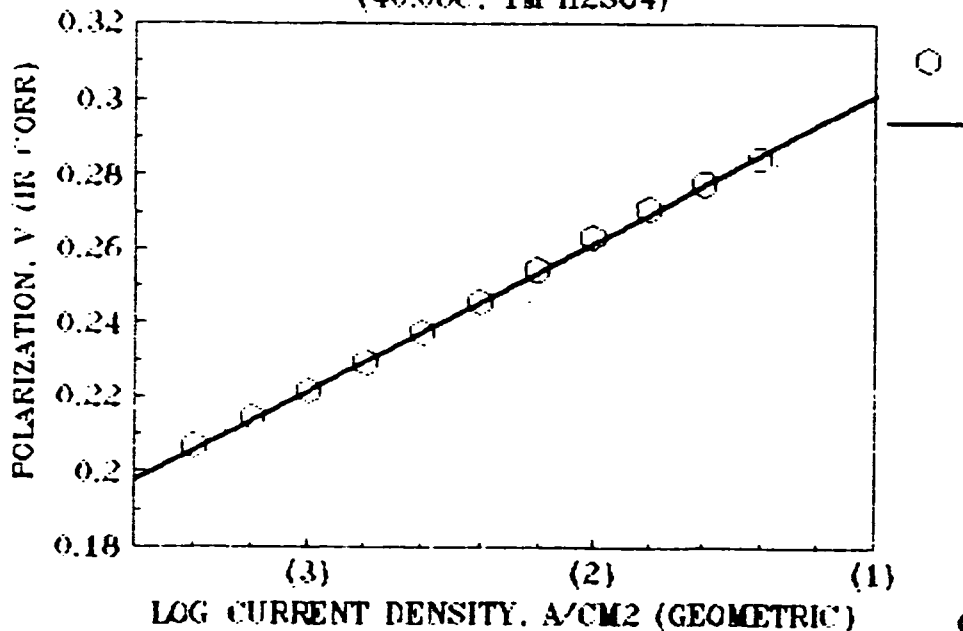
Figure 127. TAFEL PLOT FOR O2 EVOLUTION  
GINER PEM/IR02,PT ELECTRODE ONLY  
(80.0oC, 1M H2SO4)



S=0.0475(I=0.3377)(-2.765)  
S=0.039(I=0.3142)  
AFTER 2 MIN

GPT471  
200CC/MIN O2(H2O)/O2 SIDE  
80 FOR 60 BEFORE

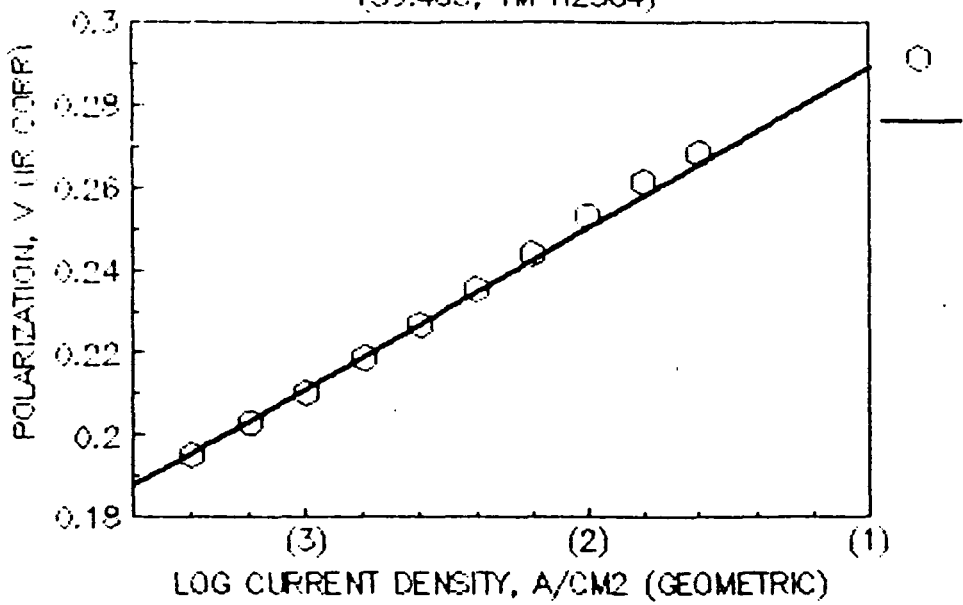
Figure 128. TAFEL PLOT FOR O2 EVOLUTION  
GINER PEM/IR02,PT ELECTRODE ONLY  
(40.0oC, 1M H2SO4)



S=0.0397(I=0.3412)  
AFTER 2 MIN

GPT473  
200CC/MIN O2(H2O)/O2 SIDE  
80,60,40oC FOR 30 BEFORE

Figure 129. TAFEL PLOT FOR O2 EVOLUTION [REDACTED]  
 GINER FEM/IR02,PT ELECTRODE ONLY  
 (59.4°C, 1M H2SO4)



0.039 REGION (i=0.3285)  
 AFTER 2 MIN

GPT472  
 200CC/MIN O2(H2O)/O2 SIDE  
 80,60°C FOR 30 BEFORE  
 8/12/72

29

## References

- 1) Advanced Electrocatalysts for Phosphoric Acid Fuel Cells.  
Jalan, V., King, R. B.; Antoine, A. C., Kosek, J. A.  
Abstracts, Fuel Cell Seminar, Tucson, Arizona, 1986, p. 303.
- 2) Catalyst and Electrode Research for Phosphoric Acid Fuel Cells  
Antoine, A. C., King, R. B.  
Progress in Batteries and Solar Cells, 6, 168 (1987).
- 3) Development of Ternary Alloy Cathode Catalysts for Phosphoric Acid Fuel Cells.  
Final Report, Giner, Inc., November 1988. DOE/MC/24261-2672. NASA Contract DEN 3-294.
- 4) Organometallic Catalysts for Primary Phosphoric Acid Fuel Cells. Final Report, ECO Energy Conversion, March 1987. DOE/NASA/0206-16, NASA CR-179490.
- 5) Investigation of Electrode Structure and Electrocatalyst Surface Areas. Final Report, Stonehart Associates, Inc, February 1987. DE AC 2183 MC 24263. NASA Contract DEN 3-350.
- 6) Technical Base for Flight Qualified Materials for Advanced Concentrators.  
Albert C. Antoine, Preliminary Information Report, 1988.
- 7) Characterization of MBR Radiator Materials  
Antoine, A. C., Memorandum, January 1989.
- 8) Regenerative Fuel Cell Energy Storage Systems for Future Manned Space Missions.  
Prokopius, Paul R.; Antoine, Albert C.; King, Robert B.  
Abstracts, (Addendum) Fuel Cell Seminar, Phoenix, Arizona, 1990.
- 9) Technology Assessment and Trade-off Study of Fuel Cell and Electrolyzer Technologies for the Project Pathfinder Energy Storage System.  
Huff, J.; Vanderborgh, N.; Hedstrom, J.  
Los Alamos National Laboratory. LA-UR-90-3244.
- 10) Mathematical Modeling of Solid Oxide Fuel Cells.  
Lu, Cheng-Yi; Maloney, Thomas M.  
Abstracts, Fuel Cell Seminar, Long Beach, California, 1988, pp 78-83
- 11) Predicted Restrictions on Reactant Gas Utilizations in Monolithic Solid Oxide Fuel Cell Operation.  
Maloney, T. M.; Lu, C.-Y.; Coulman, G. A. Progress in Batteries & Solar Cells, 8, pp. 298-301 (1989)
- 12) Performance Predictions for Monolithic Solid Oxide Electrolyzer Arrays  
Maloney, Thomas M.; Coulman, George A.  
Abstracts, Fuel Cell Seminar, Phoenix, Arizona, 1990, pp. 239-243.

- 13) A Study of  $\text{Na}_x\text{Pt}_3\text{O}_4$  as an  $\text{O}_2$  Electrode Bifunctional Electrocatalyst.  
Fieldner, William L.; Singer, Joseph. NASA TM 105311, December, 1991.
- 14) PEM Regenerative Fuel Cells  
Swette, Larry L.; LaConti, Anthony B., McCarty, Stephen A. NASA Space  
Electrochemical Research and Technology Conference, NASA Conference  
Publication 3228, 1993, pp. 139-148.

**“PAGE MISSING FROM AVAILABLE VERSION”**

#2

ADVANCED ELECTROCATALYSTS  
FOR  
PHOSPHORIC ACID FUEL CELLS

V. Jalan  
ElectroChem  
Woburn, MA 01801

R. King & A. Antoine  
NASA - Lewis Research Center  
Cleveland, OH 44135

J.A. Kosek  
Giner, Inc.  
Waltham, MA 02254-9147

Over the last decade advances in the phosphoric acid fuel cell technology have brought it to "almost commercial" status. Today's acid fuel cells are intended to use oxygen from ambient air and relatively reduced fuel (light distillates, methanol, natural gas, etc.) or coal gas from a gasifier. Two applications are envisioned for commercializations: as a dispersed power plant for electric power in the 7.5-11 megawatt size, operating at 70-120 psig and 210-250°C, and as on-site cogeneration plants of 40-200 kilowatt size for buildings utilizing waste heat, operating at ambient pressure. Both types of power plants use concentrated phosphoric acid immobilized in a matrix with Teflon bonded gas diffusion medium containing 0.25 and 0.5 mg Pt/sq.cm at the anode and cathode, respectively. Typical goals for cell voltage at ambient pressure and 120°C are 0.7 and 0.6 V at 200 mA/sq.cm and 760 mV at 250 mA/sq.cm, using flow rates 1.4 and 1.2 times the stoichiometric requirements for air and fuel, respectively. About five years of operating life with minimal decay (less than 3 mV/1000 hrs) is targeted.

Platinum catalysts for phosphoric acid fuel cells typically consist of platinum which is prepared in a finely divided form dispersed uniformly on the surface of a conductive carbon black. Much current research is directed toward enhancing the efficiency as well as extending the lifetime of the catalyst electrodes, specifically the oxygen electrode. Both catalyst development as well as electrode degradation mechanisms are involved. Simultaneous achievement of high efficiency and long life is a major objective.

Major causes of performance decay are support corrosion and catalyst deactivation, mainly through surface area loss due to sintering of platinum particles. Several modifications of carbon blacks and substitutive materials such as TiC are being investigated to improve the corrosion resistance of supports. Many modifications of platinum are being investigated to enhance the efficiency and lifetime of the platinum catalyst during the operation of a fuel cell, electrochemical sintering of dispersed platinum takes place. The associated decrease in surface area as the extent increases its "activity" for oxygen reduction but increases Tafel slope; the net result is a significant loss in activity.

Some advances were made in reducing the sintering of platinum by heat-treatment of the platinum on carbon catalyst; this heat-treatment had a surprising effect on activity. In spite of a significant

with a lower effect was not. A heat-treatment one hour was made, mostly with high surface area platinum catalysts. Platinum catalysts are not stable in performance in the structure. With the platinum catalysts

by alloying with free energy, platinum, mixed among many of platinum between activity of platinum catalysts. even by the concept of using environment at the science of



ADVANCED ELECTROCATALYSTS  
FOR  
PHOSPHORIC ACID FUEL CELLS

3

V. Jalan  
ElectroChem  
Woburn, MA 01801

R. King & A. Antoine  
NASA - Lewis Research Center  
Cleveland, OH 44135

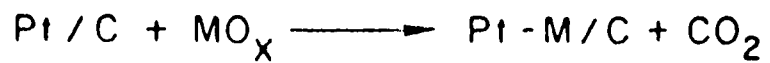
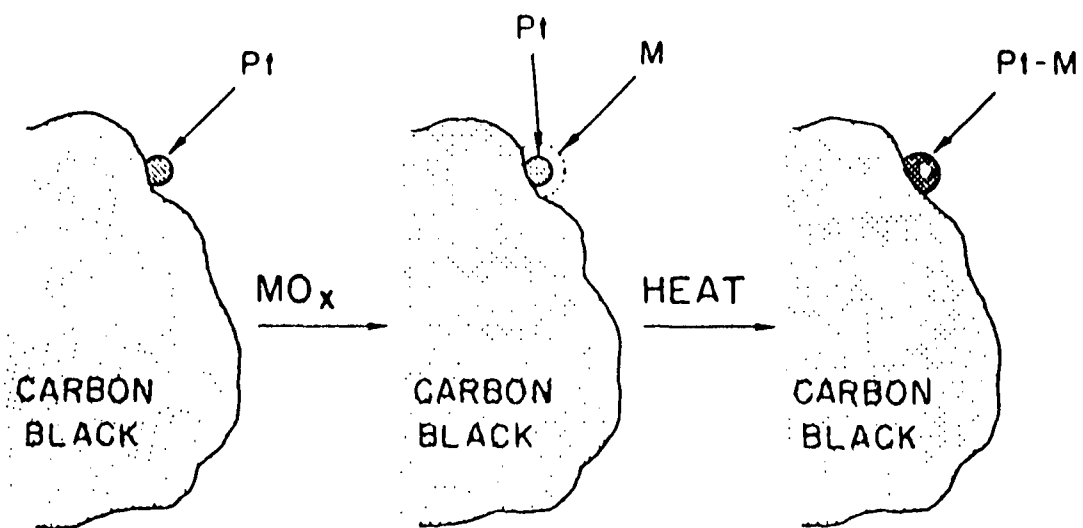
J. A. Kosck  
Giner, Inc.  
Waltham, MA 02254-9147

PRECEDING PAGE BLANK NOT FILMED

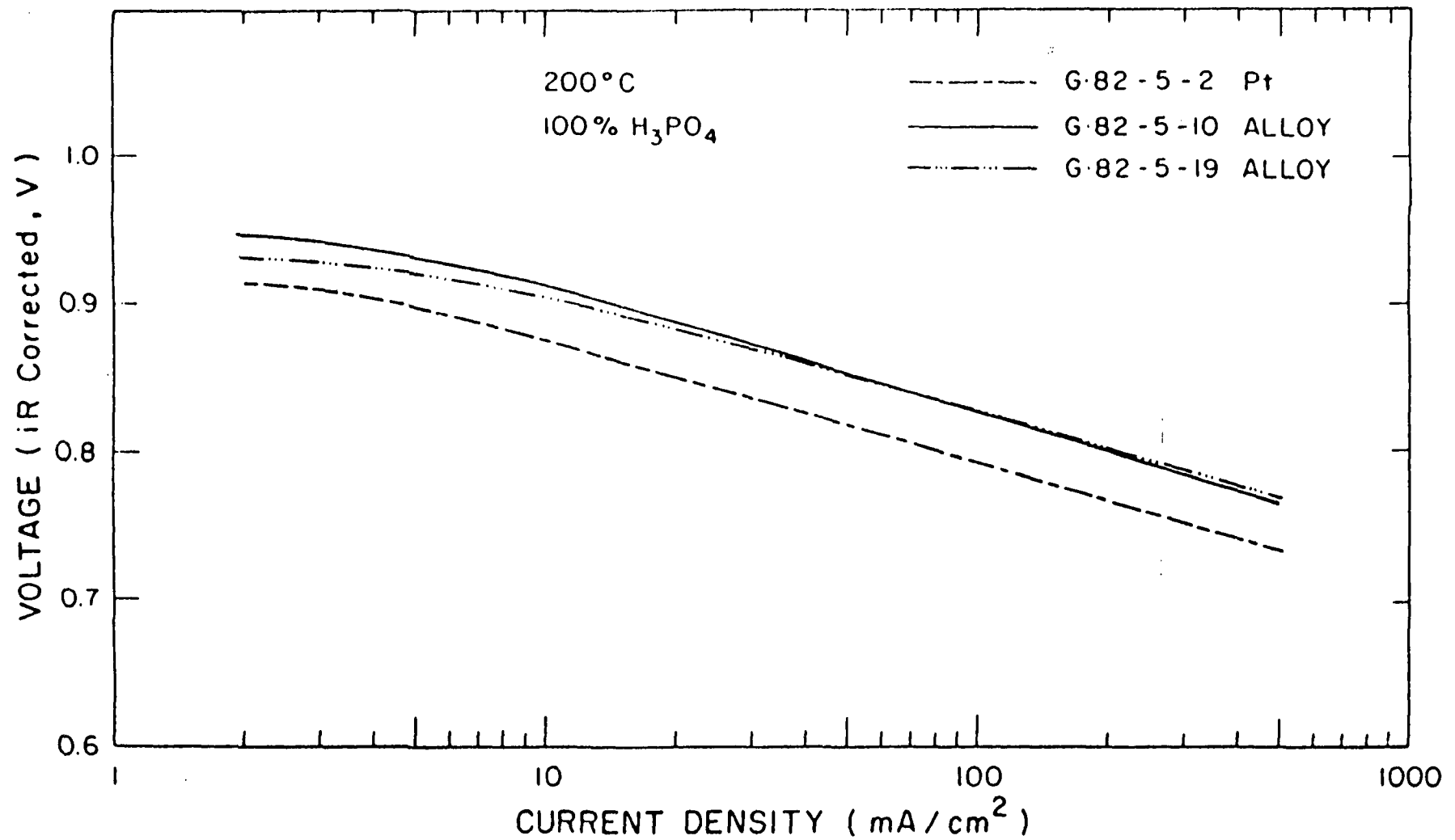
## OBJECTIVES AND SCOPE

- \* DEVELOP CATALYSTS WITH APPROXIMATELY FIVE YEARS LIFE
- \* IMPROVE PERFORMANCE USING PLATINUM ALLOY CATALYSTS
- \* IMPROVE STABILITY USING PLATINUM ALLOY CATALYSTS

# GENERAL ALLOYING TECHNIQUE



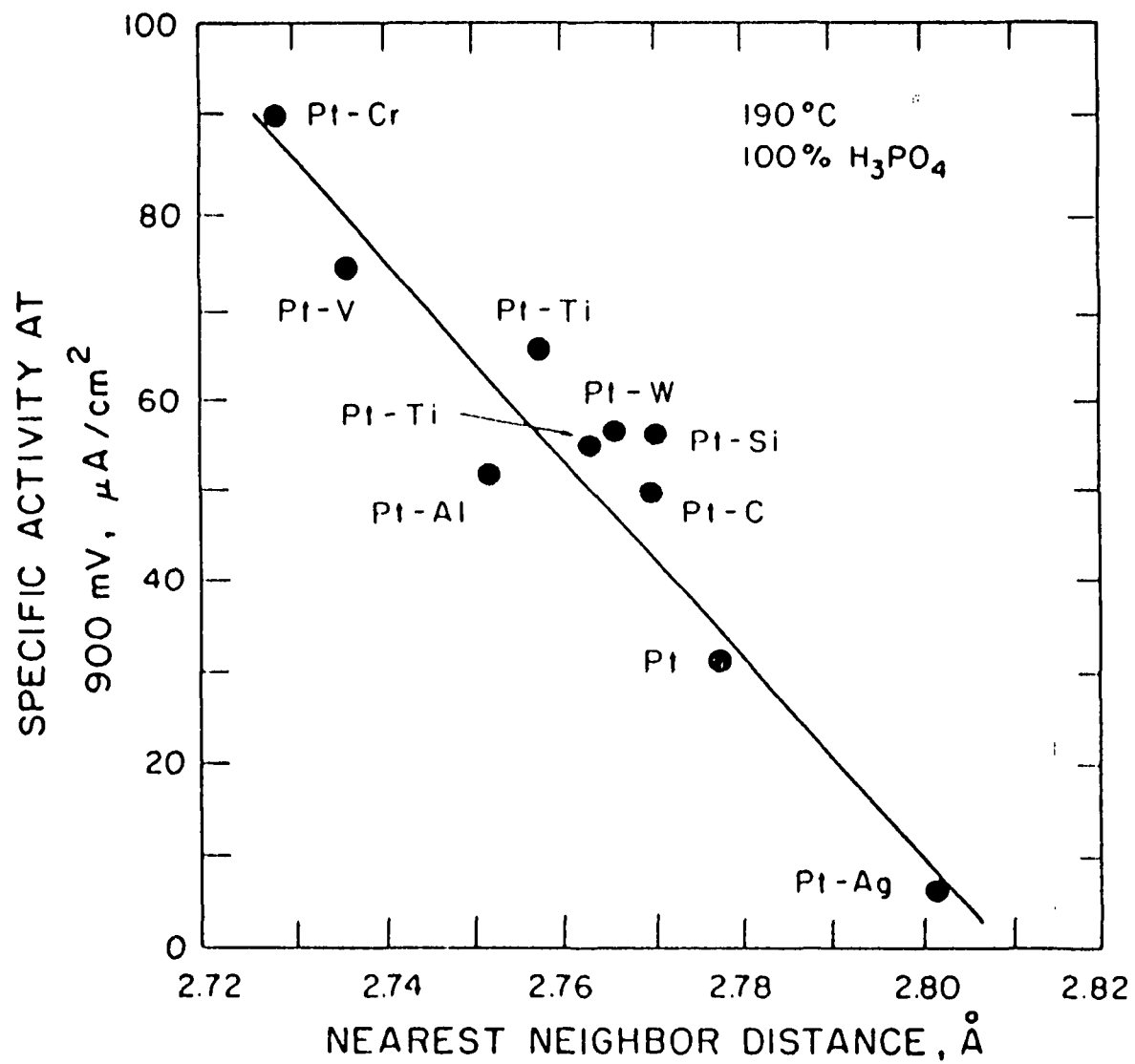
# PERFORMANCE OF Pt AND Pt ALLOY CATALYSTS



7

8

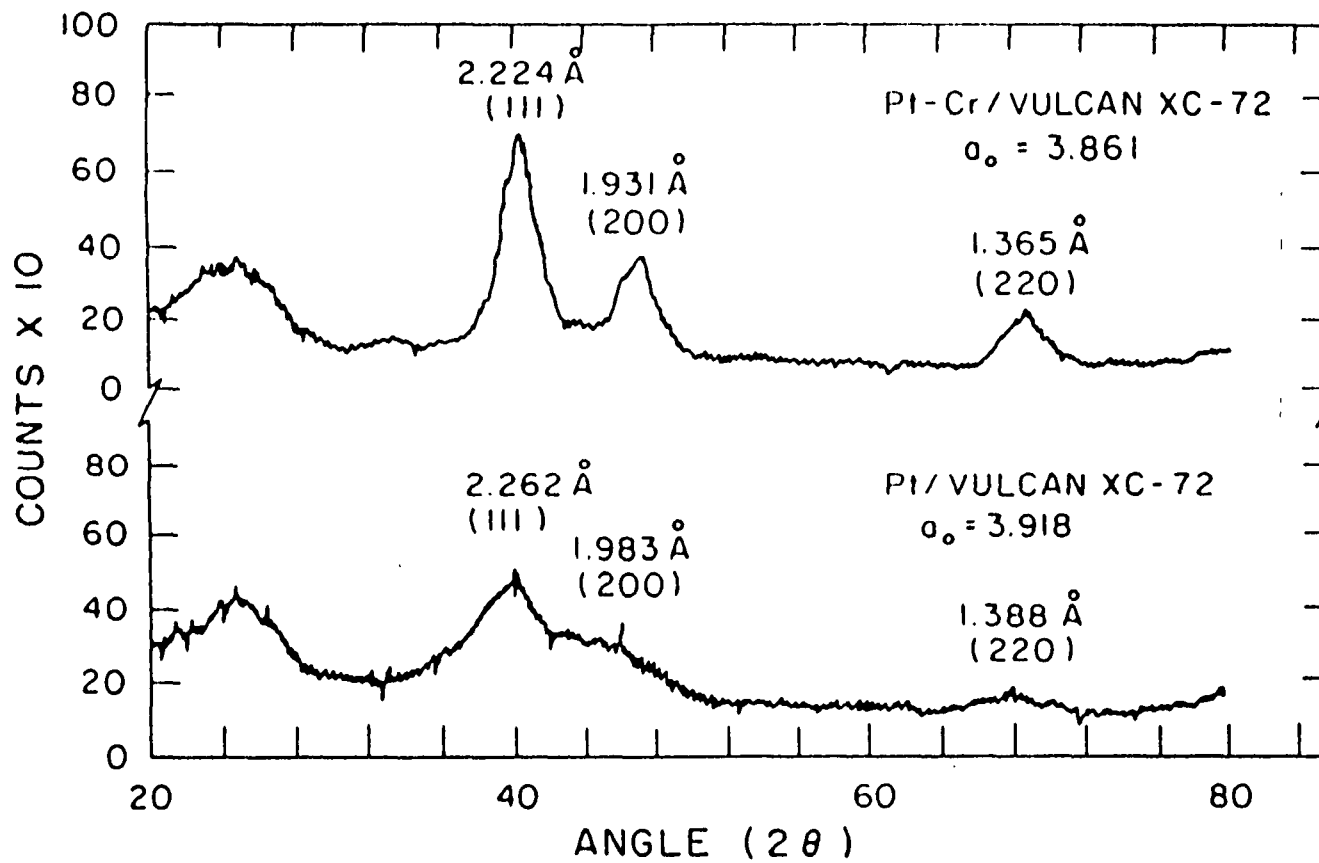
# SPECIFIC O<sub>2</sub> REDUCTION ACTIVITY



## CHARACTERIZATION TECHNIQUES

- \* X-RAY DIFFRACTION
- \* TEM
- \* EDAX

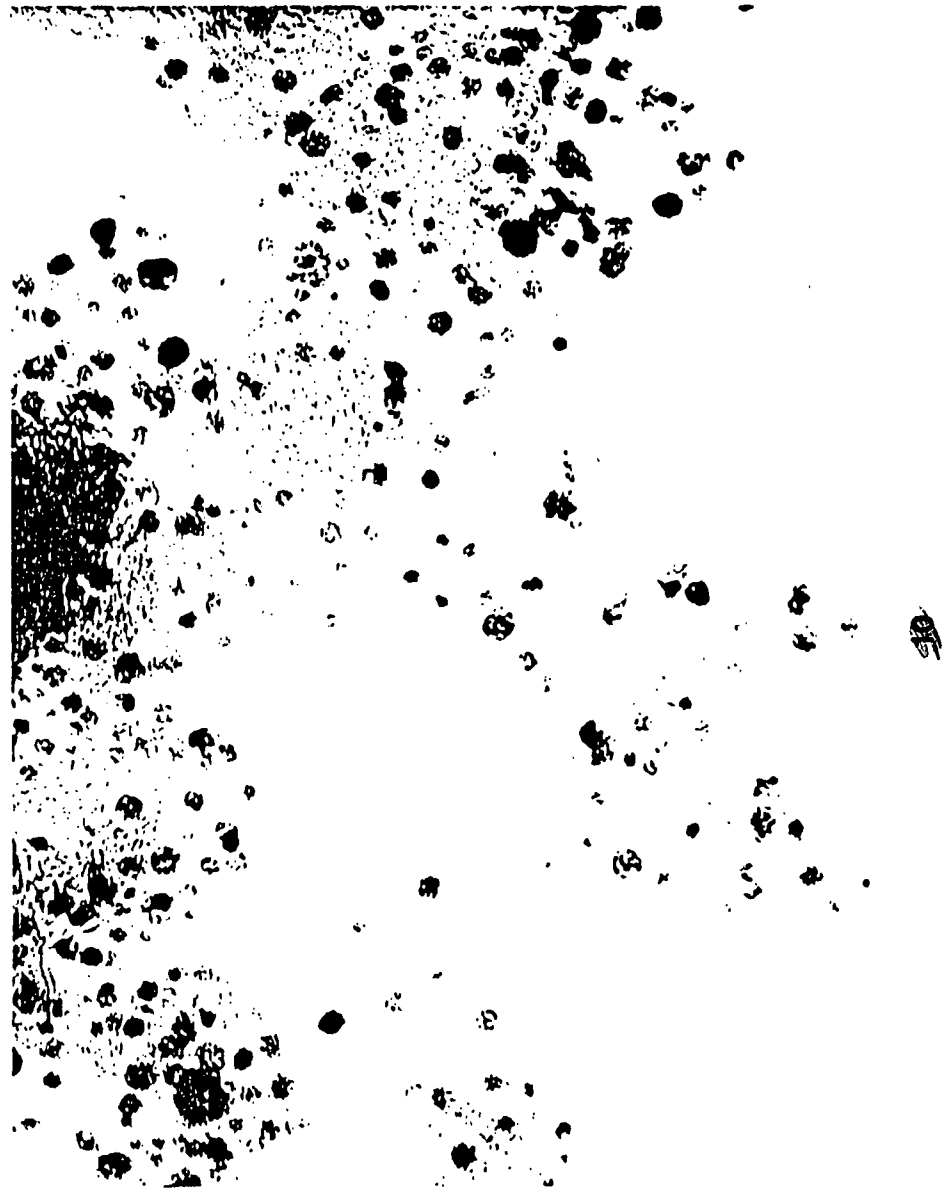
XRD OF Pt / VULCAN XC-72 AND Pt-Cr / VULCAN XC-72



10



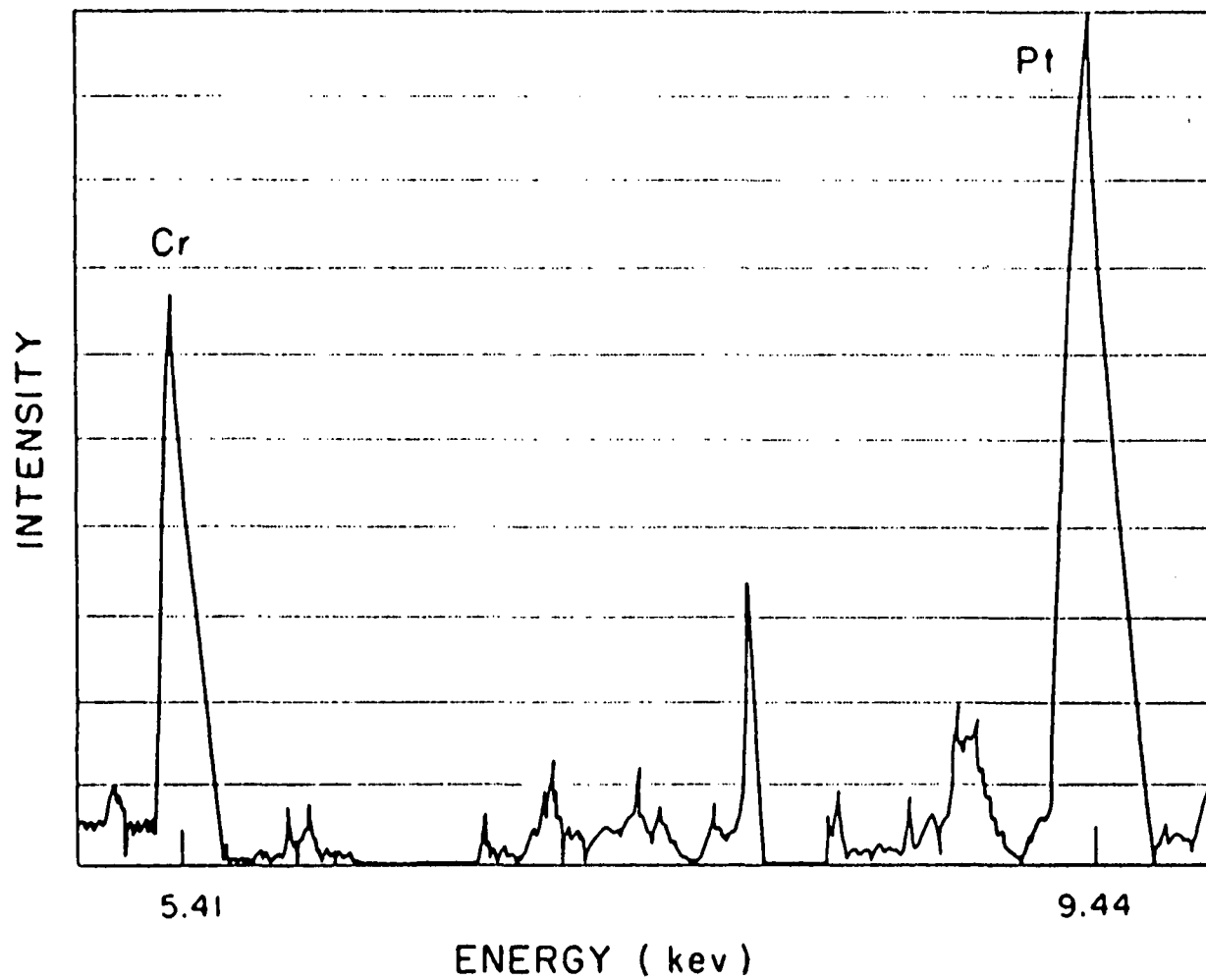
STANDARD 108 PL/C



PC TERNARY ALLOY/C



EDAX OF SINGLE Pt-Cr/VULCAN XC-72 PARTICLE



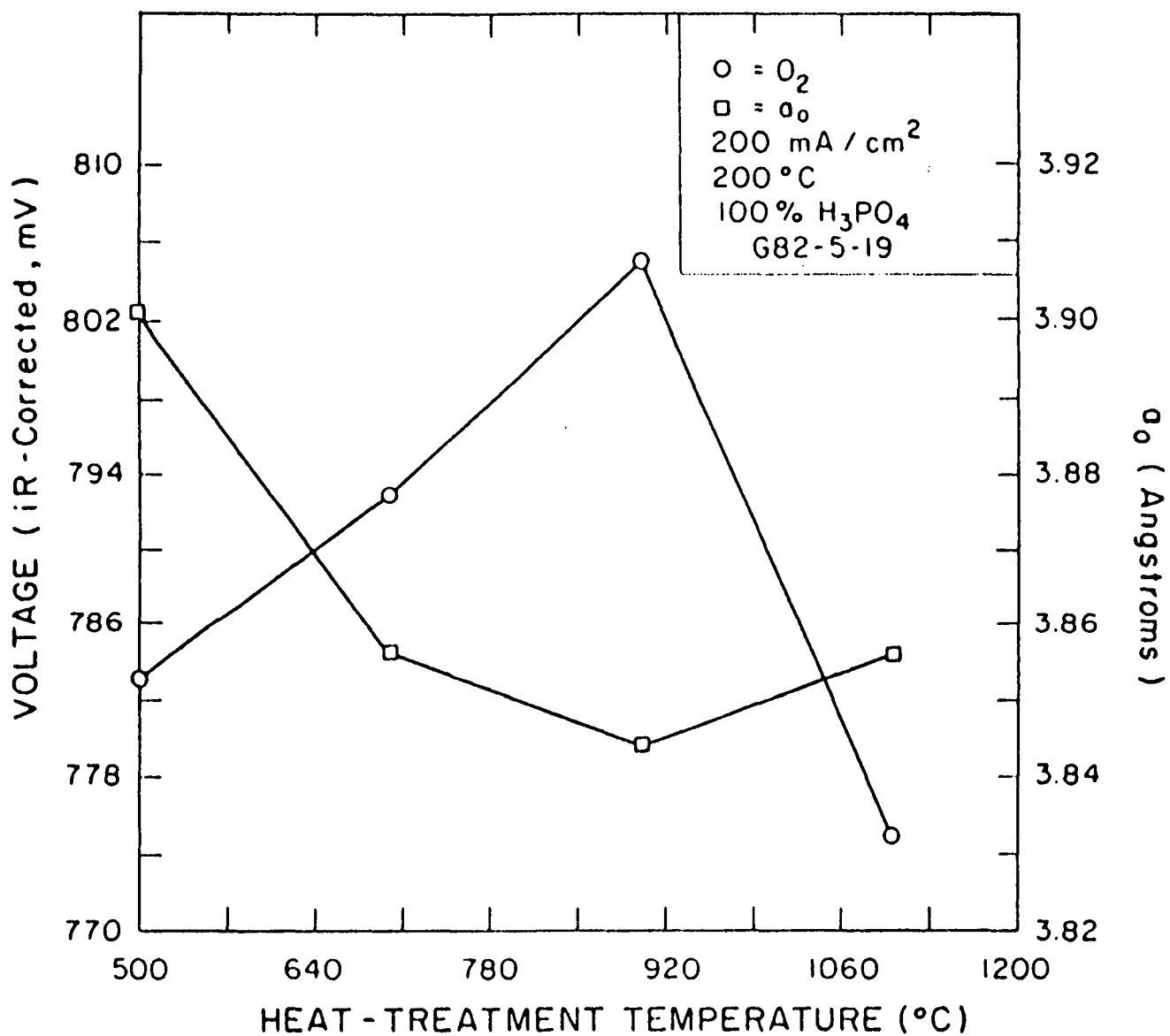
## OPTIMIZATION OF G82-5-19

- \* EFFECT OF HEAT-TREATMENT TEMPERATURE
- \* EFFECT OF PLATINUM CONTENT

12

12

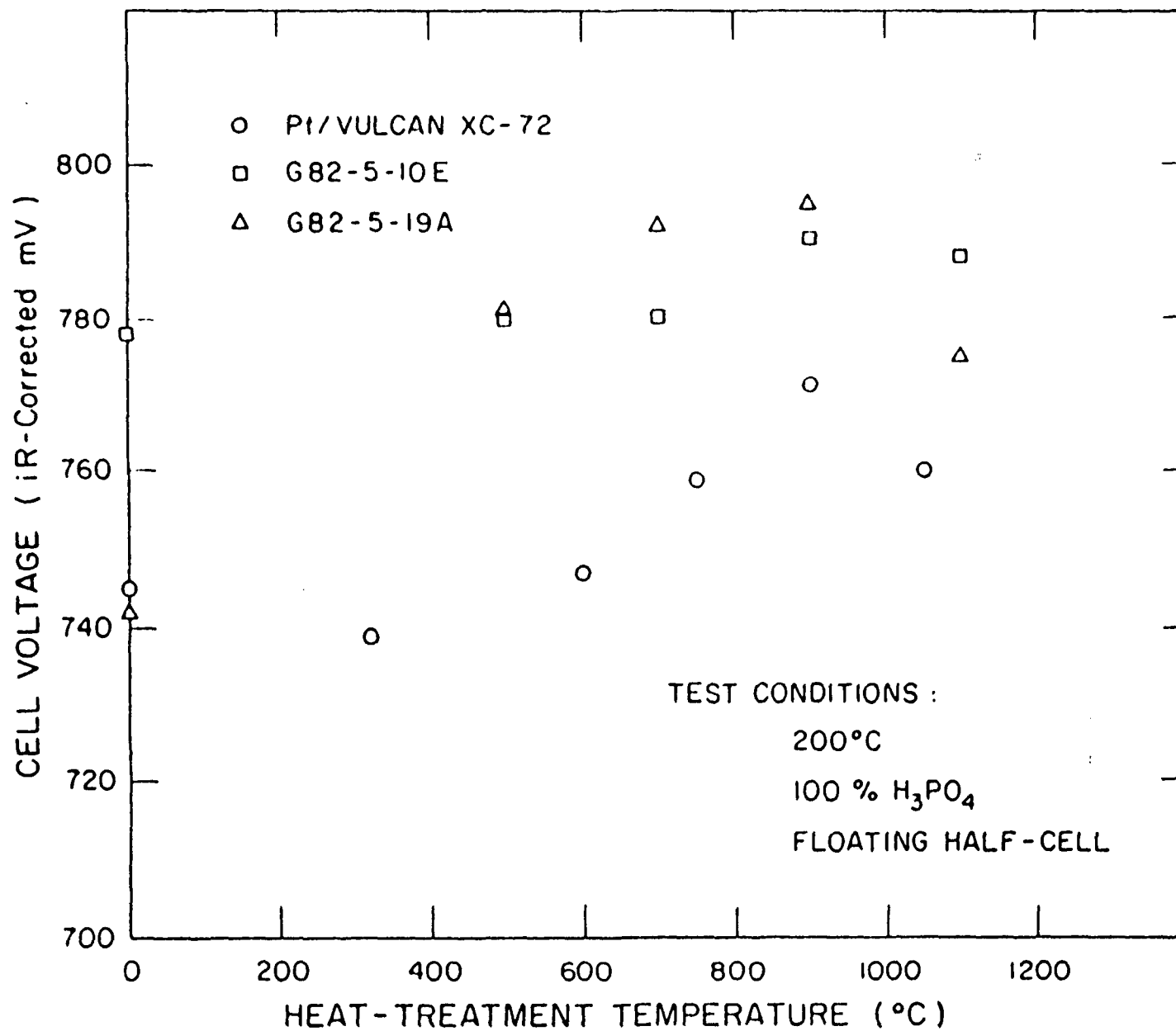
EFFECT OF HEAT-TREATMENT TEMPERATURE ON O<sub>2</sub>  
PERFORMANCE AND LATTICE PARAMETER



13

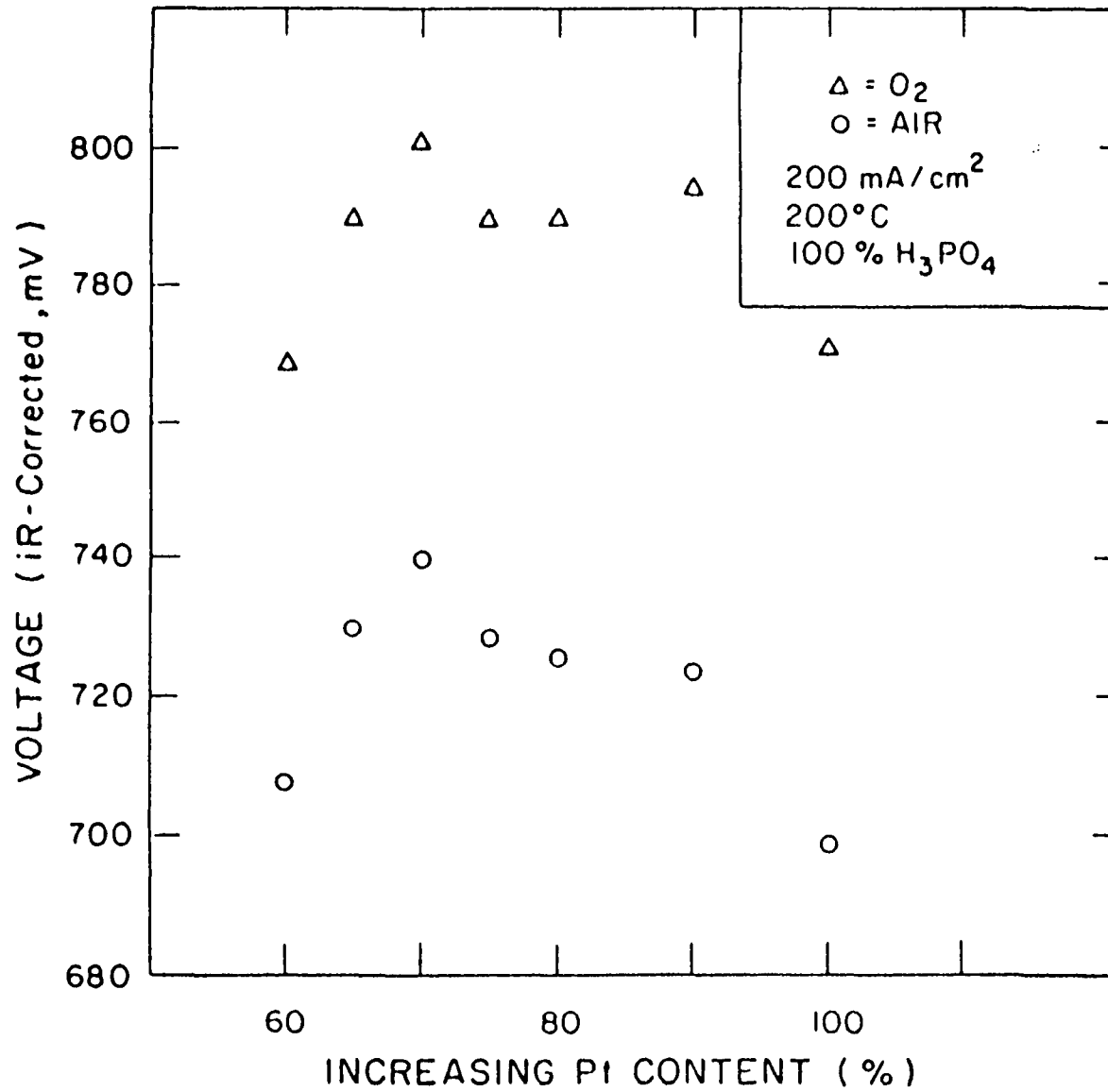
13

EFFECT OF HEAT-TREATMENT TEMPERATURE ON  
O<sub>2</sub> REDUCTION PERFORMANCE



14

EFFECT OF INCREASING PI CONTENT  
ON HALF-CELL PERFORMANCE



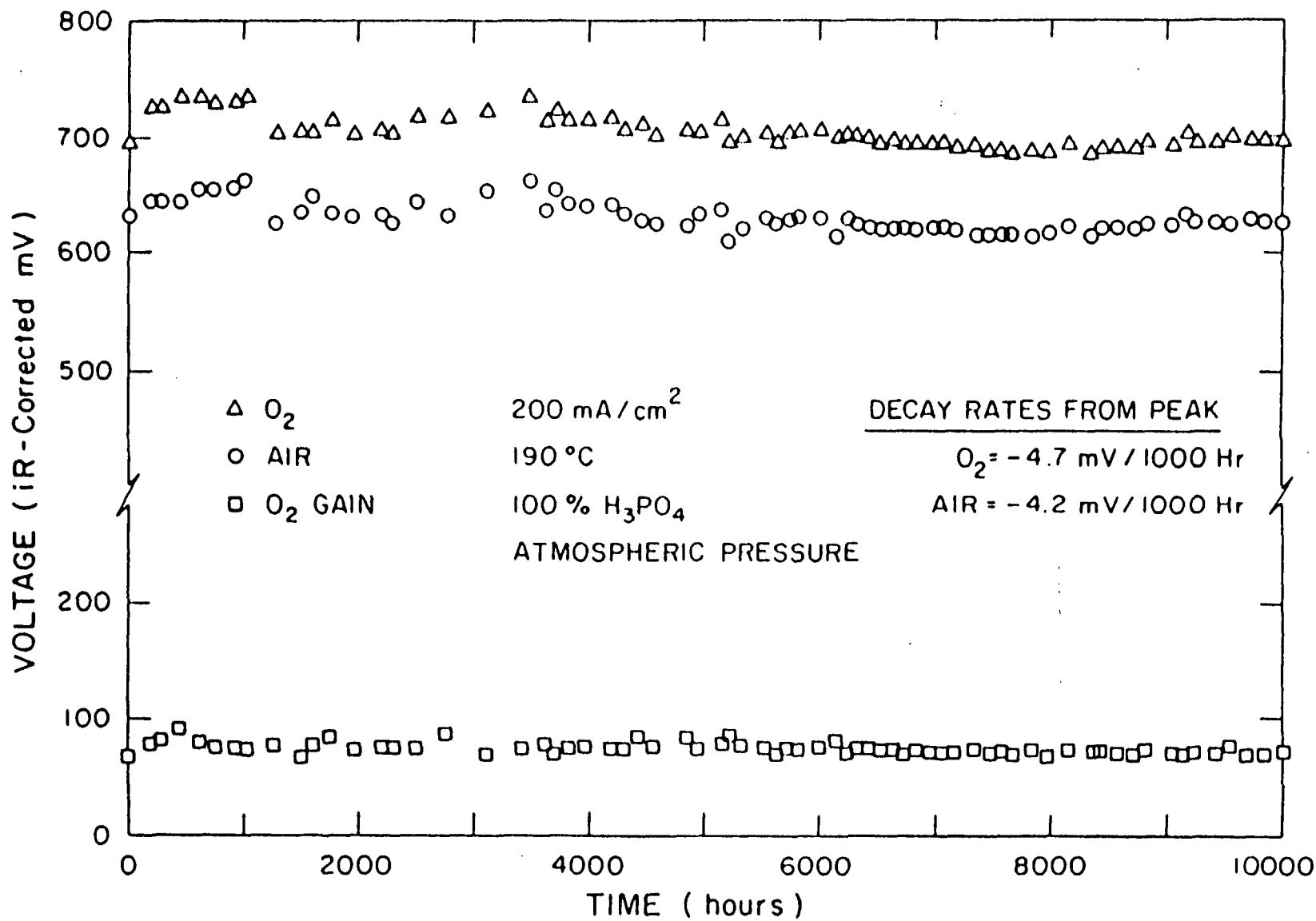
51

15

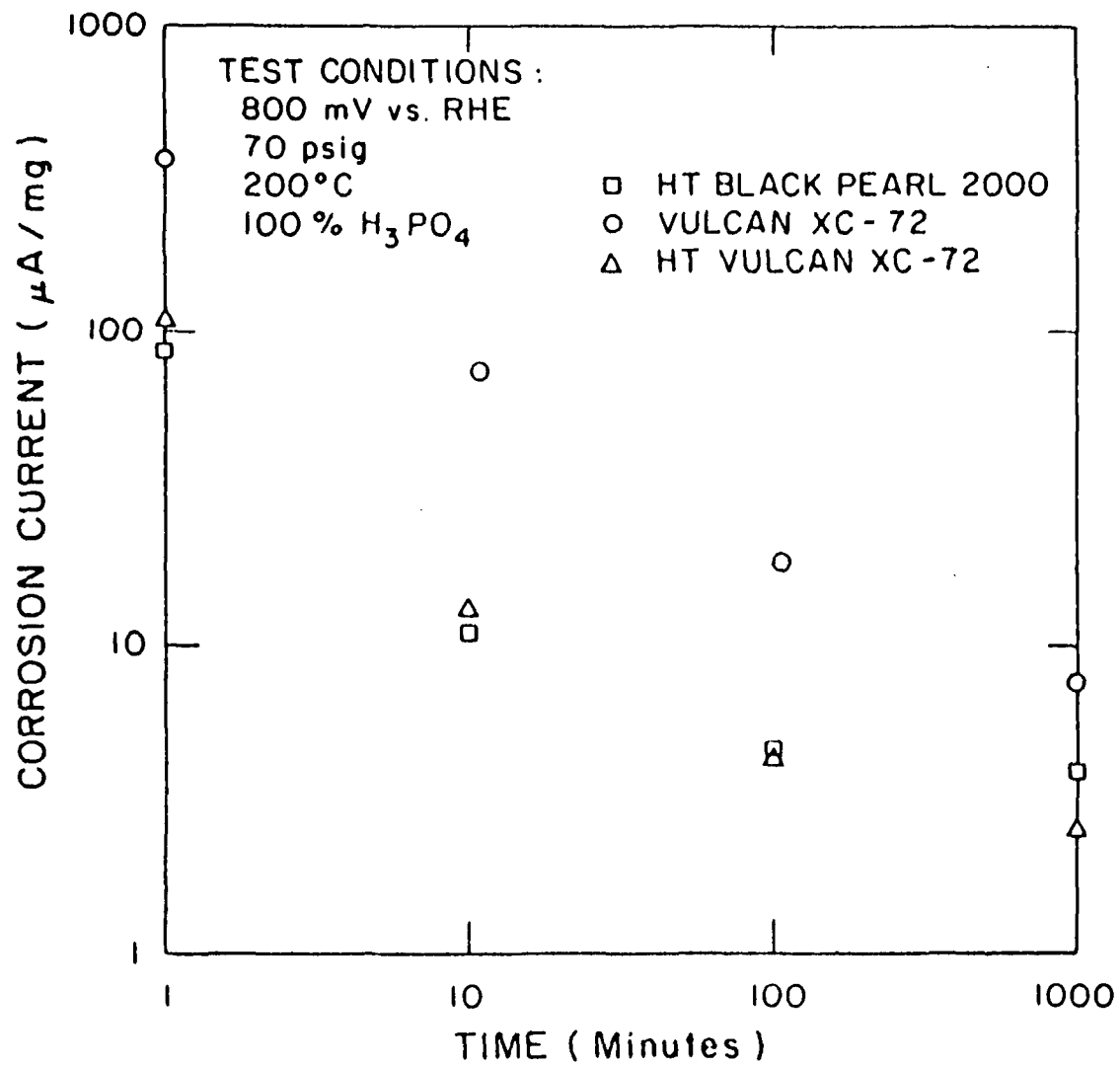
STABILITY

16 ~~18~~

LIFE PERFORMANCE OF A FULL CELL CONTAINING THE G82-5-34  
ELECTROCATALYST AT ATMOSPHERE PRESSURE (BUILD 40)



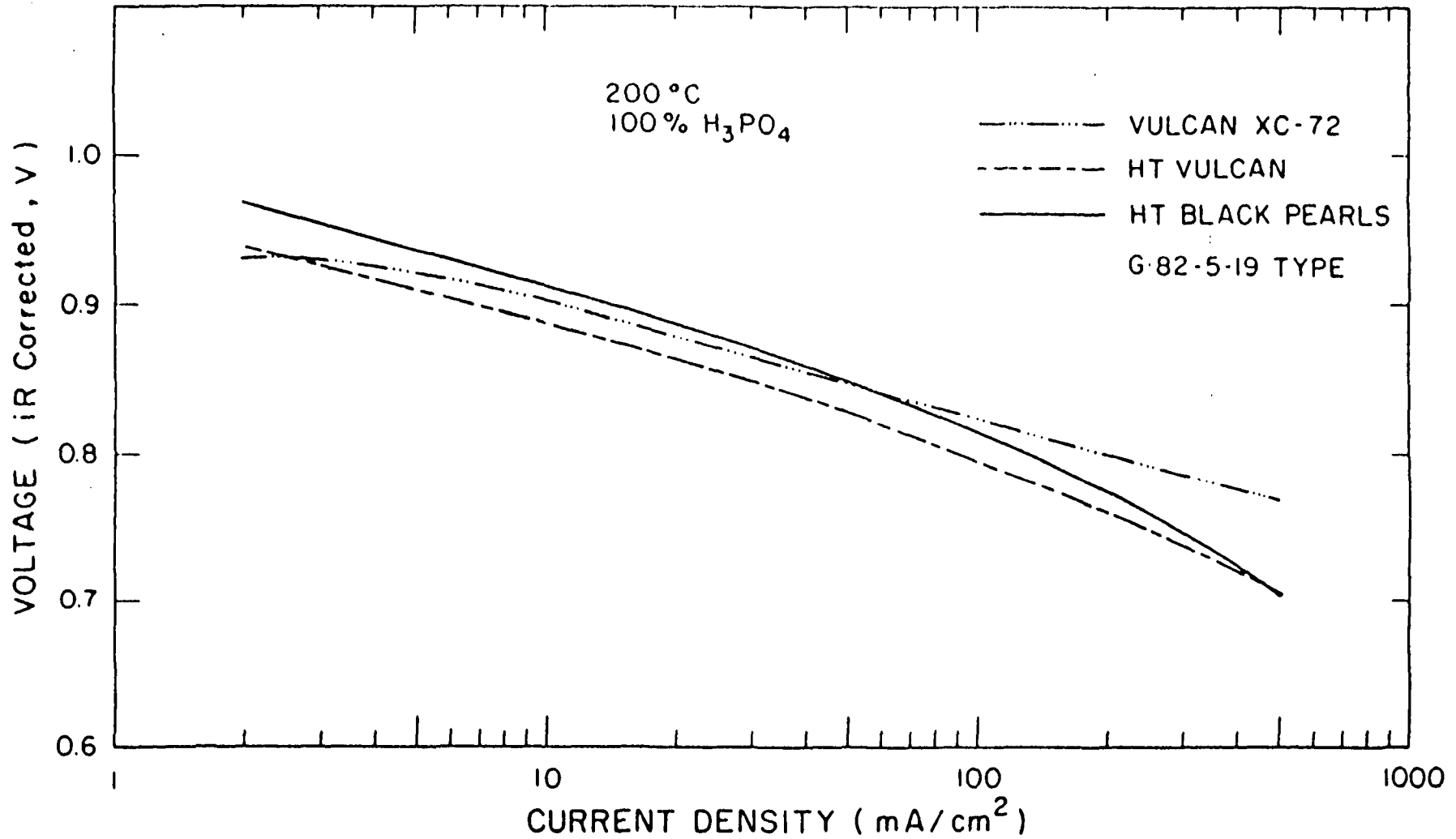
# CORROSION CURRENTS OF GRAPHITIZED AND NON-GRAPHITIZED SUPPORTS



81



# EFFECT OF CATALYST SUPPORT ON PERFORMANCE



CATALYST AND ELECTRODE RESEARCH FOR  
PHOSPHORIC ACID FUEL CELLS

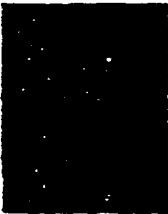
By A. C. Antoine and R. B. King\*

The U. S. Department of Energy (DOE) is funding phosphoric acid fuel cell commercialization programs at Westinghouse, Engelhard, and UTC. In support of these commercialization efforts, DOE Morgantown Energy & Technology Center, Morgantown, WV, is also funding research under an advanced research and technology development (AR&TD) program. These programs are managed by NASA Lewis Research Center, Cleveland, OH, and include, in addition to catalyst and electrode research, carbon component technology development at Great Lakes Research Corp. and fuel cell modelling and analysis support work at Cleveland State University.

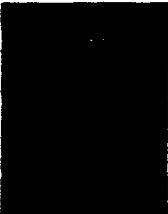
The major purpose of the AR&TD program is to conduct research on fuel cell catalysts and electrodes, the results of which will provide major improvements in electrode performance and life, and also will aid in reducing fuel cell costs. The research is being carried out at Giner, Inc., under contract DEN3-294; ECO under contract DEN3-206; and Stonehart Associates, Inc., under contract DEN 3-350. Correlated research is being carried out at Lawrence Berkeley Laboratory and Los Alamos National Laboratory.

At Giner, the original objective was the development of electrocatalysts, particularly ternary alloys of platinum which will exhibit improved activity and stability as cathodes in hot, concentrated phosphoric acid. Binary alloys were identified which exhibited increased activity over the baseline platinum catalyst. Also, using the results from X-ray diffraction measurements on binary alloys, a correlation between the electrocatalyst activity and the crystallographic nearest-neighbor distance was found. This is illustrated in Fig. 1 (1). This correlation was significant in that it provided a guideline for the selection of additional candidates.

In recent years it has become apparent that to reach the efficiency required, phosphoric acid fuel cells will have to be operated under pressure. This requirement places some additional constraints on fuel cell component parts, including the



Albert C. Antoine, Ph. D., Organic Chemistry, Ohio State University. More than 20 years at NASA Lewis Research Center in research and project management involving fuels analyses and characterization, fuel cells and batteries. Senior Research Associate, Cleveland State University since 1983.



Robert B. King, M. S. Physical Chemistry, Case Western Reserve University, 1951. Engaged at NASA Lewis Research Center as a government project manager in developing non-aqueous batteries and phosphoric acid fuel cells for 23 years. Worked in private industry for ten years developing chemical resistant coatings and plastics for use in the chemical process industries.

\* NASA Lewis Research Center, Cleveland, OH 44135, USA. Telephone: (216)-433-6123/6122.

catalyst support. Although the usual support, Vulcan XC-72, shows good stability in long-time testing, it lacks the corrosion resistance needed for pressurized operation. Therefore, another objective of the Giner program is to prepare the high activity ternary alloy catalysts on more corrosion-resistant materials. The materials selected are graphitized carbon blacks, and several promising candidates have been identified which have shown good corrosion resistance under pressurized conditions. At present, heat-treated (2700°C) Black Pearls 2000 is the material of choice and the major emphasis is being put on developing efficient electrodes with this carbon support.

In developing efficient electrodes with the new supports, particular attention will be paid to the preparation of oxide-free ternary alloys. Recent tests have shown that standard methods of preparing ternary alloys in some cases leads to a resultant mixture of alloys and oxides. Further, in addition to oxide-free alloys, known mixtures of alloy-free mixed oxides will be prepared and studied. The purpose is to obtain a better understanding of the chemical and physical states of the catalysts and their effects on the catalytic activity.

Throughout this research, attention has been given to understanding the reason for the increased activity of alloy catalysts. This effort will be aided by some analyses using advanced techniques that have been brought into the electrocatalyst development program. These analyses will be performed by the DOE National Laboratories. They will be using an ion beam equipped with a nuclear microprobe with PIXE and RBS analyses. TDS, XRF, XPS, and EXAFS will also be used. These analytical tools will be used to characterize the electrode preparation before as well as after use in a fuel cell - for example, after 1,000 hours. An important part of this effort is the monitoring of changes in catalyst and electrode form, composition, and structure during use, and effects on activity and stability.

At ECO, efforts to improve cell performance and reduce catalyst costs were attempted by the investigation of a class of organometallic cathode catalysts primarily represented by the tetraazaannulenes (TTAs). Under the program, a new mixed catalyst was developed. This catalyst is a mixture of carbons catalyzed with an organometallic and a noble metal. The stability and performance of the mixed catalyst was verified in 1,000-hour tests in half-cells and in full cells using oxygen or air and hydrogen as reactants. Test conditions included constant current loads in 85 percent  $H_3PO_4$  in the temperature range of 160°-200°C. At a load of 100 mA/cm<sup>2</sup> with platinum as the noble metal and CoTAA as the organometallic, the performance achieved was in the range of 720-750 mV versus the DHE. This cathode performance is 15-25mV higher than that obtained by using platinum alone.

A model for the improved performance observed with the mixed catalyst was developed; these catalysts act to reduce oxygen on the organometallic and to further reduce the hydrogen peroxide formed on the noble metal. This model was verified based on cathode performance response to hydrogen peroxide addition, on the effect of the use of non-noble metal peroxide reducing agents, on rotating ring-disk evaluation, and on observed increases in open-circuit potential.

With continued emphasis on seeking ways to reduce costs, additional work was done to develop non-noble metal alternatives for the noble metal in the mixed catalyst. Among the best identified was a mixed catalyst of Mn and CoTAA. Testing in a complete cell was done for 1,000 hours with hydrogen and oxygen as reactants. During this test period, the cathode performance decayed by 19 mV (from 676 to 657 versus DHE) and the anode performance by 15 mV (74 mV to 89 mV versus DHE). (This test demonstrates that the TAA-based mixed catalyst is stable in the 200°C,  $H_3PO_4$  environment, and that whatever degradation products are produced at the

the cathode do not significantly affect anode performance.) A patent application on "Mixed Catalyst for Primary Acid Fuel Cell" has been filed.

The purpose of the work at Stonehart Associates, Inc., is to study diffusion processes in gas diffusion electrode structures. The reason for this approach is the premise that the preparation of efficient gas diffusion electrodes is recognized to be, to a large extent, an art and that the detailed mechanisms of their operation are not understood. Using the results of the study, and considering models that have been presented in the literature (2, 3), the contractor was required to formulate a series of guidelines for making improvements in electrode structures.

The work under this program has been both experimental, trying different approaches, and theoretical, developing a mathematical model that fits the experimental data. One of the experimental approaches tried involved the flocking of the electrode materials using various quantities of benzyl alcohol to reduce the agglomerate size in the finished electrode.

In another experimental approach, a dry blending of three carbon components (one catalyzed, two uncatalyzed) was chosen to improve ionic conduction and to provide gas channels that are not filled with electrolyte.

Other attempts are being made using a water-floc fabrication technique for ultrasonic dispersion. Also, surfactants with different physical and chemical properties are being screened for their carbon dispersing ability in the formation of electrode structures. Experimental investigations will also be carried out in other areas. The effect of the thickness of the electrocatalyst backing layer on gas diffusion through the backing layer will be determined. Other electrodes of constant thickness, but with different platinum loadings will be investigated. Finally, the pore volume within the electrode structure will be progressively modified with the use of selected pore formers.

Parallel to, and in conjunction with, the experimental work, using the models of Ref. 2 and Ref. 3, Stonehart Associates, Inc., has developed computer software for a mathematical theory of mass transport of reactants in porous gas diffusion electrodes. In the theory, a simplified model for the electrode structure was used and fitted to experimental data. Various numerical parameters contributing to the electrode structure were examined. Comparisons of the model to experimental performance data were carried out using diagnostic gas mixtures of oxygen, air, one percent oxygen in helium, and one percent oxygen in nitrogen. Fig. 2 shows the results using a standard electrode. The fit is especially good for the low concentrations.

Additional work has been done, and more is in progress, to develop a detailed model of the electrode structure. This model will encompass numerical values for all of the physical parameters operating within the electrode structure and will hold for all four gas compositions. Using the model, it will be possible to show to what extent the various resistances that influence electrode performance are operative at various potentials and corresponding current densities. This use of the model can give valuable information in a convenient form to aid in selecting the parameters for the electrode formulation process, where the goal is the development of more effective electrode structures.

ORIGINAL PAGE IS  
OF POOR QUALITY

**Fig. 1.** Specific activity for oxygen reduction versus electro-catalyst nearest-neighbor distance.

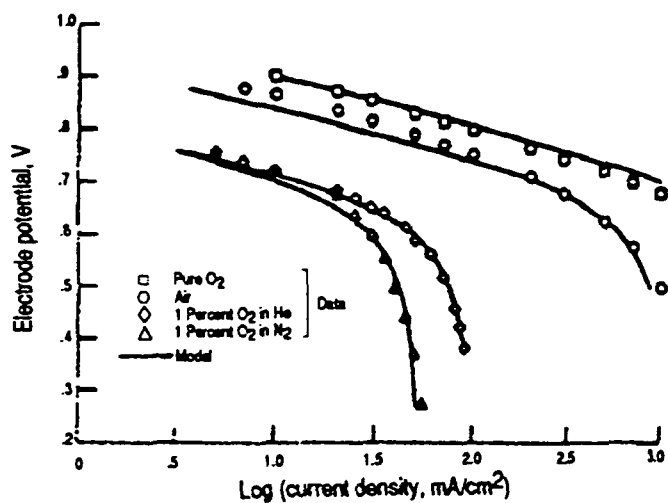
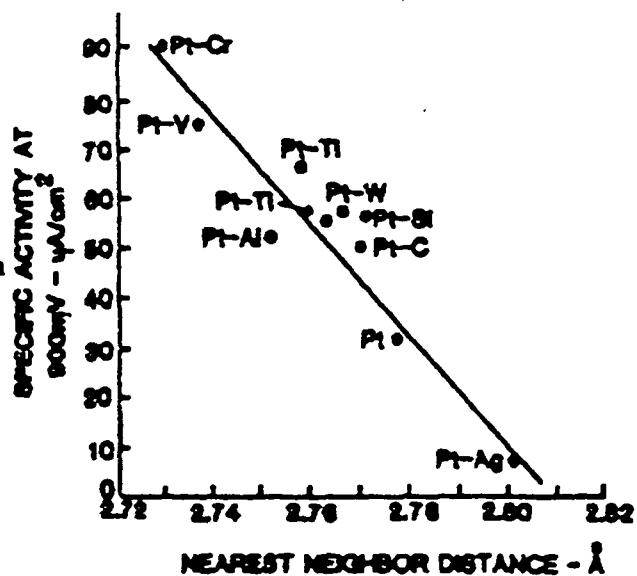


**Fig. 2.** Cathode performance curves.

### References

1. V. Jalan and E. J. Taylor, *J. Electrochem. Soc.*, **130** (11) 2299 (1983).
2. M. B. Cutlip, *Electrochimica Acta*, **20**, 767 (1975).
3. R. P. Lczkowski and M. B. Cutlip, *J. Electrochem. Soc.*, **127**, 1433 (1980).

PRELIMINARY INFORMATION REPORT 1988  
ALBERT C. ANTOINE  
NUCLEAR AND THERMAL SYSTEMS OFFICE

**Technical Base for Flight Qualified Materials for Advanced Concentrators**

The purpose of this effort was to aid in assessing the technical base for flight qualified materials for advanced concentrators. At present, no firm technical data base exists for concentrator materials. Thus, no material is commercially available that can be certified for long-term application. Included in the consideration of concentrator materials are materials of construction, optical films, and coatings.

Some general 'reference' books are available such as the "Space Materials Handbook (3rd ed.) 1969." (Ref. 1) In it are new materials knowledge and data obtained from the design and successful launching of a wide variety of space systems. Selections and recommendations for a variety of materials are made, based on space experience and ground-based simulation. Further, materials are recommended for the performance of several hypothetical space missions, with the space environments varying depending on the specific mission parameters. Selections are made for thermal control materials, optical materials, lubricants for several systems, polymeric materials for adhesives, seals, and structural applications, spacecraft antennas, electronic and miscellaneous components and materials. In addition to organic structural materials, inorganic structural materials are also considered, though their selection is not usually determined by the effects of the space environment on them.

Another 'reference' book is the "Engineered Materials Handbook, Vol. 1, Composites, 1987," (Ref. 2) which contains in-depth engineering information on composite materials. Contents include information on the properties and forms of the basic fibers and matrix materials, as well as of the composite materials themselves. Included, also, are analysis and design of composite materials and of the structures made from them; testing of composites, manufacturing and fabrication processes, quality control, failure analysis, applications and experience are also included. For space structures, trusses, platforms, pressure vessels and tanks, and shells are considered. A chapter on long-term environmental effects is included, but these were primarily related to ground and flight environments on composites used in aircraft.

In 1986, Marshall Space Flight Center published the "Materials Selection List for Space Hardware

Systems" (Revisions of MSFC Hdbk - 527 and Johnson Space Center 09604). (Ref. 3). Ratings for metallic materials are based on corrosion resistance, stress corrosion cracking susceptibility,  $N_2O_4$  and  $N_2H_4$  fluid system compatibility, compatibility with liquid and gaseous oxygen, mechanical impact with liquid and gaseous oxygen, gaseous oxygen pneumatic impact, and fluid system compatibility with low and high pressure gaseous hydrogen. For nonmetallic materials, ratings are based on flammability, toxicity/offgassing, odor, thermal vacuum stability, static age life, and fluid system compatibility (nitrogen tetroxide, hydrazine, hydraulic fluid, liquid oxygen, and gaseous oxygen).

Standard/Commercial parts are also rated for flammability, toxicity, thermal vacuum stability, static age life (for nonmetallics) fluid systems compatibility, stress corrosion cracking, and corrosion.

Mention is made of atomic oxygen effects, but no ratings are given. Mention is also made of the fact that long term effects on metals are unknown, but that some protective coatings which show promise include silicone based coatings, fluorinated overcoats, thin metal overcoats and metal oxide overcoats.

More specific information can be found in reports such as NASA Technical Paper 1220, Evaluation of Materials for High Performance Solar Arrays (Status Report No. 1), (1978), Ref. 4).

About 50 materials were identified as candidates from the following functional categories: (1) solar cell covers, (2) adhesives, (3) substrate paddings, (4) harness materials, (5) substrate strength materials, (6) mast materials, and (7) thermal control treatments. About 25 materials were tested and evaluated. The UV/vacuum test series consisted of exposures of 500 Equivalent Sun Hours (ESH) at 1 sun, 1500 ESH at 3 suns, 1500 ESH at 6 suns, and 500 ESH at 10 suns at  $10^{-4}$  pascal. Particle irradiation/vacuum test series consisted of electron flux densities of  $10^{12}$  particles/cm<sup>2</sup> to  $10^{16}$  particles/cm<sup>2</sup> at  $10^{-4}$  pascal. The portion of the tests covered included out-gassing exposures, UV/vacuum exposure through 1500 ESH at 3 suns, and proton exposures in vacuum to  $10^{16}$  particles/cm<sup>2</sup>. Property determinations considered were absorptivity, emissivity, spectral reflectance, breaking strength, elongation, and flexure for appropriate materials. Some of the results are given in Tables 1, 2, 3, and 4. It was concluded from this work that all non-metallic materials selected for long duration mission spacecraft must be evaluated. Further, that deleterious effects of synergistic interactions of different particulate and solar radiation must also be determined for otherwise acceptable materials. A next phase in the test program was

planned with exposures at higher levels of particulate and solar radiations, and an assessment made of the damage mechanisms. No further report, though, has been made.

Another report with more specific information is NASA TM-78306, Space Environmental Effects on Materials, 1980. (Ref. 5) This report describes research oriented toward the acquisition of long-term environmental effects data needed to support the design and development of large Low Earth Orbit (LEO) and Geosynchronous Earth Orbit (GEO) space platforms and systems for the decade of the eighties. The space vacuum, electromagnetic radiation, particulate radiation, and space debris were considered. Charged particle radiation on silicon solar cells was studied. Results are shown in Figure 1. It was noted that the combined electron and proton effects were not known. Another report was referred to (Ref. 6) in which it was noted that a major portion of that study effort was directed toward developing a laboratory facility that would provide a suitable combined simulation of the critical space environmental conditions, and in which simultaneous irradiation could be done. The results from testing 23 different flexible film materials exposed to a simulated 5-year GEO equatorial environment showed the initial analytical unpredictability of the synergistic effects of electrons, protons, and UV encountered in the GEO environment. Teflon materials (FEP and PFA) undergo substantial changes in optical, thermophysical, and mechanical properties. For example, Teflon specimens subjected to combined near UV and high energy electron radiation became brittle after 17 to 30 months of exposure, while specimens exposed to 5-year equivalent electron radiation, only, retained a percentage of their original ultimate elongation. The spectral reflectance of aluminized Kapton holds up well in LEO, where UV only need be considered, but is seriously affected by a combined UV, electron, and proton environment. The results for a 5-year exposure are shown in Figure 2. Among the conclusions from this NASA TM is that the acquisition of additional data from long duration exposure in the combined environment is mandatory.

Other evidence for the need for combined radiation testing is given in Reference 7. The purpose of that investigation was to compare the effects of UV-only radiation on the solar absorptance of contaminated second surface thermal control mirrors. Optical solar reflectors were contaminated with volatile condensable material outgassed from inertial upper stage solid propellant. The combined radiation simulation consisted of 40 keV electrons and 30 keV protons at a flux of  $5 \times 10^9$  particles/cm<sup>2</sup>-sec each and a one sun level of UV. Total fluence of each type of particle, by the end of 245 hrs of testing, was estimated at  $5 \times 10^{15}$  particles/cm<sup>2</sup>. The radiation environment of the second test used the same one-



sun level of UV, but had no charged particles. The results from the two tests showed a larger increase in solar absorptance with combined radiation (protons, electrons, and UV) than with UV radiation alone. The degrading effect of combined radiation was more than twice that of UV alone.

For making selections of materials from the data available to date, some guidelines are becoming available. One such, in a preliminary (not yet published) version, has been prepared by Johnson Space Center. The title is "Material Selection Guidelines to Limit Atomic Oxygen Effects on Spacecraft Surfaces" (Ref 8). The purpose is to provide guidelines in selecting materials for satellites and space platforms, designed to operate within the LEO environment, which limit the effects of atomic oxygen interactions with spacecraft surfaces. The guidelines apply to spacecraft which require extensive use of organic films, polymeric materials, and composite structures. Included in the specification is a nomograph for estimating atomic oxygen fluence and, consequently, the degree of surface erosion the spacecraft will experience over its lifetime. Use of the nomograph is included in this report as Appendix 1. A summary of data obtained from spaceflight experiments are shown in Tables 5, 6, and 7. The reaction rate data can be used for general assessment of the effects of atomic oxygen on spacecraft surfaces. The authors claim that, "sufficient data exists at this time to permit generalizations which can be used to provide a gross assessment of surface effects. These generalizations are...

1. Unfilled organic materials containing only C, H, O, N, and S react with approximately the same reaction efficiency, ( $2-4 \times 10^{-24}$  cm<sup>3</sup>/atom).
2. Perfluorinated carbon-based polymers and silicones have lower reaction efficiencies by a factor of ten or more than organics.
3. Filled or composite materials have reaction efficiencies that are strongly dependent upon the characteristics of the fillers.
4. Metals, except for silver and osmium, do not show macroscopic changes. Microscopic changes have, however, been observed and should be investigated for systems very sensitive to surface properties. Silver and osmium react rapidly and are generally considered unacceptable for use in uncoated applications.

## 5 Magnesium fluoride and oxides in various forms show good stability."

A complete list of "basically everything that is known from the actual flight experiments," on the effects of atomic oxygen on materials, is given in Table 8. This table was obtained from JPL in January 1988.

Selections of best candidate materials (when considering atomic oxygen effects) to date (as of May 1988) were made after consideration of advantages and disadvantages of the materials use in the space environment. These results are shown in Tables 9 and 10. The material was presented at a workshop in June 1988. (Ref. 9).

Effects other than atomic oxygen and for materials other than for surfaces have also been considered. A bibliography entitled, "Durability of Materials for Precision Space Structural Applications" was compiled at Langley in late 1987. The papers included relate to moisture effects, thermal expansion, impact penetration, microcracking, thermal cycling effects, and space radiation, primarily on composites. The bibliography is included as Appendix II in this report.

Specific attention is being paid to solar dynamic concentrator materials at LeRC. The Electro-Physics Branch of the Power Technology Division has prepared a list of candidate materials (substrates, optical coatings, protective coatings), (Table 11) together with some results of optical performance and atomic oxygen durability (Table 12). The laboratory tests used an RF plasma asher. In other work with Kapton solar array blankets, protective coatings of silicon dioxide or a mixture of silicon dioxide and polytetrafluoroethylene are projected to be durable for more than 27 years in a 500 km Space Station orbit (Ref. 10). With expected use of adhesives in solar dynamic concentrator, durability tests must be conducted. One recent study (Ref. 11) evaluated selected adhesive/adherend bonded joints after a simulated, ten-year thermal-vacuum cycling, ( $\pm 250^\circ\text{F}$ ,  $10^{-15}$  torr 3650 cycles) space environment exposure. The adhesives (all epoxies) were used to bond titanium, aluminum, and magnesium to various composite adherends.

In the preparation of concentrators in the past a recurring problem has been that of differing (unmatched) coefficients of thermal expansion of materials being bonded together. In Figure 3 some thermal expansion

coefficients of various material are shown (Ref. 12). It can be seen that the metals have smaller coefficients than the usual epoxy resin or silicone rubber. Recently, though, low thermal expansion polyimides have become available, and a desired CTE can be obtained by blending of low and high CTE material, or by copolymerization. In Figure 4 the extent of warping in polyimide coated silicon wafers is shown. PIQ (Hitachi Chemical Co., LTD) is a conventional polyimide; PIQ 100 is a modified low thermal expansion polyimide. Figure 5 shows the relation between the thermal expansion coefficient of polyimide films and the radius of curvature of stainless steel foil. A flat shape results when the CTEs (about  $1.8 \times 10^{-5} \text{ K}^{-1}$ ) are close.

Polyimides are also being developed as adhesives for high temperature use with Kapton film. At M&T Chemicals Inc., a siloxane modified flexible thermoplastic polyimide (called M&T 4605-40 adhesive) has been developed which behaves excellently as a high temperature adhesive for Kapton film. Kapton to copper adhesion for flexible circuit applications has been accomplished, and aluminum to aluminum bonding is being evaluated. Epoxy coatings that do not shrink on curing are being prepared at Epolin. These are based on a ring-opening, expansion polymerization technology during which monomers expand in volume on polymerization. Enhanced adhesion can occur also, since expanding resins can penetrate microcracks in substrates, rather than shrink away from substrates on curing, as conventional coating resins do.

Aromatic polyimides are being considered for use on large space structures where the need exists for high temperature ( $200^{\circ} - 300^{\circ}\text{C}$ ) stable, flexible polymeric film and coating materials, that have high optical transparency in the 300 - 600 nm range. Currently available polymers which are transparent/colorless (polyesters, aliphatic polyimides) have limited long-term thermal stability. Thermally stable aromatic polyimides generally have poor transparency in the visible range. A recent research effort was made to synthesize and characterize linear aromatic polyimide film having maximum optical transparency (Ref. 13). Some of the more optically transparent were evaluated for potential use in a space environment. The results are shown in Figures 6 and 7. The UV transmission cut-offs ranged from 310 to 388 nm compared to 450 nm for commercial polyimide film of the same thickness. Following electron irradiation, the films were 2 to 2.5 times more transparent at 500 nm than commercial polyimide film (Kapton). Further, the films are all relatively thermally stable in air at  $300^{\circ}\text{C}$ . In addition, some of these new polymers are soluble in common organic solvents, such as chloroform, and can then be spray-coated for space applications where the substrate cannot endure the traditional  $300^{\circ}\text{C}$  polyimide cure temperature.

Radiation effects, electrons and protons, on four polysulfone films were studied (Ref. 14). These materials are prime candidates for graphite fiber/polymeric matrix composites for use in structural application in large space systems. The preliminary results show that both chain scission and crosslinking occur as a result of irradiation, and that a threshold for major property changes occurs at approximately  $10^9$  rads total dose. In GEO, it is estimated that the interior dose of a 4-ply composite would be about  $10^9$  rads during a 30-year use life. Some of the results are shown in Figure 8, and the conclusion is reached that the polysulfones studied (3 commercial, 1 experimental) seem to be relatively stable to both electron and proton radiation. Recent work on the combined effects of UV and charged particle radiation on aluminized Kapton was reported at the Workshop on Solar Concentrators for Space Solar Dynamic Power Systems (LeRC, June 7, 1988). Samples of direct - manufactured Kapton polyimide film were exposed on the aluminized side to continuum ultraviolet radiation and monoenergetic electrons and protons nearly continuously for 1363 hours. Irradiation rates were set to provide exposure at real-time intensities, and the exposure was in "ultra-high" ( $10^{-8}$  torr) vacuum. In past tests, polyimides exposed at rates greater than one sun have shown questionable stability. These tests show that the tensile, dimensional, and reflective properties of these Kapton samples were much more stable and a conclusion was reached that a threshold for damage was found to be above one sun. Therefore, these Kapton polyimide films may be usable in long-term space applications where they are deployed in tension and unsupported or without thermal contact. Some of the results of the tests are shown in Table 13 and Figure 9.

Some thermal cycling durability tests of coated Kapton were also recently reported (private communication, Electro-Physics Branch). The results are shown in Figure 10. HMDS/TFE 8/5 and 8% PTFE-92% SiO<sub>2</sub> coated Kapton were thermal cycled from +80 to -80C for 10,000 cycles (each cycle lasted approximately one minute). Following thermal cycling, these samples and similarly coated but not thermal cycled samples were fully dehydrated under vacuum and ashed for 66.58 hours. Thermal cycling appears to have little or no effect on the atomic oxygen durability of the plasma polymerized coatings evaluated.

An example of ground-based simulation facilities to provide meaningful data was given at Space Environmental Effects on Materials Workshop (SEEM), June 1988. This was testing the effects of

thermal cycling on composite materials for space structures. Some of the results are shown in Figures 11, 12, and 13. Testing to date showed little difference in the crack density.

### Closing Remarks

The means of obtaining a reliable data base for materials for long-term application in space can be summarized by the key issues described in the NASA Workshop on AO effects, November 1986:

- “1) The ability to develop a reliable prediction model to assess the effects of long-term exposure of materials to the LEO environment,
- 2) The ability of ground-based simulation facilities to provide meaningful data in the development of LEO durable materials; and
- 3) Aeronometric determination of the compositional details of the low earth orbital environment.”

Thus, despite the amount of information available regarding the reactivity of spacecraft materials to atomic oxygen, it was recognized that the existing data base was limited in its application, and not adequate for long-lived (30-year) missions. Therefore, ground-based simulation must be accomplished. For atomic oxygen, simulation facilities are being developed that will accurately simulate the LEO environment. The goal is a beam of neutral atomic oxygen at an energy level of 5eV, with a flux in the range of  $10^{16}$  -  $10^{17}$  atoms/cm<sup>2</sup>-sec. An exposure of 50 hours would give the needed fluence of  $10^{22}$  -  $10^{23}$  atoms/cm<sup>2</sup>. With simulations characteristic of the natural environment, basic interaction mechanisms can be studied. With a reliable materials interaction data base and an understanding of the surface chemistry which gives rise to the interactions, development of new materials or coatings that do not degrade in the LEO environment can be accomplished. This approach must of course be taken with regard to other environmental factors.

One of the outputs of the SEEM Workshop was an evaluation of the current status of various environmental effects, and the needs and recommendations for future work. In this report, only the material related to solar (UV) radiation will be addressed. The current status includes the recognition that most materials degrade as result of solar radiation. It is also recognized that the information

available on UV effects on materials is almost entirely short-term, and thus provides a limited data base. Flight data on coating degradation is confused by contamination. In ground testing, there is little correlation between testing laboratories in regard to UV exposure conditions, calibration techniques, and detectors. Further, there are few facilities with EUV exposure capability. Lastly, there is limited data on thermal cycling effects from laboratories and from space.

Needed information would include material behavior for a 30-year lifetime under UV + AO + thermal cycling, and for 5 to 15-year lifetime (SDI missions) UV + high energy radiation and UV + AO + thermal cycling. To obtain the information, UV testing methodology with standardized test procedures for accelerated UV testing has to be developed. This would be complemented by a data base of flight data from long-term missions. Also needed would be a flight data base on UV flux/distribution. Finally, long-term thermal cycling data is needed. The composites on board the LDEF could provide 5-year flight data, for example.

## REFERENCES

1. **Space Materials Handbook (3rd Edition). NASA SP-3051. John B. Rittenhouse and John B. Singletary, 1969.**
2. **Engineered Materials Handbook, Vol. 1 Composites ASM International, 1987.**
3. **Materials Selection List for Space Hardware Systems MSFC-HDBK-527 REVE - JSC 09604 REVE, November 15, 1986, NASA George C. Marshall Space Flight Center.**
4. **"Evaluation of Materials for High Performance Solar Arrays (Status Report No. 1)," NASA Technical Paper 1220 - A. F. Whitaker, C. F. Smith, Jr., C. L. Peacock, Jr., and S. A. Little, 1978.**
5. **"Space Environmental Effects on Materials," R. J. Schwinghamer, August 1980 - NASA TM-78306.**
6. **"Properties of Metallized Flexible Materials in the Space Environment," TRW Defense and Space Systems Group, TRW 26177-6048-RU-00, or, SAMSO TR 78-31, January 1978.**
7. **"Effects of a Simulated Synchronous Altitude Environment on Contaminated Optical Solar Reflectors," J. A. Neff, C. R. Mullen, L. B. Fogdall. Journal of Spacecraft and Rockets, Vol. 23, Number 4, July - August, 1986, pg. 386.**
8. **"Material Selection Guidelines to Limit Atomic Oxygen Effects on Spacecraft Surfaces," James T. Visentine, Johnson Space Center. Preliminary draft report.**
9. **Space Environmental Effects on Materials Workshop (SDIO/NASA), NASA Conference Publication 3035, NASA Langley Research Center, June 28 - July 1, 1988.**
10. **"Protection of Solar Array Blankets from Attack by Low Earth Orbital Atomic Oxygen," Bruce A. Banks, Michael J. Mirtich, Sharon K. Rutledge, and Henry K. Nahra. Eighteenth Photovoltaic**

**Specialists Conference - 1985. (IEEE Photovoltaic Specialists Conference.)**

11. **"Influence of Space Environment on Adhesives," B. J. Mulroy, Jr. and Y. D.. Izu, 13th National SAMPE Technical Conference, October 1981, pg. 270.**
12. **"Chemical Structures and Properties of Low Thermal Expansion Polyimides," Shunichi Numata, Koji Fujisaki, Daisuke Makino, and Noriyuki Kinjo. Recent Advances in Polyimide Science and Technology - Proceedings of the Second International Conference on Polyimides: Chemistry, Characterization and Applications. Dr. W. D. Weber, Dr. M. R. Gupta, eds., pg. 164, 1985.**
13. **ibid, pg. 16.**
14. **Ref. 11, pg. 256.**



TABLE 1. MATERIALS IDENTIFICATION (REF. 4)

Name	Code	Supplier	Generic Nomenclature	Functional Category
Kapton H (0.5 mil)	S-1	DuPont	Polyimide	Substrate Strength
Epoxy Fiberglass Longerons	M-1	Astromast	Epoxy/Fiberglass	Mast
Epoxy Fiberglass Battens	M-2	Astromast	Polyimide/Fiberglass	Mast
Polyimide Fiberglass Longerons	M-3	Astromast	Polyimide/Fiberglass	Mast
AR Coated No. 7940 Fused Silica	C-1	SCLI	Magnesium Fluoride/Fused Silica	Cell Cover
Kapton F (0.5 mil)	A-1	DuPont	Polyimide/FEP Teflon	Adhesive Substrate Lamination
Pyralux (0.5 mil Kapton + 0.5 mil Acrylic Adhesive)	A-2	DuPont	Polyimide/Acrylic	Adhesive, Substrate Lamination
Kevlar 49	M-4	DuPont	Aramid Fiber	Panel Skin Containment Box Cover and Bottom
CMC-122-1/2-1/2 (0.5 mil Kapton + 0.5 mil Polyester Adhesive)	A-3	Circuit Materials	Polyimide/Polyester Adhesive	Adhesive, Substrate Lamination
Aluminized Kapton Tape	T-1	Sheldahl	Aluminum/Polyimide	Thermal Control
Aluminized Kapton (0.5 mil Kapton)	T-2a	Hastings	Aluminum/Polyimide	Thermal Control
Aluminized Kapton (1 mil)	T-2b	Hastings	Aluminum/Polyimide	Thermal Control
M380-3 Fluoroglas Fabric	S-2	Dodge Industries	PTFE Teflon/Fiberglass	(Panel Hinge) Hinge Loop, Substrate Edge Reinforcement

TABLE 1. (Concluded)

Name	Code	Supplier	Generic Nomenclature	Functional Category
M365-5 Fluoroglas Fabric	S-3	Dode Industries	PTFE Teflon / Fiberglass	Hinge Loop, Substrate Edge Reinforcement
PTFE Coated Teflon E-12 Fiberglass Thread	P-1	Owen- Corning	Fiberglass / PTFE Teflon	On Array Padding
Fairprene SS-5550	P-2	DuPont	Silicone Rubber	Substrate Padding
White Paint S13GLO	T-3	ITRI	Silicone Paint / Low Outgassing	Thermal Control
Aluminized Teflon - Acrylic PSA	T-4	Sheldahl	Aluminum / Teflon Acrylic	Thermal Control
Graphite Epoxy HMF 330C 34	M-3	Fiberite Corporation	High Modulus Graphite / 934 Epoxy	Panel Skin Containment Box Cover and Bottom
Scotchcast Epoxy 250	P-3	3M	Epoxy	On Array Padding
Kapton - Silicone PSA	A-4	Sheldahl	Polyimide / Silicone	Adhesive System
Silvered (3 mil) Mylar	T-5	Sheldahl	Silver / Poly- ester	Thermal Control
Aluminum - (1 mil) Mylar	T-6	Sheldahl	Aluminum / Polyester	Thermal Control
Aluminum - (2 mil) Mylar - (2 mil) Teflon Coating	T-7	Sheldahl	Aluminum / Polyester Teflon	Thermal Control
Silvered (1 mil) Polyester with 4 mil Acrylic Coating	T-8	Sheldahl	Silver / Polyester / Acrylic	Thermal Control

TABLE 2. PERCENTAGE CHANGE IN MECHANICAL PROPERTIES OF PROTON IRRADIATED MATERIALS  
(DATA GENERATED USING 2 $\sigma$  STATISTICS) (REF. 4)

Mechanical Property Material	Breaking Strength				Elongation				Maximum Fiber Stress			
	10 <sup>13</sup>	10 <sup>14</sup>	10 <sup>15</sup>	10 <sup>16</sup>	10 <sup>13</sup>	10 <sup>14</sup>	10 <sup>15</sup>	10 <sup>16</sup>	10 <sup>13</sup>	10 <sup>14</sup>	10 <sup>15</sup>	10 <sup>16</sup>
S-1	-	-	-	-	-	-	-	-	NA	-	-	-
M-1	NA	-	-	↑	NA	-	-	↑	NC	-	+2	+2
M-2	NA	-	-	↑	NA	-	-	↑	NC	-	NC	+11
M-3	NA	-	-	↑	NA	-	-	↑	-	-	NC	NC
A-2	NC	NC	NC	-	-5	+15	+11	-	NA	-	-	↑
P-2	-42	-54	-69	-	-36	-50	-65	-	NA	-	-	↑
M-5	-	-	-	-	-	-	-	-	-	-	-	NC
P-3	-	-	NC	-1	-	-	-30	-77	NA	-	-	↑
A-4	-	NC	-19	•	-	NC	-54	•	NA	-	-	↑
T-6	•	-	↑	-	•	-	↑	-	NA	-	-	↑

NA = Data not applicable to sample.

NC = No significant change, within 2 $\sigma$  statistics.

- = Data not available for this report.

• = Vacuum produced severe warpage and degradation.

**TABLE 3. PERCENTAGE CHANGE IN MECHANICAL PROPERTIES OF UV IRRADIATED MATERIALS  
(DATA GENERATED USING 2 $\sigma$  STATISTICS) (REF. 4)**

Mechanical Property Material	Breaking Strength		Elongation		Maximum Fiber Stress	
	500 ESH at 1 sun	1500 ESH at 3 suns	500 ESH at 1 sun	1500 ESH at 3 suns	500 ESH at 1 sun	1500 ESH at 3 suns
S-1	-	-15	-	-32	NA	↑
S-2	-1	NC	NC	NC	NA	↑
S-3	NC	-10	+21	+4	NA	↑
M-1	-	-	NA	↑	NC	+2
M-2	-	-	NA	↑	NC	+16
M-4	NC	-	-86	-	NA	↑
A-1	NC	-	NC	-	NA	↑
A-2	NC	-8	NC	-21	NA	↑
A-3	-	+1	-	+33	NA	↑
P-2	-	-54	-	-85	NA	↑
P-3*	-	+54	-	-93	NA	↑

NA = Data not applicable to sample.

NC = No significant change, data within 2 $\sigma$  limits.

- = Data not available.

\* = Data obtained after only 4 h/12 ESH exposure due to excessive outgassing.

TABLE 4. PERCENTAGE CHANGE IN OPTICAL PROPERTIES OF UV IRRADIATED MATERIALS  
(DATA GENERATED USING 2 $\sigma$  STATISTICS) (Ref. 4)

Optical Property Material	Absorptivity		Emissivity		Spectral Reflectance	
	500 ESH at 1 sun	1500 ESH at 3 suns	500 ESH at 1 sun	1500 ESH at 3 suns	500 ESH at 1 sun	1500 ESH at 3 suns
T-2a	NC	NC	NC	NC	-	-
T-4	-	NC	-	NC	-	-
T-3 <sup>a</sup>	NC, NC	-	NC, NC	-	-3, -7 percent	-
T-8 <sup>b</sup>	NA					

a. Data generated for 1000 ESH and 3000 ESH at 1 sun

b. Severe degradation during weight loss test.

NA = Data not applicable to sample.

NC = No significant change, data within 2 $\sigma$  limits.

- = Data not available.

**TABLE 5. REACTION EFFICIENCIES OF SELECTED MATERIALS WITH ATOMIC OXYGEN IN LOW EARTH ORBIT (REF. 8)**

<u>MATERIAL</u>	<u>REACTION EFFICIENCY CM<sup>3</sup>/ATOM</u>
KAPTON	$3 \times 10^{-24}$
MYLAR	3.4
TEDLAR	3.2
POLYETHYLENE	3.7
POLYSULFONE	2.4
GRAPHITE/EPOXY	
1034C	2.1
5208/T300	2.6
EPOXY	1.7
POLYSTYRENE	1.7
POLYBENZIMIDAZOLE	1.5
25% POLYSILOXANE/45% POLYIMIDE	0.3
POLYESTER 7% POLYSILANE/93% POLYIMIDE	0.6
POLYESTER	HEAVILY ATTACKED
POLYESTER WITH ANTIOXIDANT	HEAVILY ATTACKED
SILICONES	
RTV-560	0.2*
DC6-2204	0.2*
T-650	0.2*
DC1-2577	0.2*
BLACK PAINT Z306	0.3-0.4*
WHITE PAINT A276	0.3-0.4*
BLACK PAINT Z302	2.03*
PERFLUORONATED POLYMERS	
TFE	<0.05
FEP	<0.05
CARBON (VARIOUS FORMS)	0.9-1.7
SILVER (VARIOUS FORMS)	HEAVILY ATTACKED
OSMIUM	0.026

UNITS OF MG/CM<sup>2</sup> FOR STS-8 MISSION. LOSS IS ASSUMED TO OCCUR IN EARLY PART OF EXPOSURE; THEREFORE, NO ASSESSMENT OF EFFICIENCY CAN BE MADE.

TABLE 6. Some Effects Observed on Thin Films Exposed to  $3.5 \times 10^{20}$  Oxygen Atoms  $\text{cm}^{-2}$  in Low Earth Orbits (Ref. 8)

Sample	Optical Transmission Results				Step measurements of films with 2 $\mu\text{m}$ diameter slits (nm)				Optical heterodyne measurements						
	Optical density		Metal thickness (nm) from optical absorption		Film thickness		Surface roughness		rms surface roughness (nm)		Estimated thickness changes (nm)		Metal	Metal + oxide	
	Unexposed	Exposed	Unexposed	Exposed	Unexposed	Exposed	Unexposed	Exposed	Unexposed	Exposed	Metal	Metal + oxide			
Incon film	1.78	1.66	32.3	29.4	32.2	29.7	0.5	0.5	1.66	1.61	-2.9	-2.5			
Au/Al film	1.29	1.29	—	—	35.5/39.5	35.5/39.5	1	1	—	—	None	None			
Al film	0.28	0.21	3.4	2.6	15.0	16.5	0.5	0.5	2.06	1.77	-0.8	+1.5			
Ni film	1.79	1.76	54.2	53.3	Unable to remove Ni except at pinholes which gave ~81 nm in both regions.	~17.0	~17.0	0.5	1	1.79	1.76	-0.9	—		
W film	0.35	0.31	4.8	4.1	~17.0	~17.0	0.5	1	2.17	2.62	-0.7	—			
Au/Ag film	2.51	2.55	—	—	100	100	0.5	0.5	2.13	1.98	Unable to separate any film thickness; apparently slight darkening.	-1.3			
Ni film	0.60	0.54	16.8	15.1	Unable to remove Ni films except at one pinhole (5.5 nm) in exposed area of the Au film	—	—	—	—	3.75	3.68	-0.8	—		
Ni film	1.02	1.66	47.3	46.5	—	—	—	—	3.85	3.34	—	—			
10 nm Pt/Au	2.55	2.52	~73.2	~72.3	10/6.1	~73 Pt + 6Au	0.5	0.5	—	—	-0.9	Undetected			
6 nm Pt/Au	—	—	—	—	1/10	~21 Pt + 6Au	0.5	2.5	—	—	—	-1.2			

\* Results were corrected for both contamination and temperature as described in the text; results shown are for ambient temperature believed to be between 273 and 300 K.

† Films were deposited on fused silica flats described in text unless noted otherwise.

‡ See text for details. 6 nm Pt/Au was poorly protected, we were unable to make measurements of the 6 nm Pt/Au because the back of the substrate was rough ground.

**Table 7. A & B**  
**MSFC STS 41-G Results (Ref. 8)**

The Materials were exposed to the RAM direction  
to obtain a total atomic oxygen fluence of  
 $2.45 \times 10^{10}$  atoms/cm<sup>2</sup>



**TABLE 7.A**  
**STS - 41G PROPERTY DATA ON OVERCOATED PAINTS**

<u>Evaluations</u>	<u>2302 Glossy Black with CI 651 Overcoat</u>	<u>2302 Glossy Black with RTV-602 Overcoat</u>	<u>2302 Glossy Black with MN-1-1104-0 Overcoat</u>	<u>2853 Glossy Yellow with MN-1-1104-0 Overcoat</u>
Exposed Flight Specimens Optical Property, Absorptivity (a)	.972	.969	.970	.469
Nominal Control Values of Absorptivity (a)	.972	.973	.972	.458
Mass Loss of Flight Specimen due to Atomic Oxygen Exposure	None	Negligible	Negligible	Negligible
Comments on Exposure Effects	Maintains specu- lar character of 2302	Loss of 2302 specular character	Loss of 2302 specular character	Loss of 2853 specular character, slight increase partially due to UV darkening

**NOTE:** The effect of applying an overcoat to these paints is to increase the initial absorptivity by 1 to 22.

## TABLE 7.B

### STS - 41G RESULTS ON PROTECTIVE OVERCOATS FOR SILVER

<u>Overcoat Material/ Nominal Thickness</u>	<u>Preparation Technique</u>	<u>Comments on Protection Effectiveness</u>
Aluminum 500 Å	Vapor deposition	Aluminum generally protective, but spots and streaks indicate some silver oxidation. Film thickness considered insufficient for good protection.
Gold 500 Å	Vapor deposition	No evidence of silver oxidation (scaling) and very few surface imperfections. Film thickness insufficient based on discoloration for long term protection.
Gold 5000 Å	Vapor deposition	Significant amount of spots and scaling which tend to indicate contamination of the interconnect before and during plating yielding a porous, non-uniform coating. Analyses complicated by contamination effects.
Gold 2500 Å	Electroplated	Significant scaling on surface.
Gold 5000 Å	Electroplated	Generally provided good protection. Film thickness insufficient based on discoloration for long term exposure.
Palladium 500 Å	Vapor deposition	Poor protection, extensive discoloration and spots. Oxygen in palladium.
Palladium 5000 Å	Vapor deposition	Slightly better protection than 500 Å. Oxygen in palladium. Poor adhesion.
DC-1104 ~ (0.5 mil)	Brushed	No silver oxidation. Good adhesion. Thick coating.
DC-1200 Primer ~ (0.1 to 0.5 mil)	Brushed	Inadequate protection.

TABLE 8. EFFECTS OF ATOMIC OXYGEN ON MATERIALS

MATERIAL	REACTION EFFICIENCY		SWEEPING VELOCITY VECTOR (STS-364)	DIRTCT VELOCITY VECTOR (STS-8)	AVG. (10 <sup>-24</sup> CM <sup>3</sup> /ATOM)	RANGE OF REACTION EFFICIENCY	NO. OF SAMPLES (YST.)	OPTICAL PROPERTY CHANGES			COMMENTS	DATA SOURCE	
	ΔR <sub>1</sub>	ΔC						ΔR <sub>2</sub>					
TEFLON	<0.2	<0.03	<0.1	<0.1	<0.1	0-<0.2	>22					JSC	
75% POLYSILOXANE													
POLYIMIDE	0.3	0.3	0.3	0.3	0.3								LARC
TEFLON, WHITE	0.4	0.6	0.5	0.5	0.5	0.4-0.6	>11						JSC/MSFC
7% POLYSILOXANE													
POLYIMIDE	0.6	0.6	0.6	0.6	0.6								LARC
CARBON	1.2	1.2	1.2	1.2	1.2	0.9-1.7	≥ 4						LARC/MSFC/UA
POLYBENZIMIDAZOLE													
(PBI)	1.5	1.5	1.5	1.5	1.5								LARC
PPOXY	1.7	1.7	1.7	1.7	1.7								JPL
POLYSTYRENE	1.7	1.7	1.7	1.7	1.7								JPL
KAPTON, BLACK	1.4	2.2	1.8	1.8	1.8	1.4-2.2	>13			-5.1			JSC/MSFC
TEFLON, CLEAR	1.3	3.2	2.3	2.3	2.3	1.3-3.2	16						JBC
POLYSULFONE	2.4	2.4	2.4	2.4	2.4								JPL
KAPTON	2.5	3.0	2.6	2.6	2.6	2.2-3.1	>81			-2.4			JSC
MYLAR	2.3	3.9	2.8	2.8	2.8	1.8-4.5	>46						JSC
PMDA	3.1	3.1	3.1	3.1	3.1								JPL
POLYIMIDE	3.3	3.3	3.3	3.3	3.3	2.3-4.7	10						LARC
POLYETHYLENE	3.7	3.7	3.7	3.7	3.7	3.3-4.1	≥ 2						JSC/JPL

Reaction Efficiencies Not Determined

- POLYESTER . Heavily Attached
- POLYESTER WITH ANTIOXIDANT Heavily Attached
- MYLAR WITH ANTIOXIDANT Heavily Attached

\* For most materials without an estimate of the number of samples tested, the efficiency OR mass loss data is based on only one (1) sample.

ORGANIZATION: EH11	MARSHALL SPACE FLIGHT CENTER ATOMIC OXYGEN EFFECTS APPLICATIONS TO SPACECRAFT	NAME: ANN F. WHITAKER
CHART NO.:		DATE: JUNE 1988

**TABLE 9. MATERIALS APPLICATIONS IN SPACE ENVIRONMENT**

**SILICONES/FLUOROSILICONES:**

**ADVANTAGES**

FORM TOUGH, FLEXIBLE COATINGS

CURED CONTROLLED VOLATILITY VERSIONS EXHIBIT LOW OUTGASSING

FLEXIBLE AT LOW TEMPERATURES (DIMETHYLSILICONE: T<sub>g</sub> ~ -60°C)

SILICONES AVAILABLE IN MANY COMMERCIAL FORMULATIONS

EASILY APPLIED (SPRAY, DIP, BRUSH)

SPACE USE/QUALIFICATION DATABASE AVAILABLE

RELATIVELY CHEMICALLY INERT

**DISADVANTAGES**

STRIPPED, SPACE GRADE CONTROLLED VOLATILITY FLUOROSILICONES WILL BE SIGNIFICANTLY MORE EXPENSIVE THAN SILICONES

FLUOROSILICONES MAY BE DIFFICULT TO BOND

LONG TERM SOLAR UV EFFECTS ARE UNKNOWN

LONG TERM CONVERSION OF SILICONE TO SILICA UNDER ATOMIC OXYGEN EXPOSURE, CAUSING LOSS OF FLEXIBILITY

FLUOROSILICONES LESS DEVELOPED THAN SILICONES

ORGANIZATION:  EH11	MARSHALL SPACE FLIGHT CENTER ATOMIC OXYGEN EFFECTS APPLICATIONS TO SPACECRAFT	NAME: ANN F. WHITAKER
CHART NO.:		DATE: JUNE 1988

**TABLE 9. (cont'd) MATERIALS APPLICATIONS IN SPACE ENVIRONMENT**

**FLUOROCARBONS:**

**ADVANTAGES**

COMMERCIALY AVAILABLE:

- AS COATING ON KAPTON
- AS FREE STANDING FILM

SPACE USE/QUALIFICATION DATABASE AVAILABLE

RELATIVELY CHEMICALLY INERT

FORMS FLEXIBLE COATINGS

LOW OUTGASSING

**METALS:**

**ADVANTAGES**

THIN ( $\leq$  0.1 MIL) COATINGS READILY FORMED

LARGE AREA SUBSTRATES CAN BE COATED BY CONTINUOUS ROLL-TO-ROLL COMMERCIAL PROCESSES

LOW OUTGASSING

SPACE USE/QUALIFICATION DATABASE AVAILABLE

INERT TO ELECTROMAGNETIC RADIATION IN SOLAR UV REGION

MANY RELATIVELY INERT/SELF PASSIVATING

**DISADVANTAGES**

EMBRITTLED BY SOLAR UV/AO COMBINATION  
DIFFICULT TO BOND

**DISADVANTAGES**

LIMITED FLEXIBILITY  
DIFFICULT TO PRODUCE DEFECT-FREE COATINGS  
OPAQUE-REQUIRES COATING FOR ACCEPTABLE

ORGANIZATION: EH11	MARSHALL SPACE FLIGHT CENTER ATOMIC OXYGEN EFFECTS APPLICATIONS TO SPACECRAFT	NAME: ANN F. WHITAKER
CHART NO.:		DATE: JUNE 1988

**TABLE 10. BEST CANDIDATE MATERIALS AS OF MAY 1988**

MATERIALS	SILICONES	COMMENTS
PLASMA DEPOSITED	HMDS HMDS/TFE	RESTRICTED AVAIL; THICKER FILMS LESS FLEXIBLE
CV1-1144-0		AO RESISTANT, TACK-FREE, LOW OUTGASSING
S13G-L0		AO RESISTANT, LOW OUTGASSING, FLEXIBLE, ROLL-TO-ROLL PROCESS
		WIDE RANGE- APPLICATION, LOW OUTGASSING, TACK FREE
FLUOROSILICONES		ENVIR. AGING
CV-3530		AO RESISTANT, LOW OUTGASSING, FLEXIBLE, ROLL-TO-ROLL PROCESS
FLUOROCARBONS		SOME MICRO- CRACKING
TFE		AO RESISTANT, LOW OUTGASSING, LOW TACK FREE
FEP		BONDING CONCERNS, DEGRADATION-COMB. ENVIRONMENTS EXPOSURE
HYBRID		
S10/A1		AO RESISTANT, TAILORED OPTICAL PROPERTIES, TACK FREE, LOW OUTGASSING
		LIMITED FLEX.

## TABLE 11. SOLAR DYNAMIC CONCENTRATOR MATERIALS

### Candidate Substrate Materials:

Graphite/epoxy  
Titanium honeycomb sandwich  
Aluminum honeycomb sandwich  
Aluminum honeycomb  
Aluminum foam  
Vitreous carbon foam  
Stainless steel with Sol-Gel  
Boron carbide  
Boron carbide foam  
Kevlar  
Ultra-low expansion glass  
Silicon carbide foam  
Zerodur  
Silicon dioxide  
Beryllium

### Candidate Optical Coatings:

Aluminum  
Silver  
Platinum  
Beryllium

### Candidate Protective Coatings:

Silicon dioxide  
Aluminum oxide  
Silicon nitride  
Aluminum nitride  
Magnesium oxide  
Magnesium fluoride  
Beryllium oxide  
Beryllium nitride

**TABLE 12. SDP CONCENTRATOR MATERIALS OPTICAL PERFORMANCE AND ATOMIC OXYGEN DURABILITY**

A.	SUBSTRATE	INITIAL SOLAR SPEC. REFLECTANCE	FINAL SOLAR SPEC. REFLECTANCE	HOURS ASHED	EQUIVALENT KAPTON A/O FLUENCE ATOMS/CM <sup>2</sup> SEC
1.	Reflective Coating				
a.	Protective Coating (thickness, Å)				
A.	ALUMINUM				
1.	Platinum	0.698	0.691	39.3	4.6 x 1020
a.	None				
2.	Rhodium	0.656	0.631	54.3	6.4 x 1020
a.	None				
3.	Silver				
a.	Al <sub>2</sub> O <sub>3</sub> (350 Å)	0.850	0.823	62.0	7.3 x 1020
b.	MgF <sub>2</sub> (920 Å)	0.892	0.879	88.5	1.0 x 1021
c.	SiO <sub>2</sub> (400 Å)	0.886	0.762	62.0	7.3 x 1020
d.	Si <sub>3</sub> N <sub>4</sub> (820 Å)	0.907	0.518	48.5	5.7 x 1020
e.	Si <sub>3</sub> N <sub>4</sub> (2,000 Å)	0.789	0.725	400.5	4.7 x 1021
f.	Si <sub>3</sub> N <sub>4</sub> (2,500 Å)	0.545	0.482	271.5	3.2 x 1021
B.	BERYLLIUM				
1.	Platinum	0.697	0.685	39.3	4.6 x 1020
a.	None				
2.	Rhodium	0.634	0.418	54.3	6.4 x 1020
a.	None				
3.	Silver				
a.	Al <sub>2</sub> O <sub>3</sub> (350 Å)	0.866	0.779	62.0	7.3 x 1020
b.	SiO <sub>2</sub> (400 Å)	0.914	0.859	62.0	7.3 x 1020
c.	Si <sub>3</sub> N <sub>4</sub> (820 Å)	0.914	0.634	48.5	5.7 x 1020
C.	BERYLLIUM/COPPER				
1.	Silver	0.886	0.854	400.5	4.7 x 1021
a.	Si <sub>3</sub> N <sub>4</sub> (2,000 Å)				



**TABLE 13. TENSILE PROPERTIES**

KAPTON SAMPLE	BREAKING STRENGTH	ELONGATION AT BREAKING
<u>Unirradiated</u>		
1	0.70 lb. $2.4 \times 10^4$ psi	15%
2	0.68 2.3	16
3	0.64 2.2	12.5**
4	0.66 2.3	13
5	0.64 2.2	12
<u>Irradiated*</u>		
1	0.60 lb $2.1 \times 10^4$ psi	5.7%
2	0.45 1.6	2.2
3	0.60 2.1	5.0

\*After 1363 equivalent solar UV hours,  $1.5 \times 10^{16}$  electrons/cm<sup>2</sup> (50-keV), and  $1.5 \times 10^{16}$  protons/cm<sup>2</sup> (50-keV), as described in detail on page 5.

\*\*The third digit is not "significant". It is shown since it is the value read out by the equipment operator, and to indicate a trend.

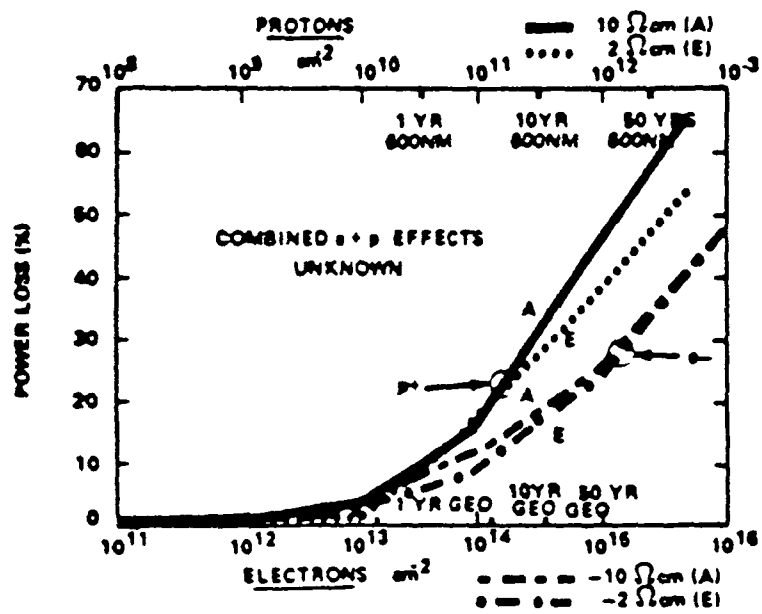


Figure 1. Electron and proton degradation of silicon solar cells. (Ref. 5)

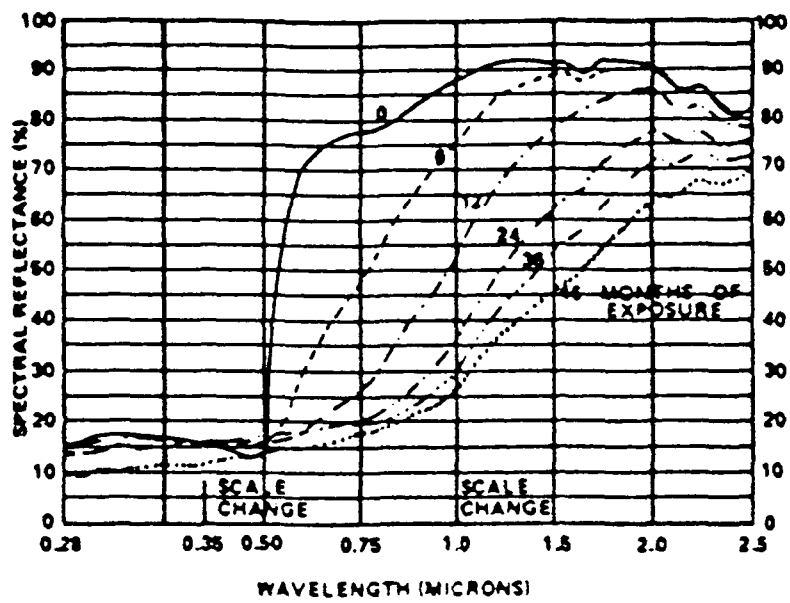


Figure 2. Directional spectral reflectance of 2-mil second surface aluminized kapton. (Ref. 5)

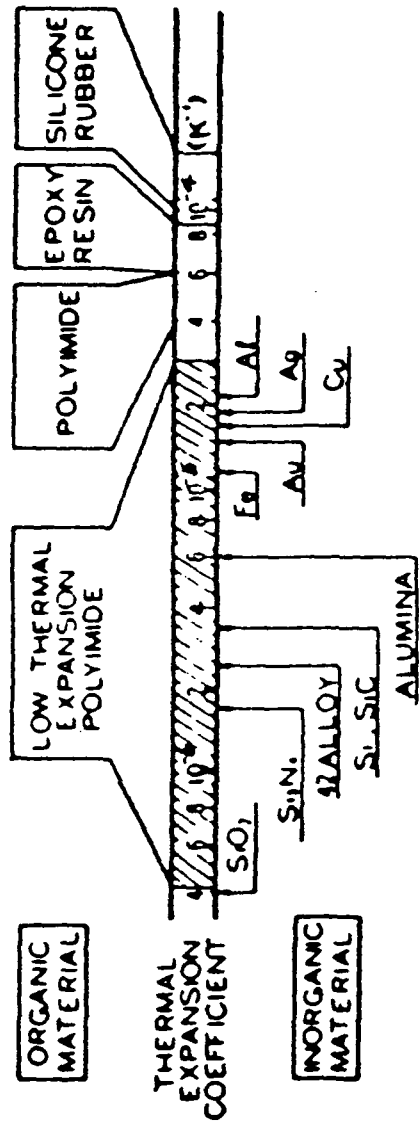


Figure 3. Thermal expansion coefficients of various materials. (Ref. 12)

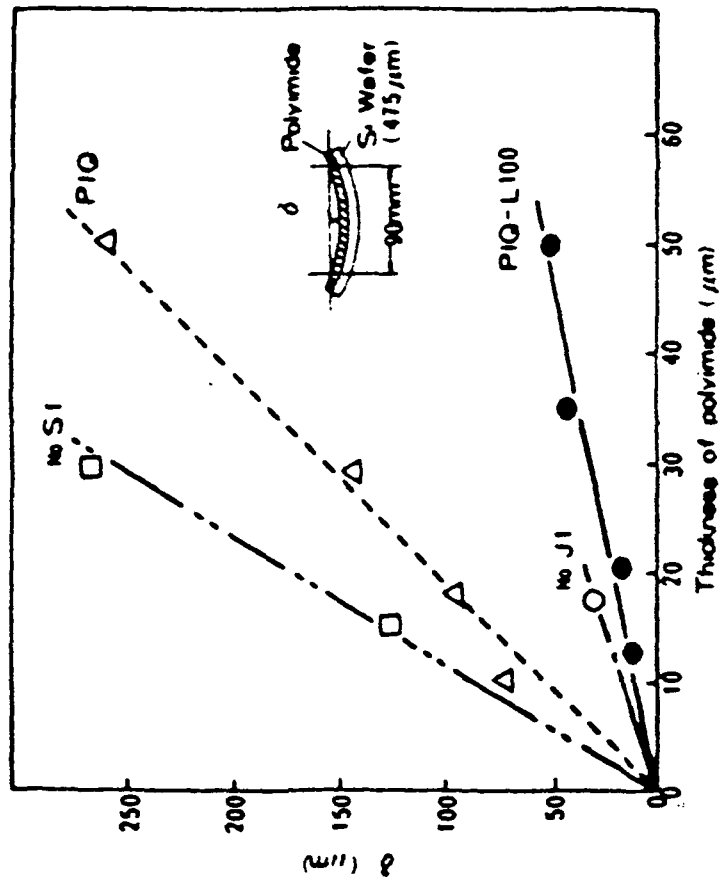


Figure 4. Extent of warping in polyimide coated silicon wafer. (Ref. 12)

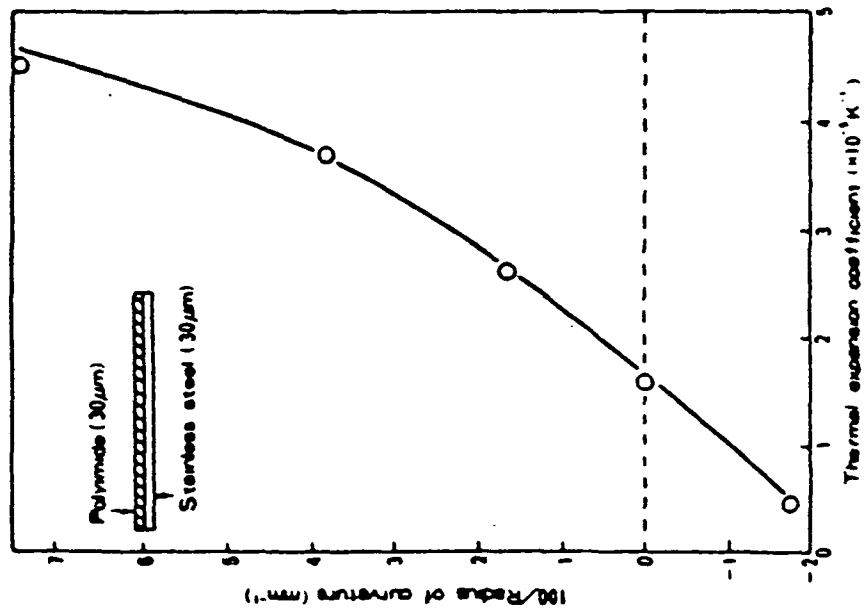


Figure 5. Relation between thermal expansion coefficient of polyimide film and radius of curvature of stainless steel foil. (Ref. 12)

ORIGINAL PAGE IS  
OF POOR QUALITY

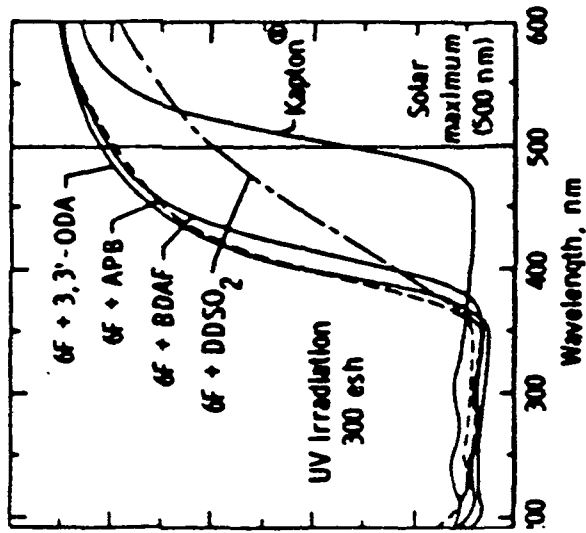
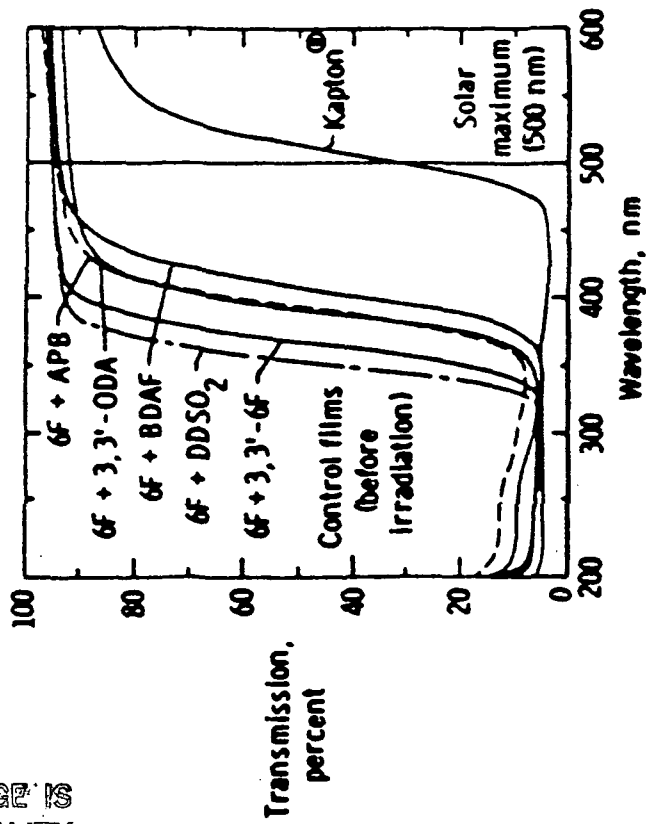


Figure 6a. UV-visible spectra of 0.5 ml 6F-containing polyimide films before irradiation. (Ref. 13)  
films before irradiation. (Ref. 13)  
b. UV-visible spectra of UV-irradiated 6F-containing polyimide

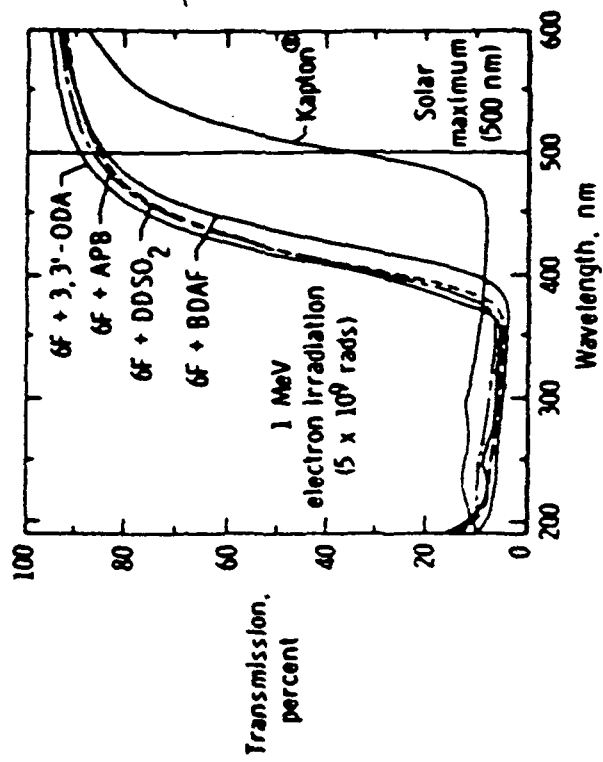
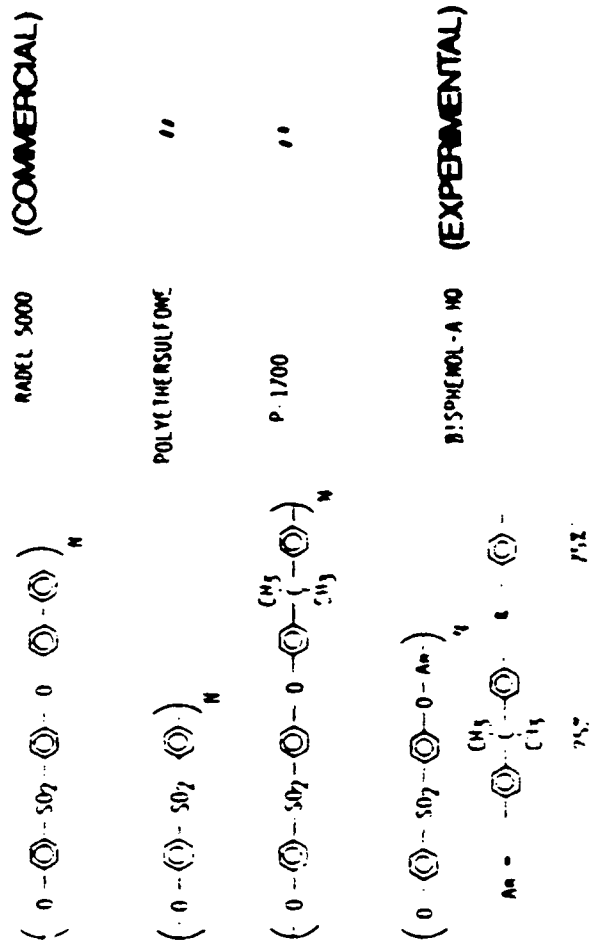


Figure 7. UV-visible spectra of e-irradiated 6F-containing polyimide films (Ref. 13)



Figure 8. Radiation effects on four polysulfone films. (Ref. 14)

(10<sup>20</sup> - 10<sup>10</sup> rads @ 2(10)<sup>16</sup> rad/hr) (1 Mev protons or electrons)



A. The Chemical Structures of Four Polysulfones.

Figure 8. (cont.)

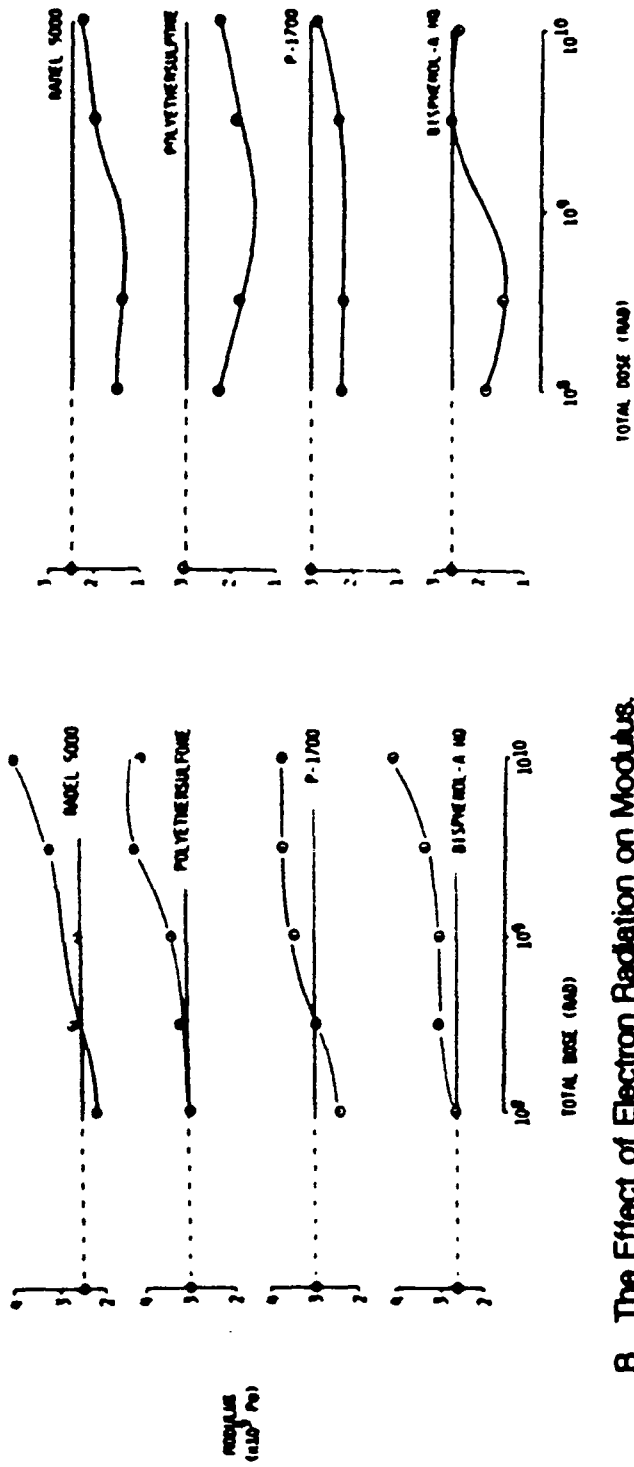


FIGURE 9. REFLECTANCE OF 0.1-MIL ALUMINIZED KAPTON BEFORE AND AFTER UV, PROTON, AND ELECTRON IRRADIATION FOR 1363 HOURS

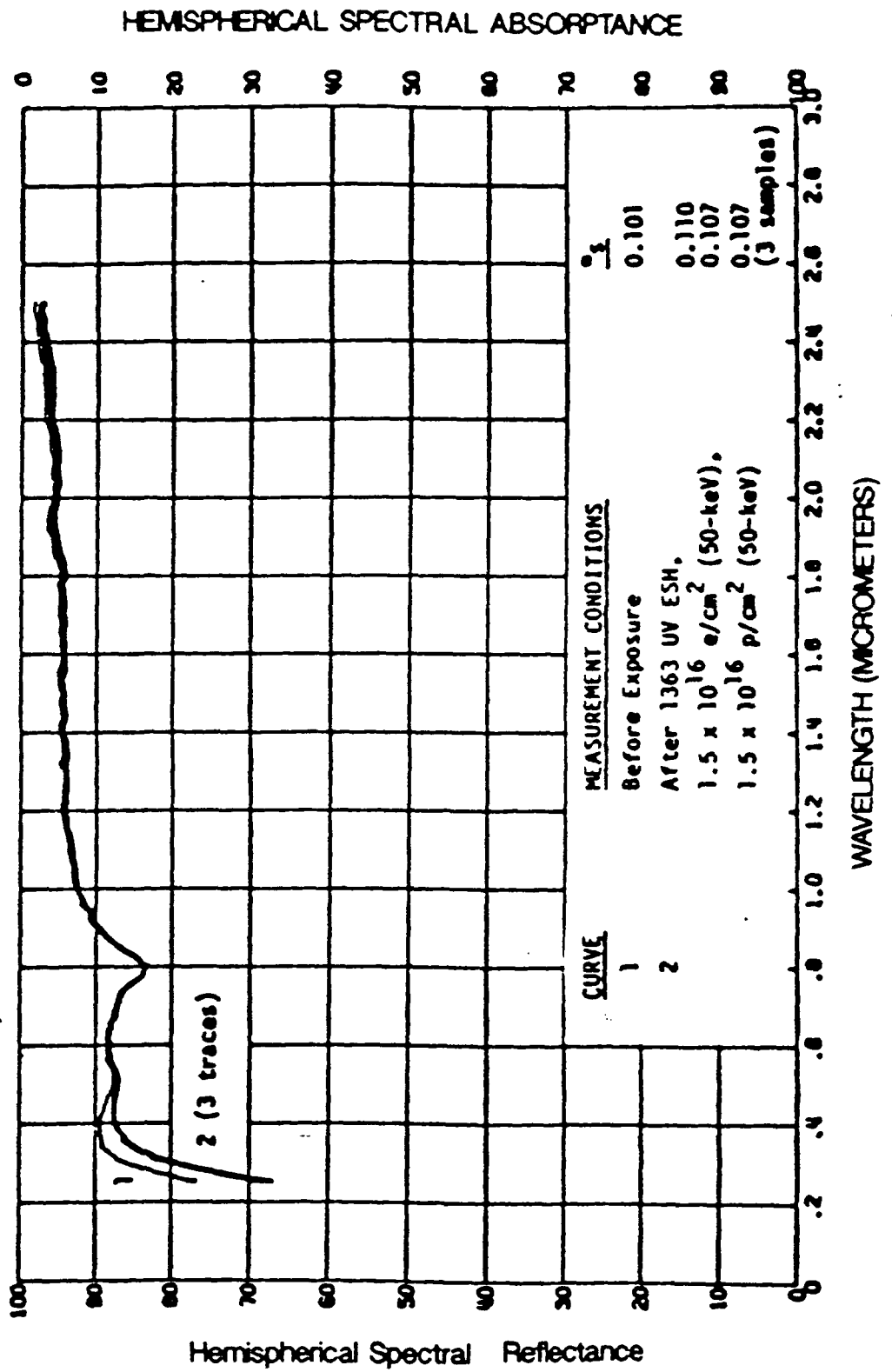
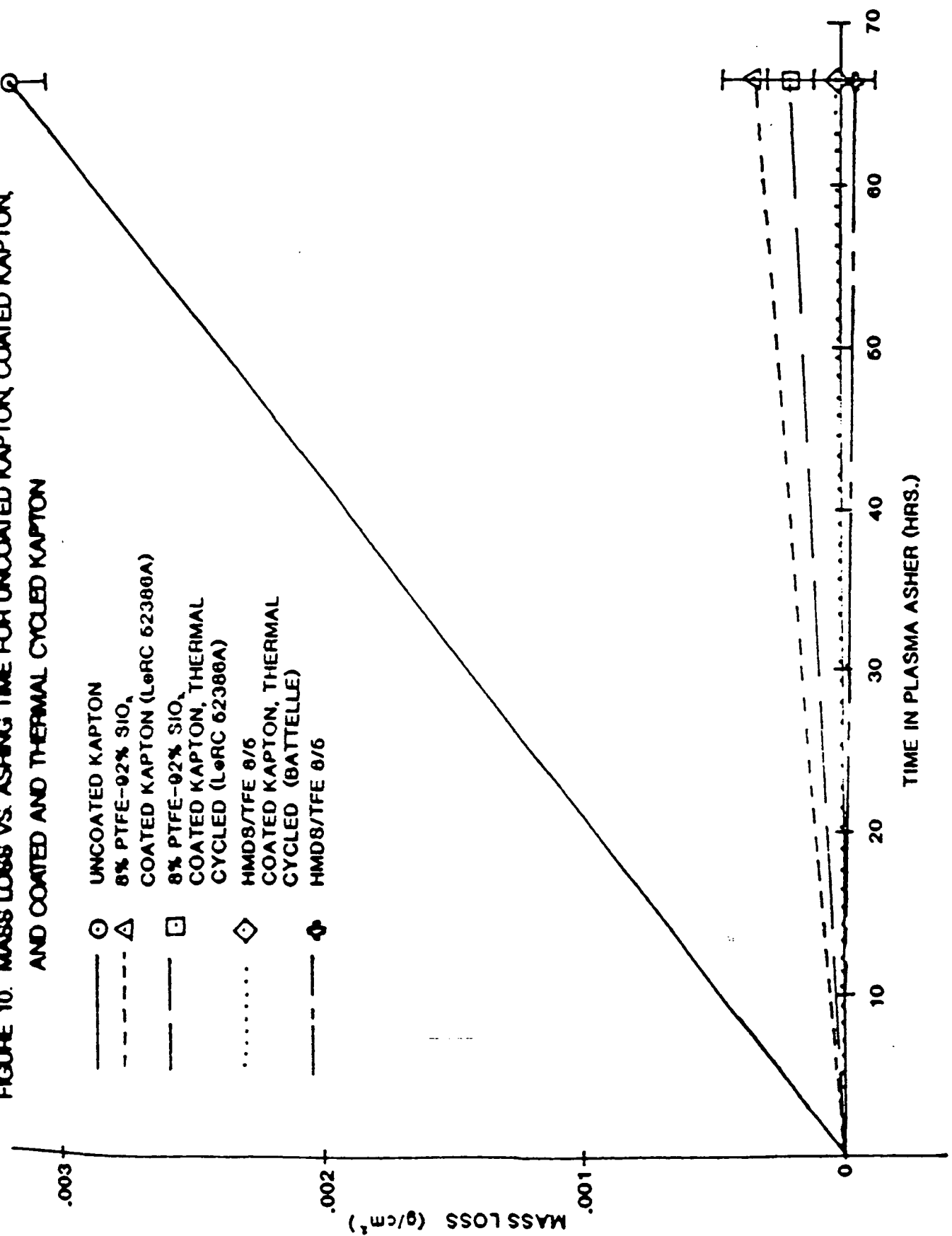


FIGURE 10. MASS LOSS VS. ASHING TIME FOR UNCOATED KAPTON, COATED KAPTON, AND COATED AND THERMAL CYCLED KAPTON



# FIGURE 11. MISSION LIFE VS. THERMAL CYCLES

Mission life	No. of 90-min cycles
1 yr.	5840
5 yrs.	29200
10 yrs.	58400
20 yrs.	116800
30 yrs.	175200

**FIGURE 12. COMPARISON OF ACCELERATED AND REAL TIME THERMAL CYCLE IN SPACE**

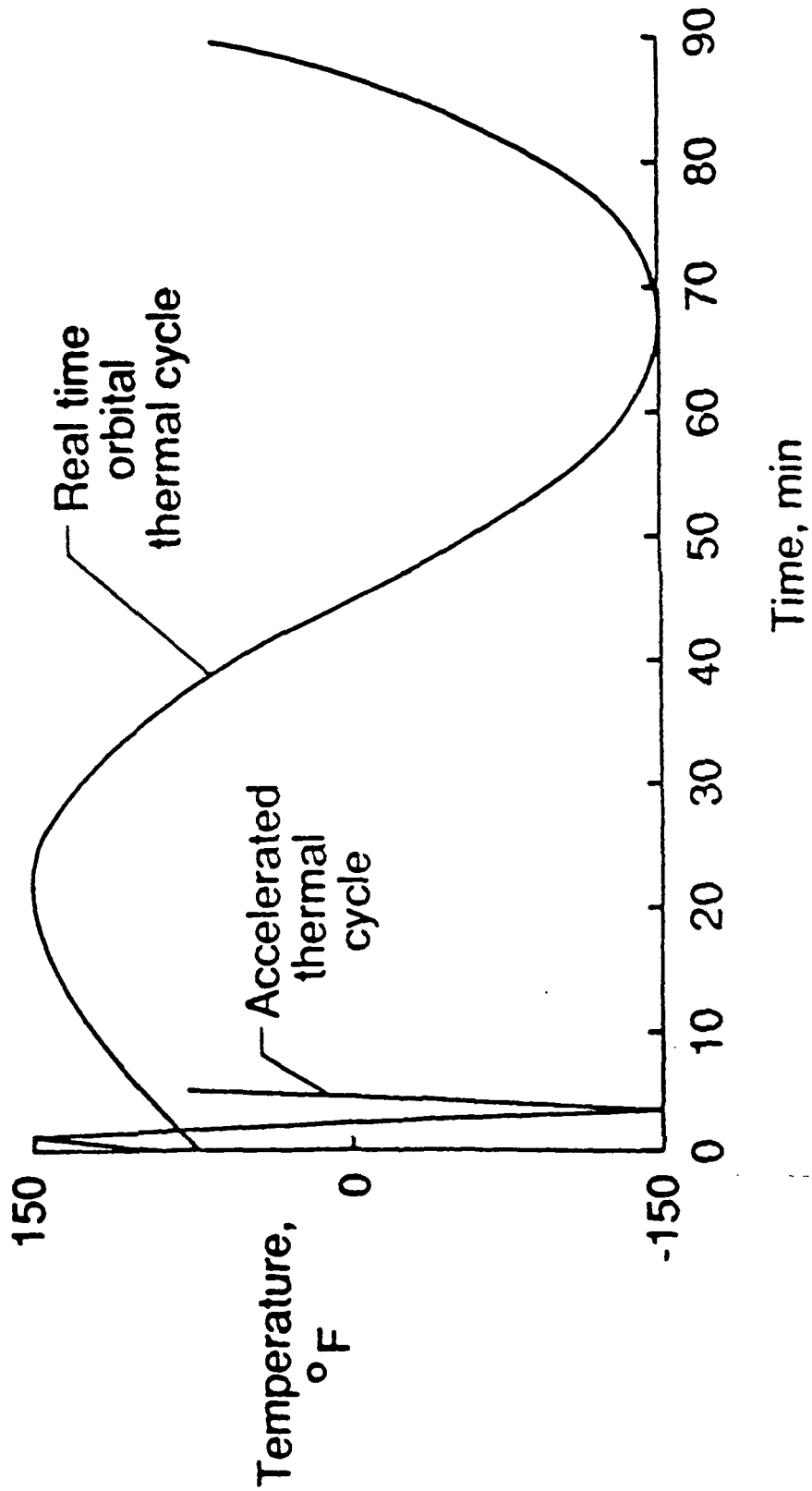
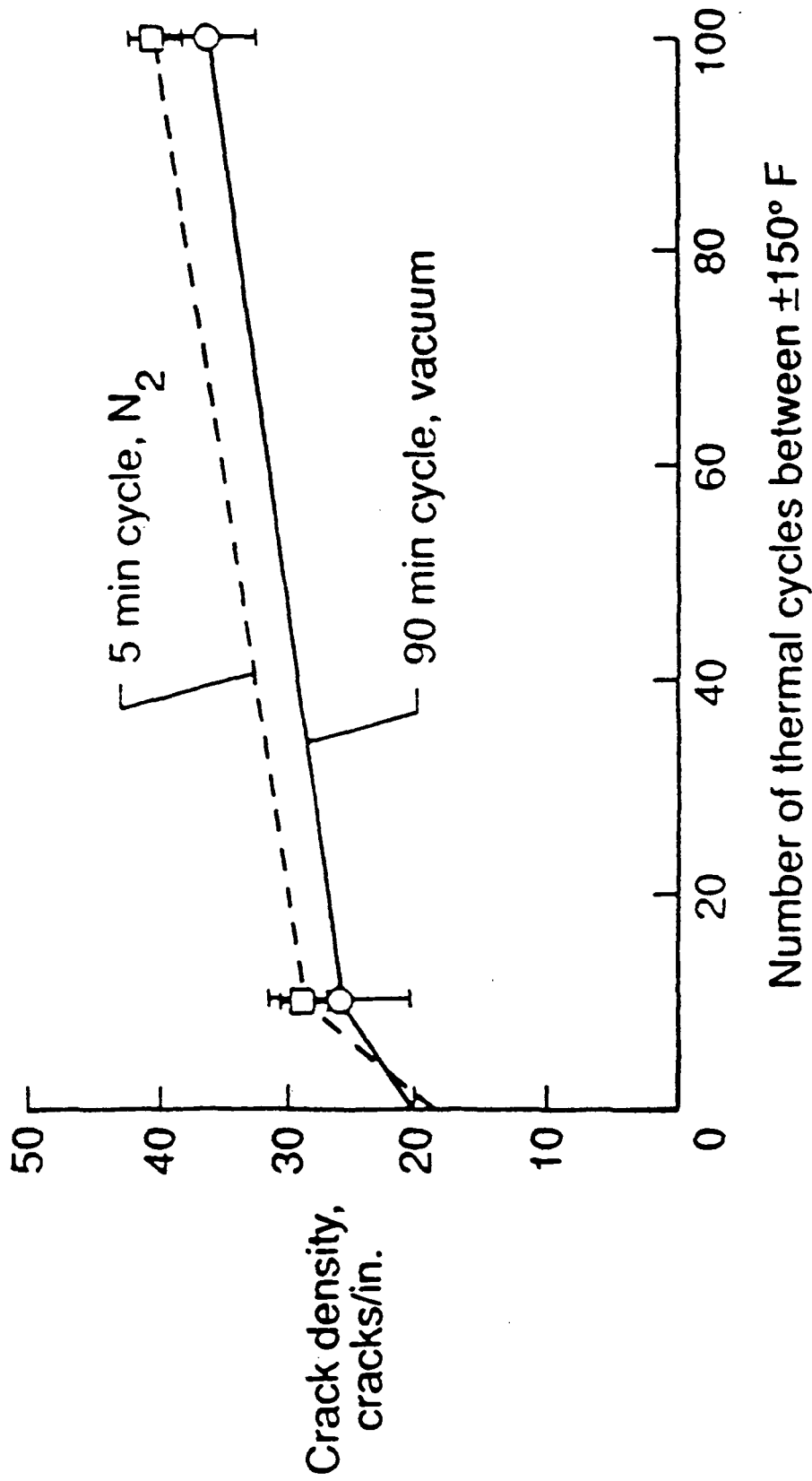


**FIGURE 13. EFFECTS OF THERMAL CYCLE RATE  
AND ATMOSPHERE ON MICROCRACKING IN  
[0/90/0/90]<sub>s</sub> O75/934 LAMINATE**



### SURFACE RECESSION PREDICTIONS

As discussed earlier, the amount of surface recession for a material of known reactivity is directly proportional to atomic oxygen fluence, or the total number of atoms impinging on each square centimeter or surface area during the duration of the intended mission. Fluence, in turn, is dependent on such parameters as spacecraft altitude, surface altitude relative to the spacecraft velocity vector, orbit inclination, duration of exposure, and solar activity conditions during the lifetime of the spacecraft.

To aid the spacecraft developer in estimating the fluence on specific surfaces under question and, consequently, the amount of surface erosion for given solar activity conditions, a nomograph (see Figure 1) has been developed which depicts atomic oxygen fluence as functions of altitude, surface altitude and solar activity conditions. To use this nomograph, one should proceed as follows:

1. Using Figure 2, which shows solar activity predictions for solar cycle 22, our next cycle beginning in 1988, estimate the solar flux index ( $F_{10.7}$  number) for each year the spacecraft is exposed to the LEO environment.
2. Select spacecraft altitude and orbital attitude of the surface in question.
3. Using the above information, read from the lower nomograph scale the amount of fluence per year the spacecraft is in operation. To obtain an estimate of the amount of surface recession on a per year basis for the material in question, multiply these fluence values by the material reactivity shown in Table 5 (in the text). These calculations yield the amount of surface recession (in centimeters) for each year the spacecraft is exposed to orbital conditions. NOTE: If the material is highly reactive such as Kapton ( $R_e = 3.0 \times 10^{-24}$  cm<sup>3</sup>/atom), an estimate of surface erosion on a per year basis may be obtained directly from the upper horizontal scale of the nomograph.
4. Sum the values of (1) fluence per year and (2) surface recession per year calculated in Step 3 over the lifetime of the spacecraft. These quantities represent a good estimate for the total fluence and total surface recession that each surface in question will experience during the lifetime of the mission. For example, assume a spacecraft is designed to operate at an altitude of 500 km and is launched in to an orbit with an inclination of 28.5°. Also assume the spacecraft is gravity-gradient stabilized, it is delivered to orbit during 1993 and has an intended operational lifetime of one year. The amount of



surface recession on ram-oriented Kapton surface is determined from the nomograph as follows:

1. From Figure 2, a launch date of 1993 represents maximum solar activity conditions ( $F_{10.7}=230$ ).

2. From the nomograph, curve "1EMAX" represents ram exposure for these attitude conditions. Reading across the altitude scale of 500 km, the fluence and surface recession are  $2 \times 10^{21}$  atoms/cm<sup>2</sup> year and 60 m/year, respectively. Thus, a highly reactive material such as Kapton which is 127 m (5.0 mil) in thickness will lose 60 $\mu$ m, or 47% of its thickness during the time the spacecraft is in operation. Using the data in Table 7 in the text, if the material is a fluoropolymer such as Teflon, the thickness loss will be 1.2 $\mu$ m (.05 mil), or 1/50th the amount predicted for Kapton.

3. If the surface in question is solar inertial, such as solar array panel, curve "1IMAX" on the nomograph represents one side exposure for solar inertial surfaces during the time this spacecraft is intended to operate. Under these conditions, the fluence and surface erosion would be  $3 \times 10^{20}$  atoms/cm<sup>2</sup> year and 10 $\mu$ m/year, respectively. For two-sided exposure, this would represent a thickness loss of 20 $\mu$ m and if the solar array substrate is 127  $\mu$ m in thickness, 16% of the Kapton material would be eroded away during the operational period of the spacecraft. Coating the Kapton with Teflon would reduce this erosion rate by a factor of 50 (see Table 5 in the text) and would result in a thickness loss of only 0.4  $\mu$ m. Thus, materials unsuited for these applications can be protected from the LEO environment by coating them with materials having low reactivity rates.

FIGURE 1. FLUENCE PROFILES FOR ATOMIC OXYGEN INTERACTIONS

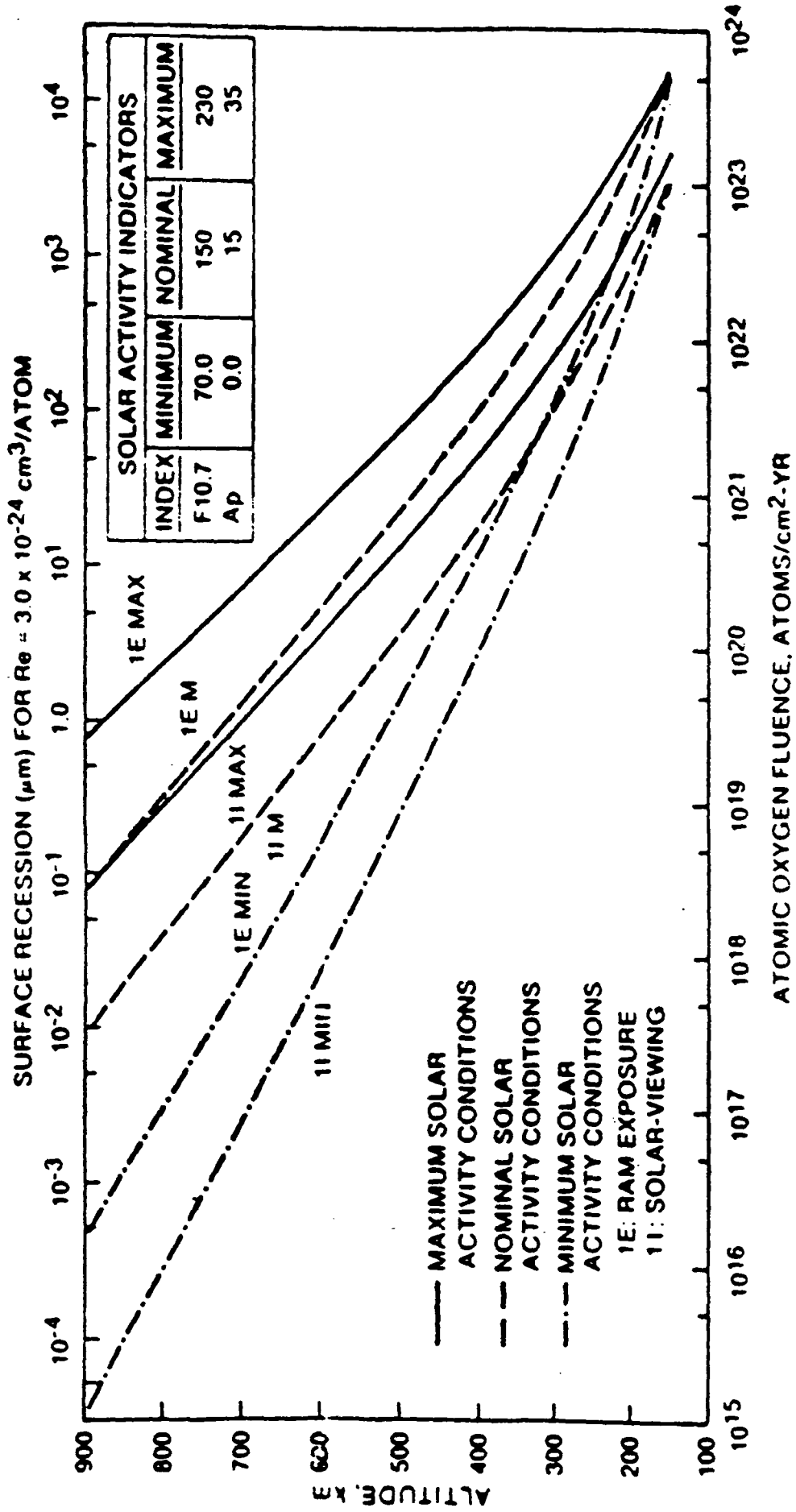
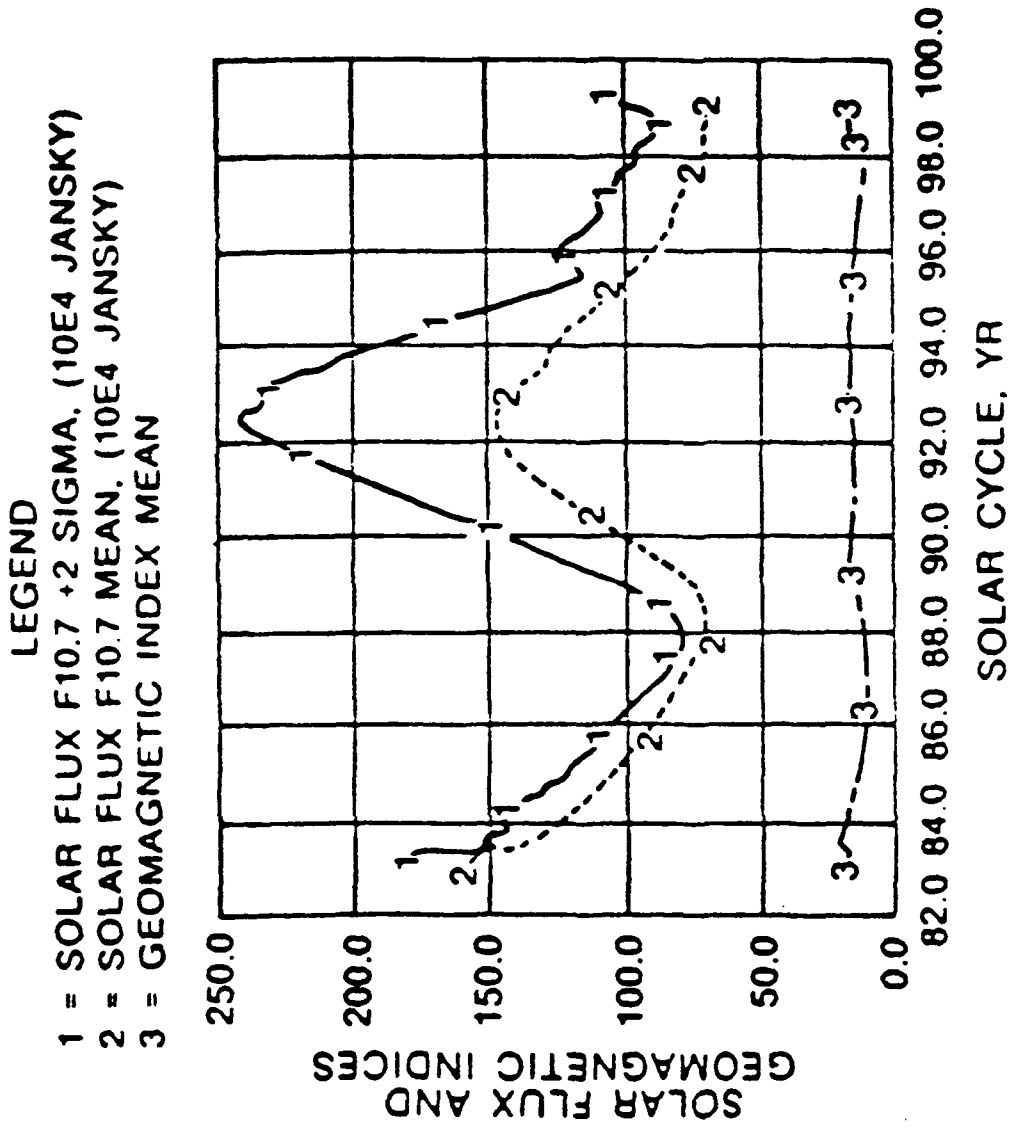


**FIGURE 2. SOLAR ACTIVITY PREDICTIONS FOR CYCLE 22**



APPENDIX II  
DURABILITY OF MATERIALS FOR PRECISION SPACE STRUCTURAL APPLICATIONS  
(LANGLEY RESEARCH CENTER)

1. Tompkins, S. S.: Analytical Study of Effects of Surface and Environmental Thermal Properties on Moisture in Composites. NASA TMX-3562, Sept. 1977.
2. Tompkins, S. S.: Influence of Surface and Environmental Thermal Properties on Moisture in Composites. Journal of Fibre Science and Technology, vol. 11, no. 3, May 1978, pp. 189-197.
3. Tompkins, S. S., Tenney, D. R. , and Unnam, J.: Prediction of Moisture and Temperature Changes in Composites during Atmospheric Exposure. Composites Materials: Testing and Design (Fifth Conf.) ASTM STP 674, 1979, pp. 368-380.
4. \*Tenney, D. R., Slemp, W. S., Long, E. R., Sykes, G. F., and Stein, B. A.: Space Environmental Effects on Structural Materials. Presented at the AIAA 12th Fluid and Plasma Dynamics Conference, Williamsburg, VA, Jul. 23-25, 1979.
5. Tenney, D. R., and Sykes, G. F., and Bowles, D. E.: Composite Materials for Space Structures. Presented at the 3rd European Symposium on Spacecraft Materials in Space Environment, Noordwijk, the Netherlands, Oct. 1-4, 1979.
6. Young, P. R., and Sykes, G. F.: Characterization and Aging Effects of LaRC 160. Resins for Aerospace, ACS Symposium Series, No. 132, American Chemical Society, Washington, DC, 1980.
7. \*Sykes, G. F., and Stoakley, D. M.: Impact Penetration Studies of Graphite/Epoxy Laminates. Presented at the 12th National SAMPE Symposium and Technical Conference, Seattle, WA, Oct. 7-9, 1980.
8. \*Bowles, D. E., and Tenney, D. R.: Thermal Expansion of Composites: Methods and Results. Presented at the 2nd Annual LSST Technical Review, NASA LaRC, NASA CP 2168, Nov. 1980.

9. \*Bowles, D. E., Post, D., Herakovich, C. T., and Tenney, D. R.: Moire Interferometry for Thermal Expansion of Composites. Proceedings SESA Spring Meeting, Dearborn, MI, June 1981.
10. \*Short, J. S., Hyer, M. W., Bowles, D. E., and Tompkins, S. S.: The Thermal Expansion of Graphite/Epoxy Between 116 K and 366 K. Presented at the Third Annual LSST Conference, NASA LaRC, NASA CP 2215, Nov. 16-19, 1981.
11. \*Bowles, D. E.: The Effect of Microrcracking on the Thermal Expansion of Graphite/Epoxy Composites. Presented at the Third Annual LSST Conference, NASA LaRC, NASA CP 2215, Nov. 16-19, 1981.
12. Bowles, D. E., Post, D., Herakovich, C. T., and Tenney, D. R.: Moire Interferometry for Thermal Expansion of Composites. Experimental Mechanics, vol. 21, no. 12, Dec. 1981.

**Lewis Research Center**  
Cleveland, Ohio  
44135

**MEMORANDUM**

Reply to Aftn of 5420

January 13, 1989

**TO:** 5400/Deputy Chief, Power Technology Division  
**FROM:** Research Associate, Cleveland State University  
**SUBJECT:** Characterization of MBR Radiator Materials

The objective of this task was to aid in establishing a data base of candidate materials which can be used in a MBR system. The database was to include the materials to be used for the heat exchange fluid bath, the fluid bath containment, and the belt to be used in the MBR concept. The hybrid belt and the solid belt were the ones to be considered.

This report focuses on belt materials only, since at present there was nothing obvious to suggest a better bath material than gallium, and containment with certain types of stainless steels has been demonstrated. In a report by A. D. Little, an example is given of the substantial heat rejection levels possible with a belt consisting of a hypothetical material having half the heat of fusion of Lithium ( $\sim 300$  kJ/kg) and an emissivity of 0.8. A search for such materials was the focus of this report. The temperature range was restricted to about 400-800K. A further (self-imposed) requirement was some demonstration of use of the materials, rather than a listed handbook or theoretical value with no demonstration of use. The materials selected are given in the Table.

*Albert C. Antoine*

Albert C. Antoine

**Enclosures**

cc:  
5440/C. Coles-Hamilton  
5490/K. Alan White

TABLE  
Selected Phase Change Materials

<u>Material</u>	<u>Melting or Transition Temperature</u>	<u>Heat of Fusion or Transition</u>	<u>Density</u>	<u>Thermal Conductivity</u>	<u>Volume Change in Transition</u>
	<u>K</u>	<u>kJ/kg</u>	<u>g/cm<sup>3</sup></u>	<u>w/mK</u>	<u>%</u>
LiOH	744	930	1.46	0.85	2.6
Penta- erythritol	457-461	303 (269-323)	1.34 1.22	1.88(443K) 0.86(478K)	9.0
NaOH-NaNO <sub>3</sub> (81.5-18.5 mol%)	529	292	---	---	---
Li <sub>2</sub> SO <sub>4</sub> - LiCl(2% by Wt.)	<851	197 ± 8	(2.2)*	---	---
HDPE	402-407	167-201	0.96	0.25***	10
NaNO <sub>3</sub> - NaOH(1% by Wt.)	576	168	(2.26)**	---	---
Al-Si	839	489	2.7	180	-7

\* Density of Li<sub>2</sub>SO<sub>4</sub>

\*\* Density of NaNO<sub>3</sub>

\*\*\* A factor of four increase in conductivity has been noted in paraffins using a metal matrix (1.6%)

## Notes

### LiOH

#### Solid Liquid Transition

Thermal cycling of LiOH has been done in canisters of low-carbon, pure nickel (Ni-201). Two (2) canisters were cycled between 683 and 803K (58 minutes heating, 36 minutes cooling), one for 12,504 cycles (19, 504 hrs.), the other for 10, 512 cycles (16,469 hrs.). Very little LiOH decomposition was found, and the rate of gravimetric corrosion of the container was measured as  $.01 \pm .002$  mm/year. In other tests, improved heat transfer (by an average of 15%) was accomplished by adding a rolled metal (copper) screen to the LiOH in the canister.

### Pentaerythritol

#### SOLID-SOLID Transition

The transition given in the table is that of solid-solid transition, from a hard brittle wax-like material to a soft, pliable, wax-like material. The melting temperature is about 531-533K. Fibers or felts of metal or carbon have been suggested as conductivity enhancers.

### NaOH-NaNO<sub>3</sub> (81.5-18.5 mol%)

#### SOLID-LIQUID Transition

Compatibility tests have been conducted, and carbon steels showed corrosion rates less than 5  $\mu$ m/year (stainless steels  $>100$   $\mu$ m/year). A 6700-hr., 1000 melting-freezing cycles, test was performed. The results of the investigation on the materials after the test were essentially the same as those obtained in the compatibility test.



### Li<sub>2</sub>SO<sub>4</sub>-LiCl(2% by Wt.)

#### SOLID-SOLID Transition

Pure Li<sub>2</sub>SO<sub>4</sub> has a transition with a latent heat of 214 kJ/kg at 851K. Thermal cycling tests (up to 3 months duration) of Li<sub>2</sub>SO<sub>4</sub> and binary and ternary mixtures of Li<sub>2</sub>SO<sub>4</sub> and other sulfates showed that all samples containing Li<sub>2</sub>SO<sub>4</sub> were gradually deformed, and this deformation resulted in the breaking of sample containers (Vycor, fused quartz, stainless steel). The deformation was completely eliminated by transforming parts of the sample into a two-phase region by adding small amounts of LiCl(2% and 4%). Temperature cycling between 793 and 923K was done, and no attack on the sample containers could be detected even after prolonged thermal cycling. No sample deformation occurred in the 4% samples and only very small traces of deformation in the 2% samples (the Vycor containers were intact).

### High Density Polyethylene

#### SOLID-SOLID Transition

High density (HDPE) or "linear" polyethylene can be crosslinked, chemically or by ionizing radiation, such that the heat of melting is preserved, but liquefaction of the polymer is prevented. The polymer is thus form stable. This material has been used as beads encapsulated in rubbers and elastomeric materials, as well as 'encapsulating' some fibrous materials.

### NaNO<sub>3</sub>-NaOH (1% by Wt)

#### SLURRY-LIQUID Transition

Off-eutectic compositions in the NaNO<sub>3</sub> containing systems were examined because of the hard freeze experienced with eutectics. It was found that NaNO<sub>3</sub> containing 1% (by wt) of NaOH forms a slurry. The mixture is thermally stable, and when kept free from moisture has an acceptable corrosion rate (with mild steel).

## Al-Si

This aluminum-silicon alloy was included because of potential use in the future. The material is prepared in a ceramic shell (alumina-silicon carbide). The usual size is about 1-2 inches, but shells of about 1/4 inch have been made. In addition to fabrication problems with smaller sizes, the heat change in the alloy may not be the same because some of the shell may be consumed.

## Environmental Compatibility

It has been recently determined that in low earth orbit the susceptibility to attack by atomic oxygen may be the limiting factor for long-lived spacecraft. In general, metals have little reactivity. Organic materials, however, are highly reactive. If high density polyethylene or pentaerythritol are to be used, they will have to be protected.

Perfluorinated polymers, such as Teflon, are considerably less reactive than the carbon-hydrogen compounds, and can be considered for use as protective coatings. (It should be noted that chemical etching of Teflon can be done, leaving the surface variously described as dark discolored, purple, even near black. The effect of atomic oxygen on a modified surface would have to be determined.)

Metal surfaces can be treated in various ways to increase their emittance, reaching 0.8 and better. In some tests, exposure to atomic oxygen in an RF plasma asher did not significantly change the emittance of those samples that had been heat treated as part of their texturing process.

## References

### LiOH

R. L. Gay, W. T. Lee, A. G. Pard, and T. H. Springer, "Thermal Cycling Tests of Energy Storage Canisters for Space Applications", Proc. 23rd IECEC (1988), Vol. 3, pg. 69.

"Thermal Energy Storage for an Organic Rankine Cycle Solar Dynamic Powered Space Station", Proc. 20th IECEC (1985) Vol. 2 pg. 2397.

### PE

D. K. Benson et al, U. S. Patent 4,572,864, February 25, 1986, "Composite Materials for Thermal Energy Storage."

D. K. Benson, R. W. Burrows and J. D. Webb, Solar Energy Materials 13 (1986) 133-152, "Solid State Phase Transitions in Pentaerythritol and Related Polyhydric Alcohols."

### NaOH-NaNO<sub>3</sub>

Y. Abe, Y. Takahashi, K. Kanari, K. Tanaka, R. Sakamoto, and M. Kamimoto, Proc. 23rd IECEC (1988), Vol. 2, pg. 159, "Molten Salt Latent Thermal Storage Using NaOH-based Eutectics."

### Li<sub>2</sub>SO<sub>4</sub>-LiCl

C.-A. Sjolom, Proc. 16th IECEC (1981), Vol. 1, pg. 958, "Heat Storage in Phase Transitions of Solid Electrolytes."

### HDPE

I. O. Salyer, A. K. Sinear, R. P. Chartoff, and D. E. Miller, "Advanced Phase-Change Materials for Passive Solar Storage Applications," Proc. 20th IECEC (1985), Vol. 3, pg. 3.699.

G. A. Lane, Ed. Vols I and II, CRC Press 1983 and 1986, "Solar Heat Storage: Latent Heat Material."

### NaNO<sub>3</sub>-NaOH

R. T. LeFrois, H. V. Venkatesetty, Sharing the Sun - Solar Technology in the Seventies, Vol. 8, pg. 107, 1976, "Inorganic Phase Change Materials for Energy Storage in Solar Thermal Program."

## Contacts

David Benson	Solar Energy Research Institute	(303) 231-1162 FTS 327-1162
John Tomlinson	Department of Energy	(615) 574-0768
Ival Salyer	University of Dayton Research Inst.	(513) 229-2113
Glenn White	DuPont/(Lanxide)	(302) 999-3417

## REGENERATIVE FUEL CELL ENERGY STORAGE SYSTEMS FOR FUTURE MANNED SPACE MISSIONS

Paul R. Prokopius  
NASA Lewis Research Center  
Cleveland, OH

Dr. Albert Antoine  
Cleveland State University  
Cleveland, OH

Robert B. King  
Sverdrup Technologies, Inc.  
Middleburg Hts., OH

### ABSTRACT

NASA's planning for the future exploration of the Solar System includes the establishment of manned outposts, as well as central base stations on the Moon and Mars. Supporting human expeditions to, and operations on, the surface of the Moon or Mars represents a substantial technology challenge for current and projected power system capabilities. The high levels of power associated with an operational base, somewhere in the 100's to 1000's of kilowatts, will require nuclear power systems. During the installation of these permanent nuclear systems, power systems based on solar energy hold the greatest promise for supplying needed power. These systems will also be required to augment and serve as back-up power sources for the permanent nuclear-powered bases.

Because the solar-based surface power system must supply usable power continuously, that is during the day as well as the night, a regenerative system is required. During the daylight hours the power generation subsystem will recharge the energy storage subsystem and also supply power directly to the system's electrical loads. Thus, continuous power is supplied to the load; it is provided by the power generation subsystem during sun periods and from the energy storage subsystem during periods of darkness.

In a Lunar application, the period of darkness extends for two weeks, while a Mars application presents a more manageable 12-hour night. Both applications require very high energy density and reliable energy storage systems. The highest potential for successfully achieving surface power storage capabilities for these applications lies in the regenerative fuel cell (RFC) concept. The regenerative fuel cell system is depicted in Figure 1. During the light portion of the orbit the photovoltaic solar arrays generate sufficient power to service the system electrical loads plus a water electrolysis unit. The amount of electrical energy required by the electrolysis unit is dictated by the amount of hydrogen and oxygen needed to generate power in a fuel cell, which supplies the electrical loads during the dark portion of the orbit. In generating this power, water is produced by the fuel cell as a by-product of the electrochemical reaction. To complete the cycle, the by-product water is collected and stored for use in the electrolyzer during the succeeding orbit.

The mass and specific energy benefits to be realized by employing a regenerative fuel cell system are displayed in Figure 2. Low system mass for a given power level is a central requirement for achieving acceptance of transportation costs

ORIGINAL PAGE IS  
OF POOR QUALITY

to the Moon or Mars. Another requirement, even more challenging, is appreciable system lifetime without sacrificing performance even after an extended period of dormancy. Also a relatively high power level requirement of 25 kW is projected to support an initial surface outpost of four to six astronauts. To develop the technology base for a system which will meet these requirements, a program has been initiated as one of the elements of NASA's Project Pathfinder. This program was developed and is being managed by NASA's Lewis Research Center. It focuses on the technology areas of solar power generation, energy storage and electrical power management. Advancing these technologies and coupling their performance potentials with an advanced low mass, reliable electrical power management subsystem can lead to surface power systems having a reliable life in excess of 20,000 hours with system specific powers of 3 W/kg for Lunar application and 8 W/kg for Martian applications. These projected specific powers represent substantial improvements over the state-of-the-art, up to a factor of 30. System mass reductions of this magnitude, coupled to the expected factor of 10 increase in life, should enable extra-terrestrial surface missions where life and mass are the driving forces for success.

The Energy Storage element of the Pathfinder Surface Power Program is a 6-year effort culminating in the verification of a regenerative fuel cell system operating in a relevant environment. The near-term, 3-year, Phase I effort, will provide the development and verification of the system critical components, those being the fuel cell and electrolyzer stacks. The second 3-year phase will focus on the development and verification of the complete RFC breadboard system.

The two candidate fuel cell and electrolyzer technologies for the Pathfinder system are the alkaline and proton exchange membrane (PEM). Because alkaline was the system of choice for both Apollo and the Space Shuttle, the state-of-the-art of alkaline systems had been advanced considerably over that of the PEM technology. However, the major deficiency facing the alkaline technology in the Pathfinder application is the lack of long term catalyst layer stability, which translates into performance degradation with time. Unlike with PEM and other acid-type fuel cells, a stabilizing catalyst support has not been developed for the alkaline system. PEM, on the other hand, offers a stable, long life system but one whose efficiency has, until recently, been significantly lower than alkaline. Recent improvements in the conductivity of PEM membranes increase the probability that this technology could replace alkaline as the Pathfinder RFC baseline. At present, the weakness in the PEM technology stems from the fact that the membrane technology improvements are very recent and, therefore, the data base needed to justify commitment to this technology does not exist. Accordingly, a technology assessment and trade-off analysis has been undertaken to provide guidelines for selecting the technology to be carried into full development in the Pathfinder Program.

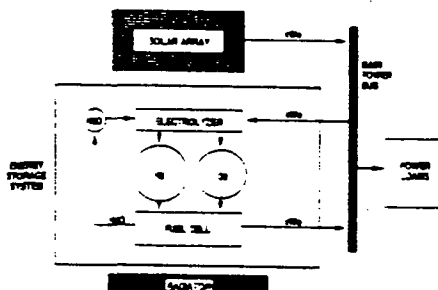
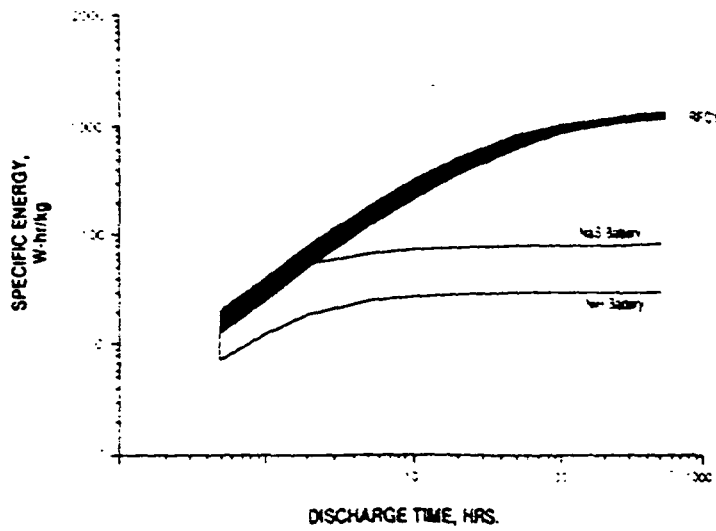


FIGURE 11. REGENERATIVE FUEL CELL SYSTEM SCHEMATIC

SPECIFIC ENERGY OF 25 kWe ENERGY STORAGE SYSTEM



TECHNOLOGY IMPACTS  
25kW SURFACE POWER SYSTEM

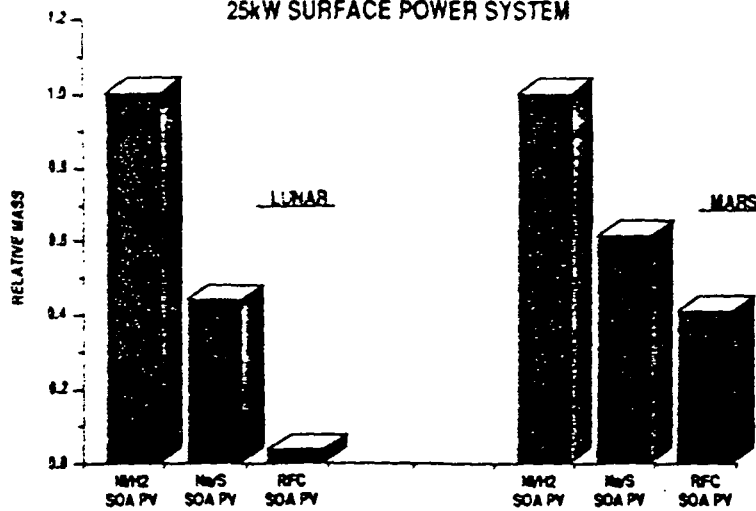


FIGURE 2: ADVANTAGES OF REGENERATIVE FUEL CELL ENERGY STORAGE VERSUS BATTERY SYSTEMS FOR LONG DISCHARGE APPLICATIONS

ORIGINAL PAGE IS  
OF POOR QUALITY

## Mathematical Modeling of Solid Oxide Fuel Cells

Cheng-Yi Lu  
Cleveland State University  
NASA Lewis Research Center  
Cleveland, OH 44135

Thomas M. Maloney  
Department of Chemical Engineering  
Cleveland State University  
Cleveland, OH 44115

Development of predictive techniques, with regard to cell behavior, under various operating conditions is needed to improve cell performance, increase energy density, reduce manufacturing cost, and to broaden utilization of various fuels. Such technology would be especially beneficial for the solid oxide fuel cell (SOFC) at its early demonstration stage.

Three designs of SOFC cell/stack configurations are now available and they are Westinghouse tubular, Argonne National Laboratory (ANL) monolithic, and Ztek planar FC models. A comparison among these designs in the previously stated areas is needed. Basically, the differences among these configurations are shape of cell, channel geometry for reactant flow, and size/thickness of cell components. These designs were compromised with manufacturability, which is still the most difficult task aspect of the SOFC development. Due to this difficulty, there are limitations on the size of monolithic and planar cells and on the weight (and cost) of tubular cell. But the manufacturability is not the only factor that limits the size of SOFC. As soon as the cell is put on operation, the temperature and the current density (CD) distributions on the plate will determine the success of the performance in the following ways: (1) hot spot temperatures exceeding the sintering, coating, or E(C)VD temperature will cause material problems, (2) severe non-uniform temperature distributions will result in cracking due to thermal stresses, and (3) non-uniform CD distribution will increase the possibility of reactant depletion at exit, especially at high utilization ratios. This paper describes the development of computer models to calculate the temperature, CD, and reactant distributions in the tubular and monolithic SOFCs. Results indicate that problems of non-uniform heat generation and fuel gas depletion in the tubular cell module, and of size limitations in the monolithic (MOD 0) design may be encountered during FC operation.

### V-I Characteristics

The SOFC semi-empirical V-I characteristics was modeled with respect to cell components (thickness) and operating conditions (temperature, pressure, inlet fuel gas

compositions, and fuel and oxidant utilization ratios).

### Tubular Cell

For the Westinghouse tubular SOFC, a two-dimensional CD profile (circumferential and axial) was generated by assuming an isothermal condition (1000 °C). Recently reported performances of tubular SOFC using DOE specified fuel (67% H<sub>2</sub>, 22% CO, 11 % H<sub>2</sub>O at 85 % fuel utilization) and air [1] were applied in this study. First, an analytic model (Figure 1) was solved and the solutions were used to calculate the circumferential CD distribution around the tubular SOFC using specific fuel and oxidant gas flow rates. Because of symmetry, only one half of a cell was modeled. Secondly, a finite difference model was used to calculate the fuel and oxidant gas flow rates along the axis of the tubular SOFC. Reforming and water shift reactions were considered at equilibrium at the operating temperature of 1000 °C. Rated operating conditions and cell dimensions of the Westinghouse 5 kW module were applied. Figure 2 shows the circumferential and axial CD profiles. It is noted that there is non-uniformity of CD along the axis and around the circumference of the tubular cell. For a 0.275 A/cm<sup>2</sup> (average) operation, the CD ranges from 0.652 to 0.164 A/cm<sup>2</sup>. The peak CD occurs at circumference equal to 1.85 cm in Figure 1, where the current flows radially out of the cell, and where the fuel and oxidant gases enter the cell axially. The lowest CD occurs at the opposite end of the cell. Figure 2 also shows that in an operating cell, the peak CD, as well as the largest heat generation, is near the interconnection. This will worsen the critical stress problem since the thermal expansion will not be compatible between the interconnection and other cell components.

Another important issue pertains to the probability of fuel gas depletion in the Westinghouse 5 kW module. The non-uniform fuel gas flow distribution in the passages (main, side, and corner) caused by the equal pressure gradient of the flow, is compared with the amount of fuel needed to achieve a parallel connection (e.g., the current for three cells in parallel is equal to 80 A). Documented performances from specimen testing [1] were adapted as the basis. Among these reported data, the performance is a function of the cell itself and the testing time. The probabilities of total fuel gas depletion (at operating time equal to 200 hours) around the edge cells for two types of flow passages and two to six cells in parallel are shown in Figure 3. It shows that in a design with three cells in parallel there is a 7% probability that fuel gas will be depleted at the exit of edge cells (corner cells and side cells in Type I & II flow distributions, respectively). In addition, a shorted cell (by assuming voltage of



arbitrarily chosen cell equal to 0) in the operation will always result in fuel gas starvation for the remaining, i.e., unshorted cells.

These results strongly imply that the design of more uniform fuel gas passages is necessary, which can be achieved by increasing the thickness of Ni felt or by redesigning the fuel gas intake plenum.

#### Monolithic Cell

Monolithic solid oxide fuel cells are currently being developed at Argonne National Laboratory. For many applications, operating conditions such as total pressure, average cell temperature and current density, as well as inlet reactant gas temperatures and compositions are fixed or are predetermined. A two dimensional computer model has been implemented to predict the effects of fuel utilization ratios (FUR), oxidant utilization ratios (OUR), and cell dimensions upon the temperature and current density distributions within cross-flow arrays of the MOD 0 design, subject to a specific set of the above mentioned operating conditions. Results from the model were used to determine limits on cell sizes and on reactant gas utilizations by evaluating the three performance indicators outlined earlier. In the subsequent analyses, the following operational parameters were maintained : pressure = 1 atm; average array temperature = 1000 °C; average current density = 500 mA/cm<sup>2</sup>; inlet molar fuel gas composition : 97% H<sub>2</sub>, 3% H<sub>2</sub>O; inlet molar oxidant gas composition : 21% O<sub>2</sub>, 79% N<sub>2</sub>; and each inlet gas temperature = 800 °C.

All V-I relationships for the monolithic fuel cells were assumed to behave linearly within the range of interest. Some representative V-I curves are displayed in Figure 4, where the best case accounts only for ohmic resistance and the estimated case includes slow polarization effects. Both the best case and the estimated case are more favorable than the experimental V-I curve, however, it is reasonable to expect that the experimental relationship has been improved since the December 1985 status [2].

Figure 5 shows the relationship between FUR and OUR that must exist in order to satisfy the specified operating conditions. While Figure 5 represents the case for a 10 cm x 10 cm array, the shape of the curve is similar for other cell dimensions as well. It is evident from the figure that lower limits on both FUR and OUR will be encountered. The effect of FUR on overall operating efficiency is also depicted in Figure 5 and it is seen that the maximum efficiency is obtained at a relatively small FUR value, near FUR = 0.2 .

A typical temperature distribution is shown in Figure 6 where the peak temperature is reached at the extreme corner of the array, since reactant gas depletion is at the maximum there. The minimum array temperature occurs at the opposite corner. In all cases, the maximum temperature is located along the edge of the array where oxidant gas departs, however, as FUR is increased, the hot spot location moves closer to the fuel gas inlet. One of the performance criteria requires that the peak cell temperature be lower than the sintering temperature used in the manufacturing process, which is approximately 1600 °K. Results obtained using the best possible V-I curve indicate that the array sizes could exceed 20 cm x 20 cm and still satisfy the hot spot requirement. For cases where the estimated V-I curve was applied, however, the peak temperature rose above 1600 °K for cell dimensions as small as 5 cm x 5 cm, as seen in the diagram.

Since the location of the minimum array temperature is invariant, both the magnitude and the relative location of the maximum temperature must be considered when assessing thermal stresses. At large FUR values, the peak temperature is in close proximity to the minimum temperature and large thermal gradients will be developed, the severity of which depends on the materials used.

Results from the computer model show that array dimensions for a cross-flow monolithic fuel cell can be restricted as a result of non-uniform temperature distributions. Improvements in the V-I curve will alleviate much of this problem. Also, a range of allowable reactant utilization ratios will be established when a set of operational parameters are specified.

#### References

- [1] Westinghouse Electric Co., "High Temperature Solid Oxide Electrolyte Fuel Cell Power Generation System - Technical Summary Report", Volume 3, DOE Contract DE-AC02-80ET17089.
- [2] Fee, D.C. et al., "Monolithic Fuel Cell Development", 1986 Fuel Cell Seminar Abstracts.

#### Acknowledgment

This study was supported by U.S. Department of Energy, Morgantown Energy Technology Center through the NASA Lewis Research Center Fuel Cell Project Office.

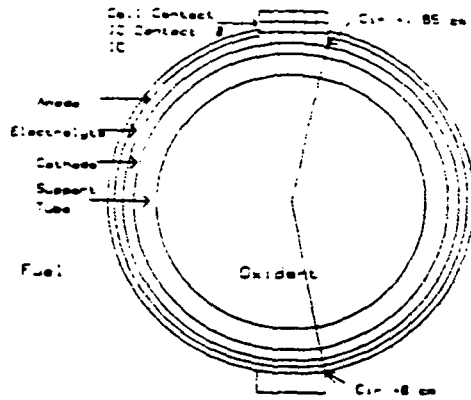


Figure 1. Model Used to Analyze Circumferential Current Density Distributions for Tubular SOFC

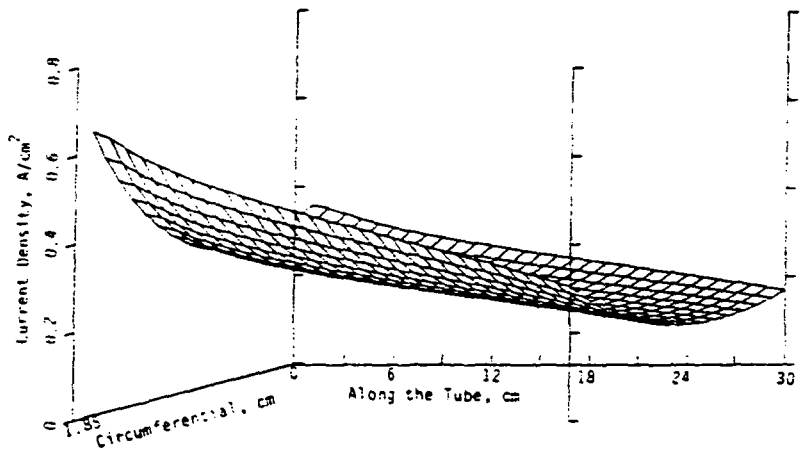


Figure 2. Tubular SOFC Current Density Profile (Isothermal)

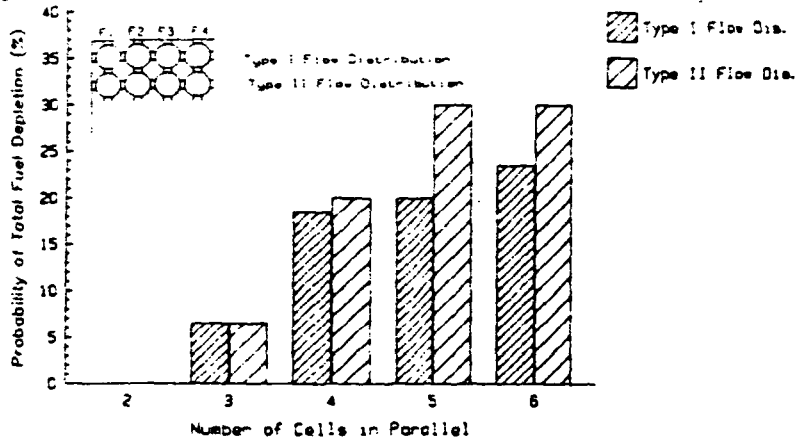


Figure 3. Probability of Fuel Depletion (of the Edge Cells) vs. Cell Configuration

ORIGINAL PAGE IS  
OF POOR QUALITY

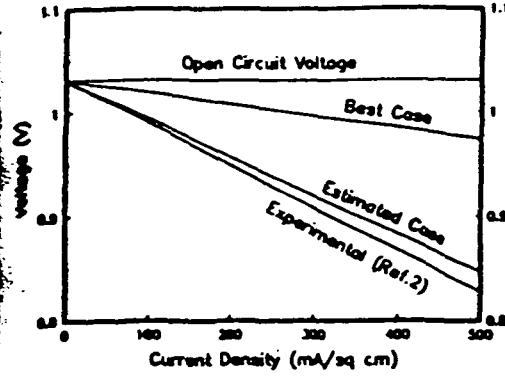


Figure 4. Monolithic SOFC V-I Curves

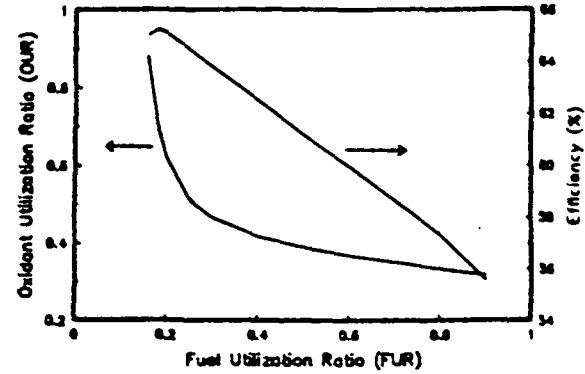


Figure 5. OUR and Efficiency vs. FUR

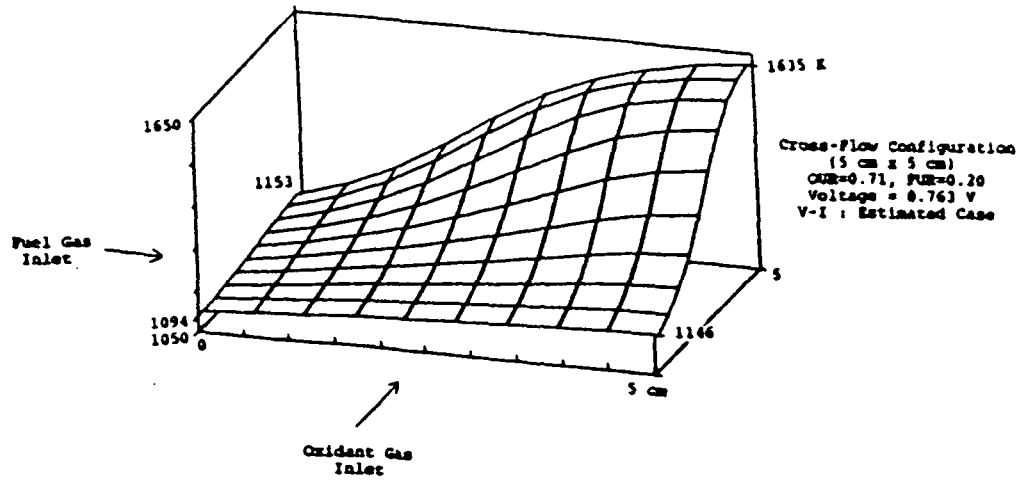


Figure 6. Monolithic SOFC Temperature Distribution for Example Case

PREDICTED RESTRICTIONS ON REACTANT GAS UTILIZATIONS IN MONOLITHIC SOLID OXIDE FUEL CELL OPERATION

By T.M. Maloney\*, C.-Y. Lu\*\*, and G.A. Coulman\*

Abstract

For power system designs that include monolithic solid oxide fuel cell (MSOFC) arrays, it is desirable to identify a fixed set of operating parameters and to maintain a certain performance level. The interrelationships among the various operating parameters impose restrictions upon the range of feasible choices of those parameters. A computer model was used to estimate the effects that the I-V characteristics, the average array temperature, and the inlet reactant gas temperatures have upon the range of feasible fuel utilization ratios (FUR) and oxidant utilization ratios (OUR). The results can be used as constraints for system optimization studies.

Introduction

Monolithic solid oxide fuel cells (MSOFC) are being developed at the Argonne National Laboratory. McPheeters et al. explained that the most important task at the present time is perfecting the fabrication procedures. While it is generally desirable to manufacture large monolithic arrays in order to achieve high power output, some restrictions on the feasible ranges



Left to Right:  
T.M. Maloney  
C.-Y. Lu  
G.A. Coulman

T.M. Maloney, Research Assistant, Cleveland State University. Presently performing Doctoral research on computer modeling of solid oxide fuel cell performance. B.S. The Ohio State University, M.S. Cleveland State University.

C.-Y. Lu, Aerospace Engineer, Rockwell International. He worked under contract with the NASA Lewis Research Center for more than five years, performing system analysis work and fuel cell simulation studies. Dr. of Engineering, Cleveland State University.

G.A. Coulman, Dean, Fenn College of Engineering, Cleveland State University. His research subjects cover many fields, including combustion phenomena, reaction engineering, computer simulation and optimization, and batch and plant synthesis and optimization. Ph.D., Case Institute of Technology.

\*Chemical Engineering Dept. Cleveland State University, Cleveland, Ohio 44115, USA. Tel: 216-687-2569.

\*\*Rockwell International/Rocketdyne Division, Canoga Park, California 91303, USA. Tel: 818-700-3168

of operating parameters will be encountered. Lu et al. have recently reported on the effects that the I-V characteristics and the array dimensions have upon hot spot temperatures and upon reactant gas depletion in the MSOFC design. A range of choices for the fuel utilization ratio (FUR), the oxidant utilization ratio (OUR), and the array dimensions were approximated for a fixed set of operating conditions. Feasible FUR and OUR ranges and feasible array sizes were defined as those values which prevented maximum array temperatures to be greater than 1600° K and also prevented reactant gas depletion. The present work investigates the effects that the average array temperature, the I-V characteristics, and the inlet reactant gas temperatures each have upon the ranges of feasible FUR and OUR values. The material problems associated with hot spots in the arrays are disregarded.

### Operating Conditions and Computer Algorithm

The fuel cell simulation algorithm developed by Lu et al. has been modified to estimate MSOFC array behavior. The following operating parameters were specified and are assumed to prevail for all subsequent analyses unless otherwise noted: operating pressure = 1 atm; average current density = 500 mA/cm<sup>2</sup>; molar fuel gas composition: 97% H<sub>2</sub>/3% H<sub>2</sub>; oxidant gas: air; array dimensions: 10 cm x 10 cm. The I-V curve, the average array temperature and the inlet reactant gas temperatures were varied, then the FUR-OUR relationships were examined. If the computer algorithm did not converge to a reasonable solution, then the set of input parameters that were used were considered to be infeasible.

### Results

Figure 1 represents two sample I-V curves that were used in the analyses. The Best Case accounts only for material resistances while the Estimated Case includes various polarization sources. Figure 2 summarizes the effects that the I-V curves have upon the range of feasible FUR and OUR values, in this case for a 5 cm x 5 cm MSOFC MOD 0 array. As the I-V characteristics are improved, the feasible FUR and OUR ranges both widen. For the Best Case, the minimum and maximum FUR values are approximately 0.15 and 0.88, respectively, while the corresponding OUR values that are required to satisfy the specified operating conditions are roughly 0.99 and 0.34, respectively. But for the Estimated Case, feasible FUR values are between 0.18 and 0.75 with corresponding OUR values between 0.84 and 0.33. In general, the range of allowable FUR values increases as the I-V curve improves and the upper OUR limit is extended.

### Effect of Average Array Temperature

One means of increasing the average MSOFC array temperature is to increase the FUR and/or the OUR. Observe in Figure 3 that the range of feasible FUR values becomes smaller as the average array temperature increases while the feasible OUR range is shifted upward. The computer model predicts FUR limits between 0.10 and 0.80 with corresponding OUR limits between 0.60 and 0.18 for an average array temperature of 1173° K. As the average array temperature increases to 1323° K, the feasible FUR values are between 0.20 and 0.47 with OUR values between 0.98 and 0.52.

### Effect of Inlet Reactant Gas Temperatures

Some system designs allow flexibility for choosing the inlet reactant gas temperatures while other systems have these temperatures defined. Figure 4 shows the effects that the inlet temperatures have upon the feasible FUR and OUR ranges for an average array temperature of 1273° K. As the inlet reactant gas temperatures increase for a fixed FUR, then the corresponding OUR must obviously decrease since more inert gas is required to remove heat. The present model predicts lower limits for feasible inlet gas temperatures, which are approximately 1050° K for a FUR of 0.20 and 985° K for a FUR of 0.50.

Considerable interest has been focused towards operating tubular solid oxide fuel cells at fuel utilization ratios up to 85% (4). Figure 5 shows the behavior of a MSOFC array operating at a FUR of 85%. As expected, the average array temperature increases as OUR increases, but note the nearly linear relationship for this case. Convergence was not achieved for OUR less than 5% and for OUR greater than 31%.

### Concluding Remarks

The practical values of computer modeling are usually realized by recognizing trends in the predicted results, rather than by accepting the results as being completely accurate and precise. While it is known that all of the operating parameters cannot be arbitrarily chosen for MSOFC operation, computer modeling results can be used for sensitivity analyses, thereby approximating the interrelationships among the operating parameters.

### References

1. McPheeters, C.C., Dees, D.W., Dorris, S.E., and Picciolo, J.J., "Argonne Monolithic Solid Oxide Fuel Cell Fabrication", 1988 Fuel Cell Seminar Abstracts, October 1988, pp. 29-32.
2. Lu, Cheng-Yi and Maloney, Thomas M., "Mathematical Modeling of Solid Oxide Fuel Cells", 1988 Fuel Cell Seminar Abstracts, October 1988, pp. 78-83.
3. Lu, Cheng-Yi and Alkasab, Kalil A., "Manual of Phosphoric Acid Fuel Cell Stack Three-Dimensional Model and Computer Program", NASA Report CR-174722.
4. Veyo, Stephen E., "SOFC Field Experiments, A Learning Experience", 1988 Fuel Cell Seminar Abstracts, October 1988, pp. 13-17.

### Acknowledgement

This study was supported by the US Department of Energy, Morgantown Energy Technology Center, through the NASA Lewis Research Center Fuel Cell Project Office.

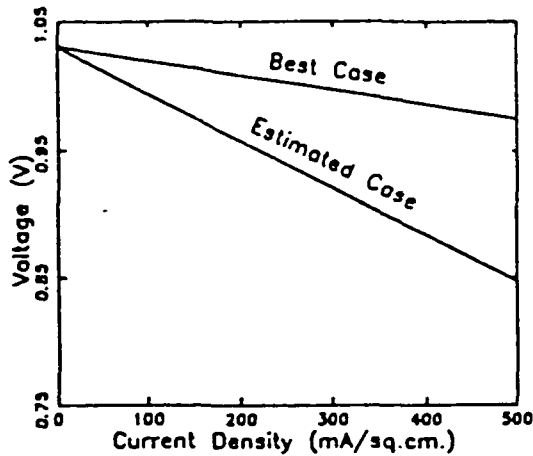


Figure 1. SOFC I-V Curves

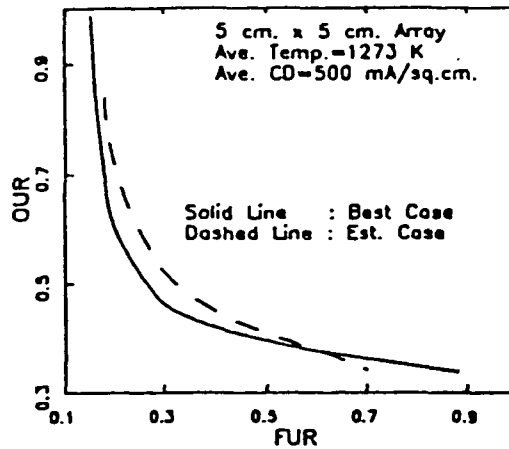


Figure 2. Effect of I-V Curve on Feasible FUR-OUR Ranges

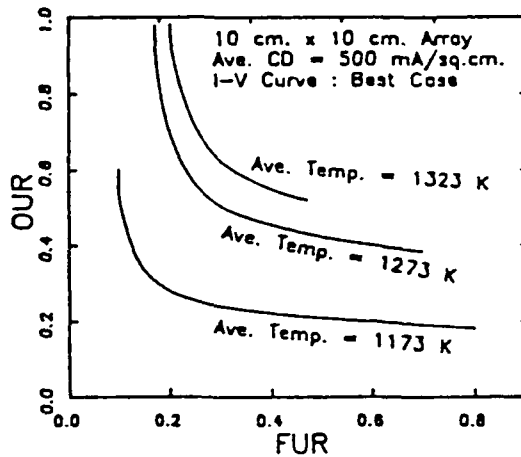


Figure 3. Effect of Avg. Array Temperature on Feasible FUR-OUR Ranges

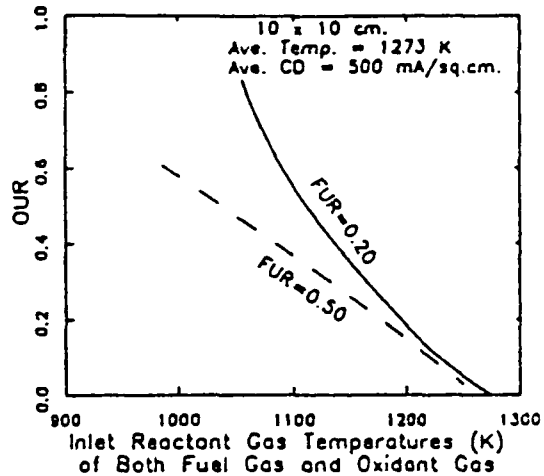


Figure 4. OUR vs. Inlet Reactant Gas Temperatures at Constant FUR

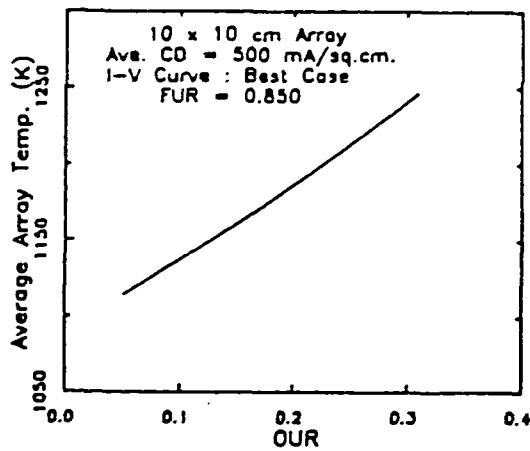


Figure 5. Feasible OUR Range for FUR = 85%



PERFORMANCE PREDICTIONS FOR MONOLITHIC  
SOLID OXIDE ELECTROLYZER ARRAYS

Thomas M. Maloney\* and George A. Coulman  
Fenn College of Engineering  
Cleveland State University  
Cleveland, Ohio 44115

Monolithic solid oxide fuel cells (MSOFC) were devised at the Argonne National Laboratory in the early 1980's (1) and are presently in the fabrication development stage at Allied Signal Aerospace (2) for various applications. The monolithic fuel cell is an all-ceramic structure which is assembled in a 'honeycomb' shape similar to that of corrugated cardboard. While fuel cell operation has been demonstrated (3), it is also possible to operate the monolithic structure in the reverse, or electrolysis, mode. Performance characteristics of monolithic solid oxide electrolyzer (MSOEL) arrays were estimated in order to determine the effects that inlet gas temperatures, i-V relationship, and the average current density, have upon the average cell temperature and upon the applied voltage requirements.

Performance predictions of MSOFC arrays have been previously reported (4,5) and the computational algorithm formulated by Lu and Maloney (4) was revised to predict performance characteristics of MSOEL arrays for the Mod 0 design. The algorithm consisted of a finite difference scheme to solve the mass and energy balance equations which pertain to the electrolyte and to the anode and cathode gas channels. The inlet reactant gas stream is a hydrogen-steam mixture and the water in that stream is electrolyzed to produce hydrogen (in the H<sub>2</sub>-H<sub>2</sub>O channel) and oxygen (in the pure O<sub>2</sub> or air channel). The solid electrolyte mass and energy balance equations were derived elsewhere (6) and Table I lists the operating conditions which were maintained constant unless otherwise noted.

TABLE I

ELECTROLYZER ARRAY OPERATING CONDITIONS

Operating Pressure = 1 atm  
Average Current Density : 500 mA/sq.cm.  
Water Utilization Ratio (WUR) : 86.6 %  
Array Dimensions : 10 cm x 10 cm  
Inlet Gas Temperatures : 1423 K

---

\*Present Address : Sverdrup Technology, Inc.; NASA LeRC  
Group ; 2001 Aerospace Pkwy; Brook Park, Ohio 44142

ORIGINAL PAGE IS  
OF POOR QUALITY

i-V Relationship

Current-voltage characteristics for single solid oxide fuel cells were predicted by Maloney (6) and simplified for implementation to both fuel cell and electrolyzer array analyses. For MSOEZ arrays, two i-V relationships were used: A Best Case i-V relationship which included only material resistance; and an Estimated Case i-V relationship which encompassed all overpotential sources. Figure 1 represents typical Best Case and Estimated Case i-V curves for electrolysis operation while Figures 2 and 3 represent calculated Temperature Distributions and Current Density Distributions, respectively, for the solid electrolyte.

Effect of Inlet Reactant Gas Temperature

MSOEZ array performance is affected by the inlet gas temperatures. As the inlet gas temperatures increased, the average MSOEZ array temperature increased for both the Best Case and Estimated Case i-V relationship, as expected. Furthermore, average array temperatures for the Estimated Case were higher than those for the Best Case since more resistive heat is generated using the former case. The required applied voltages varied with the inlet gas temperatures in the manner shown in Figure 4.

Effect of Average Electrolyzer Array Current Density

The average current density of the MSOEZ array influenced both the average array temperature and the applied voltage requirements. Array voltage increased with average current density in the manner shown in Figure 5. The effect of current density on the average MSOEZ array temperature is shown in Figure 6.

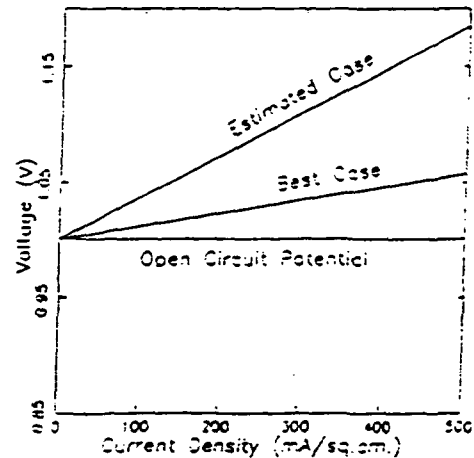


Figure 1. i-V Relationships used for Mod 0 Electrolyzer Array Analyses

ORIGINAL PAGE IS  
OF POOR QUALITY

SOLID OXIDE ELECTROLYZER TEMP. DIST.

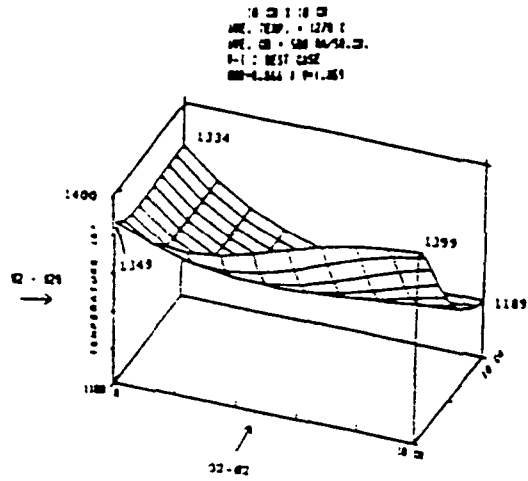


Figure 2. Temperature Distribution in 10 cm x 10 cm Mod 0 Electrolyzer Array Electrolyte with Best Case I-V Curve

Solid Oxide Electrolyzer Curr. Dens. Dist.

Ave. Temp. = 1279 K  
 Ave. C.D. = 540 mA/sq. cm.  
 I-V : Best Case  
 Wt% = 0.846 ; V = 1.359

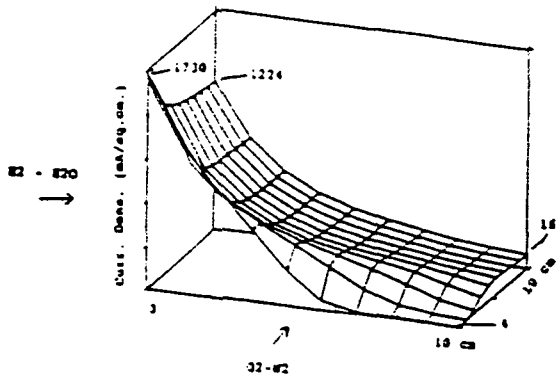


Figure 3. Current Density Distribution in 10 cm x 10 cm Mod 0 Electrolyzer Array Electrolyte with Best Case I-V Curve

ORIGINAL PAGE IS  
 OF POOR QUALITY

Conclusion

Performance estimations for Mod 0 MSOEX arrays were completed and some of the results were provided. Computer modeling results of this type may be used to aid the design of a monolithic solid oxide electrolysis sub-system and of a regenerative fuel cell system with various applications. An assessment of thermal stresses should also be undertaken as part of the design study.

REFERENCES

1. D.C. Fee, R.K. Steunenberg, T.D. Claar, R.B. Poeppel, and J.P. Ackerman, "Monolithic Fuel Cells", National Fuel Cell Seminar Abstracts, Courtesy Associates, Inc., Washington, DC., pp. 74-77, November 1983.
2. N.Q. Mingh, et al., "Fabrication and Characterization of Monolithic Solid Oxide Fuel Cells", Proceedings of the 1990 IECEC Vol. 3, Reno, Nevada, pp. 230-234, August 1990.
3. C.C. McPheeters, D.W. Dees, S.E. Dorris, and J.J. Picciolo, "Argonne Monolithic Solid Oxide Fuel Cell Fabrication", National Fuel Cell Seminar Abstracts, Courtesy Associates, Inc., Long Beach, CA, pp. 29-32, October 1988.
4. C.-Y. Lu and T.M. Maloney, "Mathematical Modeling of Solid Oxide Fuel Cells", National Fuel Cell Seminar Abstracts, Courtesy Associates, Inc., Long Beach, CA, pp. 78-83, October 1988.
5. T.M. Maloney, C.-Y. Lu, and G.A. Coulman, "Predicted Restrictions on Reactant Gas Utilizations in Monolithic Solid Oxide Fuel Cell Operation", Progress in Batteries & Solar Cells, Vol. 8, pp. 298-301, 1989.
6. T. M. Maloney, Doctoral Dissertation, Chemical Engineering Department, Penn College of Engineering, Cleveland State University, March, 1990.

Acknowledgement

This study was supported by the U.S. Department of Energy, Morgantown Energy Technology Center, through the NASA Lewis Research Center Fuel Cell Project Office.

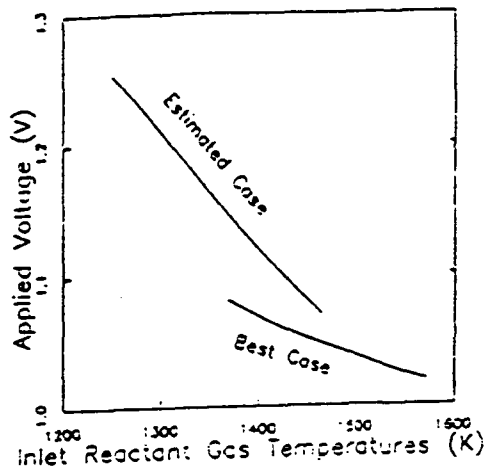


Figure 4. Effect of Inlet Electrolyzer Gas Temperature on Applied Electrolyzer Voltage

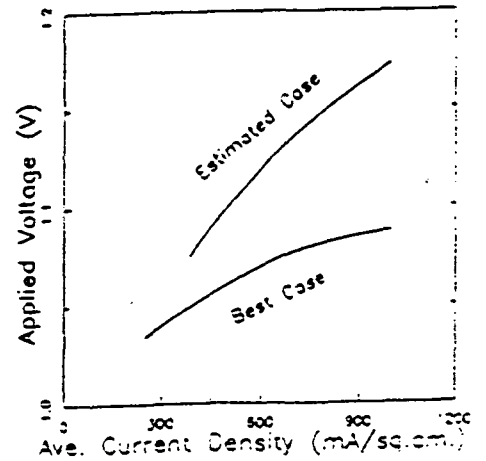


Figure 5. Relationship Between the Average Electrolyzer Array Current Density and the Applied Voltage

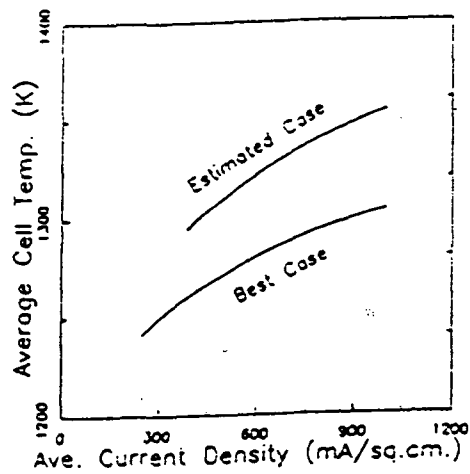


Figure 6. Effect of Electrolyzer Array Current Density on the Average Electrolyzer Array Operating Temperature

ORIGINAL PAGE IS  
OF POOR QUALITY